Novel strategies for multiplexing and fluorescence lifetime imaging in single molecule localisation microscopy

Surabhi Kottigegollahalli Sreenivas

PSL UNIVERSITÉ PARIS

THÈSE DE DOCTORAT

DE L'UNIVERSITÉ PSL

Préparée à l'École Supérieure de Physique et de Chimie Industrielles de la ville de Paris

Novel strategies for multiplexing and fluorescence lifetime imaging in single molecule localisation microscopy

Nouvelles stratégies de multiplexage et d'imagerie de la durée de vie de la fluorescence en microscopie de localisation de molécules uniques

Soutenue par

Surabhi K Sreenivas

Le 24 01 2023

École doctorale n°ED564

EDPIF

Spécialité

Physique

Préparée au

Institut Langevin, ISMO, ESPCI

Composition du jury :

Alexandra Fragola ESPCI Paris, France	*Président du jury*
Yannick de Wilde ESPCI Paris, France	*Examinateur*
Aymeric Leray Laboratoire Interdisciplinaire Carnot de Bourgogne, France	*Rapporteur*
Cyril Favard IRIM Montpellier, France	*Rapporteur*
Sandrine Lévêque-Fort ISMO, France	*Co-directrice*
Emmanuel Fort ESPCI Paris, France	*Directeur de thèse*

ESPCI PARIS | PSL

Acknowledgements

The thesis, apart from being a report of my research work at ESPCI towards my doctoral degree, is also a reflection of essential help, guidance, and good wishes that I have received from many in recent years. From the place where I stand now, I can look back to see so many others in the past who have shaped my education and thought process that has made me embark on this research work. Before starting, I am apologizing in advance for the people whom I might have forgotten to mention here, and I sincerely thank them all.

My research career in Paris started at Institut Langevin as an Intern under the prestigious French Charpak fellowship and then as a Master's student for my final year research project. I thank Prof. Emmanuel Fort for giving me those opportunities. Even today I vividly recall the joy of Paris life, stimulating discussions on topics of bouncing drops, and "time reversal" problems. Both problems are inventive while addressing broader research problems, which is a hallmark of our group. After completion of Master's degree, I joined ESPCI for my doctoral degree under the joint advisement of Prof. Emmanuel Fort and Prof. Sandrine Lévêque Fort. I sincerely thank Prof. Emmanuel Fort and Prof. Sandrine Lévêque Fort for their important role during my PhD, starting from introducing the research area of super resolution microscopy. The area of research is a confluence of biology and applied optics. It would not have been possible without their help and ingenuity to have worked on three amazing projects during my PhD. My association with the group has helped me to imbibe excitement in experimental physics, inventiveness, exposure to a variety of research problems, apart from super resolution imaging. I thank both for giving me such an amazing opportunity. I always count on their support and encouragement in my future endeavours.

I thank Prof. Ignacio Izzedin from Institut Langevin, ESPCI and Prof. Alexandra Fragola from ESPCI, Paris for being my thesis advisory committee members along with my supervisors, for keeping tabs on the progress and encouraging me throughout my PhD. And who were actively involved in discussions during my presentation and review which is a factor that helped in shaping up the research presented in this thesis. Along with them, I would like to thank Yannick de Wilde from ESPCI Paris, Cyril Favard from IRIM Montpellier and Aymeric Leray from Laboratoire Interdisciplinaire Carnot de Bourgogne for reviewing this thesis.

I would like to take this opportunity to thank everyone at Institut Langevin, ESPCI and ISMO for their involvement. I would like to thank all the members involved with the UPtoPARIS program including Virginie Cordoso, Suzanne Rera and Alexandra Marynets for their constant support and guidance. They were our points of contact for all the

procedures as well as the courses. I thank them for their time, efficiency, and helpfulness in sorting out any issues.

Institut Langevin provides an excellent environment in terms of scientific quality, exchange of ideas between researchers and faculty covering a wide research background. It was my privilege interacting with Prof. Arnaud Tourin, Prof. Yannick De Wilde, Prof. Claude Boccara and everyone else in the lab and listening to seminars. I would like to thank all my lab members at Langevin and ISMO, Maximilian Lengauer (Max), Pierre Bourdoncle, Adrien Mau, Clément Cabriel, Pierre Jouchet, Laurent Le, Abigail Illand, Lancelot Pincet and Guillaume Le Bourdelles. I would like to give a huge thanks to Viacheslav Mazlin (Slava) for all the wonderful discussions on many topics, including software interfacing and theoretical physics which made my lunch time cheerful and refreshing.

I thank my KV-IISc school teachers; Geetha P Chavan Ma'am, Jayashree Krishna Ma'am, Parimala Rao Ma'am, Sri Lakshmi Ma'am, T Rajeswari Ma'am, R Saroja Ma'am, Mukta Ma'am, Neeta Lav Ma'am, Chandran Sir and finally my most importantly Vinayak Bhat Sir who taught me Sanskrit, which added a holistic dimension to my learning.

I would also like to thank all the faculty at IISER-Pune who trained me in Biology, Math and Physics, that broad base definitely helped me during this research work. I thank Campus France India for the Internship fellowship which helped me forge contact with Prof Emmanuel Fort's group at Institut Langevin. I fondly recall my discussions and encouraging words from Prof. Yves Couder, with a heavy heart I feel it was a privilege to have those interactions with him, we all in the group truly miss him.

I thank everyone, including Dr. S Rasika, who made my stay in Paris noteworthy. Indian embassy at Paris for many cultural and social events through which I could meet people from different parts of India and France. I sincerely thank Dr. Srini Kaveri for his help and encouragement on many occasions during this period.

Finally, I would like to thank my parents, brother Suhas, my friends and extended family for their constant support throughout this endeavour. I would like to dedicate this thesis to my Ajji and Thatha (my grandparents) who always wished me the best and found happiness in my success.

Résumé

La microscopie de fluorescence super-résolue par localisation de molécules uniques appelée *Single Molecule Localisation Microscopy* (SMLM) offre une sensibilité compatible avec l'émission d'un émetteur individuel et une résolution de l'ordre de dizaines de nanomètres. La SMLM s'impose actuellement comme un outil important pour identifier les assemblages moléculaires au sein d'une cellule. Dans ce contexte, le multiplexage, c'est-à-dire l'imagerie simultanée de plusieurs émetteurs fluorescents permettant de révéler différentes biomolécules, reste un défi à relever. Dans cette thèse, les caractéristiques de fluorescence des émetteurs, telles que le flux, sont utilisées comme une nouvelle source de contraste pour imager différentes protéines, et permet également de venir améliorer des approches de demixage basées sur les propriétés spectrales des fluoropphores. La deuxième propriété, la durée de vie de fluorescence, est utilisée pour concevoir de nouvelles approches pour l'imagerie de fluorescence résolue en temps FLIM. Généralement, l'identification de différentes protéines est basée sur une méthode d'acquisition séquentielle de fluorophores ayant des spectres d'émission suffisamment différents. Ces méthodes présentent différents inconvénieents comme l'utilisation couteuse de plusieurs lasers, en fonction des gammes de longueur d'onde utilisées l'imapct des aberrations chromatiques peut entrainer des biais de mesures importants, de plus la vitesse d'acquisition est nécéssairement impactée par la nécessité des acquisitions successives. Dans la première partie de cette thèse, une nouvelle stratégie de démixage est présentée, basée sur le flux de fluorescence d'un fluorophore. Lorsque des facteurs tels que l'illumination, l'efficacité de la collection et son environnement chimique local sont contrôlés, le flux détecté dépend du type d'émetteur du fluorophore, et peut être utilisé pour distinguer différentes espèces. Comme cette technique est indépendante des spectres d'émission, elle peut être appliquée à des fluorophores dont les spectres sont très proches, et peut être mise en œuvre avec un système de microscopie SMLM monocameéra standard SMLM sans nécéssité de matériel supplémentaire. De plus, cette approche peut également permettre d'améliorer l'efficacité du démixage dans un système de spectral demixing conventionnel. La deuxième partie de la thèse se concentre sur de nouvelles approches pour la microscopie de fluorescence résolue en temps *Fluorescence Lifetime Imaging Microscopy* (FLIM) basé sur le flux émis. Nous proposons deux nouvelles stratégies basées sur le flux dans lesquelles il n'est pas nécessaire d'utiliser un laser pulsé ou un système de détection rapide et coûteux. Dans le régime de saturation d'un fluorophore, le flux émis dépend de la durée de vie de la fluorescence. Cela peut être utilisé pour estimer les durées de vie et pour distinguer deux émetteurs fluoroscents. Dans la première configuration, on utilise un laser continu déclenché pendant des portes dans

la gamme des microsecondes afin de saturer le fluorophore. À saturation, le flux détecté dépend du nombre maximal de cycles d'absorption-émission de fluorescence et donc de la durée de vie de la fluorescence. La variation du signal détecté en fonction de l'excitation jusqu'à la saturation nous permet de retrouver la durée de vie de fluorescence. Comme preuve de concept, nous avons pu distinguer deux types de billes fluorescentes incorporant deux fluorophores de durée de vie différentes. La deuxième configuration implique l'utilisation d'un laser pulsé avec une ligne à retard optique pour contrôler le délai entre deux impulsions successives. A saturation, en raison de l'anti-bunching, le signal détecté intégré sur une série donnée de doubles impulsions dépend du retard entre ces impulsions. La durée de vie de la fluorescence peut être extraite à partir d'acquisitions de signaux avec un retard variable. La théorie de cette technique et la configuration du montage sont présentées dans cette thèse.

Mots clés : Super-résolution, Microscopie, Multiplexage, Flux, SMLM, FLIM, Saturation

Abstract

Single Molecule Localization Microscopy *Single Molecule Localisation Microscopy* (SMLM) is a one of the super-resolution fluorescence microscopy, it exhibits a sensitivity down to an individual emitter and offers a resolution in the order of tens of nanometers. SMLM is central in unravelling molecular assemblies and molecular dynamics within a cell. In this context multiplexing which is the imaging of multiple fluorophore emitters simultaneously via labelling of various types of bio-molecules is still a challenge and is highly desirable. In this thesis fluorescence characteristics of fluorophore emitters such as flux is presented as a novel technique for multiplexing but also improved approach for spectral demixing, and the second property being lifetime is used to design new techniques theoretically and experimentally for Fluorescence Lifetime Imaging FLIM. Multiplexing and demixing is either based on a method of sequential acquisition of targeted fluorophores or with fluorophores having sufficiently different spectra. These methods are expensive setups due to multiple laser, prone to chromatic aberrations and slow in terms of acquisition. In the first part of this thesis, a novel demixing strategy is presented based on fluorescence-flux of a fluorophore. When factors such as illumination, collection efficiency and its local chemical environment are controlled, detected flux depends on the type of fluorophore emitter, and can be used to distinguish different species and perform simultaneous demixing. As the technique is independent of emission spectra, this technique can be applied to spectrally overlapping fluorophores, and can be implemented with standard SMLM monocamera system with no additional hardware. This can also further enhance the efficiency of demixing in a conventional spectral demixing system. The second part of the thesis focuses on novel approaches to perform *Fluorescence Lifetime Imaging Microscopy* (FLIM) based on the emitted flux. We propose two new flux-based strategies in which one does not require a pulsed laser or a fast and expensive detection systems. In the saturation regime of a fluorophore, emitted flux depends on fluorescence lifetime. This can be used to estimate lifetimes and to distinguish two fluorophore emitters. In the first configuration, a continuous wave laser gated in the microsecond range is used that can saturate the fluorophore. At saturation the detected flux depends on the maximum number of fluorescence absorption-emission cycles and hence on the fluorescence lifetime. The variation of the detected signal as a function of the excitation up to saturation enables us to retrieve the fluorescence lifetime. As a proof of concept, we distinguish two types of fluorophore beads with this configuration. The second configuration involves the use of a pulsed laser with an optical delay line to control the time delay between two successive pulses. At saturation, due to anti-bunching, detected signal integrated over a given series

of double pulses depends on the delay. The fluorescence lifetime can be retrieved from signal acquisitions with a varying delay. The theory for this technique and the configuration of the setup are presented in this thesis.

Keywords : Super-resolution, Microscopy, Multiplexing, Flux, SMLM, FLIM, Saturation

Contents

Acronyms

AOI *Area of Illumination*

AOM *Acousto-Optic Modulator*

APD *Avalanche Photo-Diode*

ASTER *Adaptable Scanning for Tunable Excitation Regions*

CI *Confidence Interval*

CMOS *Complementary Metal Oxide Semiconductor*

CRLB *Cramer-Rao Lower Bound*

CW *Continuous Wave*

DBSCAN *Density-based spatial clustering of applications with noise*

DNA-PAINT *DNA-Point Accumulation for Imaging in Nanoscale Topography*

DONALD *Direct Optical Nanoscopy with Axially Localized Detection*

DPFLIM *Double Pulse Fluorescence Lifetime Imaging*

dSTORM *direct Stochastic Optical Reconstruction Microscopy*

EGFP *Enhanced Green Fluorescent Protein*

EOM *Electro-Optic Modulator*

FCS *Fluorescence Correlation Spectroscopy*

FLIM *Fluorescence Lifetime Imaging Microscopy*

fm-DNA-PAINT *Frequency Multiplexing DNA-Point Accumulation for Imaging in Nanoscale Topography*

fmSTORM *Frequency Multiplexing Stochastic Optical Reconstruction Microscopy*

FOV *Field of View*

FPS *Frame rate Per Second*

FRET *Förster Resonance Energy Transfer*

FWHM *Full Width at Half Maximum*

GFP *Green Fluorescent Protein*

GSD *Ground State Depletion*

HiLo *Highly inclined and Laminated optical sheet*

HOMO *Highest Occupied Molecular Orbital*

IRF *Instrument Response Function*

LUMO *Lowest Unpaired Molecular Orbital*

MLE *Maximum Likelihood Estimator*

MP *Mega Pixels*

NA *Numerical Aperture*

OD *Optical Density*

PAINT *Point Accumulation for Imaging in Nanoscale Topography*

PALM *Photoactivated Localization Microscopy*

PMT *Photo-Multiplier Tube*

PSF *Point Spread Function*

Res *Resolution*

RESOLFT *Reversible Saturable OpticaL Fluorescence Transitions*

RF *Radio Frequency*

ROI *Region of Interest*

SAF *Super-critical Angle Fluorescence*

SCMOS *Scientific Complementary Metal Oxide Semiconductor*

SCW *Super-Continuum Wave*

SD *Spectral Demxing*

SIM *Structured Illumination Microscopy*

SMLM *Single Molecule Localisation Microscopy*

SNR *Signal to Noise Ratio*

SPAD *Single Photon Avalanche Diode*

SR *Super Resolution*

SR-STORM *Super Resolution Stochastic Optical Reconstruction Microscopy*

STED *Stimulated Emission Depletion*

STORM *Stochastic Optical Reconstruction Microscopy*

TAC *Time Amplitude converter Circuit*

TBS *3,5,3,5-tetra-t-butyl-p-sexiphenyl dye*

TCSPC *Time Correlated Single Photon Counting*

TG *Time Gated*

TIRF *Total Internal Reflection Fluorescence*

Chapter 1

Introduction to Fluorescence Microscopy

Summary

In this chapter we are going to briefly discuss fluorescence thereby motivating fluorescence microscopy, especially in the biological context. This chapter elucidates various techniques of fluorescence microscopy followed by techniques in super-resolution microscopy to overcome the diffraction barrier. We discuss *Single Molecule Localisation Microscopy* (SMLM) which is the go-to technique in biological fluorescence super-resolution imaging. We classify existing SMLM techniques into two types based on how sparsity of fluorophore tags is achieved. Techniques which rely on a deterministic approach and the other, on a stochastic approach. We discuss the stochastic approach of *DNA-Point Accumulation for Imaging in Nanoscale Topography* (DNA-PAINT) in depth and its versatility and advantages over other techniques. This chapter also motivates the limitations of various techniques, especially with regard to multiple fluorophore imaging (multiplexing) in biological samples.

Contents

1 Introduction to Fluorescence Microscopy

Fluorescence microscopy is one of the most common techniques used to image biological samples. Here we present an example of a fluorescence microscopy image in Figure 1.1.

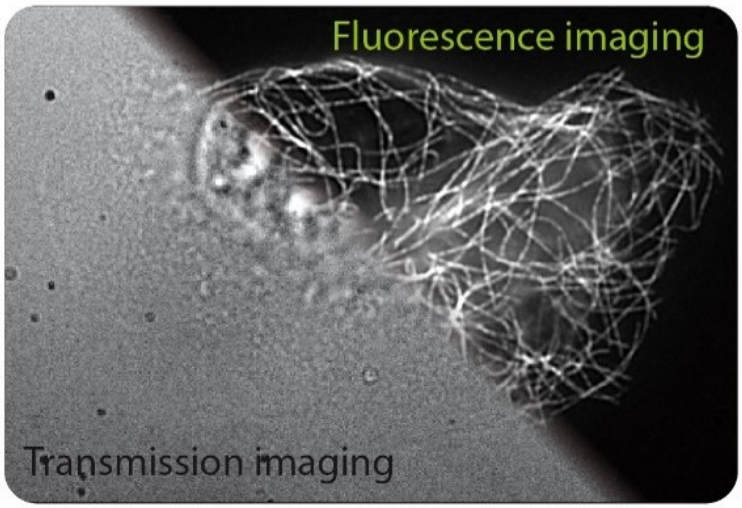

Figure 1.1: Figure illustrating transmission image through a simple microscope versus the fluorescence image of the same [Bourg, 2016]. The sample is a COS7 cell with microtubules tagged with AF560.

Before we go into further details of the system, we briefly explain what fluorescence is and why it is especially relevant for imaging biological samples. All molecules consist of atoms whose electrons can be pumped to an excited state with a certain range of wavelengths that contribute to the corresponding energy to transition from the ground state to the excited state as indicated in Figure 1.2. While spontaneously relaxing to the ground state the electrons emit photons and this process is called fluorescence. Due to the fact that an atom has several vibrational states at each energy level where electrons can transition to; within a given state, as shown in Figure 1.2, the excitation and relaxation is thus across a range of wavelengths defined as the absorption and emission spectra respectively shown in Figure 1.2 (b). An illustrative example of this is depicted in Figure 1.2 through the Jablonski diagram. The emitted fluorescence is always of lesser energy due to vibrational relaxations and this introduces a shift towards a higher wavelength for the peak emission when compared to the peak excitation for a given atom. This is called Stokes shift as we see in Figure 1.2 (b) (shift of wavelength for Blue (excitation) to Green (emission)). This is very useful for biological imaging since the emission is highly specific to the molecule. This places fluorescence imaging as a go to approach when it comes to imaging biological samples. The characteristic lifetime for decay is called the lifetime of the fluorophore. At times depending on the local environment there can be *Förster Resonance Energy Transfer* (FRET) wherein through dipole-dipole coupling of the excited atom to an ambient atom energy transfer occurs. But we will discuss more on the lifetime aspect of fluorophore

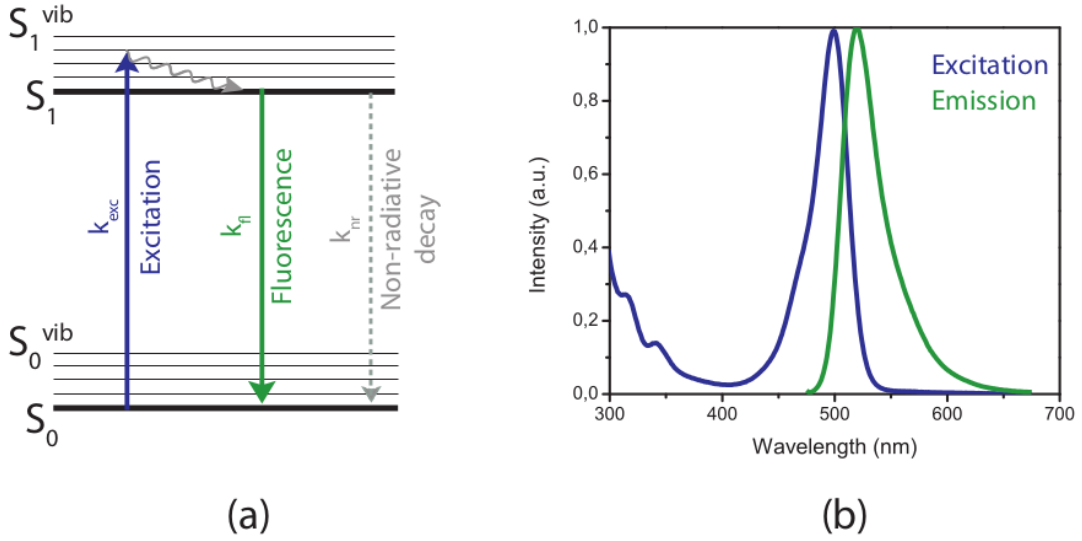

Figure 1.2: Absorption-emission spectra of a fluorophore emitter. The corresponding fine energy transitions are depicted above. Molecules in the ground state S_0 absorbs incoming photons in the excitation beam to reach the excited state S_1. They then undergo a relaxation, dissipating energy, returning to the ground state through spontaneous emission [Schreiber, 2018].

emitters in Chapter 4.

In fluorescence microscopy images as seen with an example image in Figure 1.1, molecules are used to tag organelles through binding them to the protein present in the organelle of choice, and they transition to the excited state upon illumination of light. (Some molecules in the cell do have auto-fluorescence depending on the wavelength of exposure. This does hinder fluorescence imaging but fluorophore tags are designed to have higher emission and are highly specific unlike interstitial molecules from cellular pathways.) Molecules then fluoresce, emitting photons, which are then collected by detectors as a proxy for the organelle. The fluorescent molecule is chemically designed to have affinity to the organelle of choice, this is done either by transfecting cells so that they are genetically encoded to produce fluorescence or through using antibodies as binding agents to tag target organelles in a sample, more of which will be discussed in the next Section. The sample is then illuminated with the corresponding wavelength of light using a laser which excites the molecules and they spontaneously emit photons (fluorescence) which is detected using a detector like a photon counter or a camera. If one wants instantaneous spatial information (widefield microscopy) a camera is used otherwise in the case of a confocal microscope (point based imaging) each point is scanned and the photon counter counts the signal and repeats this on moving to the next spot. The fluorescence signal is the number of photons, that is, the number of cycles of fluorescence of the fluorescent molecule (each cycle emits one photon). This has to be significant enough to be detected by the detector. Each molecule has its characteristic lifetime, absorption cross section,

quantum yield (function of local environment). We will discuss all these parameters in depth in the coming Chapters. To excite a molecule, the right wavelength of light has to be used which is decided based on the absorption spectrum of the molecule. Excitation using a laser closer to the absorption peak wavelength yields more signal/photons from the molecule for the same excitation power.

1.1 Introduction to Fluorescence Microscopy Setup

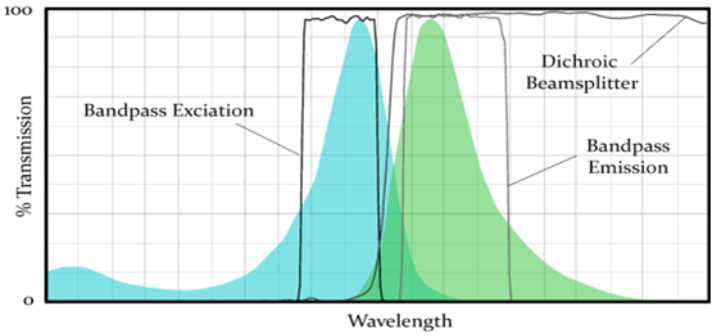

Figure 1.3: Dichroic filter wavelength range. The Spectrum highlighted in Blue doesn't get transmitted, but the spectrum highlighted in Green does get transmitted through the filter[1].

The optical setup used in fluorescence microscopy is composed of lasers to excite the fluorophore, an inverted microscope with high *Numerical Aperture* (NA), magnification, immersion objective and a detection channel with a camera and/or photon counter. As part of the detection channel, there is always a dichroic (a wavelength based filter as indicated in Figure 1.3) that transmits and reflects light based on a cut off wavelength. This is to prevent the excitation beam from registering as part of the signal/detection. The dichroic is sensitive to directionality since its properties are due to a surface coating.

As shown below in Figure 1.4 (a) The setup on the left outlines the main components for widefield fluorescence microscopy. The beam illustrated is impinging on the dichroic mirror and goes through the objective onto the sample and the emitted light from the sample passing through the dichroic mirror, then the emission filter (filter open only to emission wavelength of the fluorophore of choice) and finally reaches the detector which is a camera in this case. Widefield imaging has the main disadvantage of collecting photons from all planes, thus having a background which is usually constant and can be corrected for. But due to this, one can image up to only a few microns in the sample. However widefield also allows for the use of a camera giving all the spatial information in one frame.

[1] https:\kern-\h@ngcolonwd\kern\h@ngcolonwd//www.chroma.com/knowledge-resources/about-fluorescence/fluorescence-filters/fluorescence-filter-types

The point based method for example, the confocal has the advantage of reducing the background by using a diaphragm/pinhole to image only one plane of the sample as demonstrated in Figure 1.4 (b). But a fast photon counter/photodetector needs to be used to scan the image point by point. It also requires an optimization between scanning area and scanning speed. This is valid for 2D imaging. For 3D imaging the plane of focus has to be moved axially.

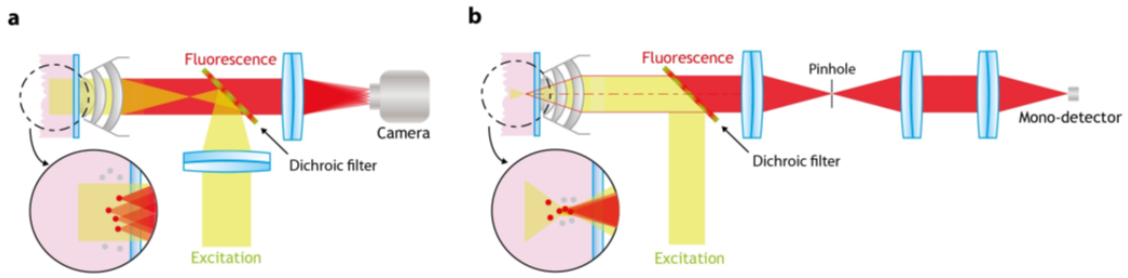

Figure 1.4: Optical setups used in fluorescence microscopy. (a) Widefield microscope. The excitation beam is sent through the objective lens to create a wide homogeneous excitation. The fluorescence is collected by the same objective and separated from the excitation beam thanks to a dichroic beam splitter. Finally, the image is formed on the camera. (b) Point scanning microscope. The excitation beam is focused through the objective on a tiny region of the sample, and the fluorescence is collected by the same objective, separated from the excitation thanks to a dichroic beam splitter, and sent on a monodetector (such as a photodiode). In the confocal microscope, a pinhole is added in the detection path to get rid of the out-of-focus signal. [Bourg, 2016]

Generally we also have microscopes implemented in *Total Internal Reflection Fluorescence* (TIRF) configuration. Wherein there is a mismatch of refractive indices and the beam gets focused in the back focal plane and is at an angle beyond the critical angle. Thus the beam is reflected at the glass interface and an evanescent wave is created at the coverslip. The penetration depth of this is around half the wavelength of the beam, thereby reducing the background to a large extent. For this a large NA is very important. And then there is *Highly inclined and Laminated optical sheet* (HiLo) which also suppresses the background. HiLo permits the benefit of having an inclined excitation which can be used for sectioning deeper but as a trade-off we have a smaller *Field of View* (FOV), within the sample due to the pseudo light sheet generated. And for an angle less than the critical angle we have epi-fluorescence which has significant background. Thus, HiLo and TIRF is used to suppress background and inhomogeneity in z (axial plane).

Now that we have covered fluorescence, fluorescence microscopy and both point based as well as widefield microscopy we move on to the challenge of optical microscopy, the diffraction limit in the coming Section.

2 Diffraction limit

All types of microscopy is limited by the diffraction limit. A physical limit often characterised as the resolution limit wherein two points located at a shorter distance than this limit cannot be discerned as two separate points, and they appear as a single point. The diffraction pattern for an $aperture(NA) = a$ is described by the airy function given by

$$I(\theta) = I_0[\frac{2J_1 ka(sin\theta)}{kasin\theta}]^2 \tag{1.1}$$

Where $J_1(x)$ is the first Bessel function and k_1 is the wave number given by $2\pi/\lambda$. The first zero of the Bessel function occurs at $x = 3.83$ so that gives us

$$kasin\theta = 3.83 \tag{1.2}$$

$$sin\theta = \frac{1.22\lambda}{2NA} \tag{1.3}$$

Thus, we have the resolution given by the minimum distance that we can discern that is, two neighboring Airy patterns are just resolvable when the maximum of one Airy pattern is at the minimum of the other Airy pattern,

The diffraction limit depends on the wavelength of light used to illuminate the sample, *Numerical Aperture* (NA) of the objective which is basically defined below (larger the NA, more photons can be collected) the range of solid angles through which light can be collected is called the angle of collection θ and the refractive index n of the medium through which the emitted light is collected.

$$Res = \frac{1.22 \quad \lambda_{illumination}}{2NA} \qquad where \qquad NA = nsin\theta \tag{1.4}$$

In order to avoid this limitation, in the early 2000s, a new technique of microscopy that could probe the sample beyond the resolution limit called super-resolution microscopy techniques [Basché, 2008] [Hell, 1994] were invented. We will discuss more about the various techniques and their respective implementation in the coming Section.

Both confocal and widefield imaging are limited by diffraction. This is a fundamental limit imposed due to the fact that the wavefronts from two "close" points interfere and form a diffraction pattern that has high intensity at the center (zero order) followed by alternating rings of constructive and destructive interference. This happens when the point is in focus. The point cannot be resolved beyond this and is limited to the size of the central peak, which is shown in Figure 1.5.

The size of the central peak is determined by the numerical aperture of the objective, refractive index of the medium and the wavelength of the light emitted by the point. For all objectives, this is called the airy disk illustrated in Figure 1.5.

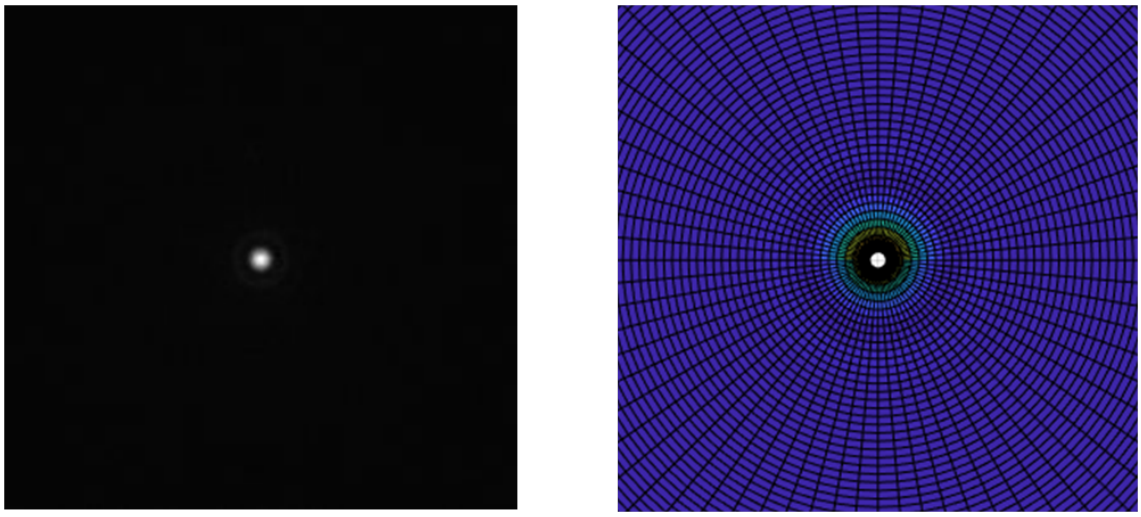

Figure 1.5: Left: Diffraction limited image of 100 nm bead Right: Airy disk simulated for a 100 nm particle diameter computed through the corresponding Bessel function for every 6 degrees radially, across a 100 x 100 grid in xy and xz planes.

Abbe's diffraction limit defined in terms of the minimum distance that can be resolved for two close points is defined as $Resolution(Res) = \frac{1.22\lambda}{2NA}$ where $NA = nsin\theta$. Thus two points below this distance cannot be resolved, that is, they cannot be demarcated as two separate points and will look identical. Confocal circumvents this by scanning a small area which is still diffraction limited but contrast enhanced. Generally, a Confocal system has a resolution limit of around 100 micrometers in the axial direction and around 250 nm in the 2D plane. In a Confocal system the parameters of scanning speed that is the dwell time and the size of the FOV have a trade off and need to be optimized to obtain the best possible resolution. Typically the airy radius is around 300 nm and it is called as the *Point Spread Function* (PSF) of the emitter. In addition to the *Point Spread Function* (PSF) being emitted by the molecule/site of interest, it is also blurred out additionally because of the detection process. This is mathematically represented as the convolution of the spatial distribution of fluorescence emission and the airy function, thus the net effective distortion is more than the average 300 nm of the airy disk. The airy disk also severely limits imaging in z as it stretches the point axially more than laterally. Image formation and localisation precision for such PSFs is discussed in the next Section. The resolution distance in the system goes as $\frac{1}{\sqrt{N}}$ and in detail we have equation 1.6 given below for the full expression.

2.1 Localisation Precision

As you can see in Figure 1.6 we see image formation occurs as follows.

In the case of widefield imaging we are limited in terms of the airy disk as shown in Figure 1.6. But using a clever way to image, we can do better even with such a diffracted PSF which we will discuss in the next Section. The localization precision of a given experiment is theoretically defined by the *Cramer-Rao Lower Bound* (CRLB) measurement.

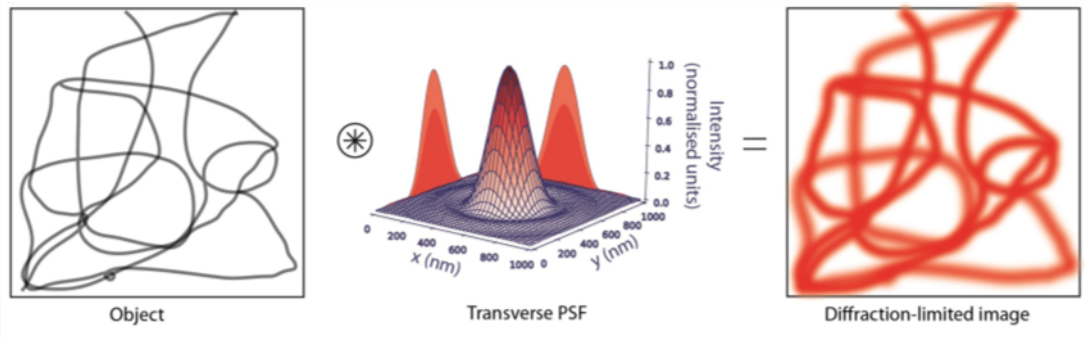

Figure 1.6: Image formation on the camera through convolution of *Point Spread Function* (PSF) at the actual location across all frames [Bourg, 2016]

This is also used as one of the parameters to report the resolution of the setup and the experiment. Theoretically CRLB is defined by looking at the minimum variance of the *Maximum Likelihood Estimator* (MLE) and then using the Cauchy-Schwartz inequality to quantify the lower bound.

$$Res \quad \propto \quad \frac{1}{\sqrt{N}} \tag{1.5}$$

Every photon captured in the image provides information about the target's position, and this error in position for each measurement exhibits itself as the standard deviation of the point spread function PSF. The best estimate of position, known as localization precision is calculated comprising all the major contributing parameters as discussed below. The error in the measurement of the PSF and its centroid is due to primarily three causes, firstly photon noise (which includes the photon shot noise in terms of the Poissonian statistics), secondly noise due to pixelation (uncertainty as to where exactly in the pixel the photon has arrived) and thirdly most importantly the noise from the background.

And for localization precision as per the CRLB we can state it as follows from [Thompson, 2002]

$$Loc.precision = \frac{s^2 + a^2/12}{N} \quad + \quad \frac{4\sqrt{\pi}s^3b^2}{aN^2} \tag{1.6}$$

Where s is the standard deviation of the PSF, a is the size of a pixel in the camera, N is the number of photons in the PSF and b is the background signal in the PSF. The localization precision thus improves with a narrower PSF or more number of photons inside the PSF as well as less background. Thus using this we can fit the PSF generally using a 2D Gaussian, which is spread across several pixels and finally obtain a sub-pixel detection resolution of the center of the PSF. This is used to calculate the resolution in SMLM.

Thus, taking advantage of the fact that we can fit a 2D Gaussian to the PSF across several pixels we need to ensure that we don't have overlapping PSFs in one frame. If we

manage to spread the PSFs sparsely across the sample in one frame we can effectively localize these points. Now repeating this process over many frames provides a reconstructed image which is super resolved. In order to do this we need to have sparse tags across a frame that can be achieve by using fluorophores that blink/photoswitchable or using click chemistry as exploited by DNA-PAINT which binds and unbinds. We will discuss more about this in the following Section. This approach is exactly what is done in *Single Molecule Localisation Microscopy* (SMLM), which we will discuss below.

3 Techniques of Super-resolution Imaging

There are various techniques of overcoming this physical limitation of diffraction limit. *Single Molecule Localisation Microscopy* (SMLM) is one such technique. The other competitor being STED which we will discuss in the next Section and *Structured Illumination Microscopy* (SIM) [Gustafsson, 2000] which only provides a factor two of improvement but a straightforward compatibility for live cells imaging.

The idea in this method is to isolate the fluorophores so that two fluorophores in a given frame are not located close to one another below the diffraction limit. Thus, we have a single molecule localized at spatial scales close to the diffraction limit. The fluorophores need to emit signal at different locations at different times/frames randomly in order to get a full picture of the sample. This cleverly eliminates the need to probe beyond the diffraction limit. We will discuss more on how this is achieved both in term of fluorophores as well as detection here.

3.1 *Single Molecule Localisation Microscopy* (SMLM)

SMLM describes a set of powerful imaging techniques that improve spatial resolution over standard, diffraction limited microscopy and can image biological structures at the nanometer scale. In SMLM, individual fluorescent molecules are localized from diffraction-limited image sequences and these localizations are used to generate a super resolved image.

In SMLM the concentration of the fluorescent probes is kept low. This way the probability of overlapping of two fluorophores and thereby their emission is not high. Thus emission from a single source can then be used to detect the coordinates of the molecule precisely by fitting the airy function of the emission data and extracting the centroid. The calculation of the coordinates can be done by fitting a 2D Gaussian and locating the center as shown in the previous Figure 1.8. This technique is illustrated in Figure 1.7. And the image obtained through this technique is given in Figure 1.9. We see that the final image is reconstructed using a series of diffraction limited images which are used to detect the centroid of the PSFs in each frame and then accumulated together for the final image across the full *Region of Interest* (ROI).

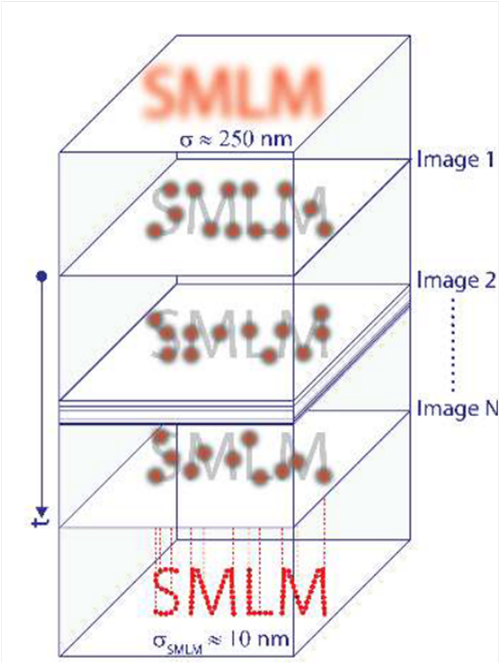

Figure 1.7: SMLM technique schematically illustrated [Bourg, 2016]

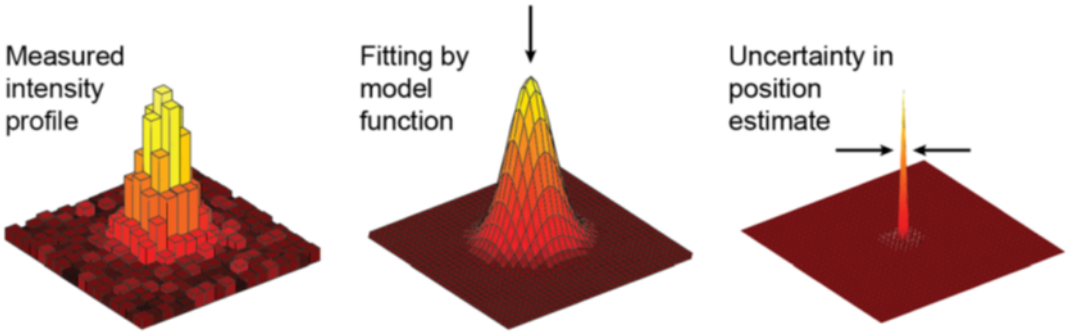

Figure 1.8: Localisation through centroid detection by fitting intensity *Point Spread Function* (PSF) with a 2D Gaussian [Bourg, 2016]

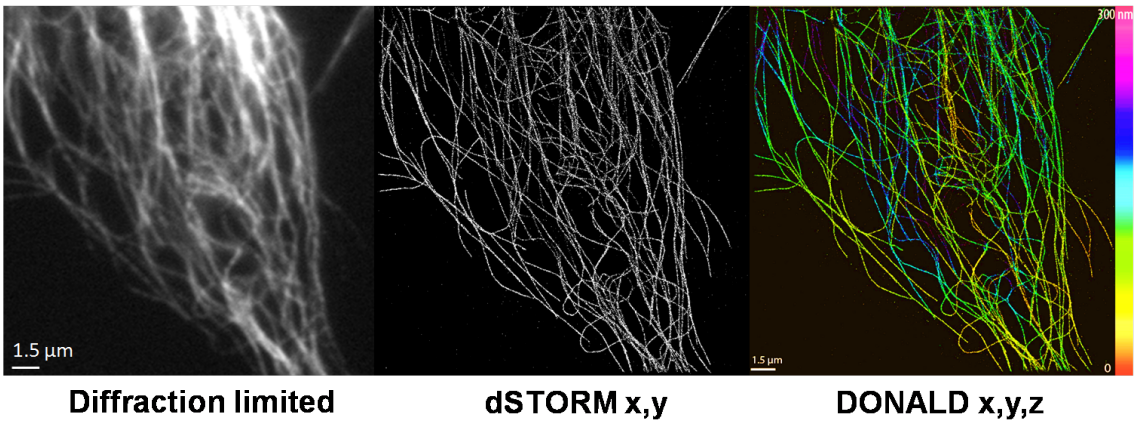

Figure 1.9: Cos7 labelled Tubulin network with AF647 STORM imaging with HiLo illumination in TIRF. Here we have a diffraction limited image, STORM image and a super resolved 3D SMLM image using *Direct Optical Nanoscopy with Axially Localized Detection* (DONALD) where the colorbar indicates the depth. Scale d550 nm.[Bourg, 2016]

3.2 Classification of Techniques

Broadly we can classify SMLM into two main categories based on how the fluorophores are made to emit at various locations at various times. The first category would be deterministic which means that all the tags are already attached to the target and one toggles them "ON" and "OFF" by exploiting the photochemistry of the fluorophore molecules sequentially in space. And the second category is stochastic wherein molecules are randomly rendered into "ON and "OFF" states either by exploiting their photochemistry or through their binding and unbinding affinities at the target. The key feature being randomness of signal emission. Both these techniques operate at the single molecule regime, thereby eliminating the need to probe sub-diffraction length scales but offering resolution of a few nanometers.

In terms of classification, broadly the deterministic techniques include all variations based on *Stimulated Emission Depletion* (STED), *Reversible Saturable OpticaL Fluorescence Transitions* (RESOLFT) and *Ground State Depletion* (GSD). And under stochastic techniques we have variations of *Stochastic Optical Reconstruction Microscopy* (STORM), *Photoactivated Localization Microscopy* (PALM) and *Point Accumulation for Imaging in Nanoscale Topography* (PAINT). We will briefly discuss each technique below.

3.3 Deterministic Techniques

Stimulated Emission Depletion (STED) is the most general application of using a scanning technique to individually probe each target location in the sample. Both RESOLFT and GSD are based on the STED principle. In all these techniques multiple wavelengths of illumination are required, to activate/ground state depletion, deactivate/stimulated depletion and for excitation. In STED all the fluorophores are initailly rendered active and excited and a depletion beam shaped like a doughnut is used to deplete all the fluorophores except the one at the center. This is then repeated across the *Region of Interest* (ROI) to obtain the super resolved image.

In *Reversible Saturable OpticaL Fluorescence Transitions* (RESOLFT) the principle of scanning from STED is implemented, the difference being that the fluorophores are turned into the dark state through illumining with a certain wavelength for example in Cy3-Alexa647 heterodimer, Alexa647, emits fluorescence upon a red laser illumination and goes into a dark state, whereas Cy3 helps the activation process under green laser irradiation [Kwon, 2015]. In *Ground State Depletion* (GSD) also uses the same principle as RESOLFT and the molecules are rendered into a triplet dark state by either illumination or oxygen depletion.

3.4 Stochastic Techniques

Techniques using stochastic randomness to do SMLM include PAINT, STORM and PALM.

To achieve blinking and stochasticity, one of the techniques called *Photoactivated Localization Microscopy* (PALM) uses proteins that can be activated using a certain wavelength of light, generally in the UV range. Once active, these proteins can be excited and then they fluoresce. The molecules undergo many such excitation and de-excitation cycles until they bleach (changes in the chemical structure that no longer allow for excitation). PALM uses photoswitchable proteins and low illumination power so that the molecules are randomly rendered activated through the first UV irradiation followed by dim illumination. This allows one to acquire localizations across many frames.

The other technique to have a stochastic distribution of "ON" molecules is *Stochastic Optical Reconstruction Microscopy* (STORM) that uses dyes that are installed into the cell sample through immonolabelling. These dyes can be rendered inactive by switching off their ON state and putting them into the dark state. This allows for blinking and reconstruction. Thus STORM typically involves activation, excitation and switching to dark state. The blinking also happens randomly at times due to not just bleaching but some random chemical processes in the sample that trigger the dark state. Thus buffers play a very important role in these imaging work flows. Unlike transfected fluorescent proteins (like GFP) the dSTORM fluorophores are attached to their respective proteins of interest by making the cell membrane permeable to the tags. Nevertheless STORM is better in terms of *Signal to Noise Ratio* (SNR) compared to PALM as it is not constrained by low illumination, thus it also has better localization precision due to less background noise on the other hand is more prone to phototoxicity. The dSTORM fluorophores are typically excited in the red wavelengths (560 nm – 750 nm). The illumination intensity is also high to render fluorophores into the dark state ($4kW.cm^{-}2$).

The final approach is using *DNA-Point Accumulation for Imaging in Nanoscale Topography* (DNA-PAINT). Wherein the fluorescent probes attached with an unbound DNA (which is complimentary) strand are present in the imaging buffer. Thanks to click chemistry and engineered affinity of the complimentary DNA strand - which is attached to the site of interest, the probes can be localized. To use more technical terms, DNA-conjugated antibodies are attached to organelles/proteins of interest through immunolabelling. The imagers contained in the buffer are composed of fluorophores functionalised with the complementary DNA strand, which ensures specific binding to the target. PAINT docked times are typically higher than the ON times of dSTORM organic dyes (a few hundred milliseconds versus a few ten milliseconds). Except in the case of imagers that are non-fluorescent as long as they are not docked, PAINT produces rather high amounts of background fluorescence light, which sometimes require the use of complementary optical sectioning

methods. A major advantage of PAINT is that the imagers are provided in large excess in the immersion buffer, and photobleaching is thus not a problem since the docking site remains accessible to unbleached molecules, enabling longer experiment times. Generally, optical power densities used in PAINT experiments are somewhat lower than in dSTORM ($1\check{}2kW.cm^{-}2$ [Cabriel, 2019b]).

3.4.1 DNA-PAINT

Single Molecule Localisation Microscopy (SMLM) is one of the conventional techniques for biological imaging, due to its edge in overcoming the diffraction limit by spreading detections across the time domain as discussed. The super-resolved image is then reconstructed by superimposing the centroid locations collected over all frames. This has opened up new ways of imaging with drastic improvement in terms of resolution being pushed to around 10 nm [Bon, 2015]. In terms of biological application it is important to augment this technique with the option of utilizing multiple labels so that multiple target sites in a cell can be visualized simultaneously. This is currently being carried out using transfection in cell as in the case of *Green Fluorescent Protein* (GFP), immunolabeling which involves using a primary antibody connected to the antigen (target molecule in the cell) and secondary antibody (which has the fluorescent probe) which attaches to the primary antibody.

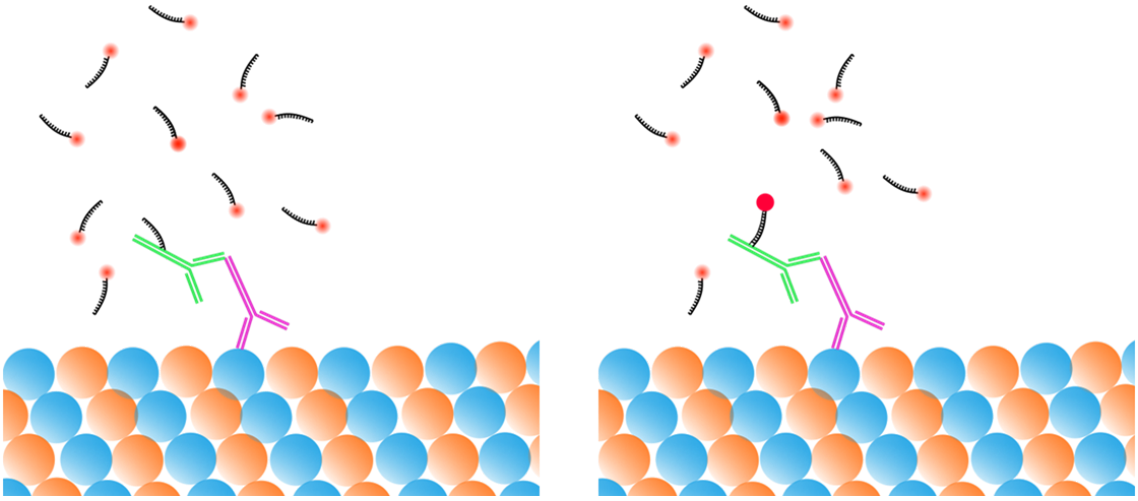

Figure 1.10: Schematic of mechanism of DNA-PAINT; target region tagged with primary antibody followed by secondary antibody. Secondary antibody is bound to a single strand of DNA, imager added into the solution contains the complimentary strand of DNA and the fluorophore Left: OFF configuration Right: ON configuration for a single site

And finally we also have a class of molecules called DNA-PAINT which utilizes immunolabeling along with click chemistry. DNA-PAINT is a method for overcoming the diffraction limit for super-resolution imaging. Molecules of interest in the cell are labeled with antibodies that are attached to single DNA strands. Complementary DNA strands

are labeled with fluorophores and added to the sample, they transiently bind to their complementary strand on the antibody according to the binding kinetics as demonstrated in Figure 1.10. In this way, the binding and unbinding of labeled DNA strands induces the same blinking effect that occurs stochastically from the dyes in traditional dSTORM, STORM and PALM as elaborated in the previous Section.

For example in Figure 1.10, we have Microtubules as illustrated schematically by the alternating orange and blue filaments corresponding to α (blue) and β (orange), Tubulin respectively. Here α tubulin is first tagged with the primary antibody (indicated with purple) and then tagged with the secondary antibody (green). The secondary antibody has a single DNA strand. This sample is then prepared for imaging by adding the imager which has the fluorescent probe attached to the complimentary DNA strand which transiently binds to the secondary antibody strand and is rendered into the "ON" state.

4 Comparing Techniques

From the previous Section we have seen that there are various methods of doing super-resolution imaging and notably we can categorise the techniques into stochastic basically PALM, STORM, PAINT and deterministic majorly into STED. All these techniques are compatible with live cell imaging with few accommodations such as short acquisition times in STED and using optimized buffers (like having lesser concentrations of reducing agents).

To summarise, *Photoactivated Localization Microscopy* (PALM) is performed on a biological specimen using fluorophores expressed exogenously in the form of genetic fusion constructs to a photoactivable fluorescent protein. The use of photoactivable proteins allows one to stochastically activate a few proteins, excite and collect photons through images up to the bleaching point at which, another activation is required. While STORM uses the concept of photoswitchable labels, putting all of them initially into the dark state stabilized through a chemical buffer and stochastically activating a few of them followed by the excitation beam and repeating the process.

PALM requires the stability of the fluorophore without slipping into the dark state whereas STORM does not. Unlike DNA-PAINT both these techniques require a lot of irradiation as well as have very short ON states of the corresponding fluorophore whereas DNA-PAINT can be in the “on/bound” state for a long time allowing for more photon collection per molecule and thereby allowing for better resolution. Also, unlike DNA-PAINT they require multiple wavelengths of lasers to activate, excite and de-activate the fluorescent probes and their composite attachments. But all of them do offer many fold sub-diffraction limit resolution.

Thus amongst all the techniques of super-resolution imaging DNA-PAINT has many advantages both in terms of the illumination power required which reduces risk of photo-

toxicity and bleaching and reversible binding allowing for reuse of fluorophores making the process stochastic effortlessly, as well as larger binding times.

A table comprising of different techniques is attached in 1.11.

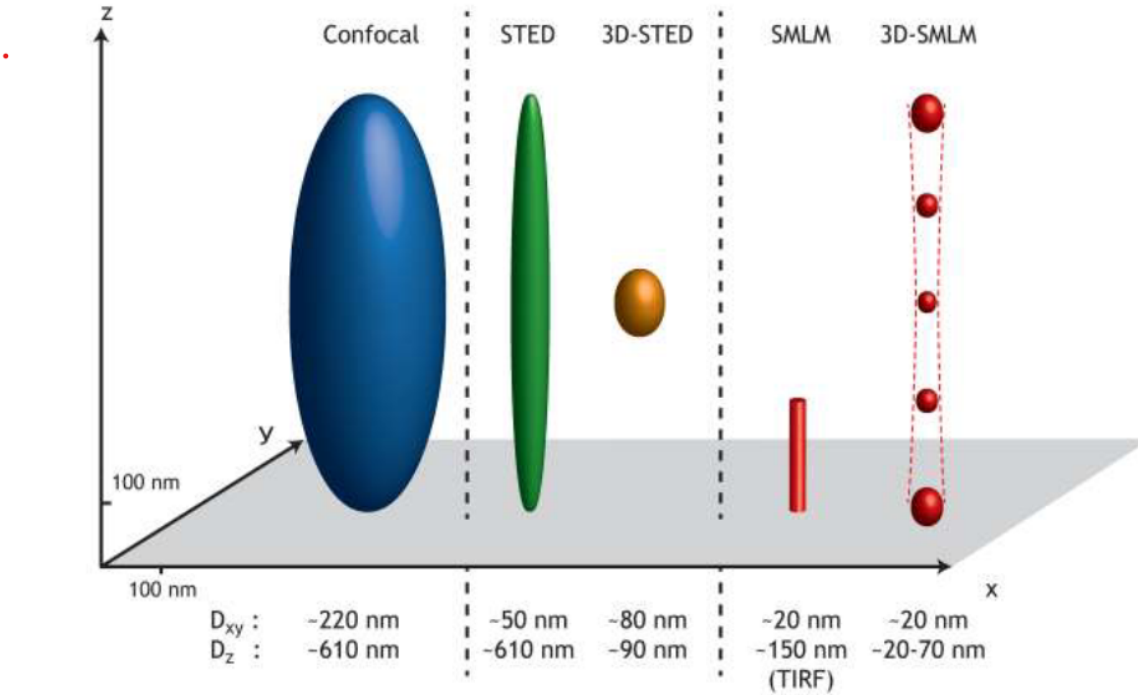

Figure 1.11: Spatial resolutions typically achievable with different imaging devices compared with the focal volume of confocal microscopy. 3D-STED performances are those of the commercial system sold by Aberrior Instruments. Performance in SMLM as given by the best possible localization precision measurement.

5 Conclusion

In this Chapter we have discussed fluorescence as a process, we will elaborate on the lifetime as well as fluorescence dynamics derived from first principles in Chapter 4 and Chapter 5. We have looked at various configurations for implementing fluorescence microscopy, widefield and point based scanning methods as well as different configurations of illumination. We have discussed the diffraction limit and super-resolution fluorescence microscopy techniques that were developed to overcome it. Then we went on to discuss SMLM and how it evades the diffraction limit by having a sparcely tagged sample thereby transposing the spatial resolution problem to the temporal domain allowing single localizations with the probability of two fluorescence emitters overlapping in one frame being insignificant. We classify the super-resolution techniques based on deterministic and stochastic blinking of the fluorophore emitters. We list the advantages and disadvantages for each technique motivating the reason for using DNA-PAINT. We discuss DNA-PAINT in depth from its mechanism to its advantages over other approaches.

Now that we have covered the fundamentals of fluorescence microscopy we move on to multiplexing which is the imaging of multiple fluorophore emitters in a given sample. Multiplexing is the main feature that makes fluorescence microscopy so useful as we discussed in Section 1. In Chapter 2 we will cover multiplexing and existing techniques for multiplexing.

Chapter 2

Multiplexing Techniques

Summary

Fluorescence microscopy is one of the most prevalent techniques in biological imaging due to its ability to have multiple types of fluorophores that can be specifically used for tagging sub-cellular structures. In this chapter we will discuss in the context of SMLM the various approaches to image multiple proteins in biological samples, and the associated limitations as well as other super-resolution multiplexing techniques. We end by listing the limitations of existing multiplexing techniques to motivate a new approach for multiplexing in Chapter 3.

Contents

Multiplexing is the use of multiple fluorophores to tag different parts of a biological sample so as to use them to image various sub-cellular structures and processes in a cell sample. Thanks to fluorescence specificity multiple proteins can be labelled to reveal organelles through localization inside cells. The specificity allows one to distinguish two fluorophores based on their spectral emission or their lifetime (which we will cover in Chapter 4 and Chapter 5). Multiplexing plays a pivotal role in biological imaging as a powerful tool to discern both the architecture of the sub-cellular structures as well as sub-cellular dynamics and pathways.

In the previous Chapter we discussed about the various techniques of super-resolution imaging. In this Chapter we will discuss the various types of multiplexing approaches that are implemented to image multiple fluorophores. We first begin with multiplexing in super-resolution imaging by describing the experimental setup, data analysis and some examples so that we can have an idea and complete picture on SMLM multiplexing approaches and finally we conclude by stating caveats to existing multiplexing techniques, thereby motivating our solution via a new approach which we will elucidate in Chapter 3.

1 Most Used Approach for multiplexing in Super-resolution Imaging

In this Section we begin by discussing the go-to technique that is mostly used for multiplexing in SMLM that is based on the ratiometric analysis of the emission spectra of fluorophore emitters.

1.1 Spectral Demixing

Characteristically speaking, fluorescent proteins and fluorescent chemical dyes have a large distribution in their absorption-emission spectra due to their chemical structure and vibrational states. Thus, their absorption and corresponding emission is across a large range of wavelengths, around 50 nm, *Full Width at Half Maximum* (FWHM). This is a huge caveat to imaging many fluorophores in fluorescence microscopy as this greatly limits the number of fluorophore emitters that can be distinguished in a sample. It is one of the major limitations of fluorescence microscopy. On one hand we cannot use very strong beams with short wavelengths close to Blue or UV due to its high energy that can damage the sample and cause phototoxicity, rendering many such molecules incompatible. And on the other hand using fluorophores excitable close to Red makes it difficult to detect the emitted fluorescence signal as it would emit the fluorescence signal in IR, and we will need to use infrared cameras for the detection. Thus, fluorophores are limited mainly to the visible range and existing techniques rely on spectral distance to make it possible to classify molecules. There are many ways that spectral demixing is done in terms of configuration and the samples used. In the next Section we look at two such implementations of spectral demixing. This concept was introduced and implemented by [Lampe, 2012]

1.2 Implementation of Simultaneous Ratiometric Spectral Demixing

The process of multiple imaging is done by splitting the emission signal into two channels spatially. Each fluorophore has a characteristic absorption-emission spectra which is exploited to image fluorophores through different channels either through sequential acquisition in time or through the division of the emitted signal-spectral demixing. In spectral demixing, the two channels are important to divide the emission signal of all the fluorophores into these two channels by using a dichroic which selectively transmits a certain ratio of photons depending on the wavelength of emission. Thereby allowing one to categorize all (up to 3 types) the fluorophores into different classes by measuring the ratio of photons in each channel through a detector as illustrated in Figure 2.1.

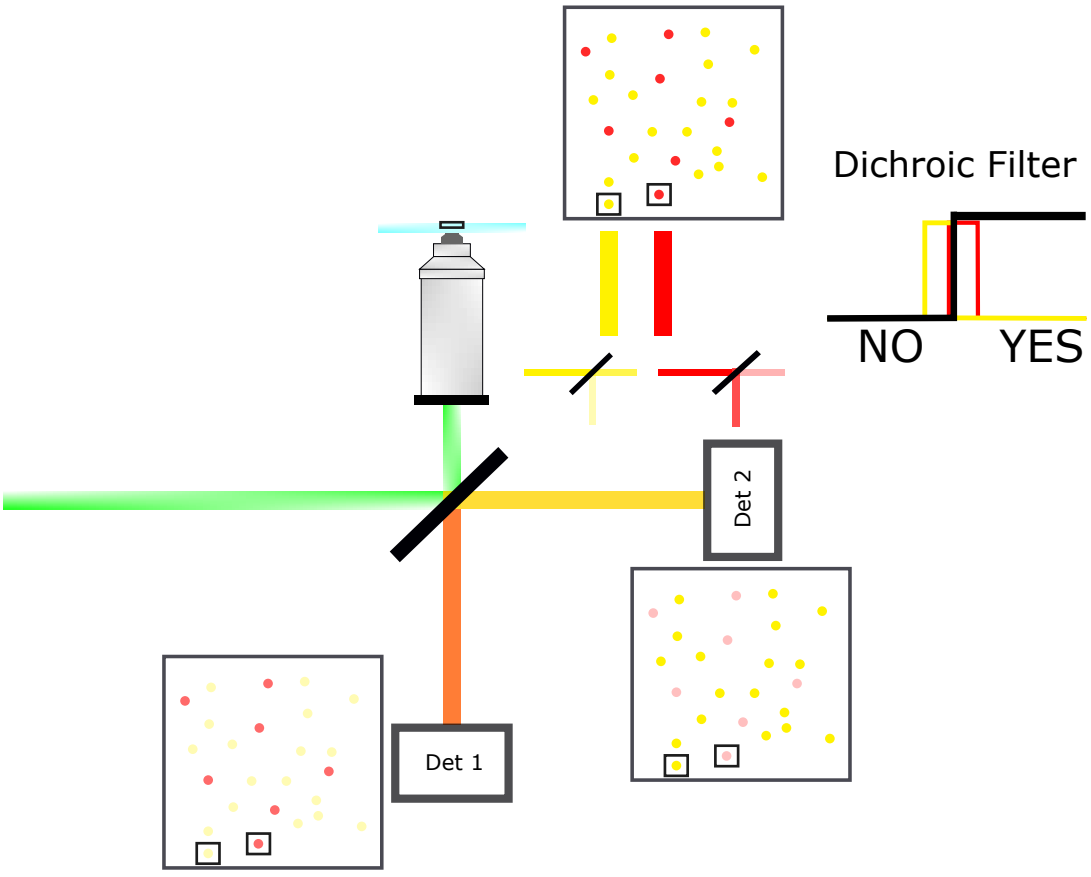

Figure 2.1: Schematic of Spectral Demixing. Yellow fluorophores are tagged to one protein on an organelle of the cell and the Red fluorophores are tagged to another. The signal emitted is divided using a dichroic filter as shown on the right. The ratio of intensities of the two are used to classify the species (only one dichroic represented above, the setup requires two; one for excitation and emission followed by the second one-shown above, for the purpose of spectral demixing).

In Figure 2.1 the excitation beam is indicated in Green, the Red is Channel 1 (transmitted by the dichroic) and the Yellow is Channel 2. On top we have the consolidated intensity map for all fluorophores in one frame. Below, on the left we have the intensity

map for Channel 1 and on the right we have the intensity map for Channel 2 for the same frame. We see in Figure 2.1 on one channel the Red fluorophores are prominent and on the other the Yellow fluorophore tags are more prominent. Thus, the ratio of their respective intensities differs depending on which channel we consider. This allows us to classify them into two species.

This technique, as shown in the schematic of Figure 2.1, involves dividing the signal from the sample into two channels and treating each channel in the same manner in order to not introduce any artefacts owing to the division of the signal itself. Noise due to this may crop up into the sample. In all the cases fluorophores with distinct emission (as distinct as possible with minimal overlap) are preferred in order to have a clear classification. This however presents a challenge owing to the fact that most fluorophores are usually clustered in terms of emission wavelength for example, most PALM fluorophores are concentrated in a spectral domain ranging from 488-nm to 561-nm excitations, while in DNA-PAINT and dSTORM, most molecules are excited with 561-nm to 637-nm excitation wavelengths. Also added is the cost of doubling all the detection treatment as well as equipment, making it costly both in terms of components as well as data storage.

Below we present an experimental implementation of the above technique. This experiment is implemented in STORM with the fluorophores AF 647 and CF 680 used to tag Clathrin and Tubulin respectively, whose emission spectra are given in Figure 2.2. We see through their emission spectra that there is an overlap between the two. The region of overlap will yield fluorescence photons that would be difficult to categorise as one or the other.

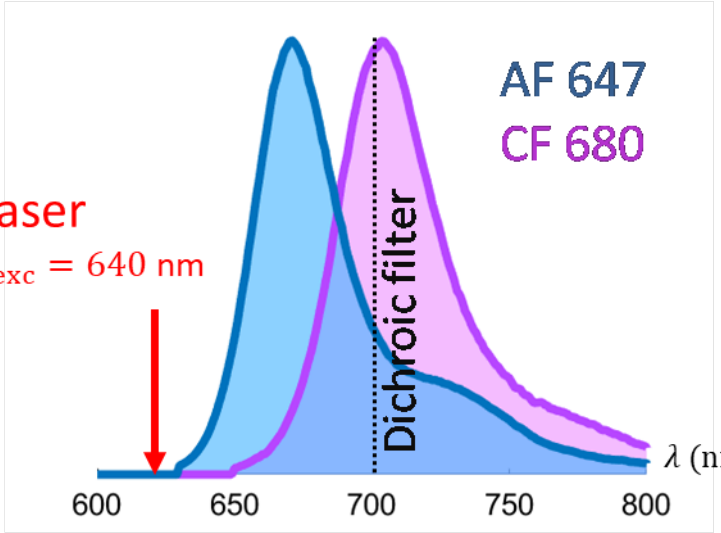

Figure 2.2: Emission spectra of AF 647 in Blue and CF 680 in Purple along with the dichroic filter (taken as an example at 700 nm) indicated via the Black dotted line (transmits to the right and reflects to the left), excitation wavelength of 640 nm indicated in Red. The X-axis represents the wavelength in nm.

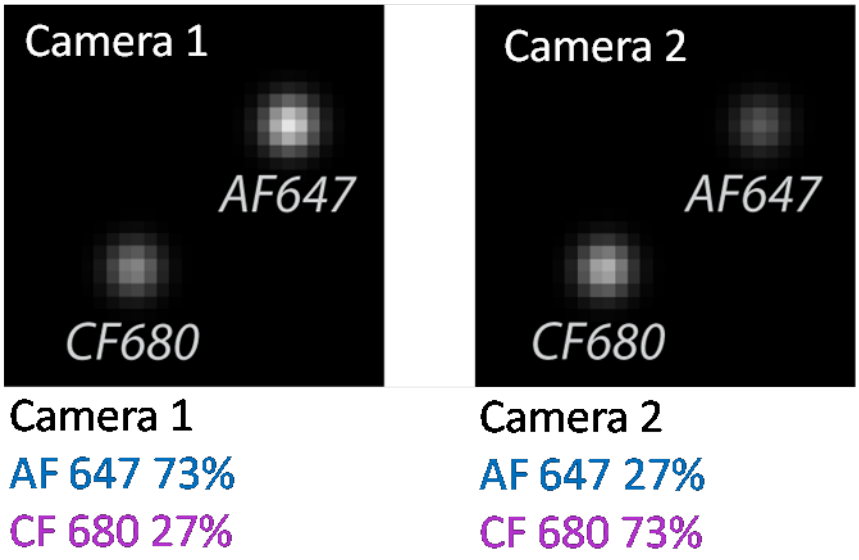

Figure 2.3: Left Image: Camera 1 with AF 657 brighter and CF 680 dimmer. Right Image: Camera 2 with AF 647 dimmer than CF 680. Below, in Blue and Purple the percentage of each species divided into two channels according to the dichroic used as shown in Figure 2.2.

A straightforward and efficient way of spectral demixing as illustrated by [Mau, 2020] wherein we have a sample of COS7 cells tagged with Alexa 647 and CF 680, which are spectrally close but separable as shown in Figure 2.2. It is important that they have an overlap as we see in Figure 2.3 but are not identical, that is having an overlap of more than 50%. If they are too similar, the ratiometric approach as shown in Figure 2.1 will not yield significant distinction between two species leading to excessive miss-classification.

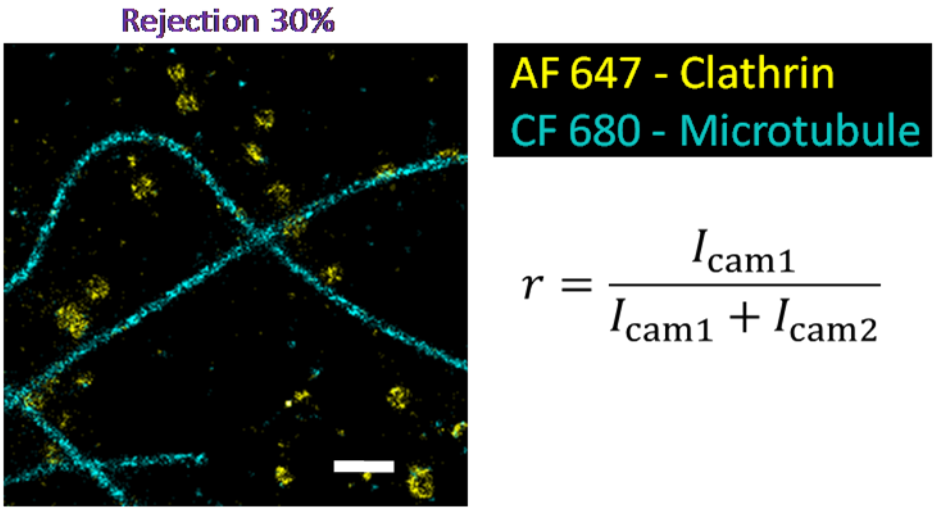

Figure 2.4: Reconstructed multiplexed image after ratiometric classification. Clathrin tagged with CF 647 in Yellow and Microtubules tagged with CF 680 in Cyan with a rejection of 30% of the molecules. On the right we have the ratio which was used to classify them into two species. scale of 200 nm [Mau, 2020]

In the sample [Mau, 2020] Clathrin was tagged with AF 647 and Tubulin was tagged with CF 680. The spectra need to have some degree of overlap in order to have a ratiometric measurement, also the concentration of the fluorophores need to be comparable in order to segregate them well. As shown in Figure 2.3 in Camera 1 we have AF 647 brighter than CF 680 and in Camera 2 we have CF 680 brighter than AF 647. This is because of the dichroic filter which divides the emitted fluorescence signal from the sample into two channels as illustrated in Figure 2.1. The dichroic used is shown in Figure 2.2 which basically sends all the photons of wavelength 700 nm or more to one channel (transmitted) and wavelengths less than that to another channel (reflected). Which is why we see that in Camera 1 AF 647 is brighter because more signal from AF 647 is present in channel 1 (contains Camera 1) and vice versa for CF 680. Now based on this difference in intensities, we can compute the ratio for each fluorophore site, which is shown in Figure 2.4, the ratio of intensities on the two cameras are different, this is used to classify the regions thereby rendering the multiplexed image for the sample as shown in Figure 2.4.

The ratio is computed by taking the ratio from one of the camera for one species to the sum of the intensities from both the cameras (which is effectively the total fluorescence signal emitted by that fluorophore emitter) as shown in Figure 2.4.

$$r = \frac{I_{Cam1}}{I_{Cam1} + I_{Cam2}} \tag{2.1}$$

Thus, for each molecule the ratio is calculated by taking its intensity in that Camera to the total intensity of that region by summing the intensity of the molecule/PSF-region across both the Cameras.

In Figure 2.4 on the left we see that using this ratio we can classify the molecule into different species. Since we know in this experiment we have two species we can manually select the demarcation ratio value and classify the species by defining say, ratio less than 0.45 is CF 680 and greater than 0.55 is AF 647 for example. The overlapping region which can be manually discarded represents the number of rejected molecules that are too close in terms of their ratio to be classified and can go either way probabilistically. In this case we have a 30% rejection.

Now that we have seen this technique implemented in DNA-PAINT we now give an example of the same concept used to multiplex two species of dnapaint molecules. In this experiment the two species used were ATTO 655 and ATTO 700 with considerably less overlap in terms of their emission spectra when compared to the previous experiment. The implementation in both DNA-PAINT and STORM is the same approach with just a change in the sample.

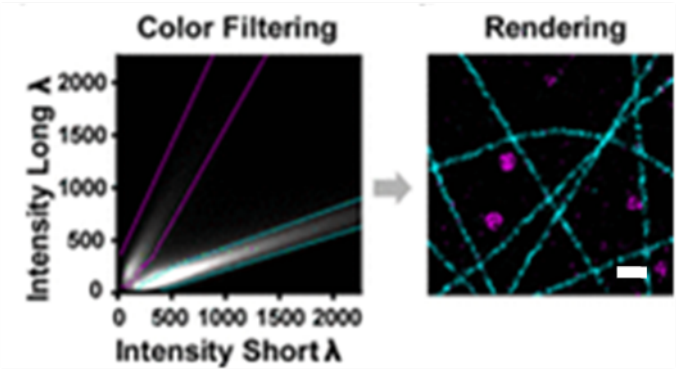

Figure 2.5: Spectral demixing using a single laser line (647 nm) of a sample tagged with Tubulin tagged with ATTO 655 and Clathrin tagged with ATTO 700. Left: The intensity map of molecules and their segmentation. Right: Classified molecules [Gimber, 2022]. Scale 200 nm

An extension to DNA-PAINT by [Gimber, 2022] in Simultaneous Multicolor DNA-PAINT without Sequential Fluid Exchange (general approach for multiplexing in DNA-PAINT sequentially changing the imager solution) using Spectral Demixing achieved high localization precision with fast, simultaneous, dual-color acquisition based on SD as shown in Figure 2.5. They uses spectrally overlapping fluorophores excited by a single laser line and a simple dichroic-based emission splitter to image short and long wavelength components of the emission on two sides of the same camera. The single-molecule localizations are "paired", while non-paired localizations, from which a large part is random noise, are excluded. Depending on their emission spectra, localizations from each dye displays a spatially distinct population within the 2D intensity histogram of long and short channel intensity values (Figure 2.5 Left).

By applying binary masks to exclude or include populations of the intensity distribution, the colors are assigned to each paired localization before multicolor rendering (Figure 2.5 Right). These color-separation masks are optimized for maximal inclusion of localizations and minimal crosstalk between the channels. However even this technique was limited with extensive spectral overlap as was observed in the experiment with ATTO 655, ATTO 680 and ATTO 700 [Gimber, 2022].

2 Other techniques in SR Multiplexing

In this section we will review some of the interesting approaches taken by other investigators in super-resolution imaging with multiplexing.

One of the first approaches to do multicolor imaging in SMLM involved sequentially acquiring images one population after the other. That is, sequential in time. However, the extension of these techniques to SR imaging multiple sites/tagged molecules (multiplexing)

in a biological system has many caveats and is usually a sequential process either in space or time.

One of the spatial displacement based sequential techniques of super-resolution multiplexing was called SR-STORM which used a prism placed in the detection setup. Which dispersed the emitted signal from the sample [Zhang, 2015]. Due to this spread, on the detector/camera there is a spread in terms of the spectra of fluorescence spatially, this lateral shift is measured to retrieve the spectral information of the fluorophore when compared to a calibrated sample. This was done through a dual-objective setup.

The comparison of the lateral positions of each PSF on the two images gave the displacement due to the dispersion. And using a correspondence curve obtained through a calibration of the system, the central fluorescence wavelength was obtained for each PSF and the corresponding molecule was classified. This techniques had a spectral resolution below 10 nm. Identification of four fluorophores in the [660 nm to 700 nm] fluorescence wavelength domain was possible [Zhang, 2015].

The technique used for multiplexing with the advent of super resolution imaging and SMLM is the use of dyes which are spectrally distinct for example in the case of [Civitci, 2020], they use Cy3b and ATTO 655 (three excitation lasers 488, 561, 647 in their setup) sequentially and they used exchange PAINT as shown in Figure 2.6.

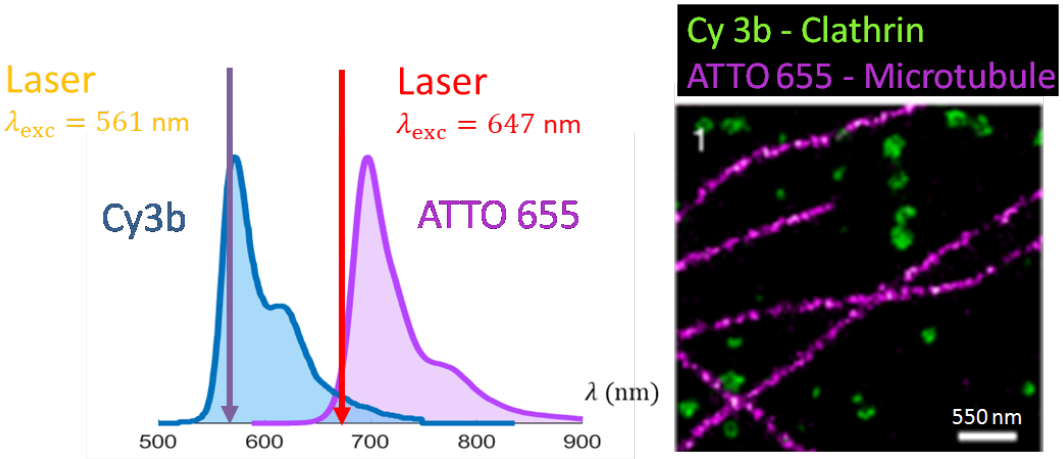

Figure 2.6: Left: Emmission Spectra of the fluorophores Cy3b and ATTO 655 along with the excitation lasers used. Right: Sample of COS 7 cell with Clathrin tagged with Cy3b and α tubulin tagged with ATTO 655.

One of the publications by [Gómez-García, 2018] on Excitation-multiplexed multicolor super-resolution imaging with fmSTORM and fm-DNA-PAINT exploits the time domain to make multicolor SMLM measurements on the sample. The data is divided into different channels by imaging the sample at different exposure times and binning the output as indicated in Figure 2.7. Using modulation of a combination of excitation wavelengths and

by binning the obtained fluorescence intensity in the frequency domain multiplexing was achieved.

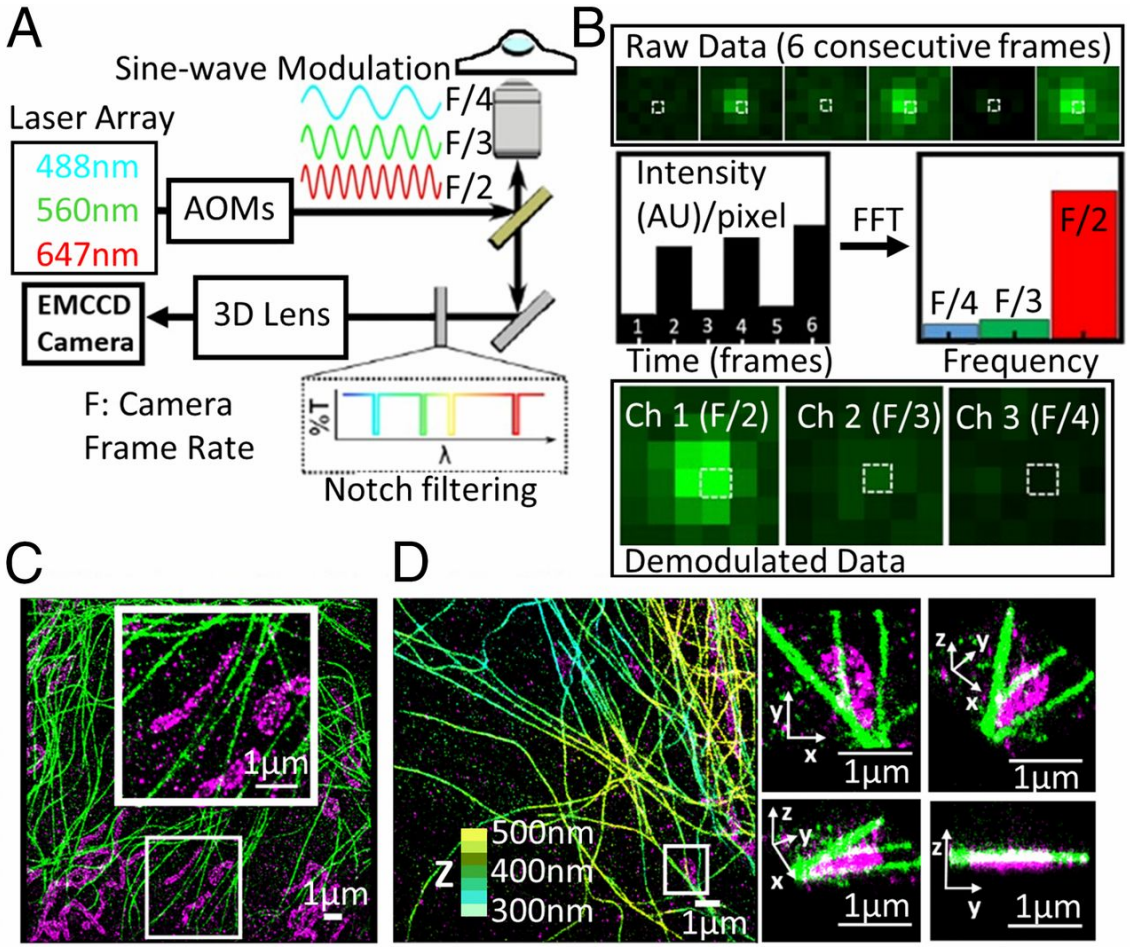

Figure 2.7: Excitation modulated multicolor super-resolution imaging with fm-STORM and fm-DNA-PAINT. (A) Schematic of the microscope setup and imaging method. An example case of three illumination lasers are shown as sinewave-modulated at three different frequencies, F/2, F/3, and F/4, where F is the camera frame rate. (B) Representative example of data processing. (B, Top) SubROI of six consecutive frames with one fluorophore present. (B, Middle) Intensity evolution of the selected pixel (white box) in the time domain and amplitudes in the frequency domain after a FFT over the six frames. (B, Bottom) Resulting demodulated data split into the three different channels. (C) Two-Color, 2D fm-DNA-PAINT image of Mitochondria (Magenta) and Microtubules (Green). (D) Two-Color 3D fm-DNA-PAINT image of mitochondria and Microtubules. Zooms on the right show 3D views of the white boxed region. Mitochondria are represented in Magenta. For the Microtubules, the color-coding indicates z-position (from 300 nm in light blue to 500 nm in yellow). [Gómez-García, 2018]

However, this approach requires a minimum of three rapidly triggered lasers and suffers from chromatic aberrations like in any other multicolor method with spectrally separate fluorophores. Compared to spectral demixing based previous experiments, this method was limited to two color channels with a compromised spatial resolution and limited to

only sparse samples. In another experiment in the same paper, a fluorophore variant used three spectrally different dyes and different binding frequencies to achieve sequential multicolor DNA-PAINT without fluid exchange in [Gómez-García, 2018] as well. The advantage of this over sequential fluid exchange techniques being the speed.

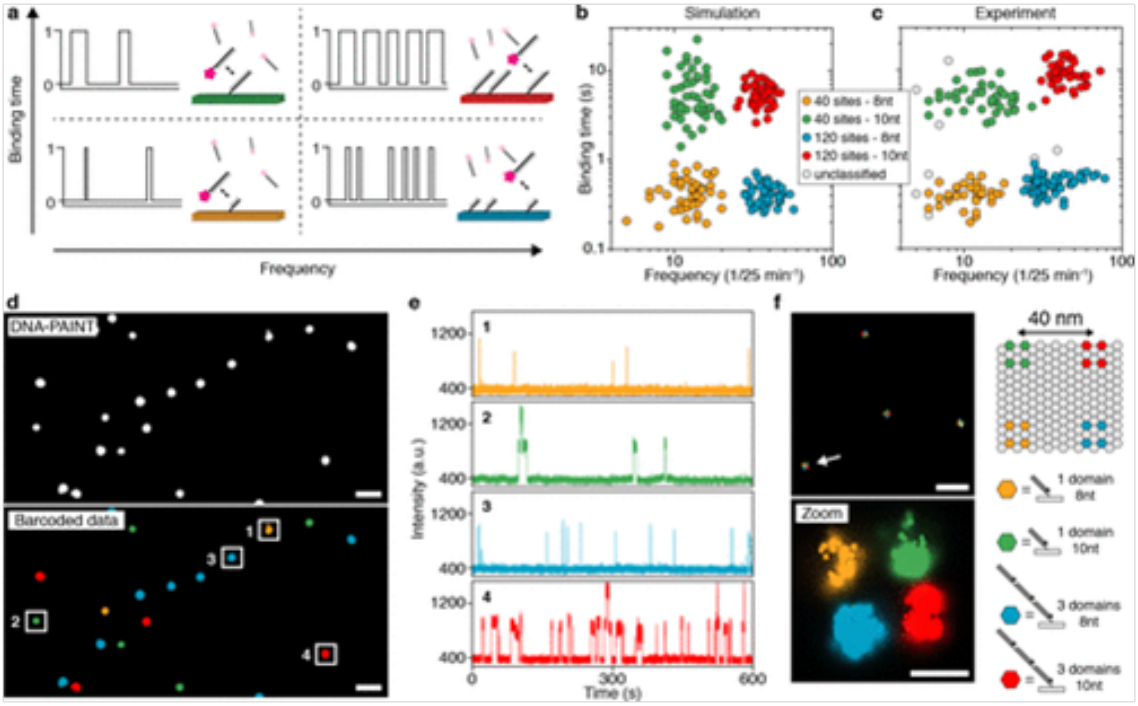

Figure 2.8: 124-Color Super-resolution Imaging by Engineering DNA-PAINT Blinking Kinetics [Wade, 2019] [Gómez-García, 2018]. (a) Binding time as well as the concentration (bonding sites) are the two parameters for disentanglement (b) Simulations of four kinetically different structures show four clearly distinguishable populations (c) Experimental results from DNA origami structures imaged using a single imager strand species show four distinguishable populations (d) Exemplary overview DNA-PAINT image of the four DNA origami structures (top). Same data set, now color-coded according to identified clusters in c (bottom). (e) Exemplary intensity versus time traces from highlighted regions in d representing each of the four unique DNA origami species. (f) Engineering frequency and duration on DNA origami below the diffraction limit. Each corner of the structure is designed to exhibit a unique kinetic fingerprint. Scale bars: 1 µm (d), 500 nm (f, top), 40 nm (f, bottom).

Another technique is to engineer the ON time of the molecules so that we can extract information based on the blinking time. As done by [Wade, 2019] in a 124-Color super-resolution imaging by engineering DNA-PAINT blinking kinetics chemically. Thus having a distinct ON time for each fluorophore tag allows one to disentangle multiple fluorophores as shown in Figure 2.8.

In another technique which makes use of *Ground State Depletion* (GSD) and is based on switching the majority of fluorophores to a metastable dark state, such as the triplet state is illustrated by GSDIM as shown in Figure 2.9. Here photoswicthing is followed by

back-calculating the position of those left in the excited state that transition spontaneously to the ground state via fluorescence [Fölling, 2008] and was used to do multicolor imaging. Continuous widefield illumination was done by a single laser and dual-color images of PtK2 cells as shown in Figure 2.9.

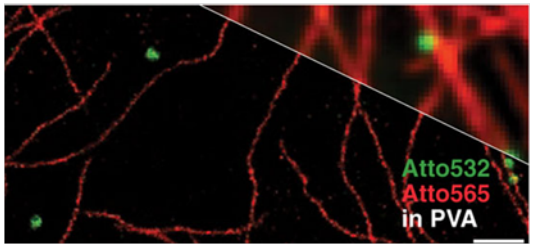

Figure 2.9: GSDIM images of immunostained (ATTO 532 Green and ATTO 565 Red) Microtubules and Peroxysomes of PtK2-cells embedded in PVA. (Epifluorescence images are shown in the upper right corners prior to super-resolution imaging) . Scale: 1 μ m[Fölling, 2008]

Multiplexing is done in biological samples is also commonly achieved through point based scanning systems like confocal setups. These setups contain multiple lasers which are sequentially used to scan the sample. Different fluorophores are used to tag different parts of the sample which have separate emission spectra. Upon sequentially scanning the sample with each laser and with the corresponding filter, the images are overlapped to create the final multicolor image of the sample with all the tags.

3 Caveats in Multiplexing Techniques

Thus, to summarise we have various techniques for multiplexing but all of them have essentially some major points of drawback. Primarily it is because of the fact that they are sequential in time to separate different fluorophores into different channels. This introduces inhomogeniety in terms of processing, and also the processes are non simultaneous. And they require spectrally separate fluorophores which renders many fluorophores useless, especially in the Red domain. And like we discussed in the beginning of the Chapter, most fluorophores are limited to the visible range which constricts the choice even further. Spectral demixing relatively solves this problem but we introduce two channels, with two detectors and optical paths for the fluorescence emission that has its own set of drawbacks. None of these approaches can perform multicolor imaging/multiplexing for close overlap in spectra.

Thus, one needs fluorophores of distinct spectra and multiple lasers to sequentially excite the sample. Spectrally separate fluorophores have to be selected to yield better disparity in classification, but fluorophores are unfortunately limited close to the red wavelengths. Also shorter wavelengths would add to phototoxicity. Temporal drift has to be corrected

along with spatial shifts through correlative algorithms. This makes it more expensive as we require more number of lasers, data heavy or more components (camera, etc).

However advantages of the sequential techniques include a single camera and straightforward acquisition repeated with different excitation wavelengths. But the drawbacks outweigh these few advantages, since many lasers are required to excite fluorophores which have to be spectrally distinct, are prone to temporal inhomogeneities (drift), have limited multiplexing due to spectra (4 fluorophores maximum) and is costly in terms of being data heavy and requirement of components (many lasers or many channels with two cameras-ratiometric approach). We will discuss more specifically spectral demixing based drawbacks in the next section.

3.1 Caveats to Spectral Demixing

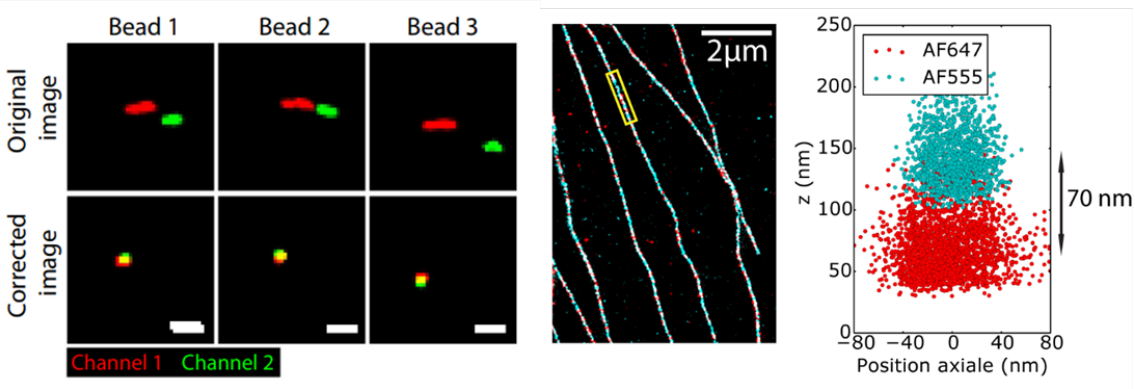

Figure 2.10: Left: Drift correction and aberration correction in the two channels. [Georgieva, 2016] Right: Colocalisation in z of different species of fluorophores [Cabriel, 2019a]

More specifically the caveats to this technique include limited availability of spectrally distinct fluorophores with optimal brightness and duty cycle. The major consequence of that is basically being unable to differentiate between molecules that have a large spectral overlap. Which is what is generally observed in the case of multiplexed SMLM techniques that we have a degree of overlap between fluorophores that is minimized in order to disentangle them (PALM, they are concentrated in a spectral domain ranging from 488-nm to 561-nm excitations, while in DNA-PAINT and dSTORM, most molecules are excited with 561-nm to 637-nm excitations wavelengths). The presence of significant cross talk between these molecules both in terms of miss-classification as well as chemical non-specificity, as well as drift correction and one to one correspondence across the channels by correction through pixel matching need to be carried out as shown in Figure 2.10.

Spectral demixing is susceptible to chromatic aberrations (splitting the channel in two), lateral drift [Georgieva, 2016] and low SNR while splitting the signal. Different treatment

is carried out to each channel separated in time(or freq) and/or space [Cabriel, 2019a]. And what if we want to use fluorophores most commonly available and used like ATTO 647, ATTO 633 and ATTO 655 together, which are very close in spectral emission? These existing techniques are not capable of disentangling such species well at all.

To summarise the limitations discussed, in order to multiplex we need to select spectrally distinct fluorophores. And in order to exploit the usage of fluorophores which are close in their absorption-emission spectra, the experimental system scales proportionately both in terms of components and expense, since we need multiple excitation sources and detection channels. Since we divide the emitted fluorescence signal into two channels for example in spectral demixing or in the case of sequential acquistion; the data can be prone to aberrations in either of the channels, lateral drift and low *Signal to Noise Ratio* (SNR). These changes in each channel separated in time (or freq) and/or space has to be corrected for.

4 Conclusions

In this Chapter we have presented Multiplexing techniques especially those relevant to the Super-resolution Fluorescence microscopy for biological imaging. Fluorescence microscopy along with Multiplexing provides a powerful tool to study cellular architecture and for knowing molecular dynamics in live samples. Most widely used technique used for this purpose is ratiometric spectral demixing. And sequential imaging of different fluorophore emitters tagged biological samples. We have presented essentials of these methods and highlighted their limitations such as requirement of distinct spectral emission for fluorophores, complexity of the system, cost, introduction of chromatic aberrations, lateral drifts and other factors. Hence, to circumvent some of these limitations, we have made a case for identifying alternate demixing techniques that can be used for super-resolution fluorescence microscopy. In the remaining part of the thesis, we propose alternate methods for this purpose. Two approaches, we are going to describe here for Multiplexing are based on (a) emission fluxes of the flurophores (which we will see in the next Chapter) and (b) Florescence lifetime (Which we will see in Chapter5) to distinguish flurophores. As seen within this chapter, identifying and classifying multiple targets in SMLM still presents a major challenge. In the following Chapter, we introduce a new parameter based on the flux emitted by the single molecule as an alternative identification strategy.

Chapter 3

Flux based Multiplexing

Summary

In this chapter we will discuss a new technique for multiplexing using fluorescence flux. We will begin by describing molecular fluorescence flux and then proceed to demonstrate how the technique can be implemented in existing SMLM setups using DNA-PAINT and then we proceed to demonstrate how this technique can be implemented in STORM samples as well. We characterise the technique and quantify its advantages and limits. We demonstrate how this technique can be used to augment existing multiplexing techniques including spectral demixing as well as a stand alone technique by its own right.

Contents

1 Molecular Flux calculation

What fundamental properties can be exploited to extract information and classify such fluorophores tagged on the same sample? And can we do it without any other modifications and simultaneously as opposed to sequentially? These are the questions that motivated us to examine the fundamental properties of the fluorescence that we detect as the output signal. And by doing so, we want to exploit some fundamental properties that can elucidate the classification process and help discern fluorophores better, especially fluorophores that are close in terms of their spectra which was the major limitation in the previous techniques that we examined.

The intensity of a molecule that we see as the signal on the camera, is fundamentally a function of its cross section σ and quantum yield Φ. Other parameters include the detection efficiency ξ and excitation wavelength (this derivation from first principles is done in Chapter 5). We will examine each of these individually. We can write the detected intensity in terms of all the parameters as well as I_{exc} as follows:

$$I_{det} \quad = \quad \xi \quad \sigma(\lambda_{exc}) \quad \Phi \quad I_{exc} \tag{3.1}$$

And the electromagnetic flux ${F_{det}}^{EM}$ defined as:

$${F_{det}}^{EM} \quad \propto \quad \xi \quad \sigma(\lambda_{exc}) \quad \Phi \quad I_{exc} \tag{3.2}$$

Where ξ is the detection efficiency which depends on the collection angle of the objective that is, the solid angle that the fluorophore makes (depends on NA) and the efficiency of the detector. Quantum yield defined by

$$\Phi \quad = \quad \frac{\Gamma_{radiative}}{\Gamma_{radiative} + \Gamma_{nonradiative}} \quad = \quad \tau\Gamma_{radiative} \tag{3.3}$$

Quantum yield is defined as the ratio of the number of photons emitted to the number of photons absorbed. Quantum yield depends on the molecule as well as the local environment that is, the fluorescence/radiative cycles to the total number of photons absorbed by the molecule. The local environment can affect the quantum yield as seen by FRET wherein we have energy transfer from an excited molecule to an ambient molecule via dipole-dipole coupling. The absorption cross section $[cm^2]$ (alternatively also given in terms of molar extinction coefficient $[M^{-1}cm^{-1}]$) is a function of the molar extinction coefficient which is more commonly measured while characterising a species of molecules. Absorption cross section is one of the fundamental properties of a molecule. It is basically the ability of the said molecule to absorb photons.

We can now define the equation in terms of the photon flux as follows

$$\frac{{F_{det}}^{EM}}{h\nu_{flu}} \quad = \quad F_{det} \quad = \quad \xi \quad \sigma(\lambda_{exc}) \quad \Phi \quad \frac{I_{exc}}{h\nu_{exc}} \tag{3.4}$$

What is of consequence is the general scenario for SMLM. In SMLM, the number of fluorophores are scarce, making the environment fairly isolated and uniform. Now, if the illumination is made as uniform as possible, the inhomogeneities that show up will then have to be sole products of the difference in species' specific properties like cross section, lifetime/spectrum. Thus, in this case we can examine the brightness defined as β to be constant. The brightness is given by the following relation [Wong, 2020] which has the same units as the absoption cross section:

$$\beta \quad = \quad \sigma(\lambda_{exc}) \quad \Phi \tag{3.5}$$

For a given molecule with the same environment, the quantum yield Φ and brightness β are constant. We can also define η to be constant as

$$\eta \quad = \quad \frac{F_{det}}{I_{exc}} \tag{3.6}$$

For two different types of molecules η depends on the excitation and the collection efficiency of the apparatus. That is, the detectors, filters, wavelength of excitation and solid angle of the molecule and the objective distance. Thus, both η and β are solely dependent on the molecular species. We should therefore exploit the brightness parameter by homogenising the sample with uniform illumination and see if we can discern molecules as separate based on their molecular properties.

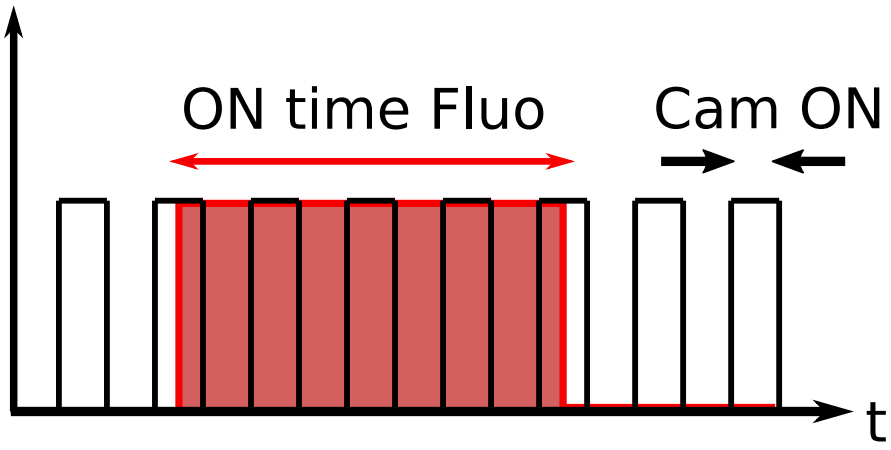

Figure 3.1: Each frame of the camera is depicted by the Black time blocks indicated in the figure. The Red time block represents the ON time of a DNA-PAINT molecule. The On-time of the DNA-PAINT of a single molecule is taken to be represented here, statistically we have a distribution of ON times - larger for DNA-PAINT molecules compared to other fluorescent probes like in the case of STORM for example.

Now that we have an overview of the various facets that go into fluorescence as well detection, the fluorescence flux is measured empirically by looking at the rate of global intensity of a given molecule. In Figure 3.1 we have the ON time of a typical DNA-PAINT

molecule and the ON time of the camera along with its frames. Each frame of the camera is depicted by the Black time blocks indicated in the figure. The Red time block represents the ON time of a DNA-PAINT molecule. We can see here that the ON time cannot be precisely known since we only have access to the integrated fluorescence signal across the ON time of the Camera. And we don't know exactly at what point the molecule came ON and went OFF. This is important since we divide the global intensity by the number of frames in which the molecule is ON to get the fluorescence flux. Thus, if the ON time is very short this can lead to a lot of error in the flux calculation, which is why we chose DNA-PAINT as our first test species since the typical ON time of DNA-PAINT is longer.

Thus we can exploit the flux of the molecule which in most general cases (sparse sample, uniform illumination and detection) depends on the molecule. This can be used to classify the molecule into one or the other categories, allowing for multiplexing. This can be done at no added cost, without extracting any other additional information as we already have access to the fluorescence photons emitted and the detector properties in any multiplexing experiment. This method will require a single detector for its purpose, single channel, and a single excitation source for multiplexing unlike in the case of previous techniques discussed in Chapter 2.

Brightness was calculated (in Table 3.1) for spectrally close species to see if their brightness values were sufficiently different to disentangle them using the Flux demixing technique. We use molar extinction coefficient (ϵ) here since its a more readily available value versus absorption cross section. The absorption cross section is often measured in terms of the molar extinction coefficient through the Beer-Lambert law of attenuating the intensity of incident light with respect to the concentration and path length that the beam traverses in a solution of the said molecular species. According to the Beer-Lambert law,

$$\frac{dI}{dx} = -I\sigma n \tag{3.7}$$

where the rate of change of intensity of the incident beam with respect to the path length traversed in a solution of the said molecule is given as a function of the absorption cross section of the molecule and the number density of molecules given in terms of the Avogadro's constant by $\frac{N_c}{10^3}$.

$$ln\frac{I_0}{I} = \sigma n d \tag{3.8}$$

Where d is the path length. This can also be written in terms of the molar concentration (c) and the molar extinction coefficient defined as follows:

$$log\frac{I_0}{I} = \epsilon c d \tag{3.9}$$

Thus, we have

$$\sigma = 2.303\epsilon\frac{c}{n} \tag{3.10}$$

And the relation between absorption cross section σ and molar extinction coefficient ϵ is as follows:

$$\sigma \quad = \quad 3.82 \times 10^{-25} \epsilon \quad [m^2] \tag{3.11}$$

Fluorophore	ε (M-1 cm-1)	φ	Brightness β
ATTO 647N	147000	0.65	9.56
ATTO 655	97500	0.30	2.93
ATTO 633	100100	0.64	6.41
ATTO 680	61250	0.30	1.84

Table 3.1: Table for brightness values based on molar extinction coefficient (absorption cross-section) and excitation wavelength of 640 nm. With molar extinction coefficient ϵ and quantum yield ϕ and Brightness β.

In Table 3.1 we have the brightness values (up to a constant pre-factor) computed for fluorophores in the Red-domain. Thus, we are now equipped to probe molecular signatures in a sample by making sure our fluorophores are sparse, have similar local environments and are uniformly excited and detected.

1.1 Using Flux for z-localization

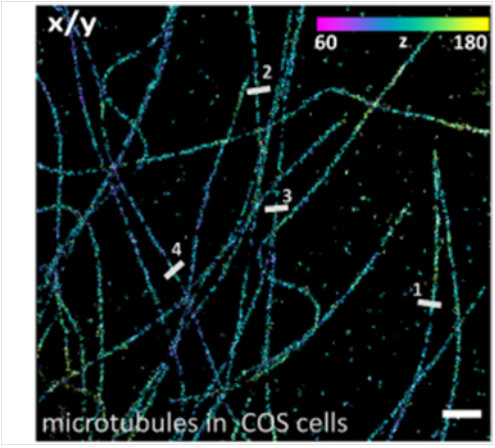

Figure 3.2: Z-localisation of molecules tagged to the tubulin network, based on the fluorescence flux in *Super-critical Angle Fluorescence* (SAF) configuration by [Szalai, 2021]

Fluorescence flux has already been used to probe the depth of a target molecule by making use of the decay rate of the flux from the sample as well as using the z-dependence of excitation. For example, z-localisation was carried out in TIRF configuration [Basché,

2008] by looking at the exponential fall of intensity as a function of axial distance.

$$I_{exc}(z) \quad \propto \quad \exp \frac{-z}{\delta} \tag{3.12}$$

And in *Super-critical Angle Fluorescence* (SAF) configuration we have $\Phi(z)$ depending on the vicinity to the interface since it is in SAF configuration (evanescent emission). And $\xi(z)$ (detection parameters) depends on the light beyond critical. [Szalai, 2021]

Thus, we see z-localization in Figure 3.2 (top right hand corner colorbar indicates z-location) for a Tubulin network in COS7 cells by measuring the photon flux and using SAF.

2 Uniform Illumination Approach

In order to reduce noise due to inhomogeneities in excitation and detection we need to ensure uniform illumination. This is implemented by using the setup developed by [Mau, 2020] called *Adaptable Scanning for Tunable Excitation Regions* (ASTER) developed in our lab at ISMO, Paris. Wherein a galvo-mirror system is used to move the beam in both axes in a tunable manner. Using a galvanometer based scanner which is driven electrically to direct a laser beam through reflection. This technique allows for very precise positioning of the mirror at a very fast rate and with low inertia. This makes it the best candidate to use for ensuring uniform illumination across the surface of the sample. The experimental setup for ASTER is given in Figure 3.3.

2.1 Experimental implementation

Fluorophore	β	Filtered β
ATTO 647N	9.56	5.76
ATTO 655	2.93	2.02
ATTO 633	6.41	3.23
ATTO 680	1.84	1.84

Table 3.2: Table for brightness values based on molar extinction coefficient (absorption cross-section) and excitation wavelength of 640 nm. With molar extinction coefficient ϵ and quantum yield ϕ and Brightness β. The brightness paramter has been calculated by taking into account the filters used.

In order to have a more accurate measure of the brightness parameter we also need to incorporate filters that have been used in our system.

Thus, we have the following set of values given in Table 3.2 for the brightness parameter β after accommodating for the photon selection bias with the filters. The filters used are the following (LF405/488/532/635-A-000 filters) for excitation, emission and dichroic filters from Newport.

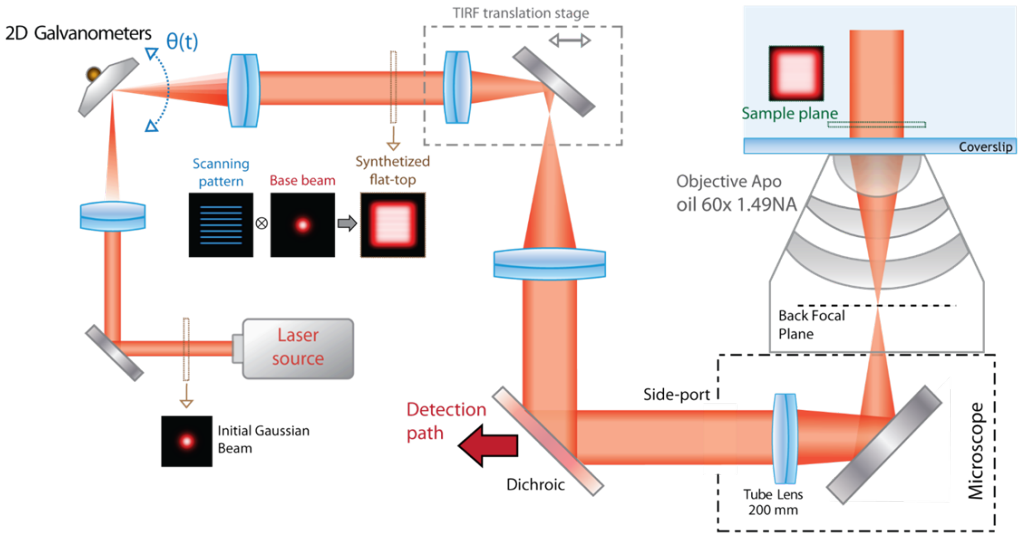

Figure 3.3: Schematic experimental setup for ASTER, the beam is moved using a galvanometer in both x and y axes, thesis work of [Mau, 2020]

The SMLM setups include primarily a wide field imaging system and additional illumination sources be it multiple lasers, filters etc. since the resolution is improved merely through the photo-chemical blinking process. We will focus on PAINT and STORM systems. For DNA-PAINT we have laser typically red (640 nm) as the main illumination. The beam is used to illuminate the sample by using a dichroic filter which basically acts like a gate (letting the excitation wavelength into the sample and allowing the emission to be collected). The light is focused on the back focal plane of the objective to produce a collimated beam on the sample and the *Numerical Aperture* (NA) of the objectives ($NA = 1.49$) is large to collect as many photons as possible emitted from the sample. Magnification of the objective is between 60x and 100x. The camera used has a frame rate up to 150 frames per second, typically in the SCMOS Camera with a Pixel size of 97 nm. A single beam is used to illumine, excite and emit. The fluorescence emission is collected by using an emission filter. The laser used is usually upto 300 mW of which 60 percent i.e. 180 mW is generally used if we look at a small *Field of View* (FOV). The field of view can be tuned and expanded (shown in Figure 3.4) using *Adaptable Scanning for Tunable Excitation Regions* (ASTER) by changing the scale of the area as well as the size of the Gaussian beam.

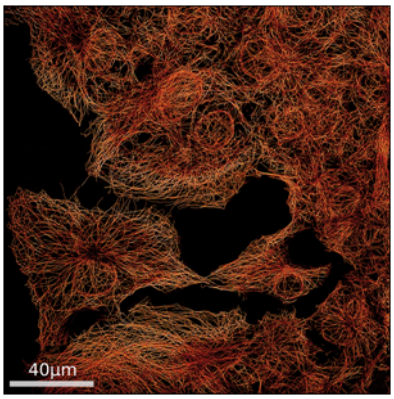

Figure 3.4: The area of illumination is increased many-fold thanks to ASTER with $200\mu m$ x $200\mu m$, thesis work of [Mau, 2020]

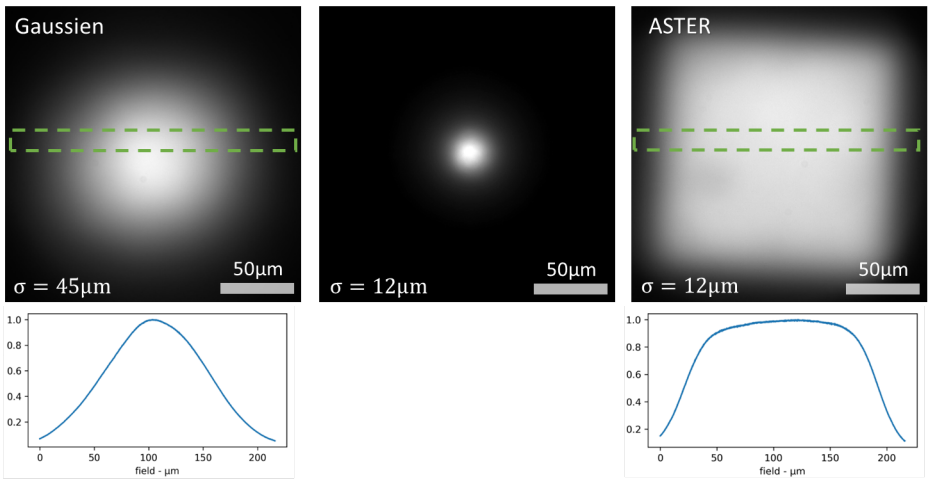

Figure 3.5: Gaussian beam initially as shown on the left with its profile indicated below is converted to a tabletop illumination by scanning the beam across the *Field of View* (FOV) [Mau, 2020].

Uniform illumination as shown in Figure 3.5 is achieved by means of scanning a Gaussian beam using the setup shown in Figure 3.3. The Gaussian beam is scanned across the FOV (which is also tunable) to attain a table-top cross section illumination.The scanning is done via a galvanometer mirror which moves based on short electrical impulses programmed to scan across a defined set of angles which gives the tunability over the size of the FOV. The scanning is done along both the axes to form the tabletop illumination profile as shown in Figure 3.5. This results in a large FOV with uniffrom illumination as shown in Figure 3.4.

3 Results

Now we use the concept of flux, but instead of tracing the z-dependence we look at the 2D plane of a COS7 cell sample in order to multiplex. In existing systems, the major caveat being the spectral overlap limitation, since most fluorophores are closer to the red

end of the spectrum as well as the necessity to have spectrally distinct fluorophores to disentangle them.

Thus, with uniform illumination and long ON time, we can separate two species theoretically. Long ON time is required in order to have the fluorescence flux and not the global intensity since the molecule can come ON and OFF at any point when the camera is on. For example if the molecule came ON in the 10^{th} frame and was OFF/disappeared in the 15^{th} frame. We don't have access to the exact timestamp of the molecule coming ON or OFF, but discounting the first and last frame, we for sure know that the molecule was ON from the 6^{th} frame to the 14^{th} frame. This gives us 9 frames, over which we can average the intensity of the molecule. Now, had the molecule come ON for just two frames, we will have added noise when we consider it as 2 frames while averaging the intensity since the percentage error increases. Thus, one of the key aspects of utilising flux is temporal averaging. If we have many frames and long ON times of the molecules, the error is very small. Thus, DNA-PAINT molecules are good candidates with their longer ON time vs STORM fluorophore emitters.

4 Characterising results

In this Section we will look at some of the biological samples that are tagged with different sets of fluorophores and elaborate on the analysis approach and results.

4.1 Characterising the Excitation and Flux empirical relationship

In this section we will be characterising the fluorescence emission based on the change in excitation power. We expect a linear relationship with the photon flux and excitation as we saw in the first Section. We do see a linear trend in Figure 3.6 but the relationship is not exactly linear especially at low SNR with low power excitation. Thus, even for quite low excitation powers we measure significant fluorescence flux difference in the examples that we have shown. We can in fact do much better once we go to a higher power, and could also do 3 fluorophore multiplexing as seen for the case in Figure 3.7 which is an outlook for this new technique of flux based multiplexing. Below we only examine three powers, primarily to obtain the trend for fluorescence flux and corroborate our theoretical calculations. Since three points would essentially be sufficient to examine the linear relationship. The goal of measuring the photon number is to check if we can classify the different species based on this flux measurement as we expect from the theoretical calculation done in the previous Section. We see that they are in good agreement but error in measurement, plays a role when molecules that have similar values of brightness, indicating that an a-priory calculation of brightness would help select fluorescent molecular probe combinations that can be best for multiplexing. Notice that we are in no way constrained by the absorption-emission spectra of these fluorophores.

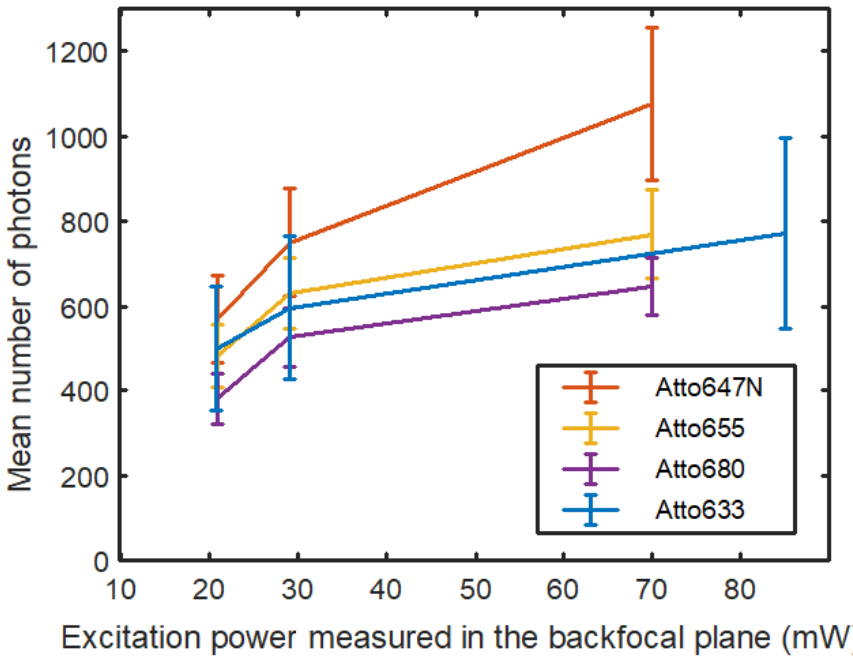

Figure 3.6: Mean number of emitted fluorescence photons from the sample for ATTO 647N (in Red), ATTO 655 (in Orange), ATTO 680 (in Purple) and ATTO 633 (in Blue) vs the excitation power measured in the back focal plane (mW) for Camera exposure time of 20 ms.

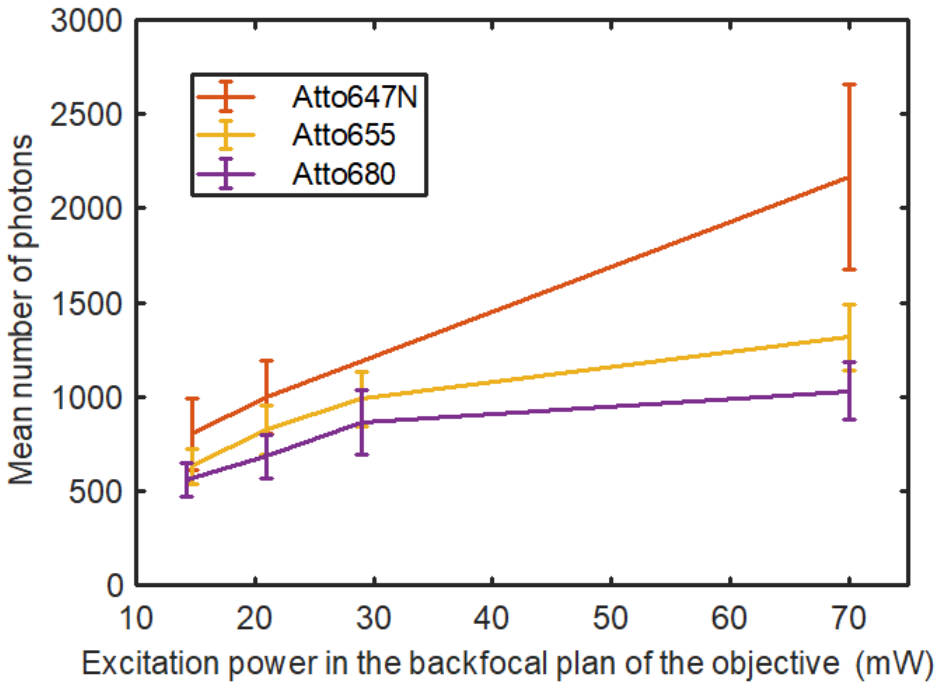

Figure 3.7: Mean number of emitted fluorescence photons from the sample for ATTO 647N (in Red), ATTO 655 (in Orange) and ATTO 680 (in Purple) for Camera exposure time of 50 ms.

4.2 Sets of Fluorophores

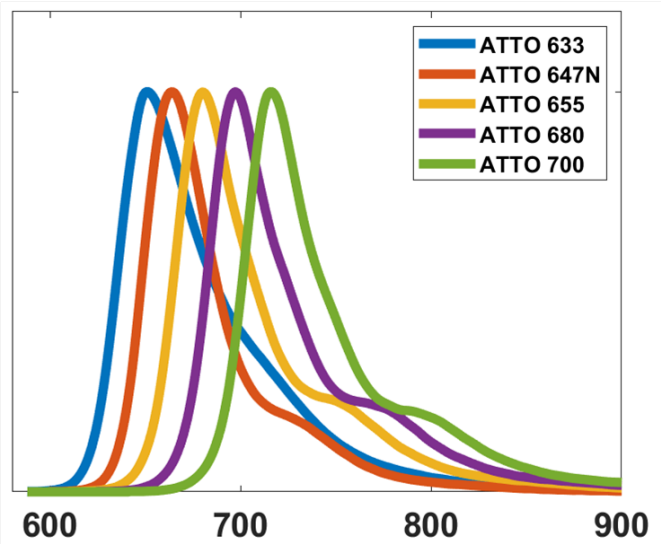

Figure 3.8: Emission Spectra of ATTO 633 (Blue), ATTO 647N (Red), ATTO 655 (Orange), ATTO 680 (Purple) and ATTO 700 (Green). The X-axis is the wavelegnth in nm. And Y-axis is the normalised fluorescence emission.

In Figure 3.8 we have the emission spectra of the major DNA-PAINT molecules in the Red domain. We see that all of them have a considerable overlap amongst one another. They are hard to separate even with spectral demixing based approaches. The emission spectra of ATTO 633 (Blue), ATTO 647N (Orange), ATTO 655 (Yellow), ATTO 680 (Purple) and ATTO 700 (Green) are plotted in Figure 3.8. Here we also see that ATTO 680 (Purple) and ATTO 647N (Orange) [the set of fluorophores that can be multiplexed using state of the art demixing techniques] are not as close as the set that we are going to experimentally multiplex. The most close, with highest overlap is ATTO 647N (Orange) and ATTO 655 (Yellow) which is what we demonstarte as a viable option for multiplexing using our new flux-based demixing technique. This would be the most difficult scenario, for conventional spectral demixing techniques. And if we are successful in disentangling the two species it would be straightforward in terms of the extension of this flux-based demixing technique to other sets of fluorophores. So we begin by examining this case.

4.3 Classification Likelihood

The assignment of molecules into different categories is based on the molecular flux distribution. Given, the molecular flux, the probability of the molecule belonging to a certain class is computed and assigned as such. The flux distribution with 2 peaks is associated to say two types of molecules A and B. Each Gaussian profile is characterized by a set of three parameters: its amplitude A, its mean value μ and its standard deviation σ.

The flux for each molecule is expected to have a normal distribution probability. Hence, for a molecule of type A with a mean flux μ_A and standard deviation σ_A, its probability follows a Gaussian

$$p(x) \quad = \quad \frac{1}{\sqrt{2\pi}\sigma_A} \quad \mathrm{e}^{\frac{-(x-\mu_A)^2}{2\sigma_A^2}} \tag{3.13}$$

The proportion of molecules type A and B in the ROIs is noted P_A and P_B respectively, satisfying $P_A + P_B = 1$. It is related to the amplitude of the Gaussian by

$$A_{A/B} \quad = \quad \frac{P_{A/B}}{\sqrt{2\pi}\sigma_A} \tag{3.14}$$

The likelihood for a molecule with flux x to be of type A with a probability of α satisfies where $p(x \mid A)$ is the probability of a molecule having flux x given that the molecule is type A.

$$\frac{P_A p(x \mid A)}{P_A p(x \mid A) + P_B p(x \mid B)} \quad = \quad \alpha \tag{3.15}$$

Which can be written as

$$p(x \mid A) \quad = \quad \beta p(x \mid B) \tag{3.16}$$

with

$$\beta \quad = \quad \frac{\alpha(1 - P_A)}{(1 - \alpha)P_A} \tag{3.17}$$

In the special case of an equal proportion of molecule of type A and type B ($P_A = P_B = 0.5$) and the threshold probability for recognition is set to $\alpha = 0.5$, then $\beta = 1$ and $p(x \mid A) \geq p(x \mid B)$.

We now move on to implementing this in a sample of COS7 cells with tagged Clathrin and Tubulin. The fluorophores used to tag are two sets of DNA-PAINT molecules in Section and one set of STORM molecules.

5 Sample of COS7 cells: Clathrin - ATTO 655 and Tubulin - ATTO 647N

We consider the entire FOV of the sample and divide into smaller ROIs. There is an optimisation in the size of the ROI, too small or too large will not yield good distributions, this was done manually. The idea is that with smaller regions would be more homogeneous both in terms of the plane of imaging as well as illumination which are both explored in the subsequent characterisations. The approach is discussed in depth below.

Figure 3.9 represents a sample image of area of $45\mu m$ x $45\mu m$ FOV, COS7 cell line with Tubulin tagged using DNA-PAINT ATTO 647N fluorescent marker and Clathrin tagged using ATTO 655 fluorescent marker with $0.2nmol$ imager/marker concentration. In the entire FOV the centroids (across all frames) detected during the processing of the

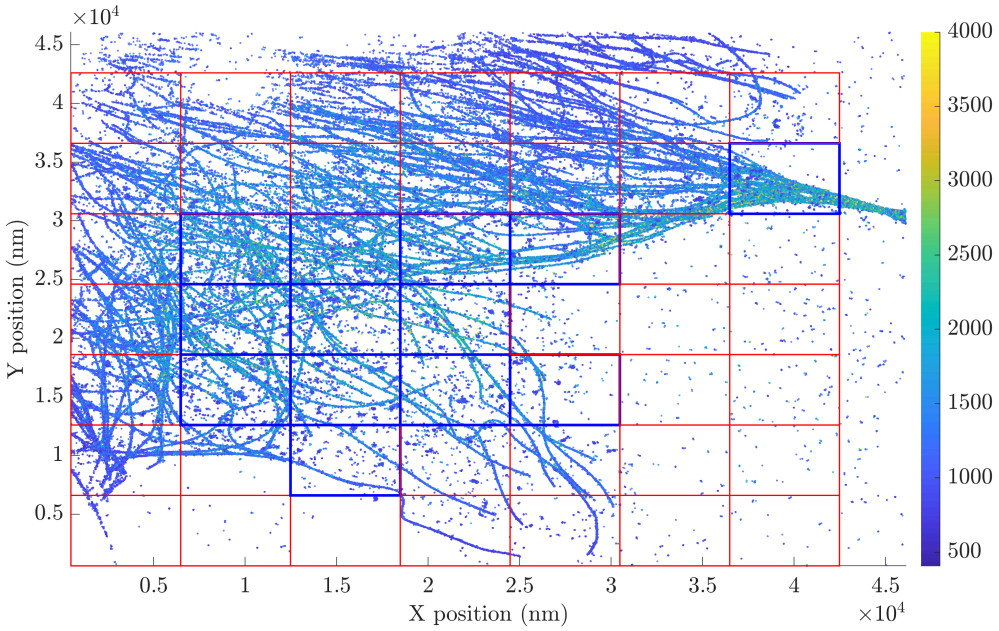

Figure 3.9: COS7 cell sample with X and Y coordinates in nm and the colorbar indicating the molecular flux with number of photons in given area per unit time. The sample is tagged with ATTO 655 Clathrin and ATTO 647N Tubulin. The FOV is divided into two types of smaller ROIs. The Blue ROIs are regions where two distinct peaks for the flux distribution can be computed and the Red ROIs are the regions where there is predominantly one type of flux population or too few molecules to have any sort of classification.

raw images, are classified as molecules based on the condition of spatial proximity (within 30 nm radius of each other). Thus, we have a set of consolidated molecules in the FOV as depicted in Figure 3.9. The flux for each molecule is calculated by taking the average of its intensity across all frames (ON time), excluding the first and last frame in which the molecule appears and disappears respectively. This exclusion is because in the first and the last frame we do not know the exact time at which the molecule appeared/disappeared. In Figure 3.9 the colorbar on the right represents the flux thus calculated for each molecule. The FOV in Figure 3.9 is treated and divided into smaller ROIs as indicated and being represented by two colors; one type represented in Blue color and the other in Red color. In each region molecular flux distribution is categorised into two Gaussian distributions with a certain threshold (confidence level of 60%). Blue color ROIs represent areas in which we successfully detect two distinct distributions of the flux. However in the Red color ROIs we are unable to detect two distinct flux distributions indicating predominantly the presence of one type of molecule.

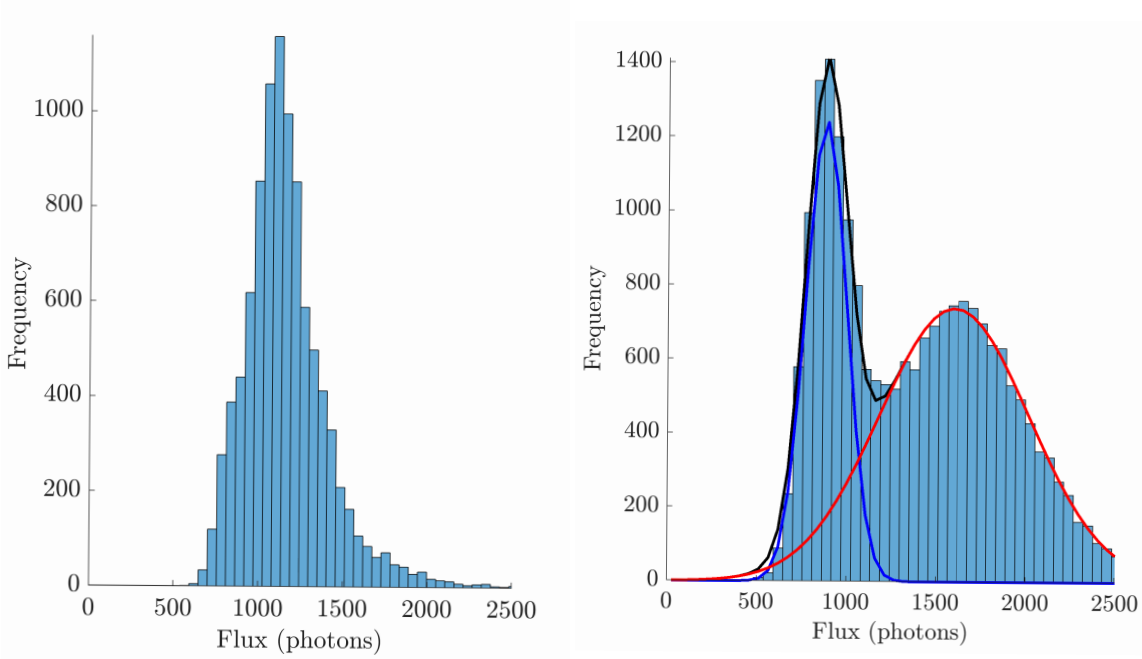

(a) Red ROIs

(b) Blue ROIs

Figure 3.10: In each of the ROIs shown in Figure 3.9 (a) Distribution of flux for Red ROIs where we have predominantly one type of flux population and unsuccessful in fitting two distributions.(b) Distribution of flux for Blue ROIs wherein we can classify and fit two normal distributions. All the ROIs are of the same size. The Blue curve represents the ATTO 655 population, the Red curve represents the ATTO 647N population and the Black curve is the cumulative of the two curves.

Figure 3.10 (a) illustrates as an example, a flux distribution binned based on molecular flux, detected in a Red ROI. Wherein X-axis represents the flux value and the Y-axis represents the number of molecules belonging to the corresponding flux bin in the histogram. In this illustration of the Red ROI the predominant flux value is around 1250 units and the range of molecular flux observed is 600 to 2500 units. Here we see that we do not detect the presence of two peaks in molecular flux distribution. Figure 3.10 (b) illustrates one of the Blue ROIs with a histogram of flux distribution with successful disentanglement into two distinct populations. One of the population (ATTO 655 fluorophore marker tagged to Clathrin) has a mean molecular flux of 750 units (represented by a Blue curve) with a range between 500 to 1200 units. Whereas the other population (ATTO 647N tagged to Tubulin, represented by a Red curve) has a mean molecular flux of 1700 units and a range from 500 and extending to beyond 2500 units. The consolidated distribution (addition of the two Red curve and Blue curve fitted distributions) is represented by the Black curve.

5.1 Probability Map

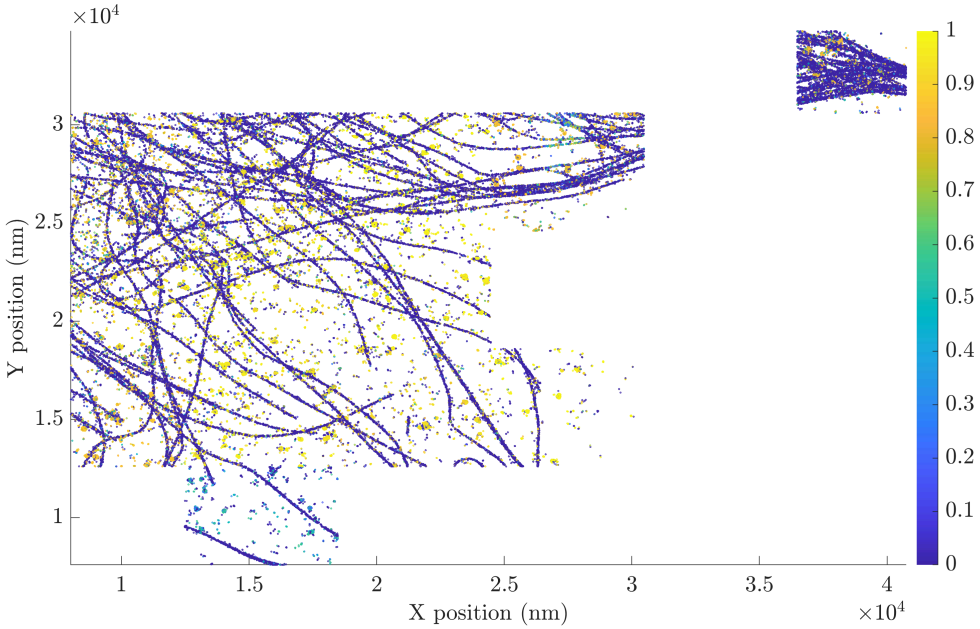

Figure 3.11: The Blue ROIs from Figure 3.9 are taken and the probability of the molecule being of species A which is ATTO 655 is computed and plotted across the FOV. The colorbar represents the probability map.

The Blue ROIs in the image (Figure 3.9) gives a flux distribution with 2 peaks associated to the two types of molecules A and B. Each Gaussian profile is characterized by a set of three parameters: its amplitude A, its mean value μ and its standard deviation σ.

Now we consider Figure 3.9 and calculate the conditional Bayesian likelihood probability for ATTO 655 and ATTO 647N (they are complimentary) in each of the Blue ROIs as described above. Figure 3.9 is further treated to remove all the Red ROIs which has only one predominant species or very few molecules (empty space). For the remaining part of the FOV in Figure 3.9 the probability of a certain value of flux occurring given the fluorescent marker being ATTO 655 is evaluated. This probability map is presented in Figure 3.11, the colorbar represents the probability of the fluorophore marker being ATTO 655. By inspection it clearly shows the classification of the two fluorophore markers is working in most part of the FOV. The lowest located ROI will be discussed along with Figure 3.13 in the coming Section. In Figure 3.12 we further present the zoomed in part of one of the ROI of Figure 3.11.

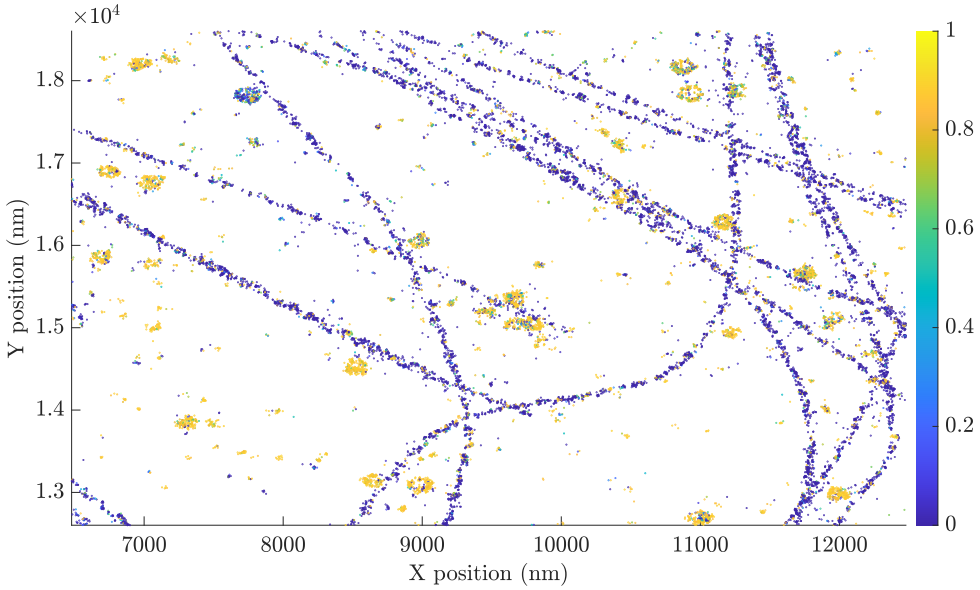

Figure 3.12: Zooming in on one of the ROIs from Figure 3.11 which indicates the probability map of a molecule being ATTO 655. That is, Yellow indicates the ATTO 655 molecules and the Blue indicates the ATTO 647N (complimentary probability) with the same colorbar.

5.2 Ratio Invariance

As discussed above two of the main characteristics of the population is the mean molecular flux and the amplitude of the Gaussian distribution. For the set of Blue ROIs we have two peaks of molecular flux distribution quantified by their respective peaks, binned in the histogram. The mean molecular flux value for each peak is calculated by taking the mean of the bin in which the peak resides. Thus, for such ROIs indicated in Blue, we have two mean peak values of molecular flux corresponding to the two species of fluorophore markers. These values appear to vary depending on the ROI locally. In order to quantify this, in Figure 3.13 (a) we plot the mean peak molecular flux values for the two species (ATTO 647N in Blue and ATTO 655 in Red) along the X-axis and the number of molecules corresponding to that peak on the Y-axis. We see that there is local variability of the mean molecular flux of each of the species across the FOV. This could be due to the axial defocusing of different parts of the cell owing to the 3D nature of the sample. This can be verified by calculating the ratio of mean fluxes of ATTO 655 to ATTO 647N in each of the ROI and checking if it has any variability by plotting against one of the mean flux (here ATTO 655). The idea of which being that if these tagged molecules are in the same plane, even though their individual mean flux values could differ, their ratio is expected to remain same. This is plotted in Figure 3.13 (b) and indicates a constant value of the ratio of the mean flux even though the individual means for each ROIs vary.

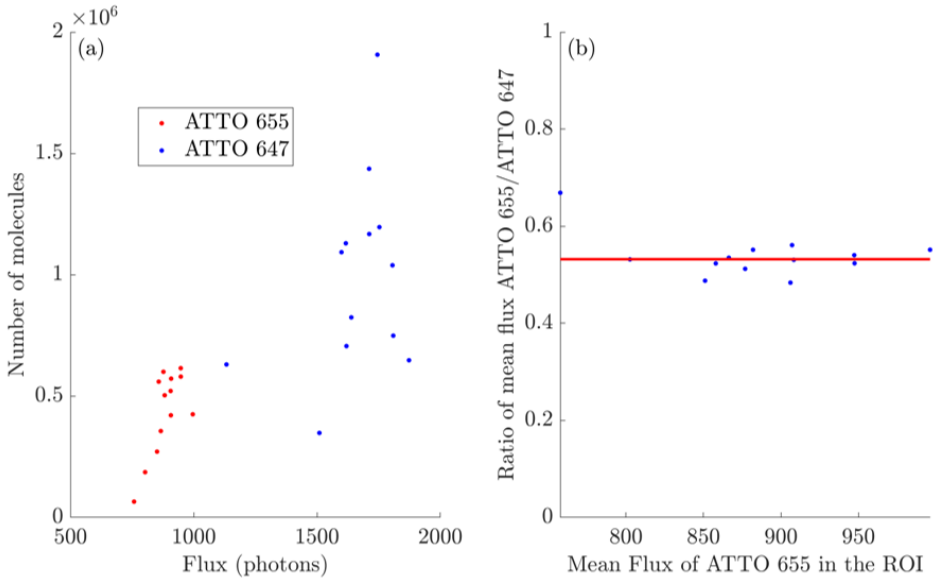

Figure 3.13: (a) Number of molecules having a certain flux is plotted according to the classification in each Blue ROI from Figure 3.9. This illustrates how the flux is changing across ROIs for both the species. (b) In order to verify if this is not due to illumination changes we plot the ratio of mean molecular flux of ATTO 655 to ATTO647N vs the mean flux of ATTO 655 in each ROI.

Our argument is therefore valid when the ROI is small thereby the two fluorescent tags exist in the same plane.

One should note if these conditions are not satisfied (as seen in lowest ROI in Figure 3.11), the flux change in the image seems to be related not to the illumination or the position in the image but more to the defocusing (axial component). Thus we conclude from simple inspection that this technique works in most parts of the FOV, as the Clathrin tagged ATTO 655 appear on an average different from the Tubulin tagged ATTO 647N.

Now we will consider the whole FOV presented in Figure 3.9 including the Red ROIs. We will evaluate the probability of a certain value of flux occurring given the marker being ATTO 655 across the whole FOV as shown in Figure 3.14. This is not a correct extension as in the Red ROIs technically, only one type of molecule is present. Hence the treatment will lead to erroneous classification as is evident from the fact that Microtubules tagged with ATTO 647N are being classified as ATTO 655 on the upper part of the FOV in Figure 3.14. This demonstrates that the presence of the two molecules in a ROI in fact helps in classifying them as separate species more successfully than when only one molecule is present due to defocusing related intensity variation as discussed in Figure 3.13. This indicates there exists an optimum size of ROI as indicated in Figure 3.24 and Figure 3.25.

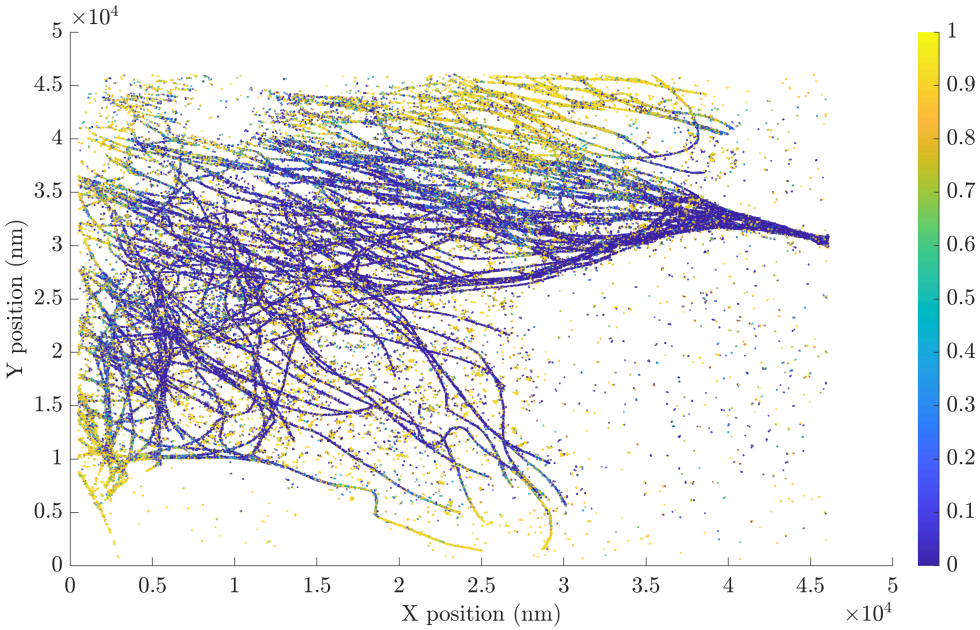

Figure 3.14: The probability map extended for the entire FOV with Yellow being ATTO 655 and Blue being ATTO 647N an the colorbar being the probability of being ATTO 655.

5.3 Renormalization

In Figure 3.15 we examine the other main parameter of the Gaussian fit which is the standard deviation. The standard deviation/width of the two Gaussians are a proxy for how tightly one can classify the two species. In Figure 3.15 (a), the histogram of flux for the ensemble of the Blue ROIs is used to normalise such that the mean flux of the ATTO 647 (2nd peak) is the same in all the ROIs. We see that there is a slight improvement of the histogram with peaks that are a bit less wide. The non-normalised distribution and the normalised distribution are then compared in Figure 3.15 (b) by plotting the standard deviation in each case (for each of the species, ATTO 647N in Red and ATTO 655 in Blue). We can see that in this treatment the width of the 2 peaks for each ROI and the value of the fit performed on the histogram of the non-normalized image (dashed lines) and on the normalized image (solid lines), there is indeed a little improvement but not enough to deserve such a complex re-normalization for this image at least. Hence we have not considered this treatment for the separation of the species as part of the analysis.

The result with the use of the image histogram and calculation of the probability of being ATTO 655 / 647 over all the ROIs give good result - it is not very different from the determination over each ROI independently.

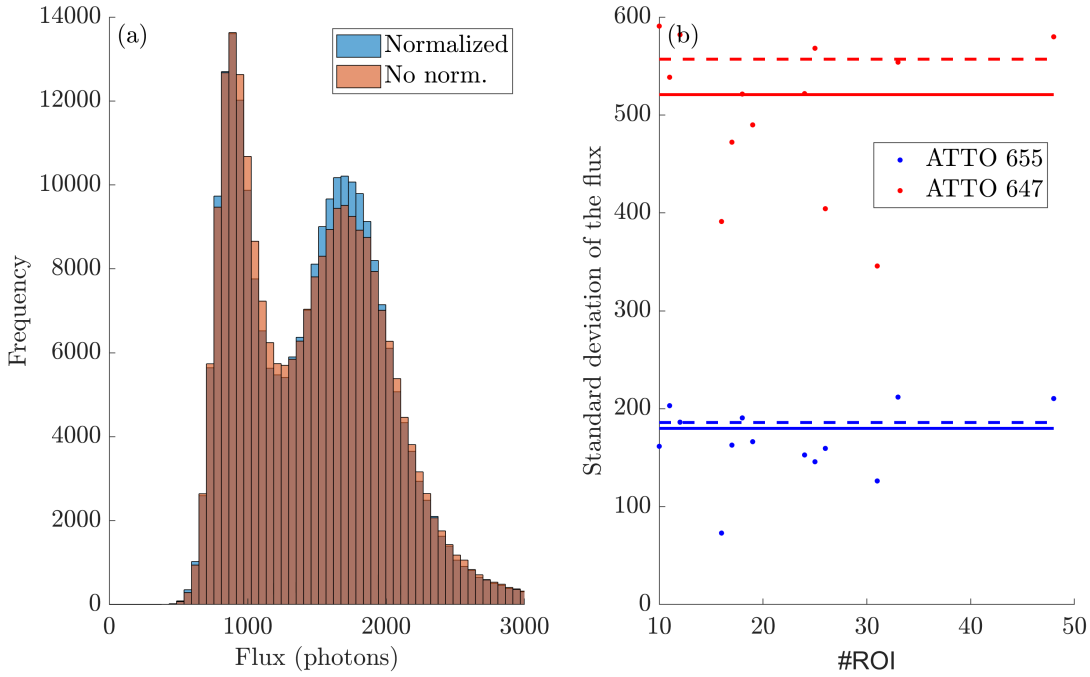

Figure 3.15: (a) Histogram of flux distribution across all Blue ROIs from Figure 3.9 in Blue and normalised flux in Orange. We see an improvement upon normalization. (b) Standard deviation of the Gaussian fits plotted for each of the species across each ROI with Red being ATTO 647N and Blue being ATTO 655 species. The dashed lines are for the case of non-normalized data and the solid lines for the normalized data for each species.

5.4 Standard Deviation

The other main parameter of the Gaussian fit is the standard deviation σ of each of the fits. This represents the amount of dispersion of values about the mean. In Figure 3.16 (a) in the X-axis we have the frame number and in the Y-axis we have the number of molecules with the corresponding ON frames, we plot the ON time for all the molecules and observe an exponential decay. This is probably due to bleaching of the molecules. We see that the molecules are ON for at least three frames since we do not consider such molecules for the analysis and treatment otherwise. In Figure 3.16 (b) we consider molecules with varying probability of being ATTO 655 along the X-axis and the mean ON time (in number of frames) along the Y-axis. That is, molecules that have the probability of being ATTO 655 closer to 1 are most certainly ATTO 655 - Clathrin (as in Figure 3.11) and on the other end of the spectrum if they are closer to zero probability of being ATTO 655 then they are most certainly the second type of species, which is ATTO 647N. Thus, we have the entire spectrum of molecules; on the right ATTO 655 and left ATTO 647N. Now for each of these probability categories we look at the corresponding mean ON time of all

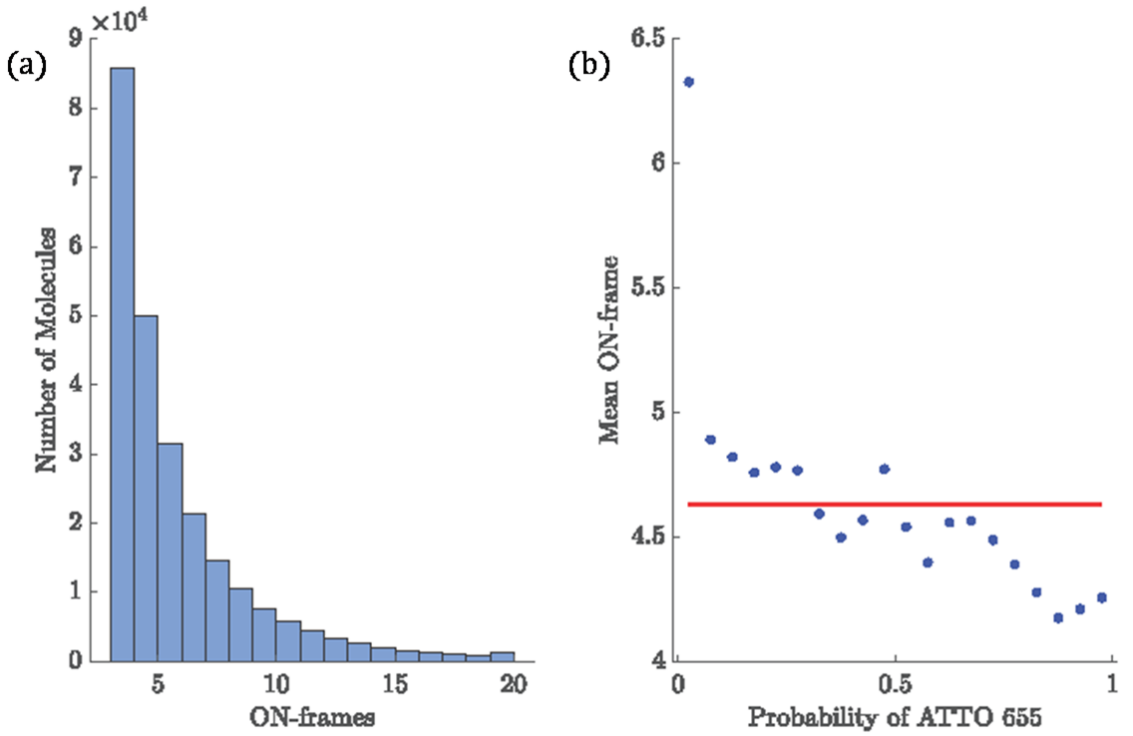

Figure 3.16: (a) ON time - histogram for all molecules that have ≥ 3 frames. (b) Based on the probability map from Figure 3.11 molecules classified based on the probability of being ATTO 655 and their corresponding mean ON time in frames. We see a trend of ATTO 647N molecules (probability of being ATTO 655 close to 0) with longer ON time.

molecules that fall into this probability. And we see that in Figure 3.16 (b) we have a trend of the mean ON time for ATTO 647N being markedly higher (close to 6.4 frames) than for ATTO 655 (close to 4.2 frames). Thus, this is an additional dimension that can be accessed to classify fluorophore markers. And in this case ATTO 647N has both a longer mean ON time and a larger mean flux, but this need not always be the case, and it depends on the DNA-PAINT molecular properties.

5.5 Quantification of the Robustness of the novel Flux-based multiplexing classification

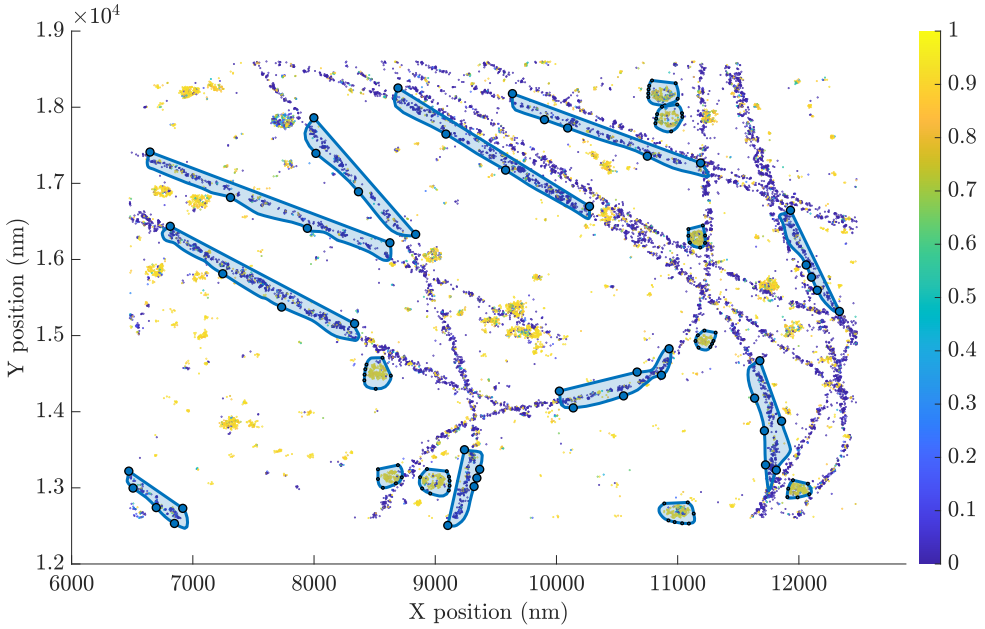

Figure 3.17: In this Figure we consider the probability map of Figure 3.12 in terms of ATTO 655, and select 10 regions of Clathrin and Tubulin each by means of spatial structure and morphology. Since morphologically, Clathrin is globular whereas Tubulin is filamentous we are able to examine the classified molecules in each of these structures to quantify the robustness of our classifxation technique.

Now that we have characterised the analysis procedure along the main parameters of the fit of the normal distributions, we now quantify the robustness of the classification and cross-talk. That is, cases wherein we clearly know that the molecules must be say ATTO 655 but are classified as ATTO 647N and vice versa. This can be done by exploiting spatial specificity of the underlying cellular structures. We know that Tubulin has a continuous filamentous rope like structure and Clathrin is interspersed through the cellular matrix with a globular architecture. Exploiting this a-priory knowledge we select 10 regions of Tubulin and Clathrin each, as shown in Figure 3.17 and analyse these regions. Since we know clearly what these regions are supposed to contain, we can have a quantifiable estimate in terms of the mis-classification and cross-talk. In Figure 3.17, we have the probability map of Figure 3.11 of the sample and the regions which are selected are highlighted in Blue.

In Figure 3.18 we have the statistics for all the selected regions in Figure 3.17. In Figure 3.18 (a) we have the percentage of molecules recognised as ATTO 655 - Calthrin indicated in Blue (closer to probability 1) and in Red (with the complimentary probability) we have

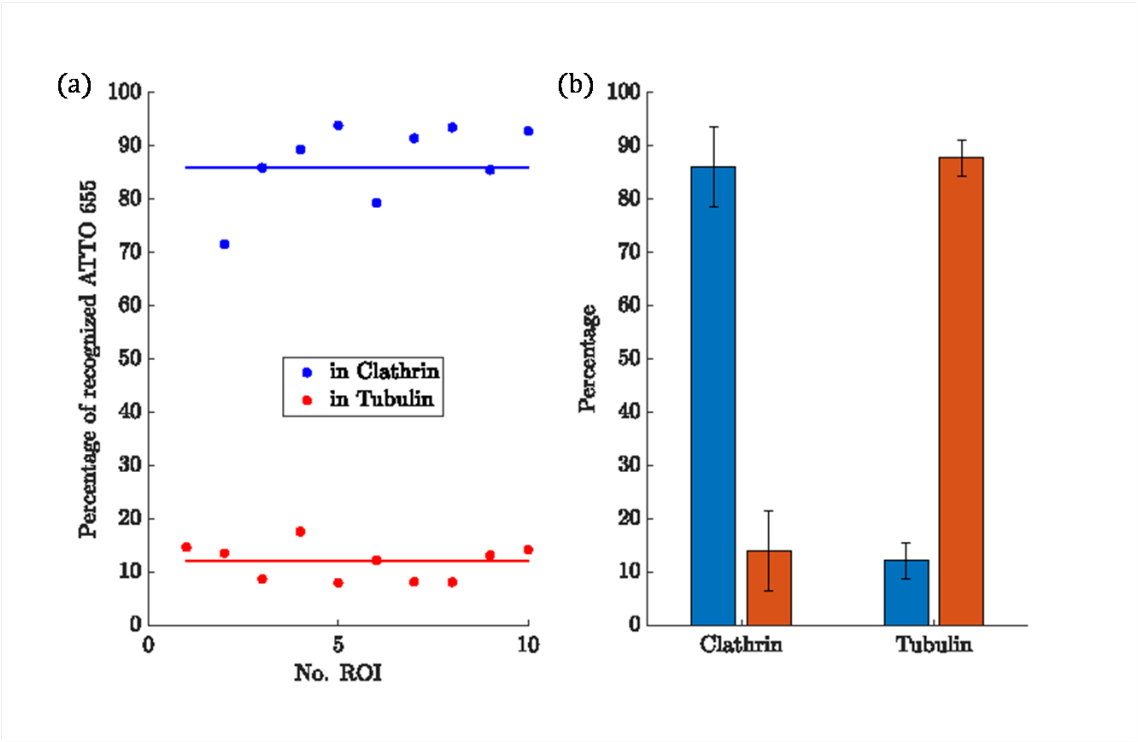

Figure 3.18: (a) Percentage of molecules recognised as ATTO 655 (complimentary for ATTO 647N) in Blue for Clathrin region (x10) and Red for Tubulin (x10). (b) In each of the 10 region sets for Clathrin and Tubulin with Tubulin species in Orange and Clathrin in Blue for quantifying the robustness of the classification of molecules with error bars as the standard deviation to quantify the cross-talk.

Tubulin for each of the selected regions of Figure 3.17. We see that we have more than 90% accuracy in Tubulin detection and we have about 10% noise due to Clathrin in the Tubulin regions. In Figure 3.18 (b) we have the statistics for each set (10 samples for Clathrin on the left and 10 samples for Tubulin on the right) with Blue being Clathrin and Orange being Tubulin with error bars as their corresponding standard deviations. Thus we see that the results are very promising as we have low mis-classification and this is assuming that Clathrin is not present atop/in congruence with Tubulin which may as well be the case in the sample, so this is an upper limit that one can consider. And we see that we are able to successfully demix the sample into two species with relatively low miss-classification based on flux. One can additionally augment this by probing the ON time as an added dimension as well but flux alone is sufficient to yield good demixing results. We see 90% and 85% accuracy for Clathrin and Tubulin respectively indicating that the method is indeed very robust.

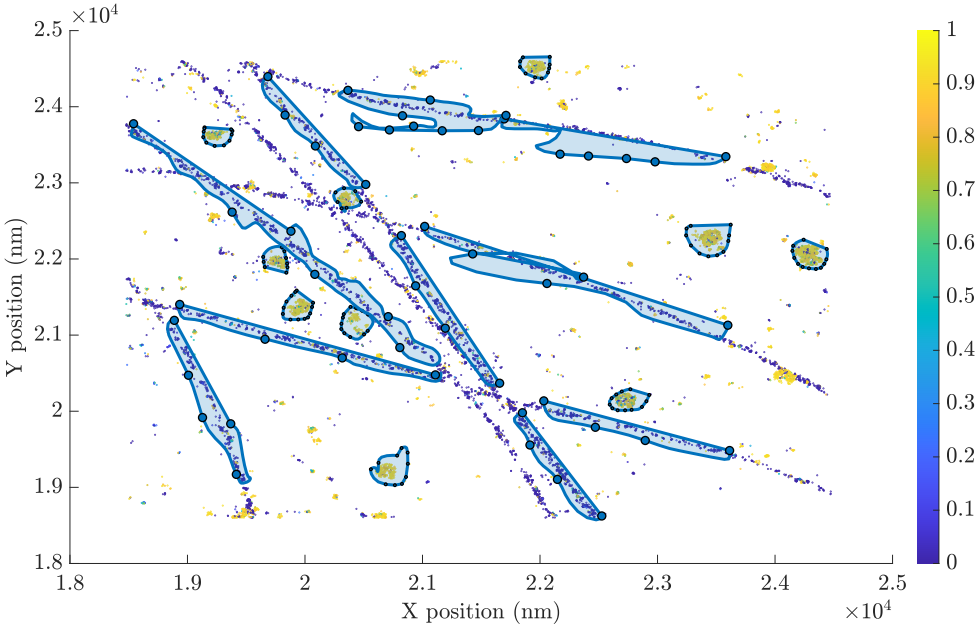

Figure 3.19: Same treatment as in Figure 3.17 but different ROI. Considering Figure 3.13 with the probability map of ATTO 655 and selecting 10 regions each for Clathrin and Tubulin by means of spatial structure to characterize misclassification.

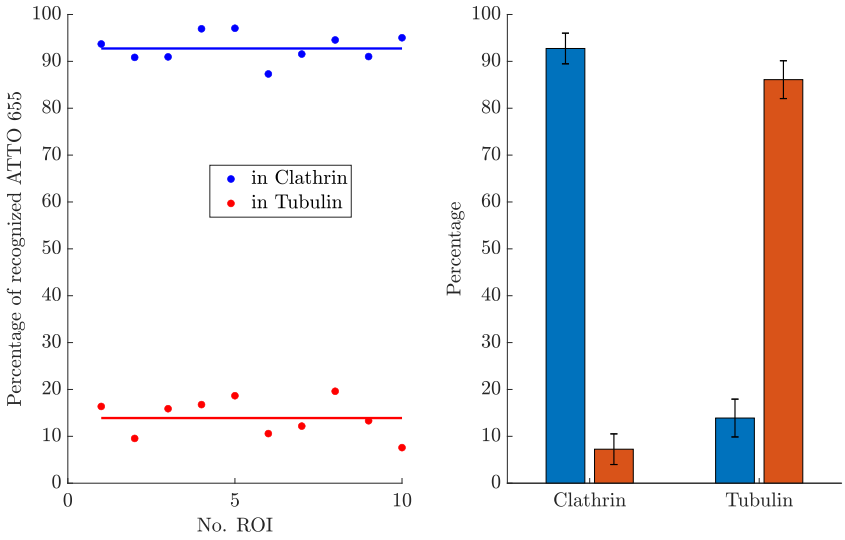

Figure 3.20: Same treatment as in Figure 3.18 but different ROI. (a) Percentage of molecules recognised as ATTO 655 (complimentary for ATTO 647N) in Blue for Clathrin region (x10) and Red for Tubulin (x10). (b) In each of the 10 region sets for Clathrin and Tubulin with Tubulin species in Orange and Clathrin in Blue for quantifying mis-classified molecules with error bars as the standard deviation.

We illustrate the same results through following the same procedure, across another ROI to ensure there is no bias in picking the ROI. And this is given in Figure 3.19 and Figure 3.20. In Figure 3.19 we again select 10 regions each for Clathrin and Tubulin and do the same analysis as shown in Figure 3.20. In Figure 3.20 we see that the classification is very similar.

5.6 Flux Demixing

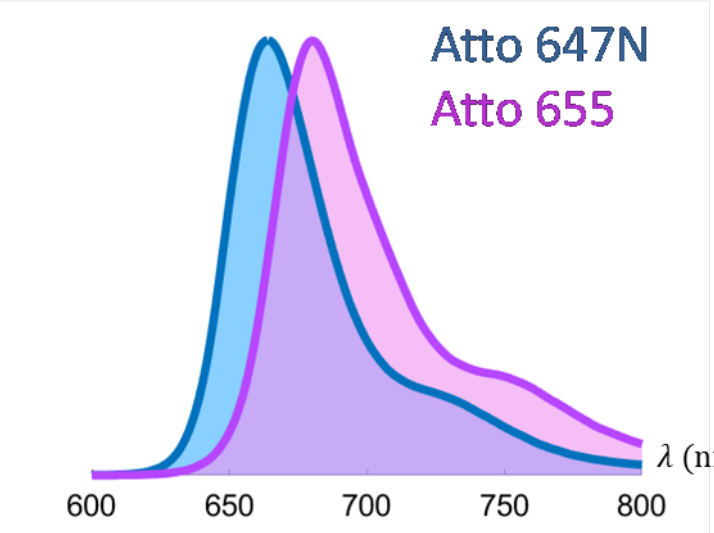

Figure 3.21: Emission spectra for ATTO species 647N (Blue) and 655 (Purple). They are very close and virtually the same in terms of their emission spectra. X-axis is wavelength in nm.

Thus, to summarise what we did, COS7 cells were immonolabelled using ATTO 655 and ATTO 647N whose emission spectra are given below in Figure 3.21. The Tubulin was labelled using ATTO 647N and Clathrin was labelled using ATTO 655. The sample was excited uniformly.

When we image a sub-area, we see that we are able to discern the difference between their fluorescence flux as show in Figure 3.22. In Figure 3.22 we have the molecular flux distribution with the colorbar on the right representing the flux for each of the molecules in the ROI with Green being Tubulin tagged with ATTO 647N and Blue being Clathrin tagged with ATTO 655. The details of flux calculation, analysis and characterization are described in the next section.

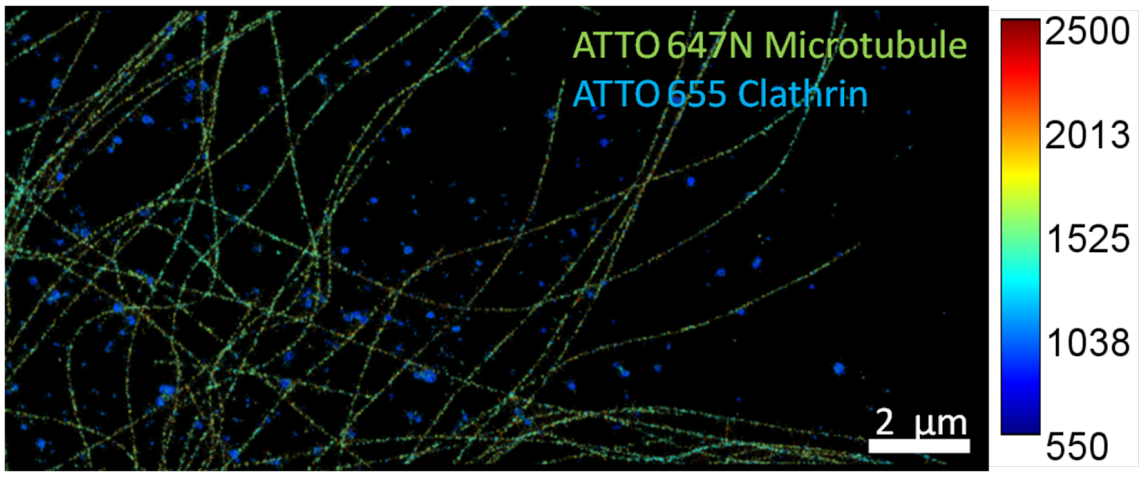

Figure 3.22: Flux distribution for a sample of COS7 cell, ATTO species 647N in Green and 655 in Blue for tubulin and clathrin respectively. Colorbar on the right indicates the flux.

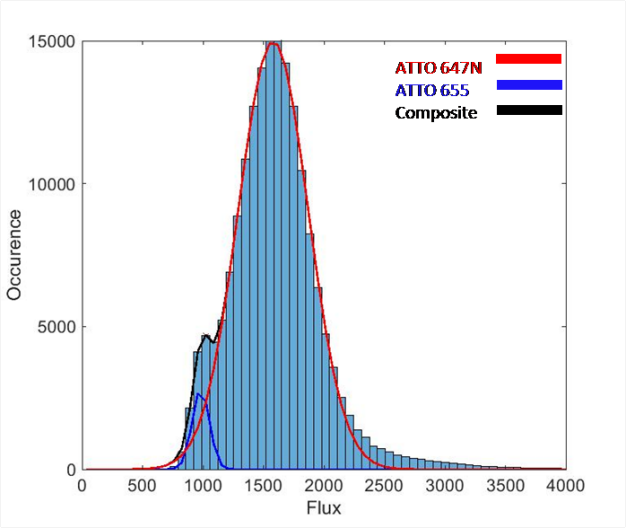

Figure 3.23: Flux distribution histogram for the sample in Figure 3.23 indicated by light Blue bars with X-axis as the flux and Y-axis with the number of molecules. The Black curve is the composite distribution, the Red curve for ATTO 647N, and Blue curve for ATTO 655 are the individual distributions for the respective species of fluorophore emitters. They are very close and virtually the same in terms of their emission spectra but we see here that there is a distinction in term of their flux distribution.

The Blue labels are used for Clathrin and the Green are for Tubulin. This was distinguished by disentangling the fluorescence distribution, as shown in Figure 3.23, into two normal distributions with Bayesian probability (in this case 60%). This is done by assigning probabilities for each point in the distribution to either classify them as one or the other species, based on the distance of the species from the center of the two normal distributions. The image was also filtered for any additional random noise by having a *Density-based spatial clustering of applications with noise* (DBSCAN) spatial cluster al-

gorithm using the Abbelight software. DBSCAN (Density-Based Spatial Clustering of Applications with Noise) is a powerful clustering algorithm employed in image processing for efficient background removal. By grouping pixels based on their density in the spatial domain, DBSCAN identifies and separates foreground objects from the background, making it particularly effective in scenarios with varying object shapes and sizes. Its ability to handle noise and outliers enhances its suitability for robust background segmentation, providing clearer and more accurate results in image analysis applications

In the histogram distribution (light Blue) we can see that upon classification to ATTO 647N (Red) and ATTO 655 (Blue) we can disentangle the ROI of interest and we also see the overlap in the two distributions is quite large owing to the low concentration of ATTO 655 as well as the proximity of the two species spectrally. More on fitting the distributions, classifying regions is elaborated in the coming section.

5.7 Zooming into the FOV

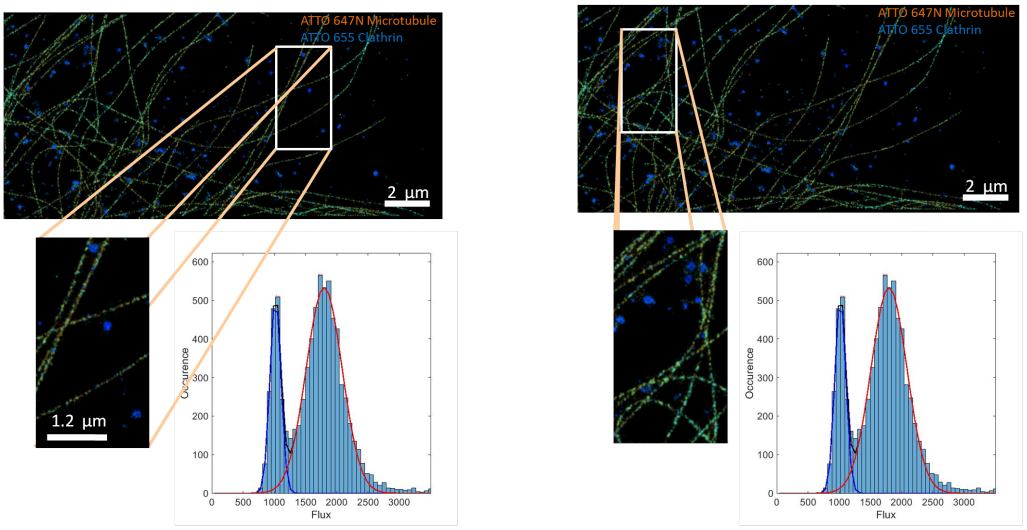

(a) Region 1 (b) Region 2

Figure 3.24: The FOV in Figure 3.22 is taken and smaller ROIs are selected as indicated by the boxed regions 1 and 2. They are further magnified and shown along with their corresponding molecular flux distribution for each of the regions. We see that the peaks and distributions are more distinct in the smaller regions 1 and 2 as compared to the entire FOV shown in Figure 3.23.

We expect that upon zooming into the FOV, with smaller pieces of ROI we should see the distribution becoming more distinctly bimodal, since the local inhomogeneities in space will reduce upon observing smaller ROI. And this is exactly what we observe as seen in Figure 3.24 and Figure 3.25. Upon looking at a smaller region of randomly selected area, we see that the classification is more distinct. This is due to the fact that locally the distributions are more distinctly classifiable owing to the comparable concentration

locally as well as the plane of both the tags being the same, when compared to the global picture. Since we have selected Clathrin and Tubulin which are interspersed in the cellular matrix, locally and globally we expect a similar bi-modal distribution. But when you have a predominance of one species we can easily classify all the points as one species in the absence of the other species and as you reduce the ROI size we see a comparable concentration of both (in regions where both are present for example Clathrin and Vimentin both close to the nuclear membrane) . If we have a very small ROI that is an issue as well, as we will see fewer set of molecules and will enter the regime of having a predominance of one of the species again. With respect to the plane of illumination, locally we expect in a small ROI to be more flat/in the same plane as opposed to looking at the global FOV. Since both the concentrations as well as the z-axis location of our fluorescent probe plays a crucial role in our classification system, we optimize the ROI size for classification based on the sample.

In the distribution of both the figures we now clearly see that the overlapping region has reduced considerably and the classification of the distribution into two separate normal distributions is more robust. Flux distribution histogram for the sample zoomed in to the region is also indicated. The Black curve is the composite distribution and the Red for ATTO 647N, and Blue for ATTO 655 are the individual species' classification. The local concentration is comparable and the distinction between the two peaks has more parity.

5.8 Local Assignment

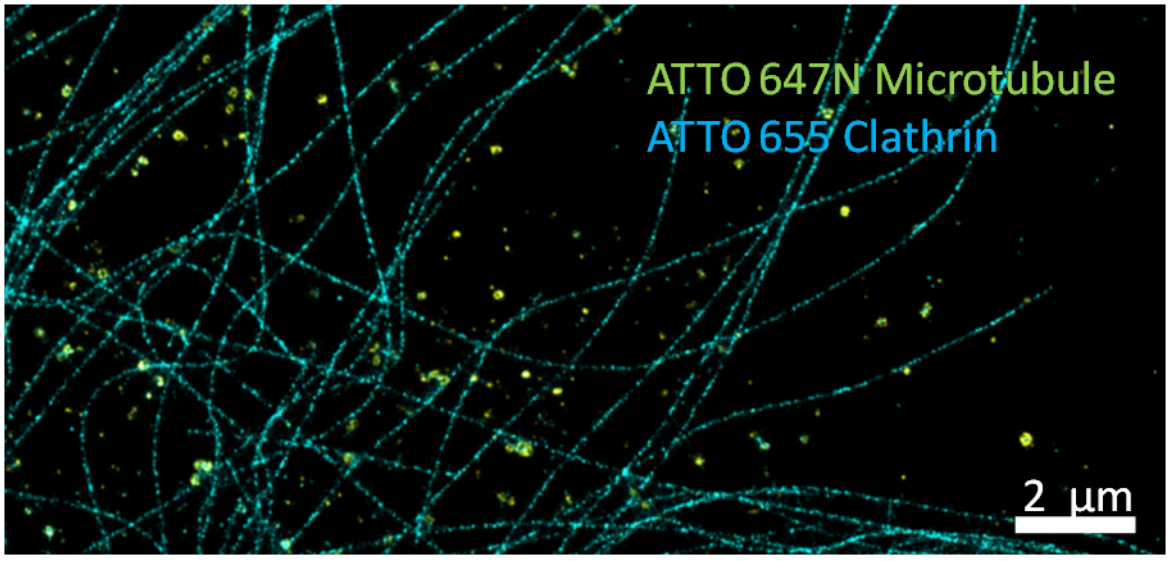

Figure 3.25: Classifying the entire FOV based on segmentation into smaller ROIs and minimum threshold of fluorophore concentration of each species. Green is one species and Blue is another species.

Since it is evident that upon picking smaller ROIs we enhance the local homogeneity and increase the segregation in the classification process, we now analyse the entire FOV by

dividing it into smaller regions. We have control over the size as well as the concentration threshold of each species of the fluorophore (Regions with small number of molecules which is basically empty space is rejected). That is, we can assign ROI sizes based on the number of fluorophores (concentration). This was used to segment the sample into smaller ROIs where we have classified the two species through local as shown in Figure 3.25. In Figure 3.25 we have ATTO 647N tagged to Microtubules in Blue and ATTO 655 tagged to Clathrin in Green.

6 Sample of COS7 cells: Clathrin - ATTO 680 and Tubulin - ATTO 647N

Now that we have seen that the flux based multiplexing technique works well, we proceed to elaborate on the detailed approach of the classification of the molecules into two species and what parameters can be used to do so for a sample of COS7 cells tagged with ATTO 680 Clathrin and ATTO 647N Tubulin. The same analysis was repeated for a sample of COS7 cell. The sample was tagged with ATTO 680 (Clathrin) and ATTO 647N (Tubulin). Here we see that ATTO 680 and ATTO 647N are not as close as the previous set that we examined which was the most close with highest overlap, that is ATTO 647N and ATTO 655. Since the technique works with such a high degree of overlap and proximity spectrally as seen in the previous set of experiments, the second sample set is to illustrate that it is not limited to just one combination of fluorophore emitters.

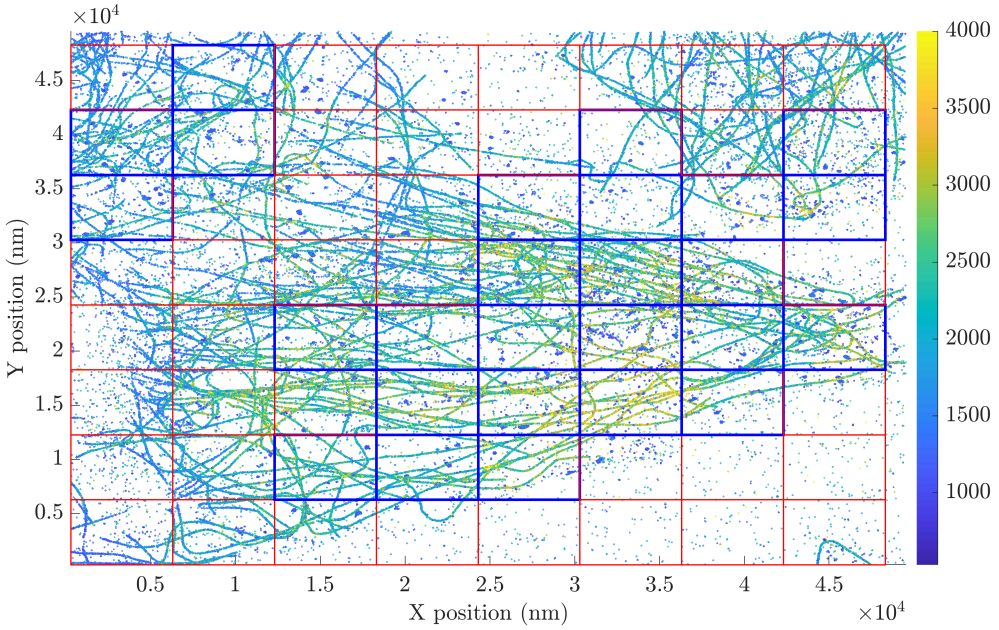

Figure 3.26: Another COS7 cell sample with X and Y coordinates in nm and the colorbar indicating the molecular flux. Tagged with ATTO 680 Clathrin and ATTO 647N Tubulin. The FOV is divided into two types of smaller ROIs. The Blue ROIs are regions where two distinct peaks for the flux distribution can be computed and the Red ROIs are the regions where there is predominantly one type of flux population or too few molecules to have any sort of classification.

In Figure 3.26 we have COS7 cells with FOV $45\mu m$ x $45\mu m$. The Blue ROIs again here indicate the presence of distinct bimodal distribution with two peaks which can be fit with two normal functions. And the Red ROIs are regions where such a classification is not possible.

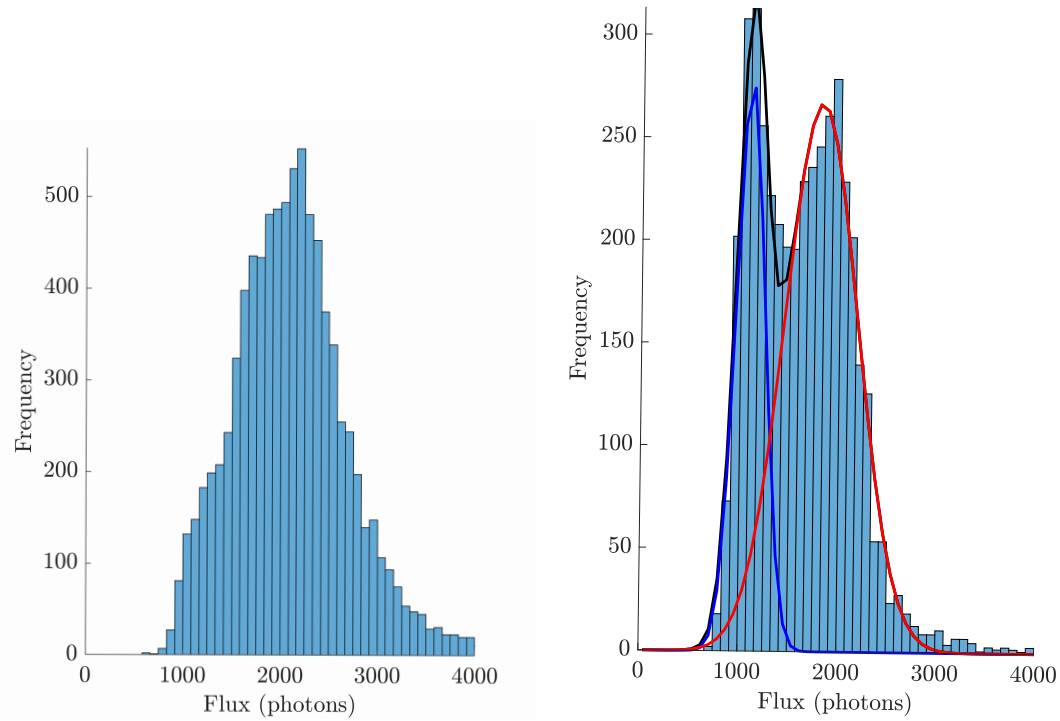

(a) Red ROIs (b) Blue ROIs

Figure 3.27: In each ROIs shown in 3.26 (subdivided into smaller parts from the full FOV, 45 μ x 45 μ), are marked by Red-ROIs and Blue-ROIs, based on observed flux distributions. (a) Red ROIs: Flux of photons with frequency of its occurrence as observed in a Red-ROI, it is evident that in Red ROIs distribution does not admit combination of two normal distributions, and (b) Blue ROIs: Flux of photons observed with their frequency of occurrence in Blue-ROIs. In the Blue-ROIs, the distribution of photon flux distribution admits combination of two normal distributions, one marked by blue-curve (representing ATTO 680 flurophores), other distribution marked by red-curve (representing photon flux from ATTO 647N) and joint (combined) distribution by black-curve.

In Figure 3.27 right, we have an example of one such Blue ROI molecular flux distribution (light Blue histogram) with two distinct peaks fitted with Gaussian. The Red and Blue curves indicate the fits for each species respectively.

Contrastingly, in Figure 3.27 left, we have predominantly only one type of population/ species of fluorophore emitter of one of the Red ROIs. Thereby we cannot classify this region into two species.

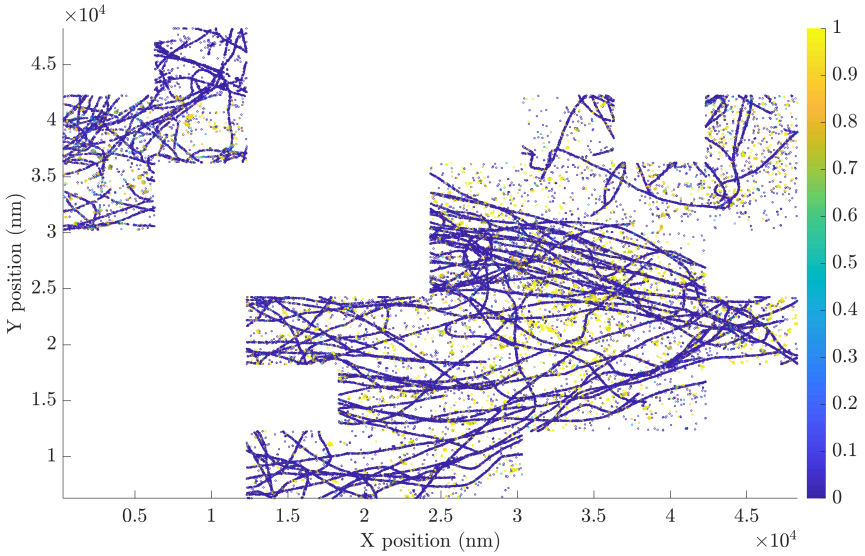

Figure 3.28: The Blue ROIs from Figure 3.26 are taken and the probability of the molecule being of species A which is ATTO 680 is computed and plotted across the FOV. The colorbar represents the probability map.

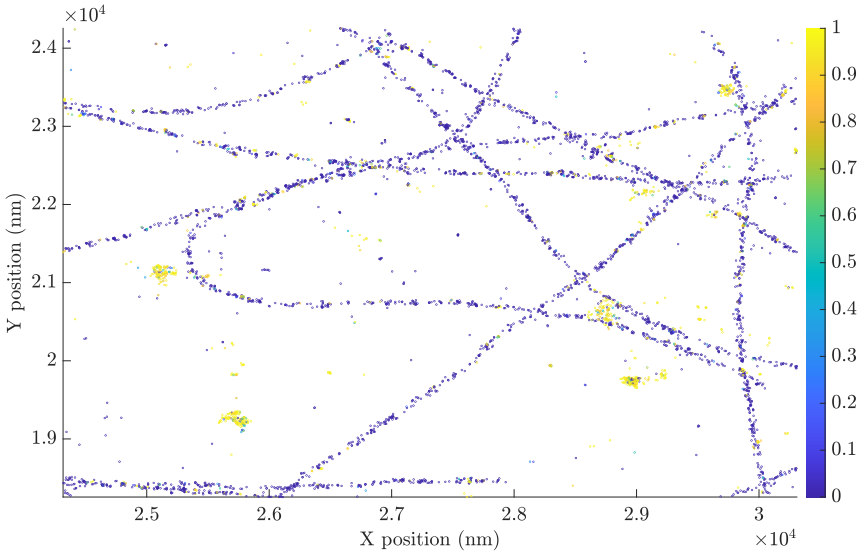

Figure 3.29: Zooming in on one of the ROIs from Figure 3.26 which indicates the probability map of a molecule being ATTO 680. That is, Yellow indicates the ATTO 680 molecules and the Blue indicates the ATTO 647N (complimentary probability) with the same colorbar.

In Figure 3.28 we have the probability map of the molecule being ATTO 680 computed based on the same analysis as done in Figure 3.11. In Figure 3.28 the X-axis and Y-axis are

in nm and the color bar represents the probability of the molecule being ATTO 680. That is, if the molecule has a probability close to 1, it is highly likely to be ATTO 680 which is indicated in Yellow. This matches the expected tagged organelle which is Clathrin as seen in Figure 3.28 and more evidently in Figure 3.29. Figure 3.29 is the zoomed in plot of one of the ROIs of Figure 3.28. And we can clearly see that Clathrin tagged with ATTO 680 is Yellow (probability close to 1 on the colorbar) and Tubulin tagged with ATTO 647N is Blue (probablity of being ATTO 680 close to 0).

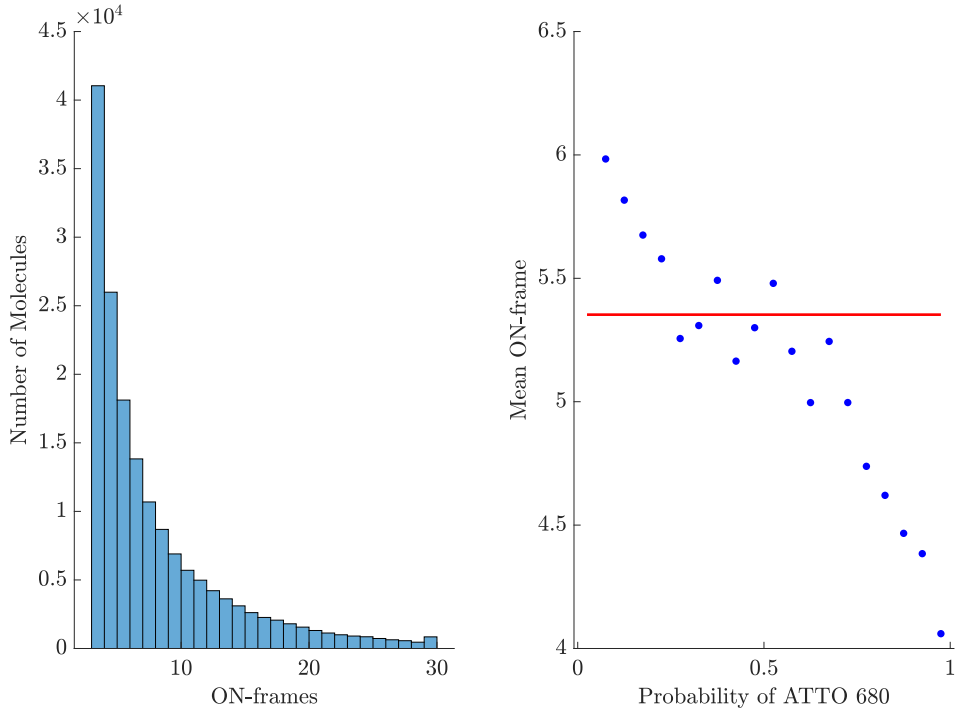

Figure 3.30: (a) On time histogram for all the molecules that have ≥ 3 frames. (b) Based on the probability map from Figure 3.26 molecules classified based on the probability of being ATTO 680 and their corresponding mean ON time in frames. We see a trend of ATTO 647N molecules (probability of being ATTO 680 close to 0) with longer ON time.

In Figure 3.30 we have the same plots as shown in Figure 3.16 for this sample. On the left we have the histogram for ON time/frame. And on the right we have the probability of the molecule being ATTO 680 along the X-axis and the corresponding mean ON time along the Y-axis. Even here like the previous experiment, we have ATTO 647N having a larger ON time close to 6 frames and ATTO 680 close to 4 frames. This analysis was done for molecules with ≥ 3 frames of ON time as in the previous experiment/sample. This further indicates that we can exploit the ON time of the molecules as another parameter to classify molecules apart from and added to their molecular flux measurements.

In Figure 3.31 we have the quantification of effectiveness of the classification between the molecules, same analysis carried out as in Figure 3.18 and Figure 3.20 with the previous sample. A single ROI was taken and 10 regions of Clathrin and 10 regions of Tubulin

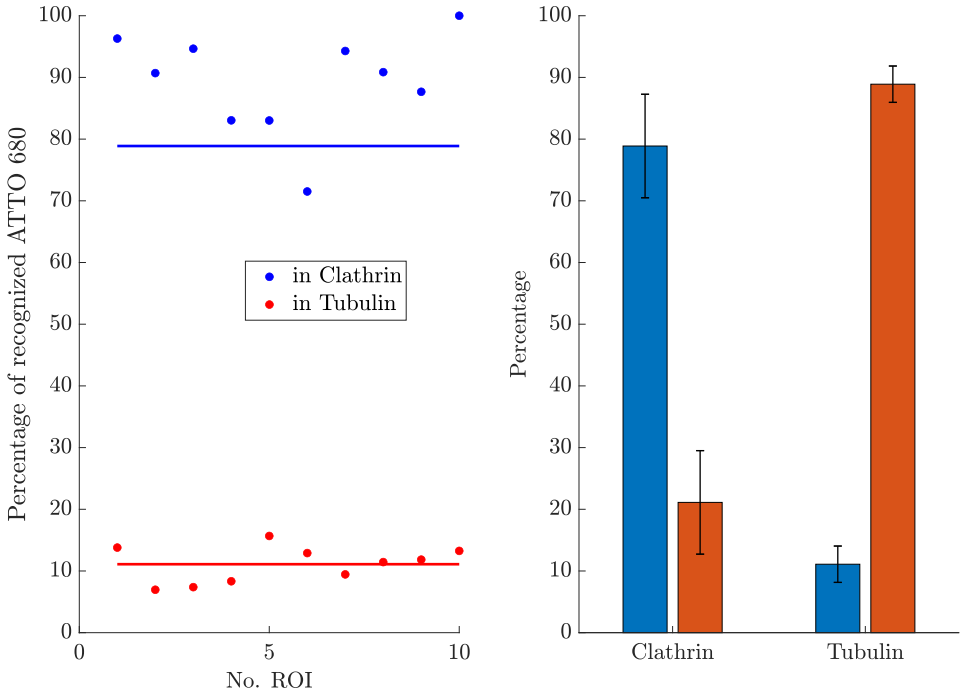

Figure 3.31: Same treatment as in Figure 3.19 but different sample (a) Percentage of molecules recognised as ATTO 680 (complimentary for ATTO 647N) in Blue for Clathrin region (x10) and Red for Tubulin (x10). (b) In each of the 10 region sets for Clathrin and Tubuli nwith Tubulin species in Orange and Clathrin in Blue for quantifying mis-classified molecules with error bars as the standard deviation.

were selected based on their spatial morphology. The number of Clathrin tags in Tubulin selected regions and vice versa were computed. We see that we have a higher Cross talk on Clathrin. This depends on three primary parameters, one the concentration of the fluorophore imager/tag, secondly the colocalization of both the imagers with one being less adding to more relative cross talk and thirdly the chemical non-specificity (for which we cannot access the ground truth). We see 80% and 90% accuracy for Clathrin and Tubulin respectively indicating that the method is indeed very robust.

6.1 STORM Sample of COS7 cells: Clathrin - CF680 and Tubulin - CF647

Now that we have established that the technique works well with different types of DNA-PAINT fluorophore emitters, we now move on to STORM fluorophore emitters. These species are not ON for a very long time like DNA-PAINT. They blink quite quickly in comparison and this will add to the error in terms of flux calculation as discussed in Section 1. But nevertheless we carry out the same analysis approach of flux calculation and classification in this sample of COS7 cells with CF647 tagged Tubulin and CF680 tagged Clathrin.

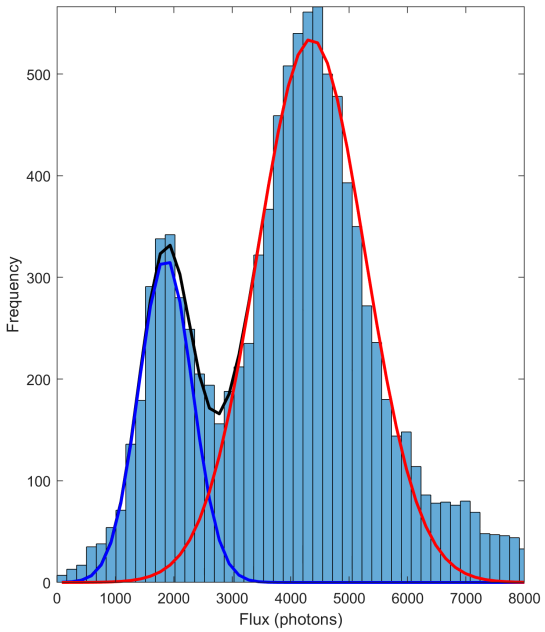

Figure 3.32: Distribution of photon flux in one of the Blue ROIs shown in Figure 3.33, wherein we can classify and fit two normal distributions. The Blue curve represents the CF680 tagged Clathrin population, the Red curve represents the CF647 tagged Tubulin population and the Black curve is the cumulative sum of the two curves, we treat this as typical distribution

We have COS7 cells tagged for STORM with a FOV $45\mu m$ x $45\mu m$. In Figure 3.32 we have an example of one such ROI wherein molecular flux distribution (light Blue histogram) with two distinct peaks is fitted with two Gaussians. The Red and Blue curves indicate the fits for each species respectively.

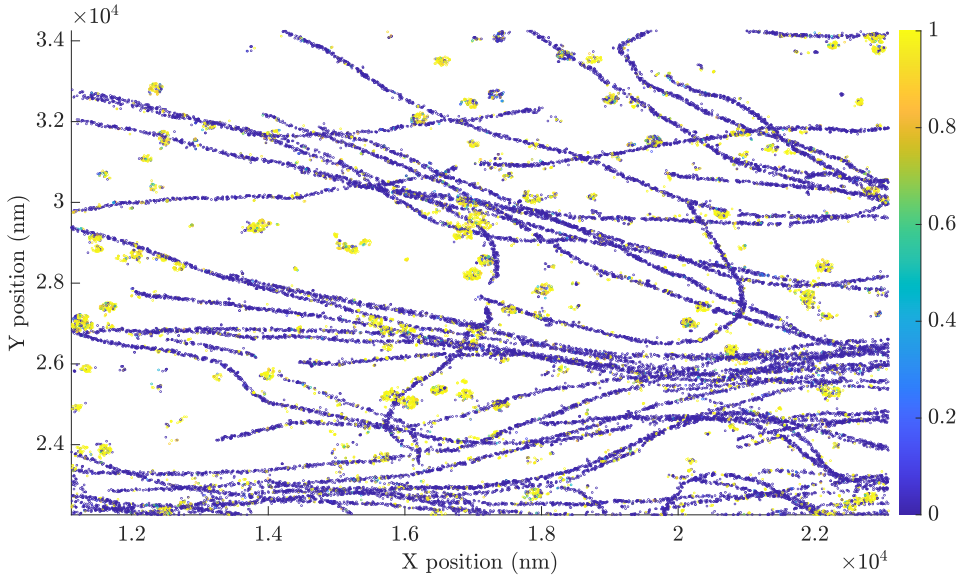

Figure 3.33: The photon flux distribution shown in Figure 3.32 is taken and the probability of the molecule being of species A, which is CF680, is computed and plotted across the ROI. The colorbar presented represents the probability map of the molecule being CF680.

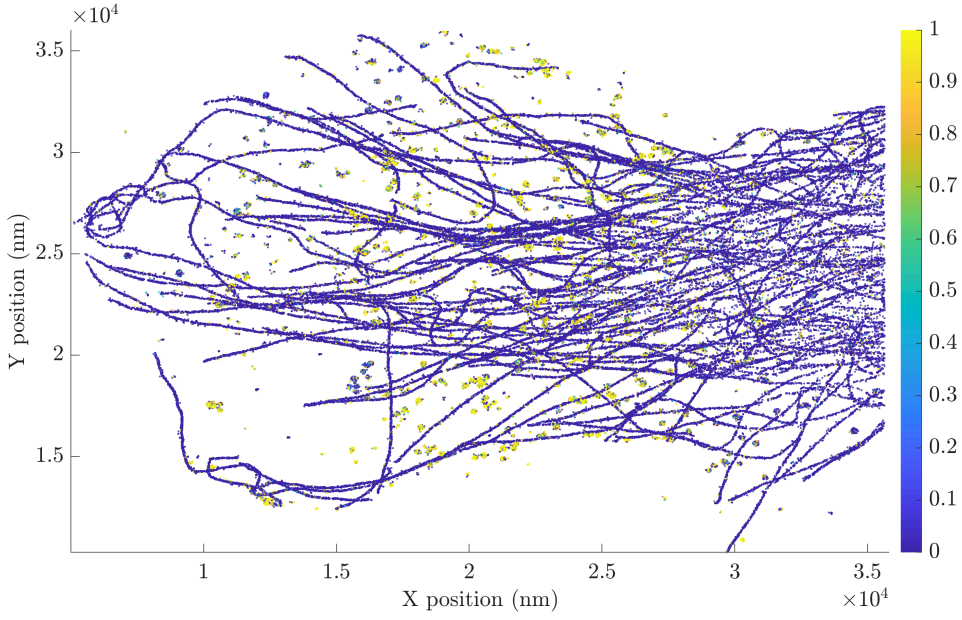

Figure 3.34: The probability map shown in 3.32 is extended over a larger FOV of 30 μ x 25 μ size with Yellow being CF680 (Clathrin) and Blue being CF647 (Tubulin) as in 3.33. The colorbar being the probability of being CF680.

In Figure 3.33 we have the probability map of the molecule being CF680 computed based on the same analysis as done in Figure 3.11. In Figure 3.33 the X-axis and Y-axis are in nm and the color bar represents the probability of the molecule being CF680. That is, if the molecule has a probability close to 1, it is highly likely to be the CF680 species which is indicated in Yellow. This matches the expected tagged organelle which is Clathrin as seen more evidently in Figure 3.33. And we can clearly see that Clathrin tagged with CF680 is Yellow (probability close to 1 on the colorbar) and Tubulin tagged with CF647 is Blue (probability of being CF680 close to 0). The probability map is extended over a larger FOV of 30 μ x 25 μ size in Figure 3.34.

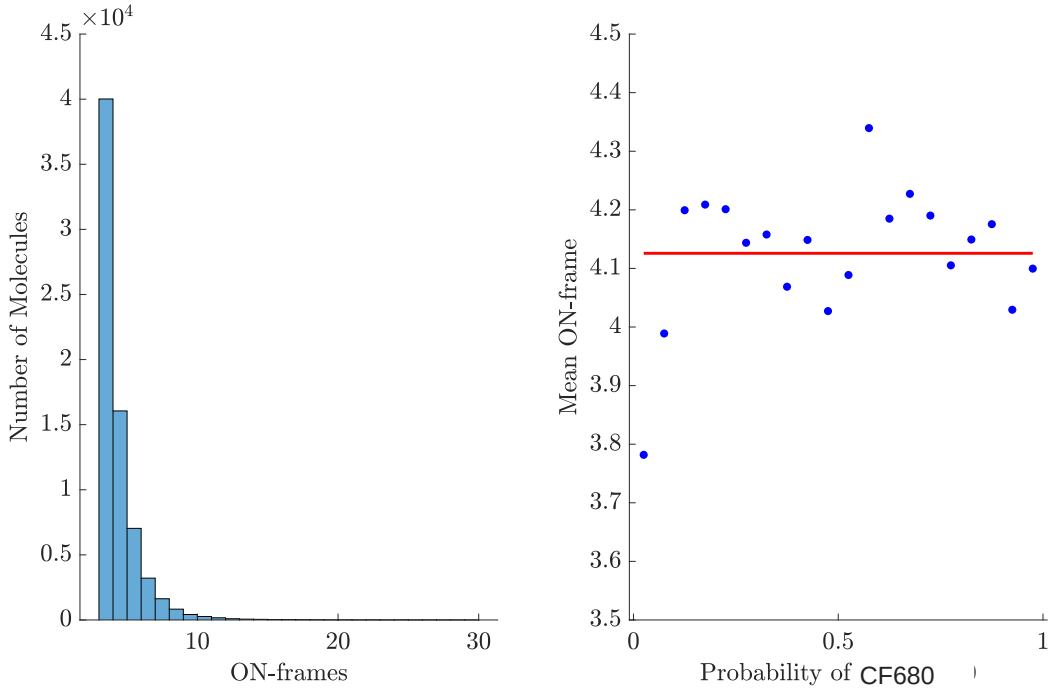

Figure 3.35: (a) On time histogram for all the molecules that have ≥ 3 frames. (b) Based on the probability map from Figure 3.32 molecules classified based on the probability of being CF680 and their corresponding mean ON time in frames. We do not observe a trend for the ON time for STORM.

In Figure 3.35 we have the same plots as shown in Figure 3.16 for this STORM sample. On the left we have the histogram for ON time/frame number. And on the right we have the probability of the molecule being CF680 along the X-axis and the corresponding mean ON time along the Y-axis. This analysis was done for molecules with ≥ 3 frames of ON time as in the previous experiment/sample. Since the ON time of molecules used in STORM is very small, we do not see a trend or correlation between the species and ON time. Thus, this illustrates the fact that fluorescence flux measurement is a more robust parameter to multiplex samples with. Th fluorescence flux is an averaged property

across each frame wheres the ON time a single measurement for each molecule. This also contributes to the robustness of multiplexing with fluorescence flux as the differentiating characteristic as opposed to the ON time.

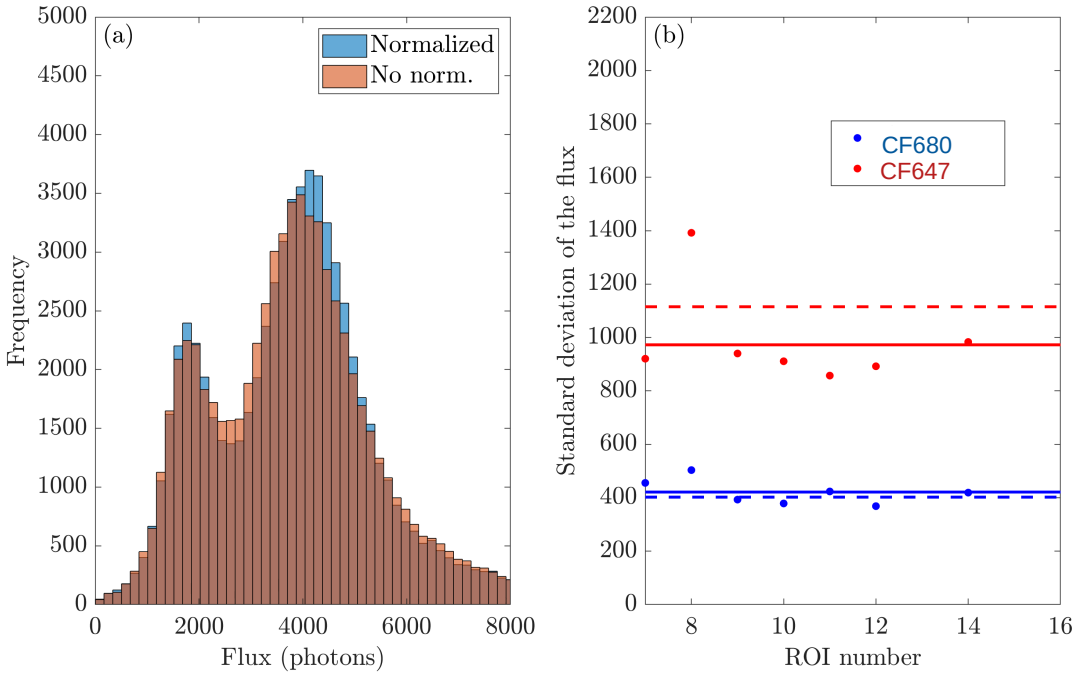

Figure 3.36: a) Histogram of flux distribution across all ROIs in light Blue and normalised flux in Orange. (b) Standard deviation of the Gaussian fits plotted for each of the species across each ROI with Red being CF647 and Blue being CF680 species. The dashed lines are for the case of non-normalized data and the solid lines for the normalized data for each species.

In Figure 3.36 as done in Figure 3.15, we examine the other main parameter of the Gaussian fit which is the standard deviation. The standard deviation/width of the two Gaussians is a measure of the confidence of the classification of the two species. For example, the distributions are broader and have a larger overlap, like in the case of the ratio parameter in spectral demixing. We have something similar while classifying based on the fluorescence flux but the key advantage of looking at the flux distribution is its independence from the emission spectra. We can have molecules with identical spectra and different brightness, and we will be successful in disentangling the two. In Figure 3.36 (a), the histogram of flux for the ensemble of the Blue ROIs is used to normalise such that the mean flux of the CF647 (2^{nd} peak) is the same in all the ROIs. The non-normalised distribution and the normalised distribution are then compared in Figure 3.36 (b) by plotting the standard deviation in each case (for each of the species, CF647 in Red and CF680 in Blue). We can see that in this treatment the width of the 2 peaks for each

ROI and the value of the fit performed on the histogram of the non-normalized image (dashed lines) and on the normalized image (solid lines). The normalization does not add to a significant improvement in the classification process when compared to the non-normalized data treatment, hence we have not considered this treatment for the separation of the species as part of the analysis.

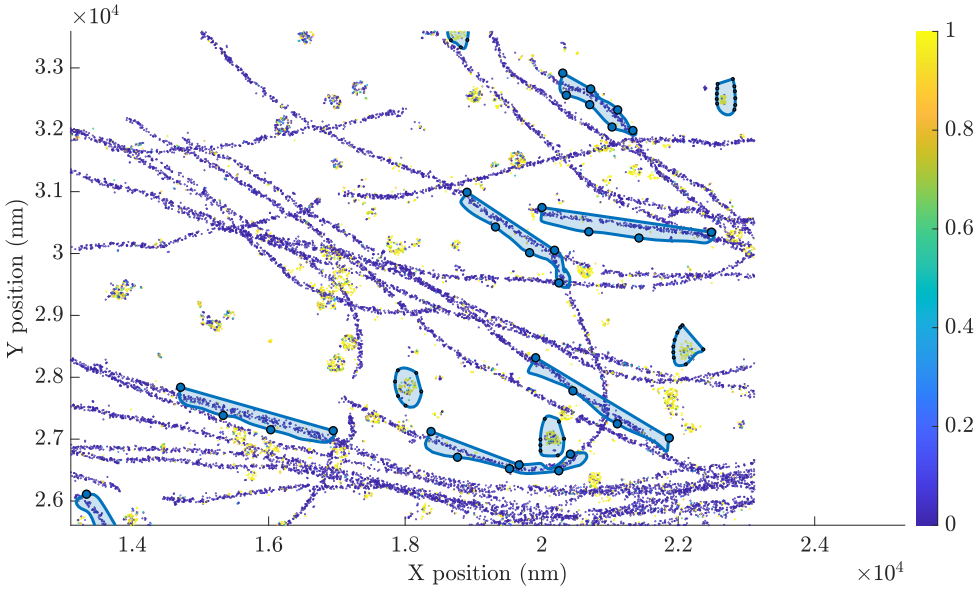

Figure 3.37: Considering Figure 3.32 with the probability map of CF680 and selecting 10 regions each for Clathrin and Tubulin by means of spatial structure to characterize miss-classification.

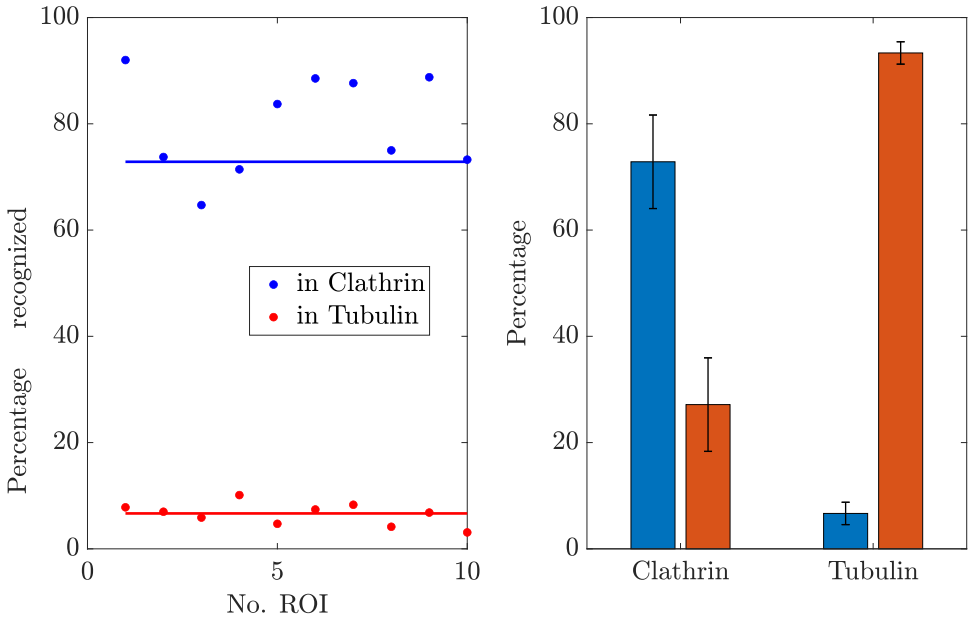

Figure 3.38: Same treatment as in Figure 3.19 but different sample (a) Percentage of molecules recognised as CF680 (complimentary for CF647) in Blue for Clathrin region (x10) and Red for Tubulin (x10). (b) In each of the 10 region sets for Clathrin and Tubulin with Tubulin species in Orange and Clathrin in Blue for quantifying miss-classified molecules with error bars as the standard deviation.

In Figure 3.37 we have the quantification for the robustness of the classification of molecules, the same analysis carried out as in Figure 3.18 and Figure 3.20 with the previous sample. A ROI was taken and 10 regions each of Clathrin and Tubulin were selected based on their spatial architecture. The number of Clathrin tags in Tubulin selected regions and vice versa were computed. We see that in Figure 3.38 we have a higher Cross talk on Clathrin. This depends on three primary parameters, one the concentration of the fluorophore imager/tag, secondly the colocalisaion of both the imagers with one being less adding to more relative cross talk and thirdly the chemical non-specificity (for which we cannot access the ground truth). We see that we can disentangle the sample well even in the case of STORM. With close to 75% for Clathrin and 95% for Tubulin.

6.2 Comparison with Spectral Demixing

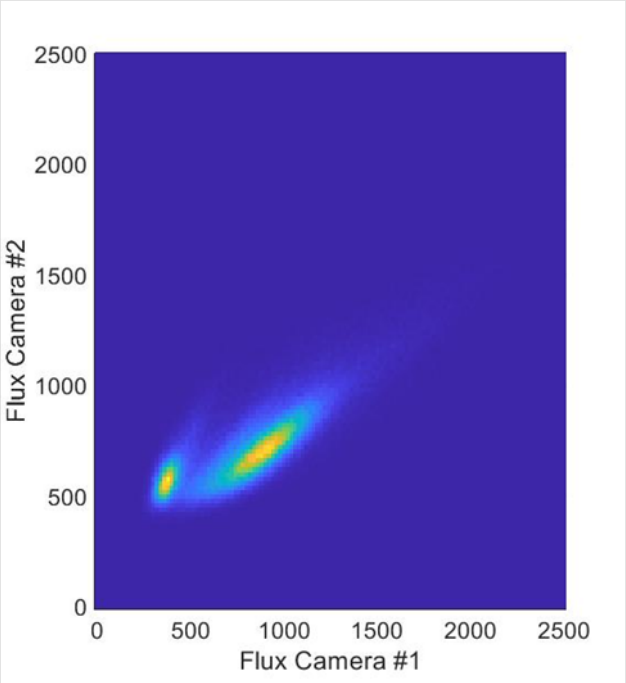

Figure 3.39: Same sample used for spectral demixing as in Section 5 with ATTO 647N and ATTO 655. In the spectral demixing configuration with the fluorescence emission split into two channels using a dichroic and flux calculated in both the cameras and plotted against each other. Along the X-axis we have the fluorophore ATTO 647N on Camera 1 and along the Y-axis we have fluorophore ATTO 655 on Camera 2. The color (Yellow-Blue, Yellow being more number of molecules) represents the number of molecules. We see a distinct separation yielding two species.

The same sample used in Section 5, was used for acquiring spectrally demixed data in order for us to compare the two techniques. This was done by having the same sample but splitting the fluorescence emission into two channels as described in the previous Chapter, and individually looking at each camera. Now that we have data from the two cameras, the flux was calculated for each of them.

In Figure 3.39 we have plotted the flux for each molecule on Camera 1 along the X-axis and flux of each molecule on Camera 2 along the Y-axis. The color (Yellow to Blue) indicates the number of molecules, that is Yellow is where the maximum molecules are located. We see that we can enhance spectral demixing as we have a very distinct disparity and separation between the two species. This gives us an extra variable to work with and add to the dimension of classification apart from calculating the ratio over two cameras. We see that the radial distance of the centroid of the distribution here is indicative of the separation between the two species.

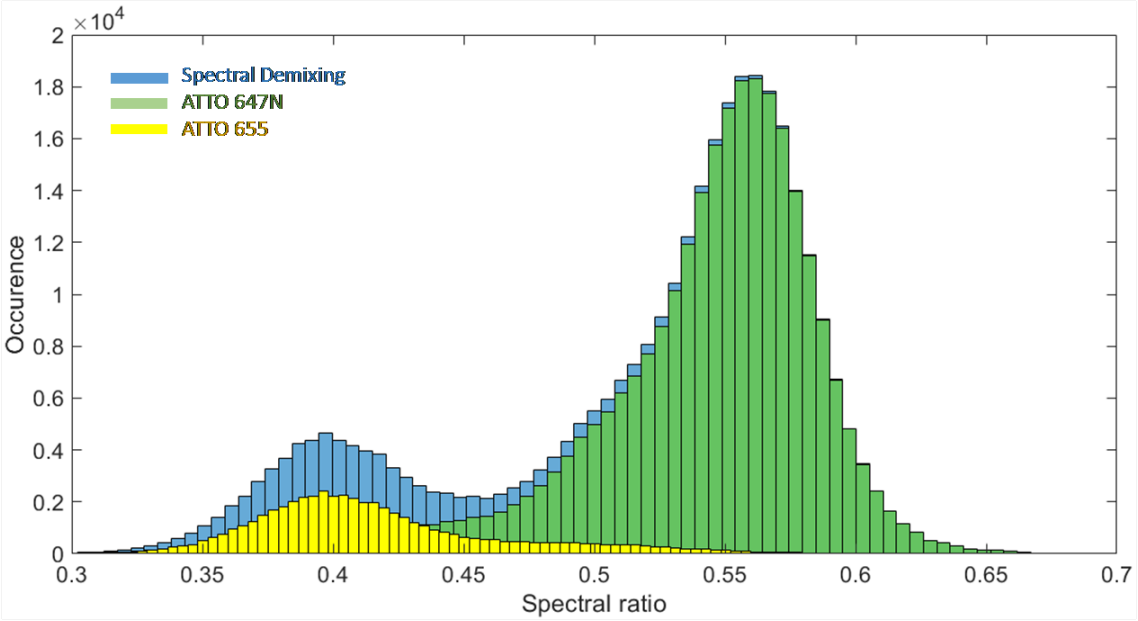

Figure 3.40: Correlation between spectral demixing ratiometric analysis (light Blue) and flux demixing based approach for the two species classified into ATTO 647N (Green) and ATTO 655 (Yellow). The Y-axis is the number of molecules.

We now compare it with the ratiometric classification used in spectral demixing to look at the spread of distribution. Since the most efficient existing technique is spectral demixing, we compare the flux based approach with spectral demixing ratiometric classification. The same sample and ROI was used for ratiometric assessment and in Figure 3.40 we see that the distributions look well correlated. The spectral demixing data is in light Blue and the flux based analysis is in Green for ATTO 647N and in Yellow for ATTO 655. Flux based approach was basically done on both the cameras. The molecules with ON time greater than two frames were taken which is why we have lesser number of molecules in the flux based approach. The Y-axis is the occurrence or number of molecules and the X-axis is the spectral ratio computed as given in the previous section for the spectral demixing approach and for the flux based approach, the same ratiometric analysis was employed. The classification was done by fitting two normal distributions.

$$r_{flux} = \frac{Flux_{Cam1}}{Flux_{Cam1} + Flux_{Cam2}} \tag{3.18}$$

In spectral demixing the next step of classification is carried out through manual selection of thresholds of the ratios as indicated in the previous section. The spectral demixing data treatment further involves classifying the molecules based on the ratio as seen from the blue distribution in Figure 3.40. The region of overlap is not included in the analysis and the threshold for selecting molecules is manually set. For example in this case, if molecules having a ratio between 0.4 to 0.6 are removed from the dataset, we can classify the rest of the molecules into either of the species. This would have a best case scenario of a rejection of around 30 % of molecules from our sample.

7 Conclusion and Outlook

We here in this Chapter have demonstrated that the Flux-based demixing technique as a reliable go to approach. We have established that this method is not limited by the spectrum of the molecule. This allows the opening up for imaging multiple fluorophores in the visible range as well as spectrally close molecules. This broad range of wavelength and spectral access has never been possible before. This technique augments existing spectral demixing techniques and has the potential to enhance the number of multiplexed channels through an added dimension on flux measurement as well as ON time (for DNA-PAINT). Proposed technique is relatively simple to implement (single detector/channel, source, data) and has been applied as a stand alone analysis for many samples and combinations of fluorophores. A set of case studies are presented to show the effectiveness of identifying fluorophores based on their fluxes and statistics are presented. The technique has also been demonstrated in STORM. To summarize this Chapter, we have demonstrated a new flux based multiplexing technique that has an accuracy of 80 % to 95 %. Spectral demixing approach has a cross- talk of around 5 % ([Mau, 2020]). The rejection rate in spectral demixing is in the range of 30 % to 50 % ([**adrien**])and in the flux based multiplexing approach we have a rejection rate of 25 % for DNA-PAINT and a large rejection rate of 75 % for STORM fluorescent probes due to its short On times. Thus, we see that the fluorescence flux based demixing technique performs very well for molecules that have comparable absorption-emission spectra which are currently not capable of being dis-entangles using cutting edge techniques such as spectral demixing. This opens up the possibility of multiplexing with a single excitation laser using a single channel of detection. This technique also allows one to select fluorophores in the Red domain (emission in red) that are less phototoxic. This technique has been demonstrated in both DNA-PAINT and STORM as a standalone technique and can be used to augment other techniques of multiplexing with an added parameter to disentangle and classify different species of fluorescent probes.

Outlook of this project would involve extending to multiple excitation sources (tuning the flux independently) with many excitation wavelengths and combining this technique with measurement of other parameters such as z-localization. And importantly, to explore the correlation between species category and spatial configuration. Since molecules that are closer in a certain morphological and spatial structure are more likely to be of the same species, this component can be used to augment the de-mixing process as an added parameter. This would work best for targets that are morphologically distinct such as Clathrin and Tubulin. And finally using these sets of raw images and post classified images using flux-based demixing to develop machine learning based algorithms to automate the process and make predictions on the category of the fluorescent probe in a guven sample.

Chapter 4

Fluorescence Lifetime Imaging Microscopy

Summary

Within this chapter, we embark on an exploration of *Fluorescence Lifetime Imaging Microscopy* (FLIM), delving into its theoretical underpinnings and elucidating the recent advancements in both experimental methodologies and data analysis techniques. Fluorescence lifetime is another fundamental property of fluorophores. This temporal parameter not only serves as a discerning factor for molecular species but also provides insights into their immediate environment. This chapter serves as the framework for the subsequent experiments conducted in both Chapter 5 and Chapter 6. Chapter 5 elaborates on a new technique that utilizes continuous-wave laser and measures lifetime through integrated flux measurement and Chapter 6 elaborates on another novel experimental technique for lifetime measurement using a pulsed laser experimental setup. In essence, this chapter introduces the prominence of FLIM and lays the groundwork for the groundbreaking techniques proposed and expounded upon in the ensuing chapters, discussing fluorescence lifetime dynamics and its multifaceted applications in molecular classification.

Contents

1 Introduction to *Fluorescence Lifetime Imaging Microscopy* (FLIM)

In this Chapter we pick up where we left off from Chapter 1 with respect to energy transition of electrons in atoms and fluorescence. The fluorescence process parameters are not just limited to the energy spectrum of the atom's ground state and excited state but also the characteristic time it takes to make that transition from the excited to the ground state. This transition time is not dependent on molecular properties alone, it also depends on the immediate environment of the fluorophore, and will be discussing each of these parameters in depth in this chapter.

Some interesting recent developments and points to note about lifetime based measurements is that due to its sensitivity in terms of the type of atom, environment and structural changes, FLIM has also been used by means of autofluorescent molecular imaging to study cellular metabolism in a non invasive manner and even in surgery of tissues recently [Gorpas, 2019]. Lifetime imaging is also used to multiplex different fluorophore markers in multi-stained samples and in autofluorescent cells as well. These components are limited by overlapping fluorescence spectra but can be differentiated by means of FLIM. We look at various means of doing FLIM in this Chapter with the focus on the complexity as well as cost of such existing FLIM systems. To highlight that these measurements basically require modulation of the excitation source which is generally achieved via a pulsed laser and a high end detector for collecting the emitted photons since we are working with very small time timescales.

1.1 Fluorescence Lifetime

Probe Species	Fluorescence Lifetime
Fluorophore tags	0.1 ns to 10 ns
Organics Markers	0.1 s to 90 s
Fluorescent Proteins	0.1 ns to 4 ns
Quantum Dots	30 ns to 500 ns
Inorganic Markers	≤ 10 µs

Table 4.1: Typical Lifetimes of Biological Markers [Ernest, 2011]

When an electron in an atom is in the ground state and gets excited to a higher energy level, it is followed by a relaxation as elaborated in Chapter 1. This intricate electron dynamics is succinctly captured by the Jablonski diagram, as shown in Figure 4.1. Only the radiative fluorescence transition from the excited state that is, S_1 to the ground state S_0 is of relevance since that is the sole contributor of fluorescence emission. The other transitions like non-radiative transfers (like in FRET as discussed in Chapter 1) and

phosphorescence are specific to the type of molecule, we won't elaborate that here since we will be focusing on fluorescence. The timescale of the decay to the ground state is in the order of a few nanoseconds for biological imaging markers. In Table 4.1 we have the typical lifetimes for different emitters used in biological imaging:

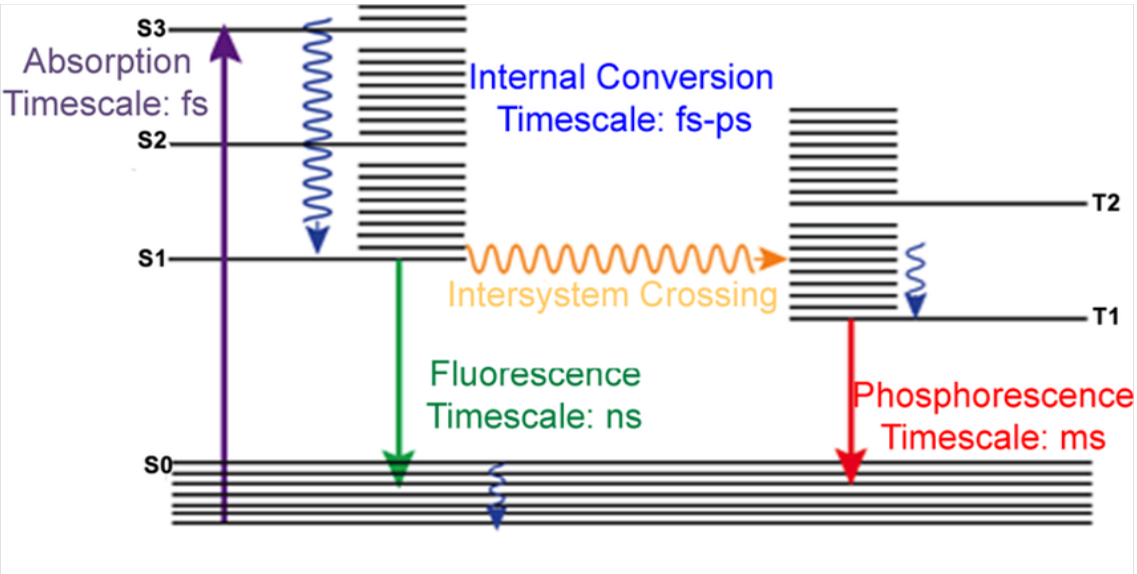

Figure 4.1: Jablonski diagram with non-radiative and radiative transitions. Absorption is indicated in Purple wherein the electron moves from S_0 to S_3. Internal conversion in Blue from S_3 to S_1 and finally fluorescence emission in Green from S_1 to S_0. In some molecules there is an intersystem crossing to an intermediate state S_1 to T_1. And from T_1 to S_0 in Red called phosphorescence. The timescale is mentioned along with the process [Ernest, 2011].

In Figure 4.1, we have the Jablonski diagram depicting the absorption - emission spectrum owing to the vibrational states available to electrons nevertheless being the same for a given atom as discussed in Chapter 1. In Figure 4.1 we see that there are some species of molecules that undergo delayed fluorescence also known as phosphorescence. How efficiently does this process of fluorescence occur? In chapter 1 we also discussed this, the quantum yield of molecules Φ which is also defined as the ratio of number of emitted photons to the number of absorbed photons gives this measurement. The quantum yield Φ can also be written in terms of radiative and non-radiative decay rates. In Figure 4.1, we have a Jablonski diagram indicating the radiative and non-radiative transitions. We see that fluorescence is the radiative (emitting photons) and the non-radiative transitions which involve vibrational relaxations which are transmitted via phonons to the environment (heat) as well as energy transfer through dipole-dipole coupling with an ambient molecule like in FRET. The general quantum yield for fluorophores range from 2% for tryptophan to 80% for fluorescein. Quantum yield is affected by and depends on the orientation of the molecule spatially with respect to the incident wavefront as well as the local environment of the molecule. The chemical stability of the molecule (some

molecules decompose chemically and lose/reduce their ability to fluoresce) is also another factor. These factors are important to note in the context of lifetime measurement since empirically lifetime is a statistical measurement which we will see in the next Section.

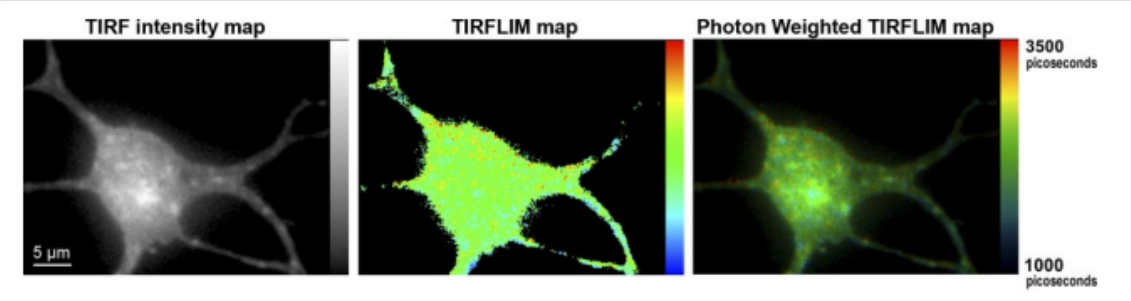

Figure 4.2: Hippocampal neuron of rat embryos brought into contact with cholera toxin labeled with Alexa 488, observed under TIRF excitation. (A) Intensity, (B) fluorescence lifetime and (C) photon-weighted image [Marquer, 2011].

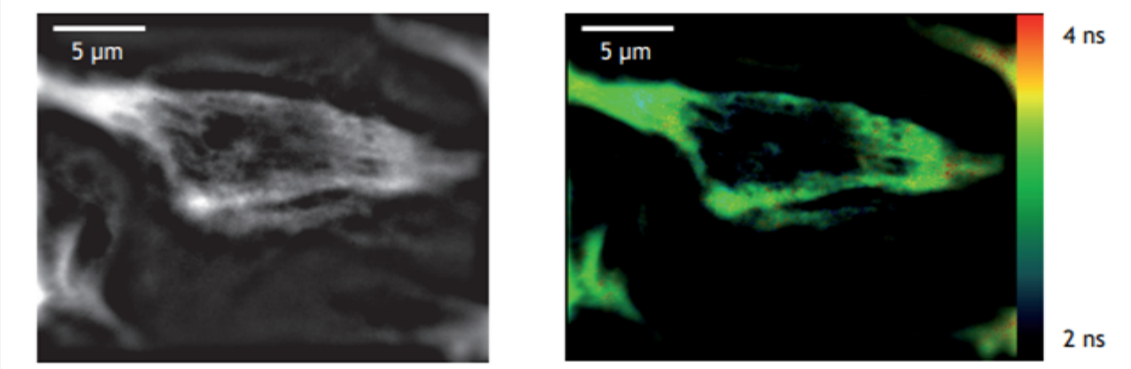

Figure 4.3: FLIM maps obtained on fixed Alexa 488 α Tubulin immunostained HeLa cells [Dupuis, 2013].

We have examples of FLIM images in Figures 4.2 and 4.3 with Alexa 488 stained neuronal toxins and Tubulin in HeLa cells respectively.

Thus, to summarise apart from the absorption - emission spectra, the second characteristic property of a fluorescent probe is its lifetime which is defined as the time measured for the number of excited molecules in S_1 to decay exponentially to N/e which is 36.8% of the original population via the loss of energy through fluorescence or non-radiative processes as indicated below, in terms of the first order kinetics summed across all molecules, where

the intensity I_{det} and where τ is the lifetime:

$$I_{det}(t) \quad = \quad \sum_n A_n e^{\frac{-t}{\tau}} \tag{4.1}$$

Thus lifetime for a single molecule can also be defined when $t = \tau$ in terms of the intensity as, $I_{det}(t)$ becomes $\frac{1}{e}$ times its original value I_0. That is $\tilde{3}6.8\%$ of its original value,

$$I_{det}(t) \quad -- > \quad \frac{I_0(t)}{e} \tag{4.2}$$

The number of molecules in the excited state is an exponentially decaying function with the amplitude pre-factor for the exponential as the original number N_0 of ground state electrons that transitioned to the excited state upon illumination. Thus, we can also define the population in the excited state at time t as $N(t)$

$$N(t) \quad = \quad N_0 e^{\frac{-t}{\tau}} \tag{4.3}$$

Individually each electron decays at a different time but statistically it is an exponential distribution as indicated above. This is also indicative that this statistical relation for $N(t)$ or the number of fluorescent photons detected, holds when excitation is followed by a period of relaxation which is longer than the lifetime. If it's shorter as in we are exposing the molecule to a continuous stream of photons, we will have more molecules propelled perpetually in the excited state and empirically we will have a continuous stream of fluorescence emission detected since as soon as decay occurs, we have immediate excitation (provided no decomposition/bleaching occurs).

Since we have a level of understanding on the importance of non-radiative emissions let us cite some examples where in non-radiative transfers occur apart from FRET, for example a quenching mechanism in molecules, Dexter energy transfer which involves transfer of electrons non-radiatively from *Lowest Unpaired Molecular Orbital* (LUMO) of one atom to the *Highest Occupied Molecular Orbital* (HOMO) of another atom [Kaur, 2017]. Thus, taking into consideration the non-radiative processes, we have

$$\Phi \quad = \quad \frac{\Gamma_r}{\Gamma_r + \Gamma_{nr}} \tag{4.4}$$

$$\tau \quad = \quad \frac{1}{\Gamma_r + \Gamma_{nr}} \tag{4.5}$$

And for no non-radiative processes, where only emission occurs we can reduce the equation to the known form as follows

$$\tau \quad = \quad \frac{1}{\Gamma_r} \tag{4.6}$$

Now that we have an idea on the basics of lifetime relationships we describe empirical approaches to lifetime measurement in the next Section. The derivation of lifetime dynamics based on first principles will be done in the next Chapter.

1.2 Overview of Lifetime Measurement

Now that we have finished with an overview of fluorescence lifetime and some nuances related to it we proceed to how fluorescence lifetime measurement is done experimentally.

Fluorescence lifetime τ is measured temporally or through converting the data into frequency space and extracting lifetime information. In a sample of one species of fluorophores, the decay rate after excitation is a statistical process as we saw above, different electrons decay at different times.

The sample has to be first excited with a short pulse (as discussed above) using a pulsed laser and the emitted photons have to be collected in real time. The photons are emitted very quickly since the lifetime is in the order of a few nanoseconds as shown in 4.1, and the detector for this reason has to be faster than the time of arrival of the photons. These detections are binned temporally to create a histogram. That is, every smallest interval possible on the detector forms the edges of the bin and the photons are tallied into this temporal bin for each such interval. This can also be analysed in the Fourier domain instead of the temporal domain. For calculating the fluorophore species lifetime, the phases that come out in the Fourier space give the relative time with respect to the excitation pulse. Thus excitation pulses and detectors have to be equipped to deal with such short times making it a very expensive process both in terms of the ultra-fast detectors and pulsed lasers.

As seen in our discussions above, due to the sensitivity of lifetime measurements they are best suited to probe the local environment and measure the dynamics of bleaching and quenching. Also, most existing experimental approaches for lifetime measurement probes the ground truth since they function at time scales close to the lifetime and classifying them statistically. Since it is an actual measurement, which is just a function of the molecule and its environment, the calibration is relatively straightforward in terms of calibrating, firstly the instruments and secondly the environmental conditions (like temperature). In the next section we look at these experimental techniques for lifetime measurement that currently exist.

2 General Methods of Experimental Implementation

There two types of experimental approaches to measuring the lifetime. Firstly we have the time domain based experimental system discussed below.

2.1 Time domain FLIM systems

Time domain fluorescence lifetime setups require a very short pulse of excitation as it has to be shorter than the lifetime of molecules, thus shorter than a nanosecond. Therefore femtosecond and picosecond lasers are needed to probe lifetimes of fluorophores. After excitation, the decay has to be tabulated/binned, thus a signal amplifier and digitisor operating at at least at nanosecond levels to assemble the decay rate statistics. The detectors have a very complex system of circuits to measure the time lags as well as count and bin these photons.

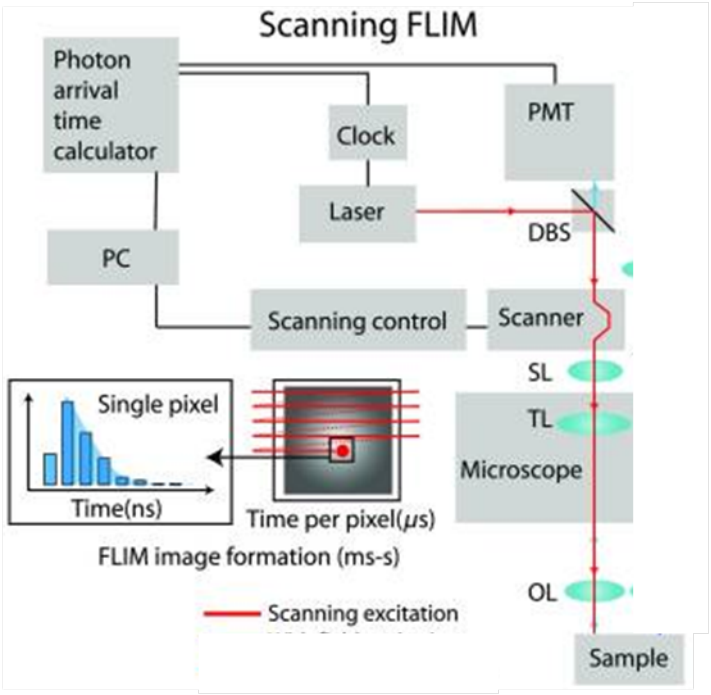

Figure 4.4: Experimental acquisition for a scanning based FLIM implementation [Datta, 2020b].

Figure 4.4 shows the workflow for time domain FLIM measurement. Conventionally to use this procedure, the most common approach is to use an electronic system called the *Time Correlated Single Photon Counting* (TCSPC) [Phillips, 1985]. This technique logs time, based on a circuit called *Time Amplitude converter Circuit* (TAC). TAC is basically like a stop watch which experimentally measures the time between the excitation pulse arrival and the fluorescence emission photon arrival. This is called the time of arrival in time based lifetime measurement systems. The time of arrival is then converted to analog voltage that gets recorded. This process gives a distribution of arrival times as shown in Figure 4.5, and based on this statistic, the lifetime is computed. In Figure 4.5, the excitation pulse is recorded by synchronising the excitation with the TCSPC and based on the instrument's response curve, the rising and falling edge of the excitation are recorded (by the Green curve, ref from Picoquant TCSPC system). The Red line in the figure, indicates the decay of emission which is constructed by counting photons across

many excitation pulses.

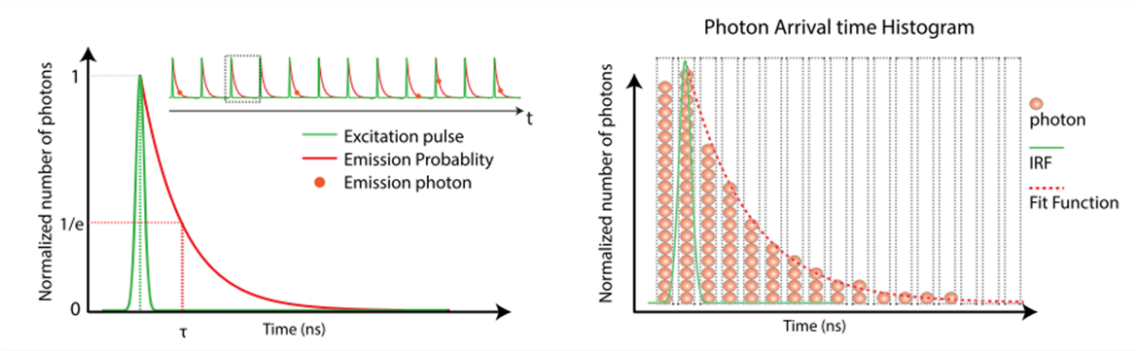

Figure 4.5: Experimental acquisition for a homogeneous sample using TCSPC where IRF is the instrument response function [Datta, 2020b].

However in the TCSPC if there are more number of photons that are emitted from the fluorophore at a time, the arrival times of all of them cannot be measured owing to the dead time of the system. What then happens with the read out would be that the photons with short arrival times are more weighted leading to skew the lifetime measurement to a shorter value. But usually since the TCSPC is used in combination with a point based scanning system such as the confocal system, the likelihood of inundation of emitted photons is very small. Also, several such excitation pulses are used to construct the statistics so as to build the histogram one photon at a time per pulse. One can also record the arrival time using a GHz detector that can directly measure the emitted times without the use of gated electronics. The *Signal to Noise Ratio* (SNR) of the system depends on the number of photons used to construct the decay trend as seen in Figure 4.5, right (b). The more the number of photons, more accurate is the lifetime. This goes as $\sqrt{N}$ where N is the total number of photons. Thus, for this reason, across each pixel/scanning unit multiple pulses (at least in hundreds) are done to construct the final histogram. In the next section we elaborate on various wide-field based FLIM approaches.

2.1.1 Wide-field FLIM

As we saw in the previous technique based on the TCSPC point scanning method, we here examine techniques with a wide-field implementation.

Another technique of acquisition is through gating the time of acquisition. Here we don't need to probe the nanosecond timescale but can integrate the emitted fluoresce photons over larger time gates thereby removing the time constraint. On the other hand, larger gates would imply that a point scanning based system would not be very compatible with such an approach. The instrument records the arrival times in a gated manner *Time Gated* (TG) [Grauw, 2001] as indicated in Figure 4.6, the width of the gate is for example, 1 ns.

Developments in camera technology of acquiring high frame rates in MHz, has made it possible to acquire arrival time statistics in each pixel rendering it possible to make

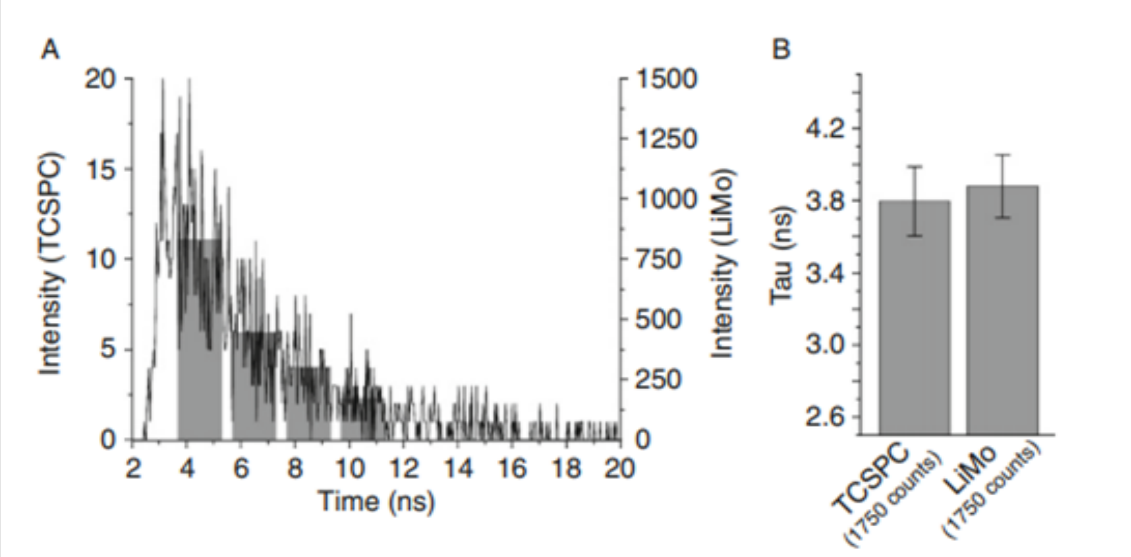

Figure 4.6: A comparison between TG and TCSPC using the same number of detected photons. (A) The distribution of photons over the time bins. (B) Bar plot of the lifetimes including error. [Grauw, 2001]

FLIM measurements in widefield. Widefield FLIM uses a CMOS camera to collect the fluorescence signal. Both time gated and frequency based approaches are implemented in widefield. Widefield techniques are less susceptible to damage samples with phototoxicity than point based scanning techniques. However, the major issue is the SNR since the signal is acquired from a large area all at once and camera sensitivity is low when compared to high end detectors. Every pixel on the camera detects scattered light from a large FOV thus the temporal log is meshed together. Since frame rate is the limiting factor, by reducing the number of pixels, we can improve temporal resolution. In a sample, temporal resolution can also be improved by using a *Single Photon Avalanche Diode* (SPAD) detector [Suhling, 2019]. The augmentation of camera CMOS with SPAD arrays allowed for each pixel to behave like a TCSPC thus logging information directly onto the camera and individually creating emission profiles that form the statistics for lifetime measurement. SPAD uses the concept of a photodiode and *Avalanche Photo-Diode* (APD)s. A single photon is able to trigger a short duration pulse, through a cascade of charge carriers in reverse bias, that is used to measure the time of arrival. Widefield FLIM is superior to the traditional point based scanning in term of acquisition time. Since all the pixels are active simultaneously. In Figure 4.7 we have an example of a widefield system with a SCW laser, a delay line and signal intensifier [Devauges, 2011].

There are also other techniques such as *Structured Illumination Microscopy* (SIM) and spinning-disk confocal techniques that can also be done at high speed. In the following section an individual case by case technique is discussed.

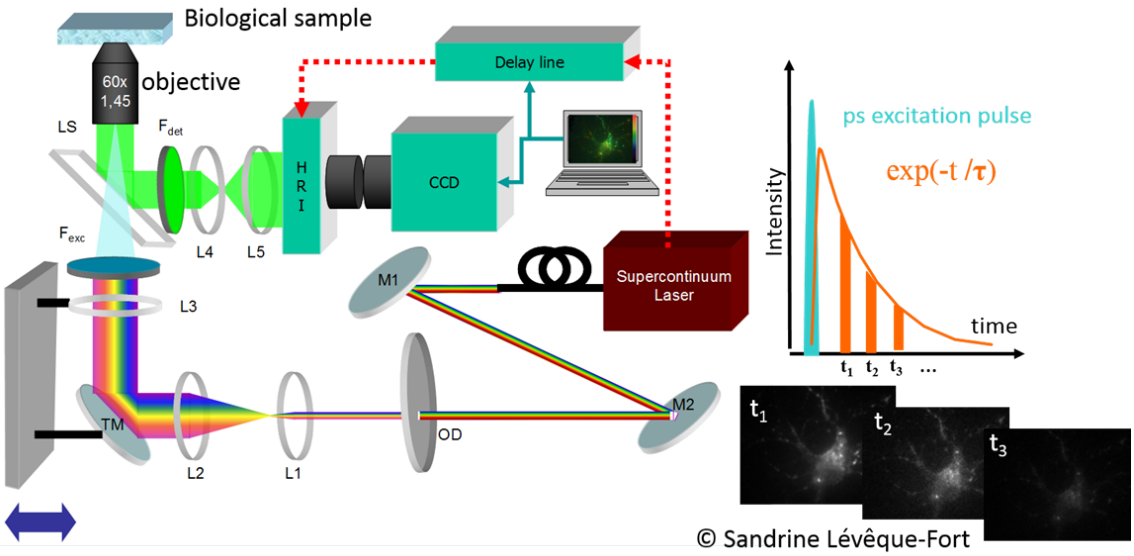

Figure 4.7: Widefield delay based FLIM setup with signal intensifier [Devauges, 2011]. SCW used for different excitation wavelengths for different fluorophores.

2.2 Frequency based FLIM Technique

Now that we have covered the main features of time domain based FLIM measurement, we will briefly touch upon frequency based FLIM technique.

Another strong candidate for FLIM is frequency based measurements. Instead of looking at the arrival times in the temporal domain, the phase delay of each photon is measured with respect to the excitation photon. The phase distribution is analysed in Fourier space. For example if the excitation is modulated sinusoidally as shown in Figure 4.8, we can write the excitation and emission as a function of time as follows,

$$Exc(t) \quad = \quad E_0 + 2E_\omega cos(\omega t + \phi_E) \tag{4.7}$$

where E_0 is the signal offset, E_w represents half the modulation amplitude and ϕ_E is a phase constant. Considering a fluorescence signal with a mono-exponential decay, the response of the system to an excitation of the type $E(t)$, oscillating at the pulsation $\omega = 2\pi f$ will be given by

$$F(t,r) \quad = \quad F_0(r) + 2F_\omega(r)cos(\omega t + \phi_F(r)) \tag{4.8}$$

where r represents the position of the pixel of choice $F_\omega(r)$ is the amplitude ϕ is a phase constant. It has been shown that in the case where the fluorescence decay is mono-exponential with a fluorescence lifetime τ, the phase difference between excitation and fluorescence emission at the chosen position is related to the fluorescence lifetime at that position by the relationship:

$$\phi(r) \quad = \quad arctan(\omega\tau) \tag{4.9}$$

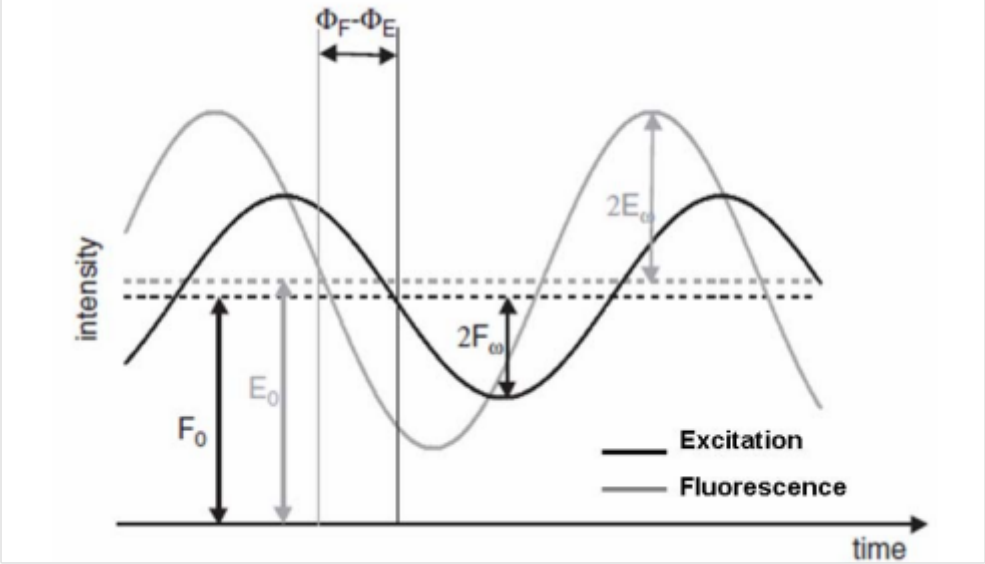

Figure 4.8: Profiles over time of excitation and fluorescence emission obtained in the field frequency. E_0 and F_0 are the amplitudes of the offset of the excitation and of the fluorescence signal while E_ω and F_ω represent half of the modulation amplitudes. The phase difference between the two signals is given by $(\phi_F - \phi_E)$ [Devauges, 2011].

In addition, the degree of modulation of the fluorescence emission is reduced by a factor $m(r)$ given by the relationship

$$m(r) \quad = \quad \frac{\frac{F_\omega(r)}{F_0(r)}}{\frac{E_\omega}{E_0}} \tag{4.10}$$

This factor is also related to the fluorescence lifetime τ by the equation:

$$m(r) \quad = \quad \frac{1}{\sqrt{1+\omega\tau^2}} \tag{4.11}$$

Thus in simple cases of mono-exponential decays, the measurement of the phase shift ϕ or of the degree of modulation m will make it possible to deduce the lifetime of fluorescence associated with each pixel of the image.

Analysis of lifetime from the data is done via phasor analysis where coordinates are defined in terms of $m(r)$ parameter, and the modulation of excitation. And physically, pixels with the same lifetimes are grouped together [Devauges, 2011] [Ross, 2008].

The general setup for frequency based lifetime measurement system has a modulator to modulate the excitation beam, and a phototodiode to pick up the emitted photons. The modulated laser is coupled to a scanning system and a microscope. the scanning system sends the emitted photons via a beam splitter and through emission filters to the APD. The modulation frequencies are changed and the process repeated. the excitation is obtained through calibrating a known reference fluorophore. Both time-domain and frequency-domain approaches discussed above have their own advantages and caveats depending on

multiple parameters like photon number, temporal resolution and, speed of excitation and acquisition.

3 Examining point based techniques in temporal FLIM

Now that we have an overview of different ways to do FLIM measurements we will look closely at three cases which are point based temporal domain lifetime measurement experimental implementations. Since most recent techniques belong to this category.

Most current techniques are based on confocal systems augmented with FLIM hardware. This is due to the low background noise levels of such systems. Confocal systems reject out of plane background illumination and enable higher SNR. Since the most limiting factor in major techniques of FLIM is background noise, this system of having a point based processing works better when compared to wide field FLIM. The detectors used are TCSPC or ultrafast photodiodes in GHz or SPAD arrays with CMOS.

All techniques, both widefield and point based scanning as well as both time domain and frequency domain techniques discussed above, require the use of pulsed lasers. Many modern pulsed laser diodes work in the range of 0.1 GHz making it possible to probe sub-nanosecond photon emissions. These pulsed lasers are also *Super-Continuum Wave* (SCW) (access to a range of excitation wavelengths) to excite multiple range of fluorophores.

3.1 Case study 1

One of the techniques of confocal based scanning point method, in the temporal domain for lifetime measurement is by [Böhmer, 2001] as shown in Figure 4.9. In this system lifetime measurement along with SMLM is measured. The scanning speed of the TCSPC is low such that many photons are collected per molecule. Single molecules can be considered to be ideal point emitters, their position on the surface can be determined with much higher resolution than the diffraction limit provided positional accuracy is maintained at around 10 nm with temporal stability.

This system employed compact electronics with measurement resolution of 40 ps and continuous recording (non time gated) of arrival time measurement with a resolution of 100 ns and a high detection rate of 2 MHz. Synchronisation of the confocal system, scanning system done with a piezo device, data acquisition (TCSPC) and tabulation with dwell time in each "pixel". The single molecules were immobilised on glass substrates.

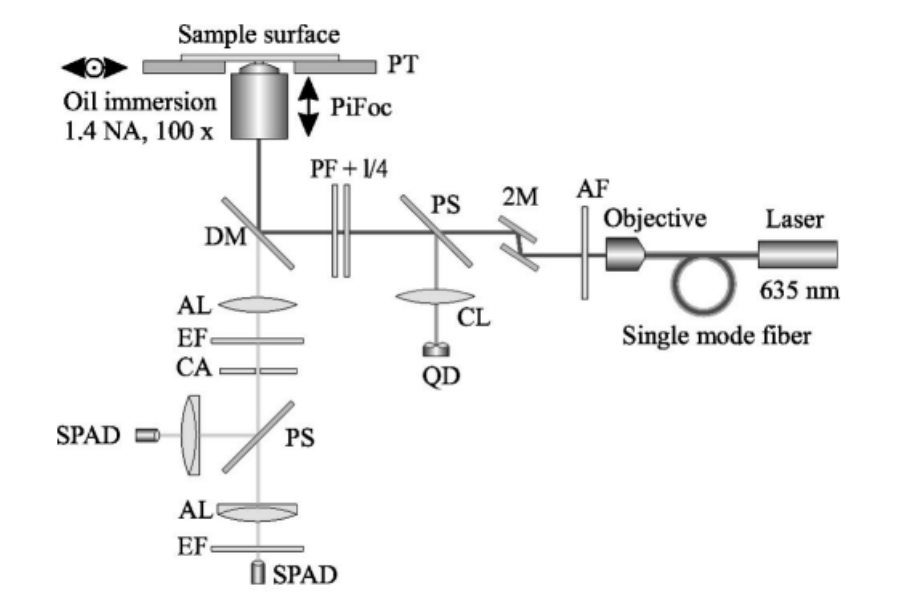

Figure 4.9: Setup for confocal scanning device for ultrasensitive fluorescence detection. (AF) excitation filter, (2M) two-mirror beam steering, (PS) polarizing beam splitter, (PF) polarizer and quarter waveplate, (DM) dichroic mirror, (EF) emission filter, (AL) achromatic lens, (CA) confocal aperture, (PT) piezo stage, (PiFoc) linear piezo actuator, (CL) cylindrical lens, (QD) quadrant diode. [Böhmer, 2001]

In Figure 4.9, pulsed laser by Picoquant, 635 nm delivers a train of pulses with 80 ps FWHM duration and a repetition rate of 40 MHz. The excitation beam passes through the excitation filter and through a double mirror steering device which allows the beam to be steered by shifting and tilting for alignment. A polariser and a quarter wave plate change the polarisation of the beam from linear to circular. Through the dichroic mirror finally the sample is illuminated. The signal from the sample is collected again through the dichroic and tube lens and emission filters, and focused via a pinhole of 100 mm size and into the confocal system which has a SPAD with 60% quantum detection efficiency at 670 nm.

This experiment was done on a sample of Cy5 dye on a coverslip and the lifetime was calculated by averaging the arrival times pixel by pixel. And the lifetime measured as 1 ns with 100 ps accuracy.

3.2 Case study 2

Nanosecond temporal resolution enables new methods for wide-field imaging like time-of-flight, gated detection, and fluorescence lifetime. As shown in Figure 4.10, the schematic for the setup implemented by [Bowman, 2019]. The optical efficiency of existing approaches, presents challenges for low-light applications common to fluorescence microscopy and single-molecule imaging. With the use of Pockels cells for wide-field image gating with nanosecond temporal resolution and high photon collection efficiency this can be circum-

vented. Two temporal frames are obtained by combining a Pockels cell with a pair of polarizing beam-splitters. In this work multi-label FLIM, single-molecule lifetime spectroscopy, and fast single-frame FLIM, a higher throughput when compared to the single photon counting technique is demonstrated. These methods enable nanosecond imaging with standard optical systems and sensors, opening a new temporal dimension for wide-field low-light microscopy [Bowman, 2019].

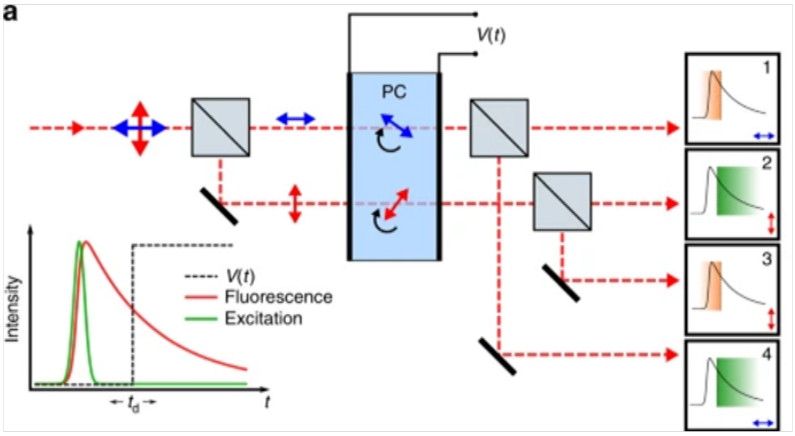

Figure 4.10: Wide-field efficient ultrafast imaging with a Pockels cell. Schematic of two temporal bin wide-field imaging for a single pixel fluorescence decay. Fluorescence emission is first polarized, a time-dependent retardance (step function illustrated) is applied by the PC, and polarizations are split again before the sensor. Two pairs of outputs correspond to integrated intensity before (1, 3) and after (2, 4) a step function gate is applied in the illustration. Other modulations V(t) may be applied beyond a simple step function as described in the text. Equal optical path lengths are used in practice. [Bowman, 2019]

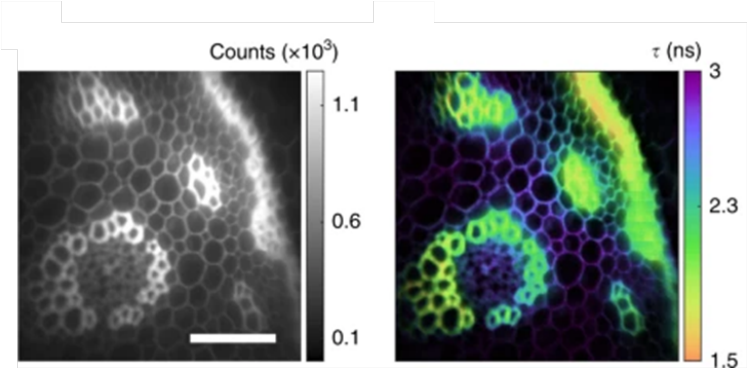

Figure 4.11: Fast FLIM Left: Intensity image of Convallaria Majalis Rhizome stained with Acridine Orange, a standard FLIM benchmark (scale bar 100 μm). Right: Lifetime image from fitting a timing trace of 100 ms exposures (50 μW excitation). [Bowman, 2019]

In Figure 4.11 are the results from [Bowman, 2019] for a biological sample with lifetime measurements as described by the authors.

3.3 Case study 3

Now that we have looked at one of the widely used techniques of time based FLIM, we now examine FLIM in conjunction with a stimulated beam and time delay control, a setup schematically depicted in Figure 4.12 and the result of which is given in Figure 4.13.

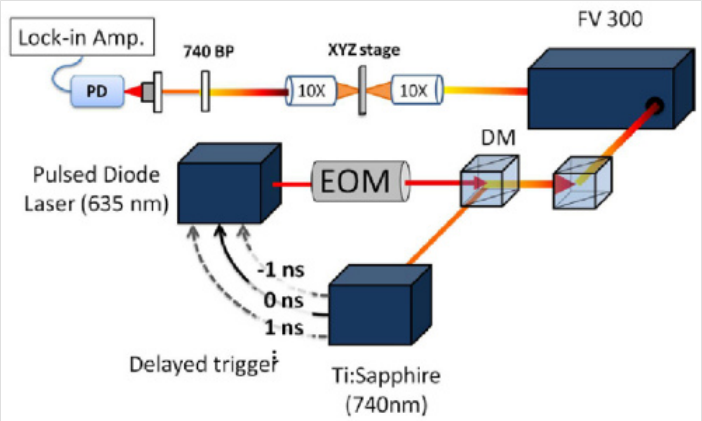

Figure 4.12: Schematic of the stimulated emission based setup. Electro optical modulator (EOM), band pass filter (BP), dichroic mirror (DM), photodiode (PD). [Lin, 2012]

The feasibility of long working distance fluorescence lifetime imaging by utilizing electronic trigger control with pump-probe configuration, by taking advantage of the stimulated emission's inherent spatial coherence.

$$\frac{I_0 - I}{I_0} = ae^{\frac{-bt_d}{\tau}} \tag{4.12}$$

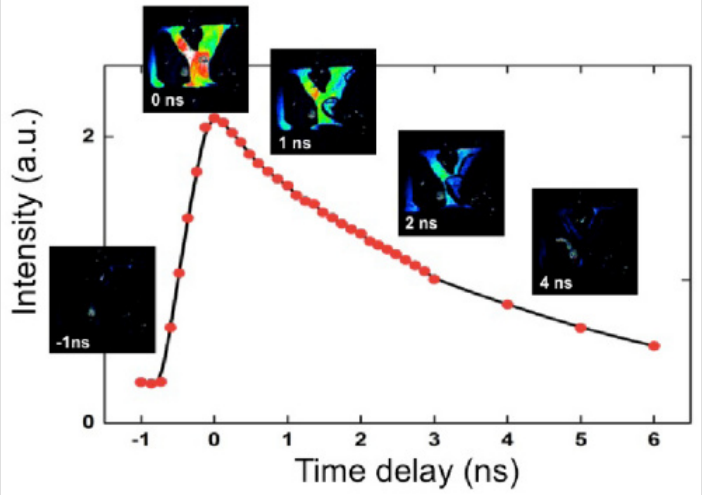

Figure 4.13: Stimulated emission signal as a function of the relative time delay between the excitation and the stimulation pulses. The decay curve is obtained from a single scan position of the sample of ATTO 647 N prepared in Y-shape microfluidic channel. The image size is 600 µm × 600 µm.[Lin, 2012]

Where I_0 is the fluorescence intensity though the pulsed diode laser (635 nm) as indicated in Figure 4.12. I_s is the stimulation pulse fluorescence intensity and ΔI_s is the difference which is the stimulated intensity as indicated in equation 4.12. The temporal delay denoted by t_d and the lifetime by τ.

$$\Delta I_s \quad \propto \quad e^{\frac{-t_d}{\tau}} \tag{4.13}$$

3.4 Case study 4

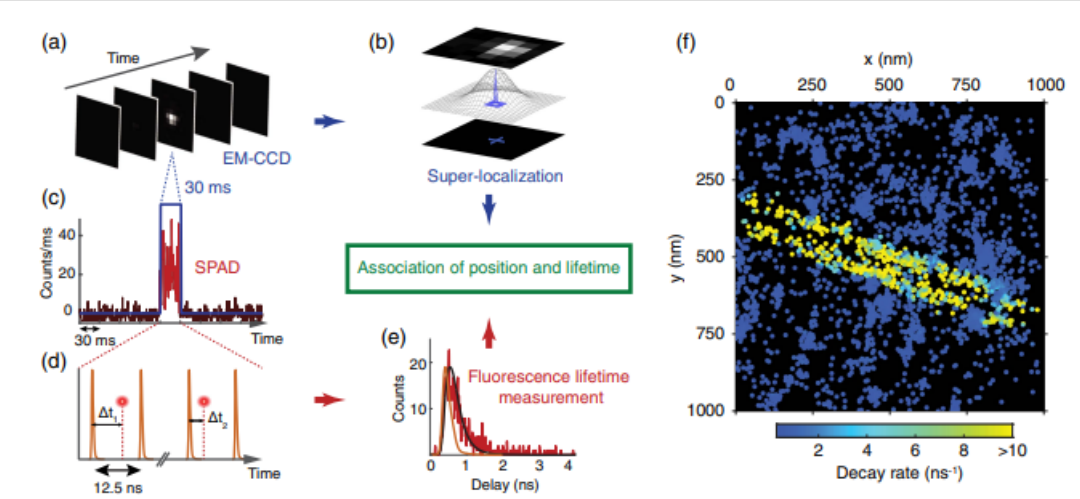

Figure 4.14: (a) The EM-CCD camera acquires a single fluorescent molecule. (b) The position of the molecule is estimated by fitting a two-dimensional Gaussian function to the measured PSF. (c) At the same time, the SPAD detects a fluorescence burst from this molecule. (d) Short laser pulses were used to excite this molecule. (e) These photons are used to construct a decay histogram. (f) Reconstructed decay rate map. [Bouchet, 2019]

The ability to efficiently couple fluorescent emitters with nanostructured materials requires sub-wavelength resolution. This approach performs super resolved fluorescence lifetime measurements on a samples densely labeled with photo-activatable fluorescent molecules. The simultaneous measurement of position and decay rate of the molecules is feasible and near field measurements for a silver nanowire were performed using this. And via a Cramér–Rao analysis localization precision of 6 nm was calculated [Bouchet, 2019]. The schematic for the implementation is given in Figure 4.14.

3.5 Case study 5

One of the major aspects of using detectors especially TCSPC is the dead time, in [Isbaner, 2016], dead-time correction of fluorescence lifetime measurements and fluorescence lifetime imaging is carried out.

In the start-stop technique for time based FLIM, laser synchronisation starts the timer and a photon detection event stops the timer. Followed by a dead time from the electronics

and detector. The laser synchronisation starts the timer again. As discussed in section 2, this leads to more weighting of the initial photons causing a shift in the measured lifetime. This is corrected by correcting for the weighting of the measured arrival times [Isbaner, 2016].

After an analysis of the statistics of dead time effects it is possible to correct for it using an algorithm. This correction was not limited to the type of the molecule. It was applicable to all single event measurements with any detector dead time including TCSPC. The algorithm was also able to correct for intensity that is changes in fluorescence due to temporal instability. The dead time can also be modelled based on the photon arrival times thus accounting for fast FLIM techniques as well.

3.5.1 Fitting Parameters

Now that we have examined the key features and examples of the time domain based FLIM measurement devices we proceed to the extraction of the lifetime from the collated data.

The histograms of time bins are used to fit the exponential decay curve to derive the time constant. The fitting itself has many details to optimise and standardise the procedure. The scanning points/pixels may have one or more fluorophores and each of them are excited multiple times to have better accuracy. An estimate of the lifetime can also be affected severely by background fluorescence. Equation 4.1 is used to fit the curve with an exponential decay, with the amplitude and the lifetime as the two fit parameters. And the fit is usually based on regression analysis by iteratively looking at the distance of the data points from the proposed fit and reducing the net distance of the points from the fit function. The coefficient of determination called R^2 is the parameter that quantifies this process. The R^2 value is defined as the sum of residuals. That is, the goodness of fit with respect to the ground truth on a scale from 0 to 1. Other techniques like *Maximum Likelihood Estimator* (MLE) and Bayesian analysis are also used. MLE gives accurate results for low counts like N less than 1000 as well, due to the difference in the way the counts are weighted [Maus, 2001]. It is for example more likely for photons to be detected in the first time bin than the rest and this is statistically implemented to weight the points differently on the decay curve formed by the histogram of time of arrival data. The noise in the least squared regression analysis and MLE are also modelled differently. The first uses Gaussian noise and the second, Poissonian. The time constant evaluated from the fit is also determined many times via global analysis, by treating each scanning point to be a source of all the data points, to make it more robust [Pelet, 2004]. This concludes the salient time-domain based FLIM experiments and data analysis. In the next section we briefly touch upon two other approaches to FLIM to give an overview and complete the story.

4 Caveats of existing FLIM techniques

In this chapter we discussed the theory and implementation of FLIM. Amongst the various implementation to measure lifetime, the time based technique is most common. Amongst which we looked at the two approaches point based and wide field imaging.

In the wide field technique, the major bottlenecks being the background noise and non specificity of fluorophore determination. And in the point based scanning technique, majorly applied using a confocal scanning system, we saw that the speed determined by the dwell time at each defined point was the bottleneck. All techniques are limited by the detector, scanning dead time due to the very short time scales involved. The dead time of devices and the electronic circuits responsible are also of great consequence. We have also examined how these factors can be improved or corrected for, through few cases of experimental implementations in recent times.

However, the limitations are not simple, and require thorough processing to correct for example the dead time of the devices. Other bottlenecks can only be minimised but not suppressed. Also, all these systems that have been discussed, through the above mentioned existing approaches for FLIM measurement; are very expensive due to devices and measurements needing to be very precise and perfectly synchronised. This is due to the subnanosecond time scales involved when it comes to measuring lifetimes of fluorescent molecules. Also the SNR is a key player and maintaining high signal in widefield techniques is difficult, and in scanning based techniques would mean more photons from each scanning point, decreasing the speed of acquisition. This further leads to other complications with the TCSPC and SPAD could be a possible solution with synchronised electronics. And the net cost of all these devices are very high, each component like the TCSPC, detectors, SPAD, APD, PMT, confocal head, etc cost tens of thousands of euros not to mention the most important component, picosecond pulsed lasers which are very expensive [Lagarto, 2017].

5 Conclusions

In Chapter 3 we demonstrated how flux from a fluorophore could be used to distinguish molecules and successfully adopted for multiplexing in SMLM microscopy. In this chapter, we explained another characteristic feature of a fluorescent molecule, namely fluorescence lifetime. Here we have described various techniques reported in the literature to measure Fluorescence Lifetime. Idea is to use distinct fluorescence lifetimes of the fluorophores to distinguish them to carryout multiplexing, even when their emission spectra could have overlap. However, as one can note, all these methods presented here require expensive instruments having the capability to resolve, measure and synchronize in nanosecond timescales. Typically, picosecond pulsed lasers are used for the excitation and fast photo detectors are needed to setup these systems. Hence, it is evident that there is a need

to develop Fluorescence Lifetime Imaging methods which could be used for multiplexing. In the next two Chapters we present two novel methods, exploiting saturation and decay dynamics of fluorophores to distinguish fluorophore species, and demonstrate Lifetime as a multiplexing tool.

Chapter 5

New technique for FLIM

Summary

In this chapter we introduce a new approach to doing FLIM measurements using a CW laser and combining it with the concept of saturation. We first introduce fluorescence lifetime dynamics from first principles elucidating the importance of saturation in our technique. This technique offers a unique way to measure fluorescence lifetime using a cw laser through measuring the integrated photon flux emitted by our target fluorescent probes. We then look at simulating the fluorescence process and saturation to better understand how this is linked to the lifetime of fluorescent probes. Then we discuss the experimental apparatus as well as results for this new technique where we differentiate between two fluorophores based on their lifetime illustrating the proof of concept for a CW laser based setup for FLIM based multiplexing.

Contents

1 Fundamentals of fluorescence lifetime from first principles

Within this chapter, we present a pioneering methodology for , seamlessly integrating a laser with the concept of saturation. Our exposition commences with a foundational exploration of fluorescence lifetime dynamics, meticulously elucidating the theoretical underpinnings that underscore the pivotal role of saturation in our proposed technique. This innovative approach not only introduces a distinctive means of gauging fluorescence lifetime but also integrates seamlessly with the modality of a laser, wherein the measurement hinges on the quantification of the integrated saturation regime-photon flux emanating from targeted fluorescent probes.

A comprehensive investigation into the intricacies of the fluorescence process and the phenomenon of saturation follows, providing a simulation to illuminate the intrinsic connection between these elements and the lifetimes of the fluorescent probes under scrutiny. Subsequently, we delve into the experimental apparatus devised for the application of this novel technique, presenting compelling results that distinguish between two distinct fluorophores based on their lifetimes. This empirical approach serves as a compelling proof of concept for the viability and efficacy of a laser-based configuration in the realm of -guided multiplexing.

In essence, our contribution not only introduces a groundbreaking technique for measurements but also substantiates its applicability through a rigorous theoretical foundation, simulations, and experimental validations. The seamless integration of a laser with the concept of saturation adds a novel dimension to the field, offering an advanced avenue for fluorescence lifetime studies with significant implications for multiplexed imaging.

In Chapter 4 we looked at lifetime derivation very simplistically, sufficient to examine the experimental implementation. In this section we derive it from first principles (which is also used in simulating the process in the next section). Based on the discussion we had in the Chapter 4, especially with regard to the drawbacks of existing FLIM techniques it is evident that we need to develop new methods to circumvent them. Hence, in continuation of the discussion presented in the previous Chapter, here we shall elaborate on the lifetime of a fluorophore emitter. Relation between fluorescence lifetime and other parameters such as emission flux, excitation illumination, detection related variables and molecular properties of the fluorophore are presented in following section.

1.1 Lifetime Dynamics

As we have discussed in the previous Chapters, fluorescence is a radiative process. Upon excitation of a molecule from the ground state to the excited state and subsequent spontaneous relaxation to the ground state, a photon is emitted called fluorescence (delayed emission phosphorescence). Thus fluorescence is defined as the spontaneous emission of a photon by an electron relaxing from a higher energy quantum state (usually singlet state, monoexponential) [Celebrano, 2010a].

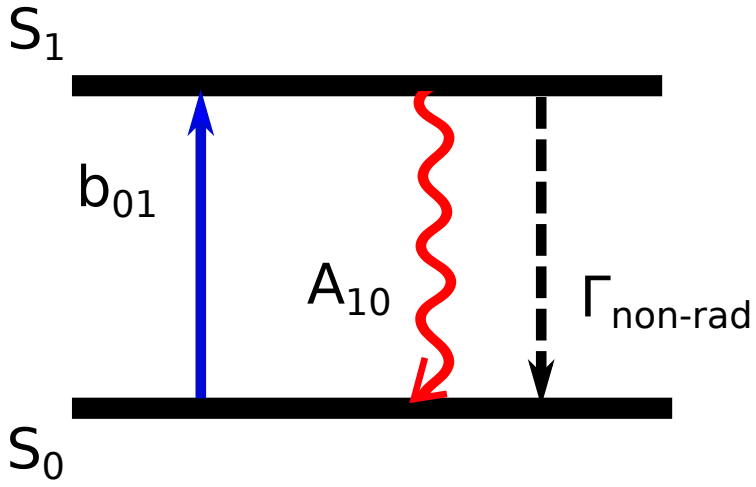

Figure 5.1: Jablonski diagram with non-radiative and radiative transitions. The absorption rate b_{01} is the transition from S_0 to S_1 followed by spontaneous emission with rate defined by b_{10}

.

Relaxation can also occur in many ways as depicted in Figure 5.1. Relaxation can be through stimulated pathways as exploited in STED microscopy which was discussed in Chapter 1. Or through bleaching and quenching pathways where the electron is no longer capable of cycling through the ground state S_0 and excited state S_1 due to molecular configuration changes, charge transfer, FRET, internal conversion or intersystem crossing [Chaze, 2016] [Datta, 2020a] which we will not consider here.

In a simple system, with two energy levels, one corresponding to the ground state S_0 and the other to the excited state S_1, with populations in each state given by N_0 and N_1. The transition dynamics between the two levels can be described as follows,

$$\frac{dN_1}{dt} = -\frac{dN_0}{dt} = N_0 b_{01} - N_1(b_{10} + A_{10} + Q_{10}) \tag{5.1}$$

Where the absorption rate b_{01} is the transition from S_0 to S_1 followed by spontaneous emission with rate defined by A_{10}. The bleaching/quenching is described with the rate of bleaching given by Q_{10} and stimulated emission with the corresponding rate b_{10}. In our analysis, we will not consider these two terms since they are not of interest in our experiment. Although bleaching could affect our system close to the saturation regime we mitigate for this by double-checking our dynamics through repetition to ensure we are not bleaching our target molecules. This finally gives us the following population dynamics,

$$\frac{dN_1}{dt} = -\frac{dN_0}{dt} = N_0 b_{01} - N_1(A_{10}) \tag{5.2}$$

Absorption and spontaneous emission are rate constants that depend on the spectral radiance of the incident laser light with intensity I_λ at the frequency of the transition as follows [Chaze, 2016].

$$b_{01} = \frac{B_{01} I_\lambda}{C_\lambda} \tag{5.3}$$

Einstein coefficients B_{01}, for absorption and C_λ is the conversion factor with the same units as intensity I_λ. The total number is constant when you sum up the number of species in both states,

$$N_0 + N_1 = N \tag{5.4}$$

Equation 5.1 for the population dynamics of N_1 can be written as

$$\frac{dN_1}{dt} = b_{01} N - \frac{N_1}{b_{01} + A_{10}} \tag{5.5}$$

We have not considered the Q_{10} term (considering which we would have equation 4.5). Now, solving for the number of excited molecules N_1,

$$\frac{dN_1}{dt} + \frac{N_1}{\tau} = b_{01} N \tag{5.6}$$

where

$$\tau = \frac{1}{b_{01} + A_{10}} \tag{5.7}$$

is the fluorescence lifetime. Solving for N_1,

$$N_1 e^{\frac{t}{\tau}} = \frac{N}{b_{01} + A_{10}} e^{\frac{t}{\tau}} + C \tag{5.8}$$

$$N_1 e^{\frac{t}{\tau}} = \frac{N B_{01} I_\lambda}{C_\lambda (b_{01} + A_{10})} e^{\frac{t}{\tau}} + C \tag{5.9}$$

$$N_1 = \frac{N B_{01} I_\lambda}{C_\lambda (b_{01} + A_{10})} + C e^{\frac{-t}{\tau}} \tag{5.10}$$

Now at $t = 0$, $N_1 = 0$ since all the population is in ground state. Thus, we have

$$C = -\frac{N B_{01} I_\lambda}{C_\lambda (b_{01} + A_{10})} \tag{5.11}$$

Then we can rewrite the population of N_1 as follows,

$$N_1 = \frac{N B_{01} I_\lambda}{C_\lambda (b_{01} + A_{10})} \; [1 - e^{\frac{-t}{\tau}}] \tag{5.12}$$

The above functional form is also discussed in [Ghauharali, 1997] as follows,

$$F = \alpha \; (1 - e^{-2A\sigma D}) \tag{5.13}$$

Where α is the constant pre-factor, σ is the absorption cross section, A is a function of the Einstein B coefficient and D is the excitation intensity.

Defining $I_{saturation}$ in terms of the rates of emission to absorption, where the satu-

ration intensity is proportional to the relaxation processes and inversely proportional to absorption as given by [Chaze, 2016],

$$I_{saturation} = \frac{A_{10}}{B_{01}} \tag{5.14}$$

$$N_1 = \frac{NB_{01}}{A_{10}} \frac{I_\lambda}{[1+\frac{I_\lambda}{I_{saturation}}]} [1-e^{\frac{-t}{\tau}}] \tag{5.15}$$

If we consider the non-radiative quenching term, the quantum yield Φ which is defined as the ratio of the number of photons emitted to the total number of photons absorbed and be written as

$$\Phi = \frac{A_{10}}{A_{01}+Q_{10}} \tag{5.16}$$

where Q_{10} is nothing but Γ_{nonrad},

$$\Phi = \frac{\Gamma_{rad}}{\Gamma_{rad}+\Gamma_{nonrad}} \tag{5.17}$$

And the fluorescence flux signal $F \propto N_1$ can be written as follows as explained in [Chaze, 2016],

$$F = \xi \frac{\Omega}{4\pi} \epsilon \Phi \frac{I_0}{[1+\frac{I_0}{I_{saturation}}]} VC [1-e^{\frac{-t}{\tau}}] \tag{5.18}$$

Where ξ is the detection efficiency, Ω is the solid angle of the molecule ϵ is the molar extinction coefficient, V is the volume of the sample, C is the molar concentration and I_0 is the excitation intensity.

As a side note, we have at long times, where $t >> \tau$ the equation reduces to just the pre-factor as given by [Chaze, 2016],

$$F = \xi \frac{\Omega}{4\pi} \epsilon \Phi \frac{I_0}{[1+\frac{I_0}{I_{saturation}}]} VC \tag{5.19}$$

Ω is also a detector property and can be included along with the detector term as well and flux for one molecule can be considered, which gives us:

$$F = \xi \epsilon \Phi \frac{I_0}{[1+\frac{I_0}{I_{saturation}}]} \tag{5.20}$$

Important to note here that the saturation dynamics is a function of the fundamental property of the molecule that is, its lifetime and through the course of probing the molecule by excitation followed by emission detection we can probe the lifetime of the molecule. Using this, our goal is to probe our system with continuous excitation, measuring the subsequent integrated flux. And using that to disentangle florescent probes and thus multiplex.

Thus, we see from first principles that the saturation intensity and lifetime both play a major role in fluorescence flux. We also see a direct evolution of the Poissonian functional form through the derivation as is expected.

2 Saturation Dynamics and Experiments

In the previous section we saw that the fluorescence lifetime limits the rate at which a fluorophore can transition to the excited state. And saturation intensity was that intensity which brings the fluorophore to the limit of transition wherein further increase of the illumination intensity will not have any effect on the emission. That is, emission will remain constant and no longer increase. In this section we look at some examples of work that has been done with saturation as a player in the approach.

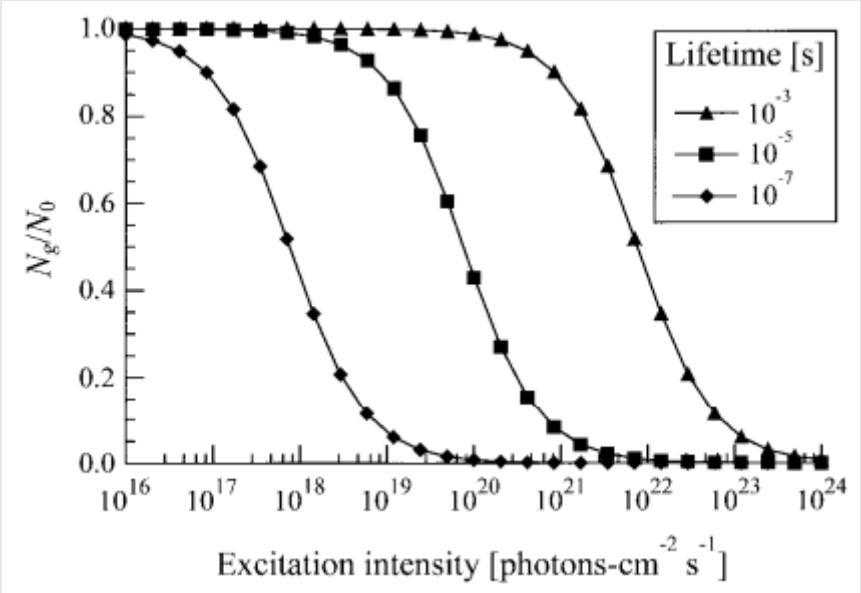

Figure 5.2: Fluorophore saturation as a function of excitation intensity for different mean lifetimes [Chang, 1997]. The lifetime in the legend is the opposite of what is written **correction by [Chang, 1997].

The lifetime of a fluorophore is thus a deciding factor when it comes to the saturation intensity and vice versa. Different lifetimes give rise to different saturation dynamics as described in [Chang, 1997]. Where the saturation intensity for different lifetimes was calculated with the same molar extinction coefficient, for a beam of 0.1 cm diameter and 0.1 W in IR range for the excitation. Unless τ is very large, there is no appreciable saturation at excitation intensity levels normally used ($< 10^{20}$ photons $cm^{-2}s^{-1}$) [Chang, 1997]. In Figure 5.2, where N_g is the population in the ground state and N_0 is the population in the excited state.

Thus, we see that upon increasing the lifetime of molecules, the intensity required for saturation decreases. As is expected from their inverse relationship that we saw from the previous Section. Generally, fluorophores have a lifetime of the order of a few nanoseconds. The energy of illumination for the same intensity can also be increased by reducing the wavelength to the visible range as well. Thus, parameters including intensity, wavelength as well as dispersion width of the intensity of illumination are key players.

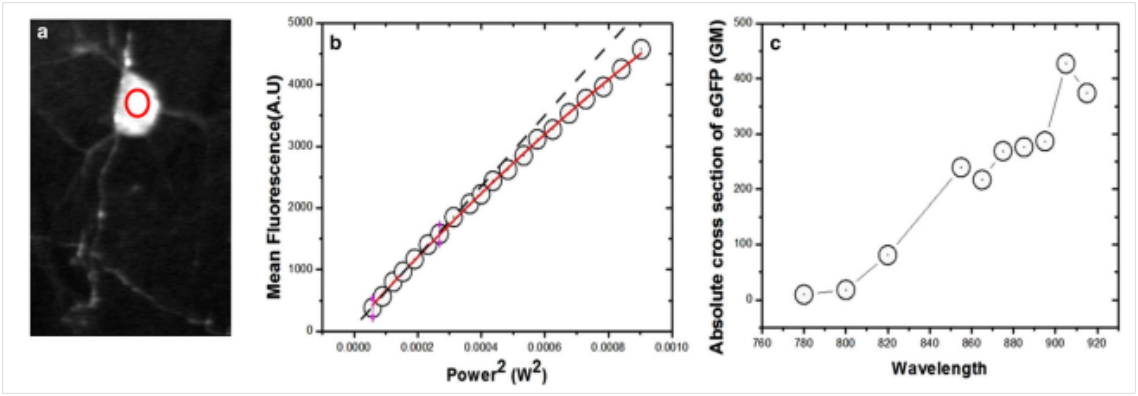

Figure 5.3: The two-photon image stacks of whole brain obtained from transgenic mice (a) The mean pixel densities within the ROI were calculated for images obtained at different excitation light intensities. (b) The intensity scan is generated at wavelength 855 nm by measuring the fluorescence. The fit parameter estimated a cross section of $\approx$ 240 GM. (c) The absolute cross sections were obtained for the entire spectrum (780 to 915 nm) [Kumar, 2016].

Saturation based experiments have been widely used to make various fluorescence related measurements. For example, in [Kumar, 2016] where saturation was used to compute the absorption cross section (in Figure 5.3) a sample of rhodamine B (two photon technique), tryptophan (3 photon technique) and two photon brain stacks from transgenic mice (Thy1-EGFP transgenic mice expressing *Enhanced Green Fluorescent Protein* (EGFP) sporadically across the hippocampus and cortex) were imaged with varying power/excitation and the cross section was calculated with known lifetime as shown in Figure 5.2. Thus, fluorescence saturation curve was used to determine the absorption cross section values.

Just to deviate briefly a bit, absorption cross section and molar extinction coefficient which are related to each other as discussed in Chapter 3, is an important factor for fluorescence flux as well as lifetime, so here I briefly mention a technique to measure cross section. The absorption cross section values can be computed for fluorophores used in SMLM, even in their photobleached state or dark state using spectrometry [Celebrano, 2010a]. And also another technique using localised heating to have absorption in IR for absorption microscopy [Chien, 2018].

Now we get back to more techniques exploiting saturation and another technique based on saturation measurements such as in [Jensen, 1992] (in Figure 5.4) where a pump probe

laser, laser amplifier, monochormator and spectrometer were used to obtain the saturation curve for TBS which is a UV based dye. This was carried out to establish that the excited state and ground state absorption cross section were the same.

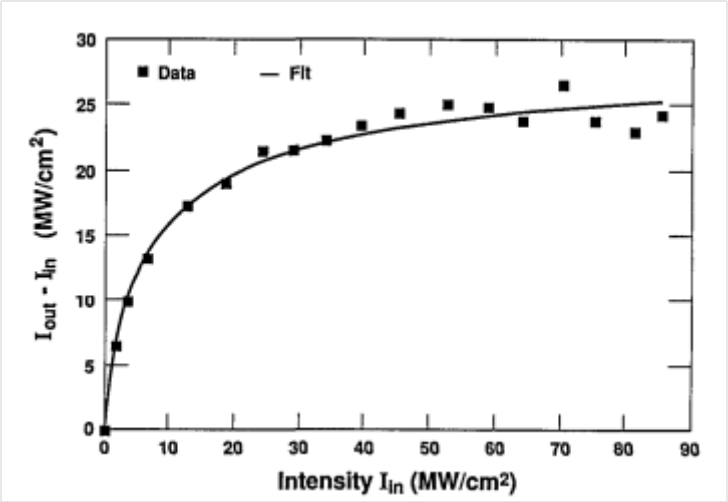

Figure 5.4: Probe laser extraction intensity versus probe laser input intensity for a XeCl laser-pumped TBS dye laser amplifier. [Jensen, 1992].

Other studies including Radiometric characterization of triggered narrow-bandwidth single-photon sources [Georgieva, 2020] also uses saturation dynamics to correlate spectral data with intensity using a spectrometer, cryostat, SPAD array and a confocal scanning system. Another similar application of saturation dynamics is used in the construction of stable, single-photon emitter for quantum-photonic devices [Polisseni, 2016] where saturation intensity is used for calibration of crystals. This was done using APDs for detection and a confocal point based scanning system for a crystal.

Studies involving usage of saturation are mostly for calibration purposes for crystals or characterisation of dyes. These experiments use pump probe lasers, confocal systems or spectrometers with high end detectors. And the working wavelength ranges are in either UV [Jensen, 1992] or IR [Polisseni, 2016] [Georgieva, 2020]. The reason lifetime measurements are not made with saturation dynamics is due to the noise. Since the lifetimes of fluorophores are very comparable and differ by a few nanoseconds at the most, it is hard to discern the lifetimes quantitatively. The work on [Chekalyuk, 1981] for laser based saturation for FLIM is one such only publication. But even here, Raman spectroscopy combined with a pulsed laser is used to probe the lifetime of rhodamine 6G dye. The reason all the apparatus in relation to probing the lifetime is so expensive is because of the approach to directly resolve nanosecond timescales. A theoretical calculation on the lifetime measurements for different excitation lasers was done by [Gregor, 2005] in order to look at saturation in *Fluorescence Correlation Spectroscopy* (FCS). The saturation curve for a *Continuous Wave* (CW) laser saturates much later than that for a pulsed laser.

Now that we have briefly looked at some examples that exploit saturation to make various measurements, in the next section we simulate saturation from our understanding from the first principles discussed in the previous Section.

3 Simulating saturation dynamics

In this section we look at the saturation process and derive the saturation curve by simulating a population of fluorophores. Simulating the process helps to distinguish between known and unknown parameters as well as the level of control one has over changing different parameters. As seen from the previous Section, the major parameters involved in the emission of fluorescence flux are the excitation illumination, detection related variables and molecular properties such as the molar extinction coefficient or the absorption cross section (for the corresponding excitation wavelength) and the environmental parameters such as the chemical composition, pH and temperature which we don't consider here in the simulation.

3.1 Parameters

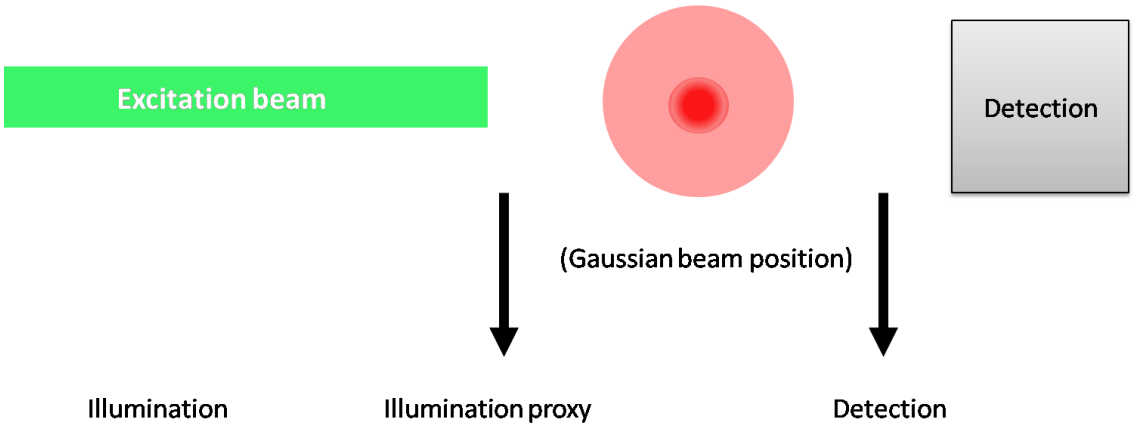

Figure 5.5: The workflow and the parameters involved in simulating the system, the excitation in green with a final beam diameter, sample being illuminated and fluorescing shown in red, detection system and the places in the workflow where noise is introduced.

The parameters used in the simulation for the variables that constitute the energy of excitation/illumination aspect of the system are three attributes: Firstly the wavelength of excitation and the power of the laser utilised, secondly the diameter of the laser beam and finally the duration of the excitation pulse. The detection is done with a detection efficiency and tunable level of noise in the detection apparatus. The lifetime of the fluorophore emitter is taken as different values to model various types of molecules. The time step for probing the process can also be fixed at various timescales for precision. The main parameters of the simulation are given in Figure 5.5.

As indicated in Figure 5.5, the fluorophore can be anywhere in the Gaussian beam which introduces a level of uncertainty that can be tuned in the model. The fluorophore is exposed to a photon, upon which it transitions to the excited state. The molecule cannot be excited again, till it reaches ground state. Upon reaching the ground state, the molecule emits a photon as the fluorescence signal and is ready to transition once more into the excited state. This gives rise to the Queuing theory or Poissonian statistics and noise inherent to the dynamics of the system as we observe in Figure 5.6.

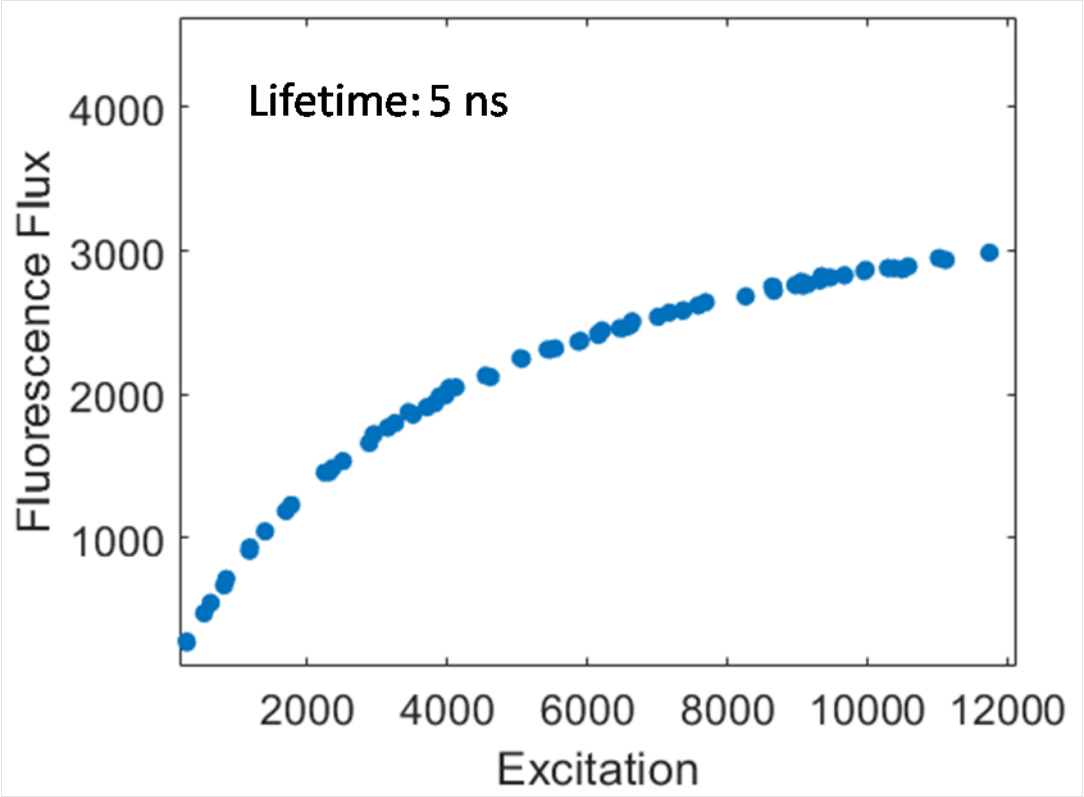

Figure 5.6: The intensity of excitation is gradually increased and decreased (two sets of data/two cycles). Fluorescence flux signal and corresponding excitation signal of increasing intensity of illumination. The spread occurring due to noise introduced in the model. X-axis is the excitation photon number. X-axis is the excitation signal photons and the Y-axis is the emitted photons here written as fluorescence flux.

In order to see the sensitivity of the excitation and emission processes, we present results for the saturation-curve from a Monte-Carlo simulation-based model. This helps us in understanding and distinguishing various factors controlling the observed saturation flux and sensitivity of saturation flux on the lifetime of the fluorophore. The variables were assigned as follows for the plot in Figure 5.6; for the excitation we have, green with a wavelength (532 nm) or a frequency of 5.64 x 10^{14} Hz with the power of the illumination being 5 W. The beam diameter being 15 x 10^{-6} m or 15 μm and the width of illumination pulse time being 20 x 10^{-6} or 20 μs. The time step for the model dt which is much shorter than the lifetime, to be 2 x 10^{-10} s. The absorption cross section of the molecule is

generally in the order of 10^{-20} m^2 so taken as such. The lifetime of the species was taken to be 5 x 10^{-9} s which is 5 ns. The molecule was excited many times (across the 20 μs time period of the laser excitation) for each excitation intensity/power and the net emitted fluorescence photon number was used to plot the fluorescence emission signal. Figure 5.6 is an idyllic case with no added noise at the different points indicated in Figure 5.5 to demonstrate how an ideal saturation curve should be.

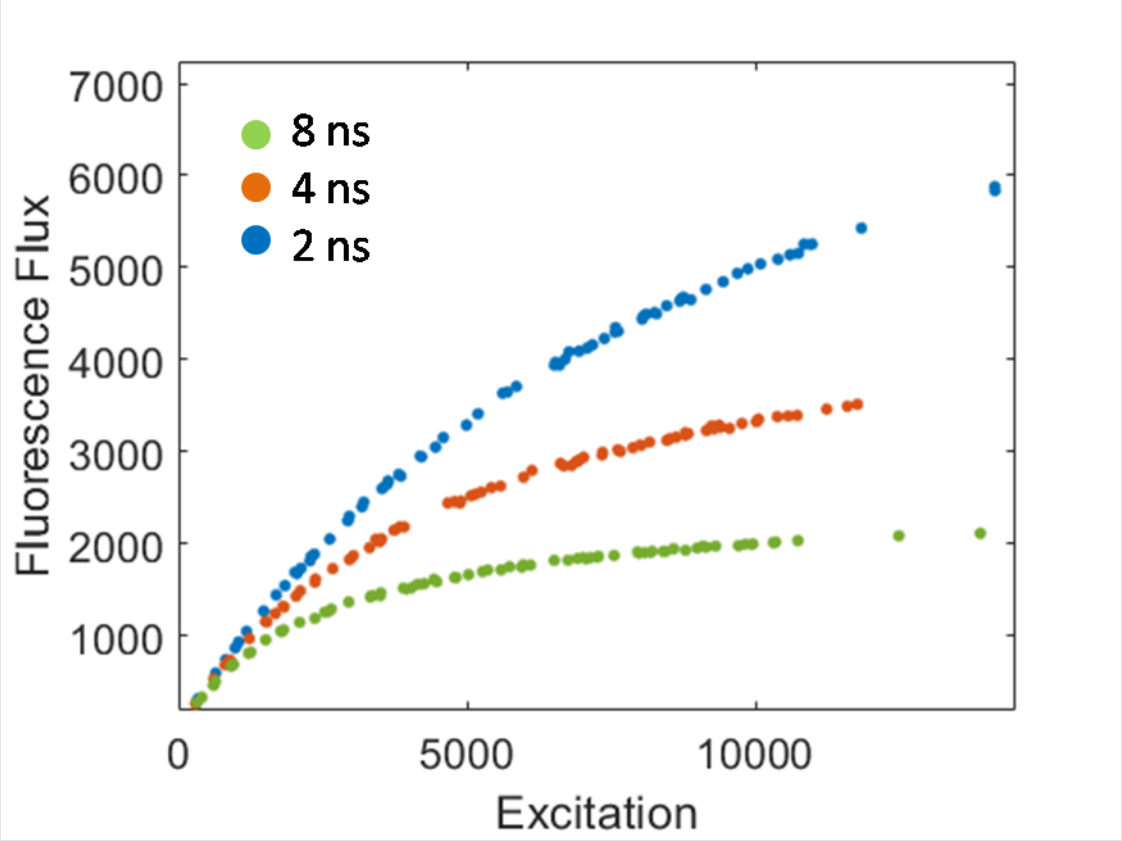

Figure 5.7: The intensity of excitation is gradually increased and decreased (two cycles). Three species with different lifetimes are depicted as 2 ns (Blue), 4 ns (Orange) and 8 ns (Green). And plotted with the X-axis as the excitation photon number and Y-axis as the emitted fluorescence photons.

In the next part, we look at the trend of various plots for different lifetimes. The variation in lifetimes leads to saturation level changes, and rate of growth of fluorescence flux allowing one to distinguish between fluorophore emitter species having different lifetimes, as demonstrated in Figure 5.7. All parameters other than the lifetimes were held constant in Figure 5.7.

Keeping the other variables and parameters the same, changing the lifetime alone, gives an idea of the kind of trend we should observe for shorter and longer lifetimes as discussed in the previous section [Chang, 1997]. We see the same trend here as well in Figure 5.7.

Changing the lifetime and looking at the trend in Figure 5.7, we see that we have three species depicted with Orange, Blue and Green with lifetimes 2 ns, 4 ns and 8 ns respectively. The species depicted in Blue have a smaller lifetime thus they saturate at a higher power. It's easier to saturate species that have a longer lifetime. Now that we have an idea of the dynamics and how they play out ideally, in the next section we define saturation in a scenario with noise to resemble a real life experiment.

The maximum fluorescence yield could change with the location of the fluorophore plane. The value for the part of constant fluorescence flux can thus change depending on the optics and plane of focus. However, the trend of the curve for the same species of fluorophore emitters will remain the same. As in, the lifetime constant will remain the same for the same species

3.2 Adding Noise

In this section we start by adding noise to the previous simulation so that we are one step closer to real life experiments. The noise added is random noise (white noise) which is suitable while considering different devices, be it at the point of detection (detection of excitation as well as fluorescence emission) and also with respect to the position of the fluorescent probe within the beam. In this Section we discuss how a typical experimental saturation curve looks, as well as define the saturation point on this plot to illustrate saturation excitation intensity/power as discussed in Section 1.

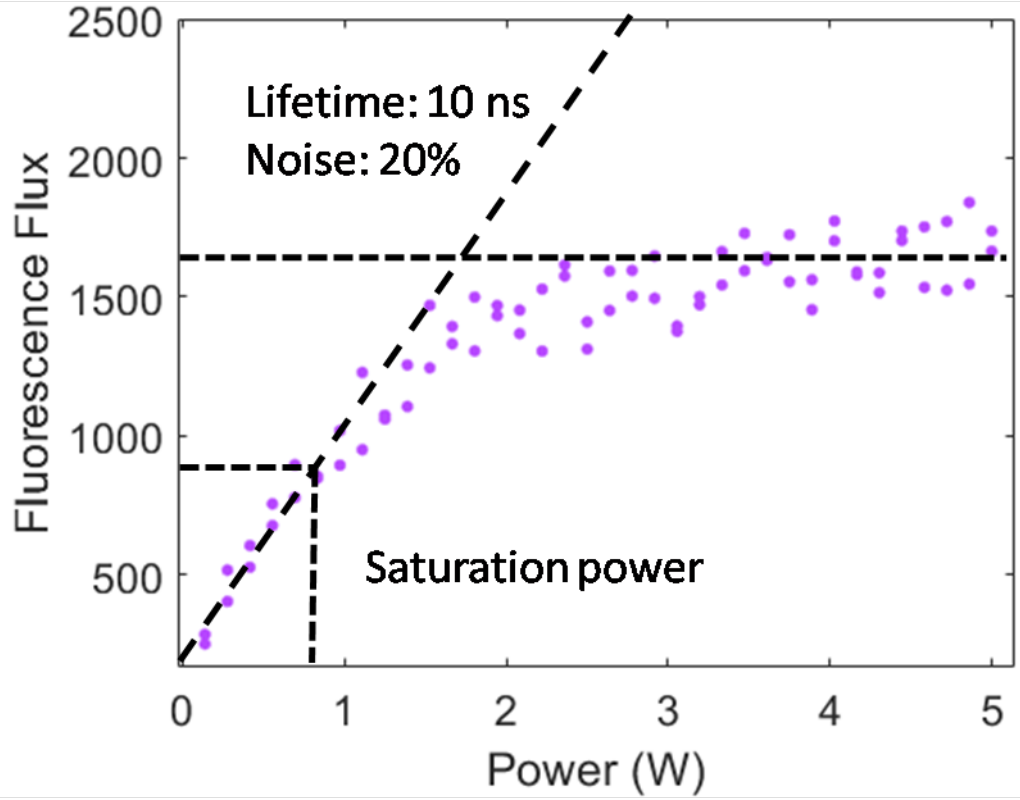

Figure 5.8: Saturation power for a fluorophore emitter with 10 ns lifetime. The power is given in the X-axis and the Y-axis is the corresponding fluorescence signal. The saturation power is close to 1 W in this case.

The saturation excitation intensity in Figure 5.9 or also in terms of saturation power (we can also use power in the X-axis as done by [Kumar, 2016] and in Figure 5.8) is the excitation for which half the saturation intensity occurs. In Figure 5.8 we depict a fluorophore emitter with 10 ns lifetime and show its corresponding saturation power. All other parameters are maintained the same as in previous cases and the lifetime is changed to 10 ns. 10 ns was chosen to better illustrate saturation as it requires lower power to saturate fluorophore emitters with longer lifetimes.

The detection of the emitted fluorophore is based on the detection efficiency of the detector, location of the fluorophore in the Gaussian beam and as well as ambient noise,

all of which are also parameters in the simulation by introducing random noise. With a 20% random noise added we have the following dynamics as shown in Figures 5.8 and 5.9.

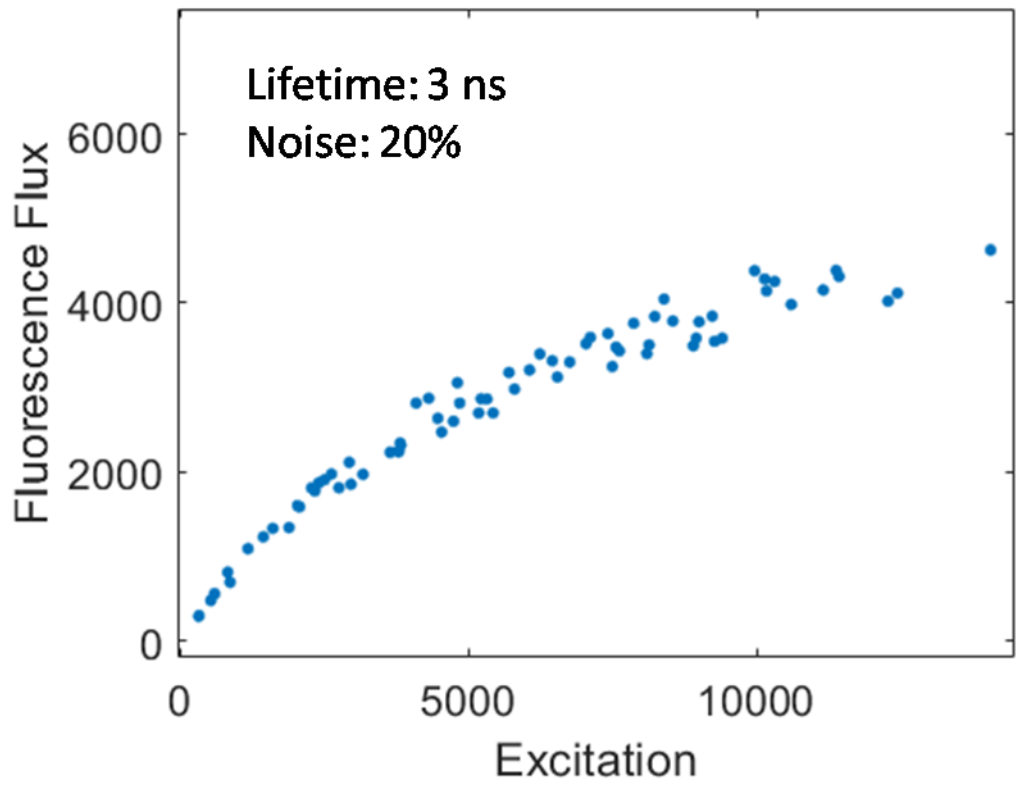

Figure 5.9: The intensity of excitation is gradually increased and decreased (two sets of data). Fluorescence flux signal and corresponding excitation signal for one cycle of increasing intensity of illumination. The spread occurring due to noise introduced in the model. X-axis is the excitation photon number.

The intensity of illumination is gradually increased in steps to the maximum and then decreased. Here the number of steps is taken to be 36 (72 points in two sets of experiment we call this two cycles). The experiment will be discussed in more detail in the next section. In Figure 5.9, the fluorescence flux for the corresponding excitation flux for a fluorophore emitter has been computed. The fluorescence signal in terms of the number of photons is plotted against the excitation number of photons. With an illumination power of 5 W and with an added noise scale of 20% we see that saturation occurs. The noise is seen as the spread in the distribution of the points as seen in the plot. The X-axis is represented in terms of the excitation photon number.

The noise level was decided based on existing detector efficiencies (usually around 85% is the quantum efficiency of camera) as well as losses due to path length and absorption, ambient temperature, and so on thereby having a 20 % random noise added to the system. This noise would increase upon an increase in the ambient temperature, also with an increase in the number of devices that the laser be am interacted with. Most lasers are

unstable at low emission powers. Thus, it is important to use a source that is capable of uniform treatment for the detection and increase of laser illumination power as much as possible.

The fluorescence signal can also be plotted against the corresponding power of illumination which is another way to visualise the same plot in Figure 5.8. Here, we have the power being gradually increased and decreased in the model to look at the corresponding signal that we have in terms of fluorescence in Figure 5.9. The power of the laser experimentally can be measured using a power meter. So it is an available parameter experimentally as well. We see similar behaviour as expected in both Figure 5.5, Figure 5.8 and Figure 5.9.

Why do we have repeated cycles of data? An important way to assess if the fluorophore emitter is undergoing repeated cycles of fluorescence and making sure it isn't bleaching or going into the dark sate is to repeat the process of laser excitation, increasing and decreasing the power of the laser in cycles to ensure that the trend of the saturation curve remains the same. Also, the illumination period is maintained at a very low time frame (in the simulation taken as 20 μs for all cases given in this section) so as to prevent bleaching. Across many such cycles of varying the laser excitation when we see the trend of the emitter remaining the same, this indicates the absence of bleaching. This demonstrates during the experiment, while examining the actual fluorophore responses to discern the level of saturation and if at all if there is bleaching. Bleaching probability owing to structural changes has not been incorporated into the simulation, but experimentally this has been incorporated to rule out probes that undergo bleaching, we will discuss more in the following section about these details.

The important aspect being the threshold levels of saturation, we see that with a maximum limit of the laser illumination, the fluorescence values appear to be constant after a certain point. The saturation power is defined as the power/excitation for which half (precisely, $\frac{1}{e}$) the value of the fluorescence signal, which becomes constant at a certain point. Thus half of the maximal fluorescence flux, is the saturation fluorescence yield and the corresponding excitation is the saturation power/excitation.

Let us now proceed further. Firstly experimentally, the maximum power available via the laser (discussed in the experimental section) is not the full range 5 Watts due to loses via the AOM, path length, etc. So we simulate a scenario with 2.5 Watts as the maximum range of power and a lifetime of 2 ns (a difficult case but experimentally relevant as many markers would fall in this set) for two cycles in various noise levels. This data is then fit to retrieve the fit parameter from the fit which is examined for its variation based on the noise dependence.

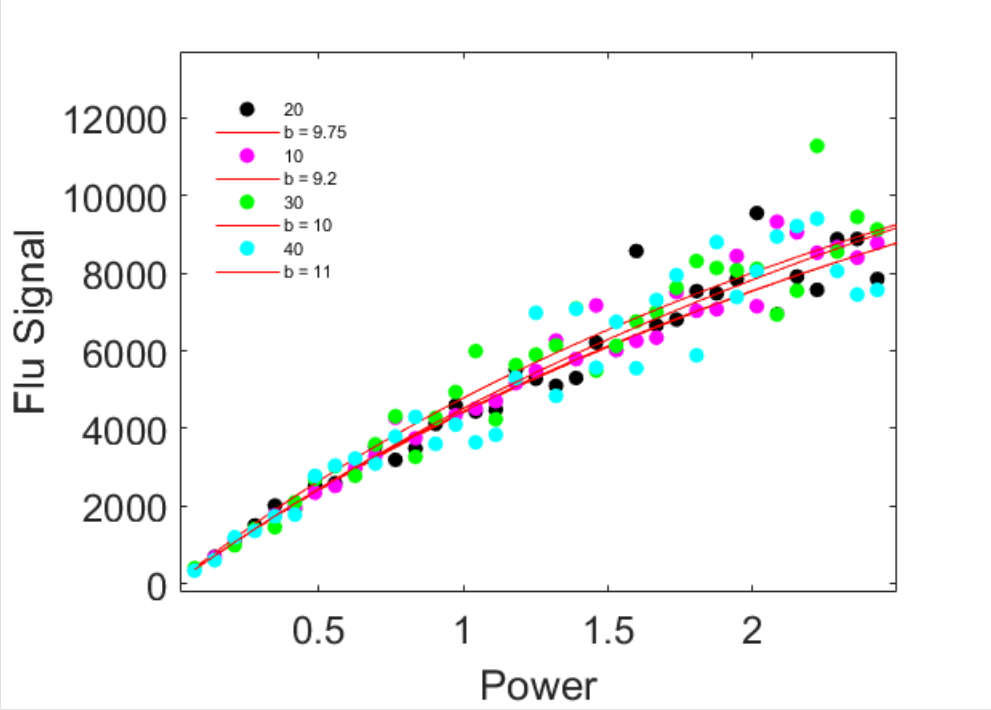

Figure 5.10: Simulation carried out various noise levels from 10% to 40%, 10% is Pink, 20% is Black, 30% is Green and 40% is Cyan. Their corresponding fits and the fit parameters varied from 9.2 to 11.

In Figure 5.10 we have the plot with varying noise levels indicated in the legend with the corresponding fits. The noise level is varied from 10% to 40 % random noise. And the fit is carried out using the functional form below that describes the trend of the saturation curve as we saw in Section 1,

$$y \quad = \quad a \quad (1 - e^{-bx}) \tag{5.21}$$

to derive the fit parameter b. In Figure 5.10 this data is plotted along with the fits and fit parameters are indicated. The fit parameter values vary from 9.2 to 11 upon increasing the noise in the system from 20 % to doubling it at 40%. Thus, we see that the saturation curve is robust and does not exhibit a proportionate change in the fit parameter to a large degree upon adding noise to the system.

The maximum fluorescence yield could change with the location of the fluorophore plane. The value for the part of constant fluorescence flux can thus change depending on the optics and plane of focus. However, the trend of the curve for the same species of fluorophore emitters will remain the same. As in, the lifetime constant will remain the same for the same species

4 Motivation for our system - CW laser based FLIM

Now that we have a good understanding of the way in which lifetime and saturation are related as well as how we can experimentally derive their relation we proceed to the implementation. It is very important to note here before we begin, the motivation for this. In Chapter 4 we saw that almost all existing systems which are employed for FLIM have pulsed lasers and high end single photon counters and other expensive equipment to probe measurements at such small time scales. Even if you could use a time gated technique for detection, we still need powerful pulsed lasers on the excitation side of the experiment. This technique is motivated by an idea to use a CW laser for FLIM. Now that we know the inherent dependence of lifetime and saturation intensity, we exploit this to establish a system using a CW Green (532 nm) laser for the excitation. We also use a Camera for fluorescence emission detection in order to have an image (this is a precursor to wide-field imaging which can be done by integrating this system with the setup from Chapter 1 for uniform illumination). Now we proceed to describe the experimental implementation.

4.1 Overview of the Experimental Implementation and Approach

The idea is to exploit using CW laser to do lifetime based measurements. To do this we have to saturate the sample. Thus we need a fairly strong laser source to saturate the sample. A 100 mW laser beam focused to $20\mu m$ has a photon flux of $10^{27}\ photons \quad s^{-1} \quad m^{-2}$. The saturation power required was calculated (for pulsed laser as well as continuous laser) using [Kumar, 2016], [Celebrano, 2010b] and [Chien, 2019] to name a few. The excitation also has to be gated to avoid bleaching of the sample which would mean that the beam has to be modulated with ON/OFF states (without using a pulsed laser). And most importantly to obtain the saturation curve, the intensity of the beam also has to be varied. All the components and acquisition have to be synchronised. The system should have a proxy for measuring the excitation of the beam and quantify it along with the corresponding fluorescence signal to plot the saturation curve. The value of the fit parameters and their robustness have to be quantified.

4.2 First Approach and setup Basis

In this section we describe our first approach that we implemented to achieve this. We use a very low end Basler Camera (around 150€) for the excitation signal read out. This was done so as to have the shape of the beam as well as a visual cue for how well the shape and focus of the beam is instead of using a detector which just gives out a read out proportional to the photon count with no spatial information.

To implement this experimentally, we have the following setup indicated in Figure 5.11. The setup consists of a powerful CW Verdi laser with a capacity of 5 Watts stable output, by Coherent. The experiment was initially carried out using a 300 mW Oxxius CW 532 nm laser but saturation was not observed, so the power was increased and the Coherent

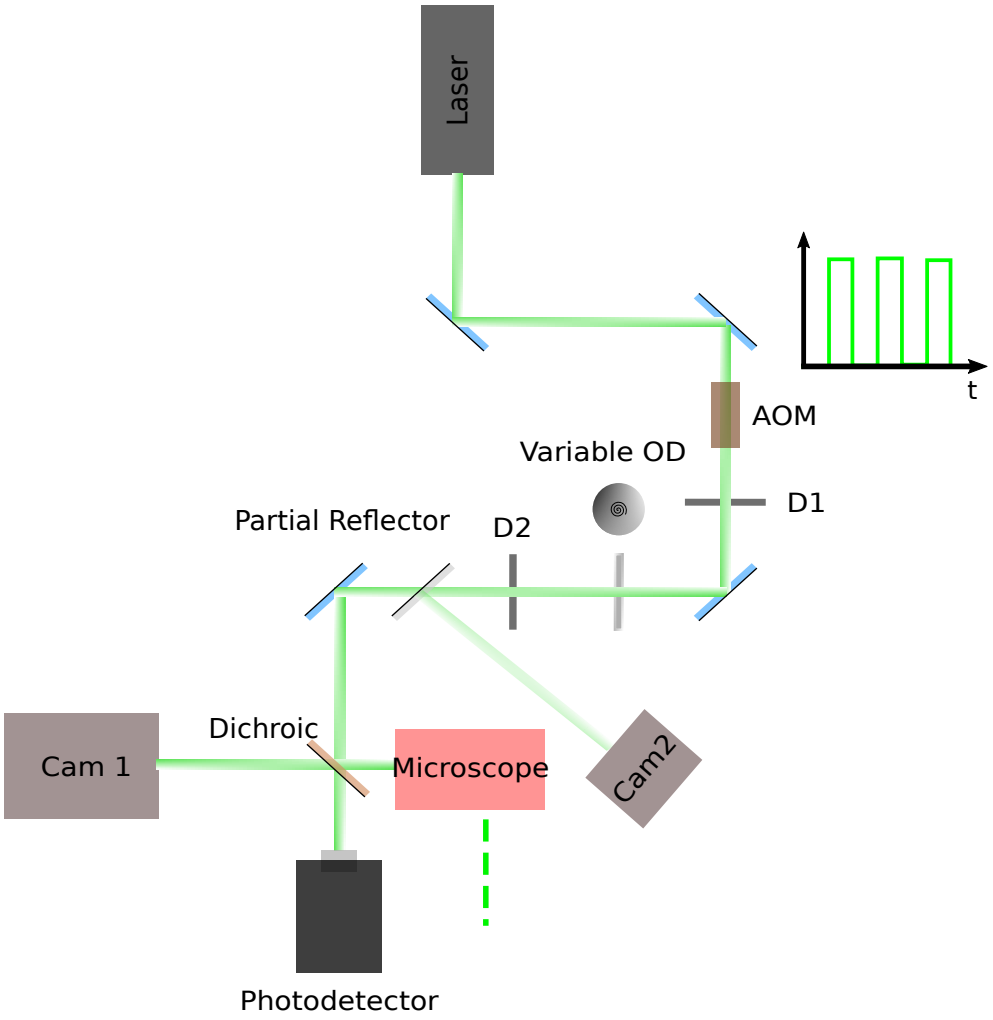

Figure 5.11: Monomodal laser with green wavelength 532 nm, focused into an *Acousto-Optic Modulator* (AOM) (which modulates the laser beam with the frequency indicated as the pulses shown in green) and through a variable density filter to regulate the intensity of excitation. The diaphragms (D1, D2) are to isolate only the beam and not ambient light. The excitation proxy is through a partially reflecting mirror (PR) and the photodetector. The fluorescence emitted from the sample is detected via the Camera.

laser was a very good candidate. High powered lasers like the Verdi based system which has been used has a stable output at high powers. The variability in the laser for different powers was measured and maximum variability was observed for the lower powers. The variability in time for the total intensity of the illumination beam was computed and plotted. The laser was stable close to 5W, thus compelling the use of other techniques of modulating the beam instead of tuning the laser itself.

Therefore a variable density filter was used to change the intensity of the beam. The variable density filter is a coated circular plate with circularly varying density. Thus transmissivity logarithmically decreases with angle. This filter was from Thorlabs [NDC-50C-4-A] and was operational for 300 nm to 750 nm wavelength beams. The plate was mounted

on a rotation mount, also from Thorlabs [ELL14K] which was driven by a piezoelectric motor and interfacing was done with Matlab. The rotating stage was moved sequentially in steps to obtain different intensity excitation beams and their corresponding fluorescent signals initially beginning with low intensity and then hitting finally at maximum. The process was repeated with increasing the excitation to maximum followed by decreasing it to minimum to check if there was bleaching in the sample, as we had discussed in the previous Section on the trend of the curve getting altered.

Now that we have a means to modulate the excitation beam intensity we now discuss the gating of the beam. This was the most important step in order to have pulses instead of a continuous stream of excitation which would bleach the sample. However unlike pulsed laser implementations, we are not restricted to nanosecond range but can have a longer period pulse in the order of microsceonds. This is one of the major advantages of this technique.

The AOM [ISOMET 1205C series] with a RF driver [AA.MOD OEM series] was used for this purpose. To modulate the beam, it was passed through this *Acousto-Optic Modulator* (AOM). The working principle of an AOM involves the use of a crystal which deforms under high radio frequency acoustic waves. These acoustic waves are generated using a piezoelectric transducer that vibrates, producing a series of compressions (acoustic wave) in the crystal medium. This changes the refractive index of the crystal sinusoidally as determined by the driving frequency of the transducer. These alternating changes in refractive index behave as multiple slits, which cause the incident beam to get diffracted. For this condition to occur, the incident light beam has to enter the crystal at the Bragg angle for maximum intensity at the center of the diffraction pattern.

The diffraction pattern has many orders and the maximum intensity can be shifted across different orders by changing the incident angle. This is the salient feature of AOMs that allow us to control the maximum intensity and in which order it falls. Also, unlike EOMs we can have better switch (ON/OFF) behaviour for the beam. The schematic of an AOM is indicated in Figure 5.12.

The incident angle θ_0 is tunable by changing the angle of the plane of the AOM. The diffraction pattern is created through the multiple changes in the refractive index of the crystal (depicted in blue) that is caused by the external RF forcing through the piezoelectric transducer. This frequency depends on the chemical composition of the crystal and its response to stress. To have the maxima located in the first order which is what we need for the experiment, we have to tune the beam with the Bragg's condition. Bragg's condition occurs when the incident angle θ_0 is the Bragg angle θ_b

$$\theta_b \quad = \quad \sin\theta_b \quad = \quad \frac{\lambda}{2n\nu} \tag{5.22}$$

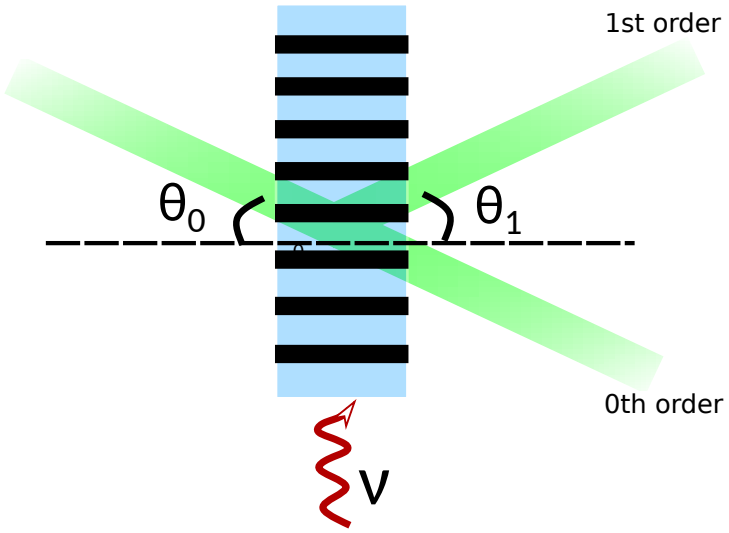

Figure 5.12: The AOM is depicted in blue, with the RF forcing is shown in red. This creates an alternating difference in the refractive index making it behave like slits. The incident beam in green since we use 532 nm excitation in the setup, is incident at θ_0 and has the corresponding zeroth and first order beams after diffraction.

And the first order under this condition occurs when the exiting angle θ_1

$$\theta_1 \quad = \quad \theta_0 \quad = \quad \theta_b \tag{5.23}$$

We use the first order of the fringe pattern why? Because the fringe pattern occurs when the transducer is ON creating this phenomena, so by triggering the device we can have ON/OFF behaviour of the first order. The zeroth order passes through the AOM without diffracting when the device is not triggered. So all alignment and positioning of the system was done with respect to this first order beam.

The first order through the AOM was used as the excitation beam which gave a handle on the ability to switch it off through triggering the AOM. In the absence of any trigger voltage the AOM will not yield any diffraction pattern thereby eliminating the excitation beam in the experiment. The 0^{th} order beam was always present and it along with its secondary sources through reflection were removed using D1 and D2 set of multiple diaphragm configurations. However it still added to ground noise of the experiment as we shall see when we discuss the results.

The excitation intensity was measured using Camera 2. Camera 2 was a basic Basler ace [acA2040-90um] with up to 90 FPS and 4MP resolution. Using a Camera allowed to check the shape of the beam by looking at its cross section and intensity profile across many pixels. The sum of all the intensities was measured to have the excitation signal. This was done by a partially reflecting mirror by Thorlabs [BP108] pellicle beamsplitter with 8 : 92 reflectance to transmission for the range 400 nm to 2400 nm, that was placed

in the optical path of the excitation beam (first order beam from the AOM).

The sample was illuminated through a homemade simple microscope using a beam splitter [Semrock Di03-R532-t1-25x36] located in a beam splitter cube [Thorlabs DFM1/M] followed by a mirror [all mirrors, Thorlabs BB1-E01] and a Nikon Apo TIRF 60XC oil immersion objective [MRD01691] with a NA of 1.49 and a working distance of 0.16 to 0.07 with coverglass thickness of 0.13 to 0.19.

The fluorescence signal was collected via the emission filter [Semrock Brightline series fluorescence filter 617/73] with a transmission wavelength range 580.5 nm to 653.5 nm, and via tube lens from Thorlabs [TTL200A] with a working focal distance of 150 mm and in the wavelength range of 400 nm to 700 nm, and compatible with the Nikon objective. The signal was collected in a Hamamatsu Orca digital CMOS camera [C13440-20CU] indicated in Figure 5.11 as Camera 1.

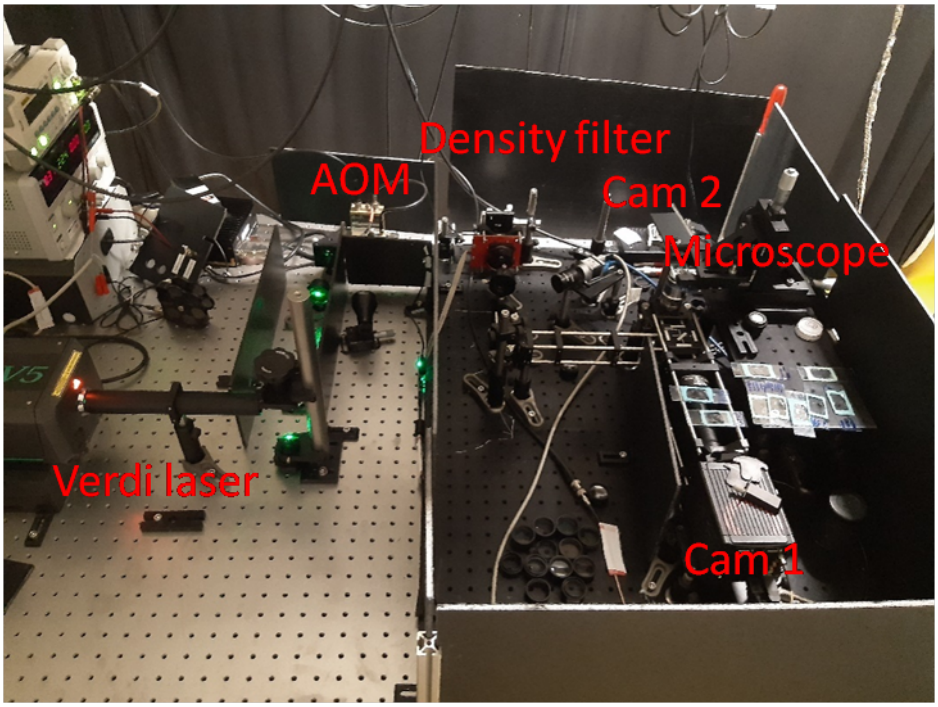

Figure 5.13: Experimental setup

The experimental results from this system is highlighted in the next Section of results. There was a lot of noise in the data and it was narrowed down to be coming from Camera 1. Since this was a low end camera, dynamic pickup of signal across pixels, enhanced the excitation non-linearly leading to increase in excitation signal which could not be corrected for due to its dynamic non-linearity. Thus, a shift was made to a photodetector to remove any such dynamic changes. The Camera 2 was used along with the photodetector, but only to check the beam shape and maximise the beam intensity upon aligning and re-aligning the beam configuration in the system as well as aligning the density filter plate.

To summarise we have all the components; the excitation beam Verdi laser, beam switching (ON/OFF) through the AOM modulator, the variable density filter along with rotation, the excitation proxy (Camera2/photodetector which will be described in the next Section), fluorescence signal measurement camera (Hamamatsu) and acquisition via Matlab which was also used to synchronise the components using function generators. The experimental setup is shown in Figure 5.13.

4.3 Adding Photodetector

We will discuss the results with Camera 1 as the excitation proxy followed by the photodetector. However, I will introduce the experimental setup here since it is just the addition of one component with minor changes.

Photodetector [LCA-S-400K-SI-FS] with Si-PIN and InGaAs-PIN photodiodes, with a wavelength range for detection from 320 nm to 1700 nm, Bandwidth from DC to 400 kHz and a maximum gain of 10^6 V/A was used. The photodetector as shown in Figure 5.11 was used as a proxy to measure the excitation intensity instead of the Basler camera. And the results are elaborated in the next Section. The photodetector works on the basis of of a reverse biased Si-PIN photodiode which provides a cascade voltage based on the number of incoming photons. The voltage is then relayed to the software interface via the buffer amplifier which isolates only the signal and not the ambient noise from the other parts of the circuits like the power source. The photodetector was controlled and synchronised with all the other components by developing an interface via Matlab from scratch.

5 Experimental Results

We will now look at the results obtained in each of the experimental setups described above. We will first start with the Basler Camera and move on to the photodetector as the excitation proxy. The sample used - had the same kind of preparation as in the case of fluorescent nanobeads. The sample for performing the experiment was made using nano fluorescent beads by ThermoFisher. The fluorescent beads had a diameter of 100 nm. The beads were diluted 10,000x times and allowed to sit on the coverslip. The beads adhered to the surface of the glass, upon evaporation of water/alcohol solvent. And they are highly diluted, allowing us to select a bead such that the bead is not having overlap with other beads. These nanobeads tend to clump together so they are sonicated prior to making the sample to separate them. The coverslip was then sealed to the slide using the dentist mould setting mixture and was used to image.

During imaging, the bead was brought to the center of the excitation beam by moving it along both X and Y axes to maximise the emitted intensity signal (done manually but using Matlab as the camera interface for reading out as well as storing the location for each alignment and change of sample). These coordinates on Camera 1 were used to bring

a fresh bead (same sample, new bead) into this location before starting the experiment. Since the first bead used to find the centroid of the beam could be bleached (even though we try to avoid this by having as low excitation as possible based on SNR) so we start with a fresh bead every time. This was done under low power excitation to avoid bleaching and the fresh bead once located at the location coordinates, the excitation was turned "OFF" using the AOM. This was possible since triggering the AOM would give a diffraction pattern which was used for the experiment. The beam from the first fringe was used, with the beam intensity maximized through optimizing the Bragg angle. And in the absence of the triggering, there would be no diffraction and thus no first order fringe beam rendering it to its "OFF" state as discussed in the previous Section.

Thus, after placing a fresh bead at the center coordinates of the illumination, and setting the AOM to OFF mode, the power of the laser was set to its maximum of 5 Watts. The laser was allowed to stabilise for a few minutes to have less fluctuations and during this period the beam path was blocked and the AOM was not triggered. After which the optical path blocker was removed (the sample could only be irradiated with noise from the 0^{th} order ambient at this point) and the main trigger for the experiment was given.

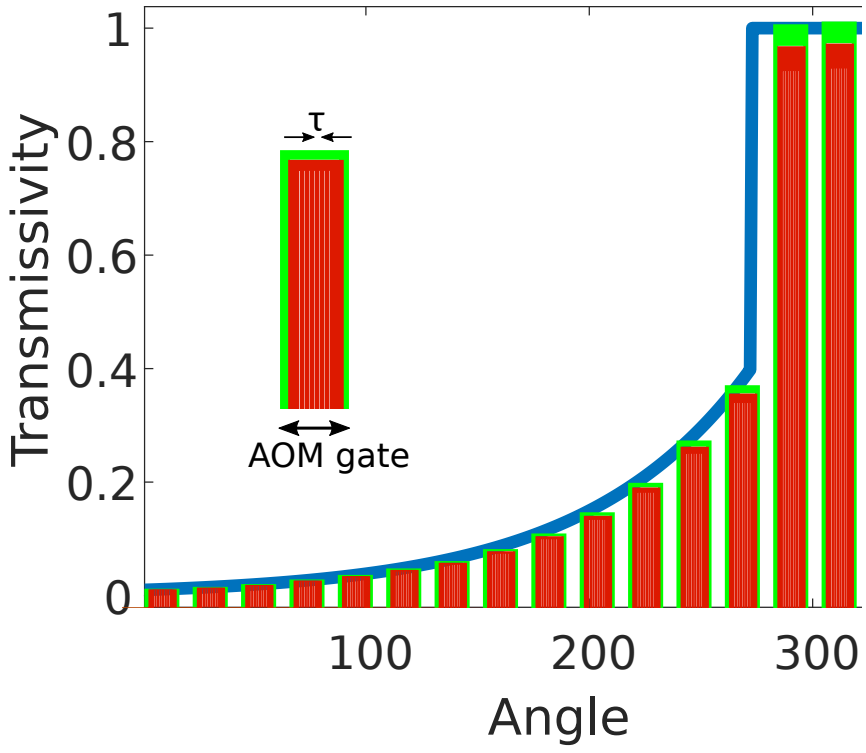

Figure 5.14: Transmissivity of the excitation beam as a function of the angle of the variable density filter along with the schematic representation of the amplitude of the pulses modulated using the variable density filter by rotation and gating controlled thorough the AOM indicated in Green. And the fluorescence lifetime τ-cycles of the fluorescent nanobead indicated in Orange (in the order of ns).

In order to quantify the ground noise levels due to the 0^{th} order and ambient reflections, the Hamamatsu camera was triggered twice. Once firstly during the presence of the first order beam and secondly in its absence. This gave a value for the ground noise fluorescence signal and this was subtracted from the image with the pulse, for the fit. The ground noise in the case of using Camera 1 for quantifying excitation was also subtracted in the same manner by having two frames one with the first order illumination and one without. In Figure 5.14 we have a schematic representation of the variation of the *Optical Density* (OD) as a function of the angle of the rotating variable density filter in the setup with the amplitude of the pulses decided by the density filter by the equation 5.24. Along with the gating of the pulses modulated using AOM indicated in Green. And the fluorescence lifetime τ - cycles of the fluorescent probe indicated in Orange. Many (1000) lifetime cycles fit in one pulse gate (of 1 μs) of the laser. We have not indicated the camera trigger here. The camera is triggered twice for each of the values of the laser power during excitation with a time period of 10 ms. The first frame contains the laser excitation and the second does not (to quantify the background/ground noise in the absence of the laser beam as discussed above). The optical density filters have the following relation with the transmitted light through the filter T:

$$OD \quad = \quad \log \frac{1}{T} \tag{5.24}$$

And in the case of the photodetector, we had a baseline ground noise that was subtracted. Since the detector area was much smaller than the beam, the noise remained more constant when compared to using the camera. The photodetector also has digitisation noise based on the range of signal detected, we will discuss more in the next section.

5.1 Camera as excitation proxy

Firstly we will look at the results with the setup with just Camera 2 used for acquiring excitation data. In this experiment, the time gate for the excitation is 20 micro seconds. The Basler camera is used for the excitation proxy and the Hamamatsu camera is used for the fluorescence signal. We will now proceed to give more details for each of the cameras.

For the Basler setup, a suitable density filter had to be used [1.3+0.6+1+0.3 = 3.2 absorptive density filter especially in the front and back belonging to the NE series from Thorlabs] to decrease the range of excitation, while doing so the range also has to be tuned to ensure that the low power excitation values are above the noise level. So there is a trade off between the range and the noise level for the entirety of the experiment involving increasing and decreasing the power (with the use of the variable density filter for the excitation) which has to be fixed prior to the experiment. This does not change once set, unless alignment changes occurred.

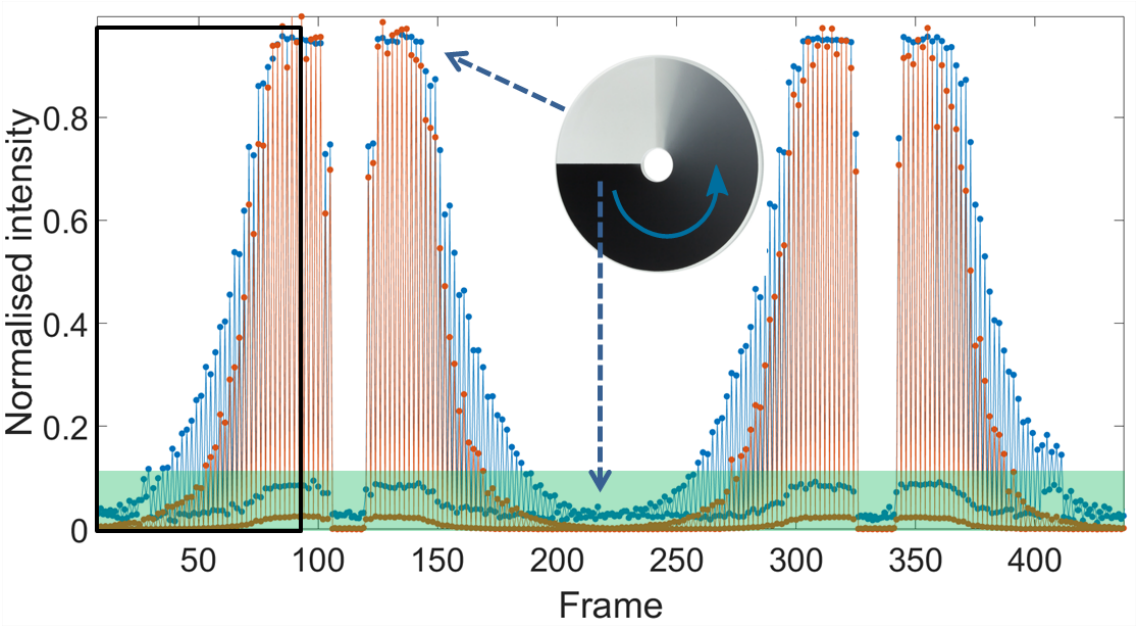

Figure 5.15: Blue line and dots indicate the excitation proxy from Camera 1 and the orange dots and line indicate the fluorescence signal from Camera 2. The frames are alternating as shown with one frame with the pulse followed by a frame without. The ground noise is also traced as shown in the frames without the pulse indicated in the Green shaded region. The Black inset is given in Figure **??** zoomed in version. The variable density filter is also shown in the figure with maximum OD and minimum indicated in the corresponding locations on the plot as well.

Both the cameras (Camera 1, Basler and Camera 2 for excitation signal, Hamamatsu for fluorescence signal) was set to an exposure time of 5 milliseconds. Both the cameras were synchronised along with the pulse, which was started with a delay of 23 milliseconds (first frame does not have the pulse). The 3 milliseconds was to ensure that the cameras were ON and ready to acquire with overlap in exposure time. The first frame did not have the pulse and accounted for 20 milliseconds of the time (10 milliseconds ON and 10 milliseconds OFF). The second frame contained the pulse as depicted in Figure **??** which is the zoomed in version of Figure 5.15. In Figures 5.15, **??** and 5.16 we have the raw data tabulated for both the cameras, to illustrate how the processing is done. In Figure 5.15 we have a case of very stable output with a small rate of bleaching, we show both the cases to illustrate the individuality of the nanobeads which we don't have control over.

The nanobeads are highly specific; in some cases we observe bleaching and in some cases there is no bleaching across multiple cycles as indicated in Figure 5.15. Wherein we see that the rate of bleaching is slower and occurs across multiple cycles (16 cycles) with a pulse duration of not just 20 micro seconds but 200 microseconds which is ten times larger. This would be an ideal fluorescent nanobead and statistically we observe a range of different bleaching rates for different beads. Generally for many nanobeads, within a few cycles we will start to see bleaching effects. This best case scenario and another bead demonstrating

bleaching as shown in 5.16 was plotted just to illustrate the variability in the bleaching time scales depending on the environment. There is also variability in excitation due to the laser especially at lower excitation powers, and the laser has fluctuations in time as well but these are registered in the corresponding fluorescence signal emitted from the probe.

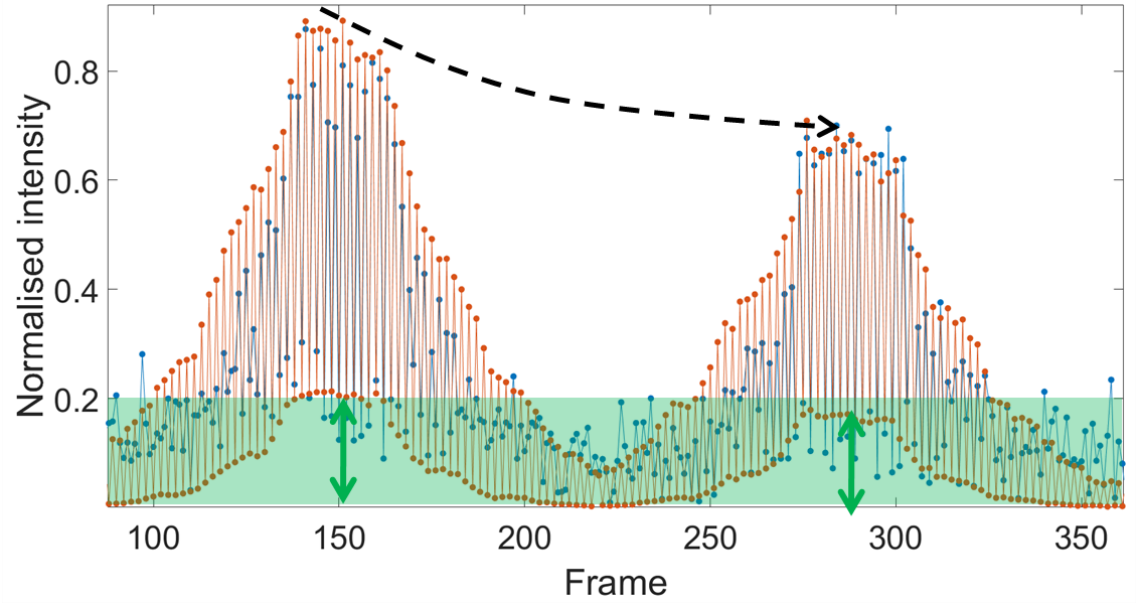

Figure 5.16: Blue line and dots indicate the excitation proxy from Camera 1 and the orange dots and line indicate the fluorescence signal from Camera 2. The frames are alternating as shown with one frame with the pulse followed by a frame without. The ground noise is also traced as shown in the frames without the pulse. The starting point of the variable density filter gives the cyclical starting point.

For the case wherein we see the bleaching effect, as shown in Figure 5.16, the fluorescence signal (Orange) and excitation signal (Blue) are recorded for both presence and absence of the pulse (which is the noise, indicated in the Green shaded region from the zeroth order of the beam from the AOM). This gives us the ground state noise from the zeroth order beam as well as other sources of noise from detection, excitation proxy and illumination, which is used to subtract from the total signal. The signal for both excitation and fluorescence is the sum of intensities across pixels on both cameras.

The green region indicates the noise level for the excitation and fluorescence. We see that the noise levels remain constant across cycles but change with changing excitation intensity. The higher the intensity of the laser beam, more the noise. This is clearly illustrated across all these plots, observed in 5.15 as well. We will discuss more about this in the next section as well.

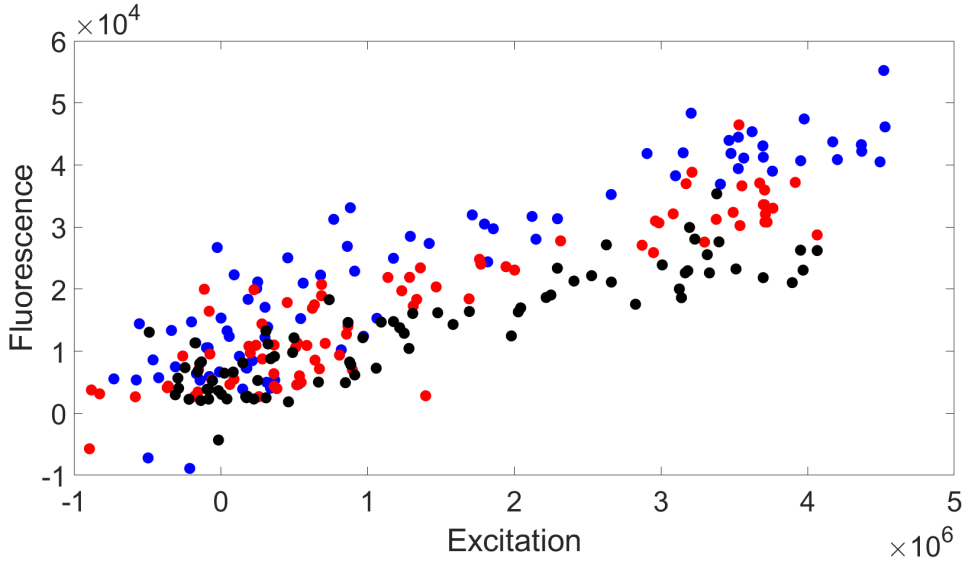

Figure 5.17: Blue indicates set one (each set is two cycles of increasing and decreasing excitation power cyclically by rotating the the variable density filter), Red indicates set 2 and Black indicates set 3. This figure illustrates progressive less emission.

The base level ground noise for each frame was subtracted for each individual frame, for both excitation as well as fluorescence emission signals. Since the excitation proxy was highly dynamic as well as quite erratic at lower excitation powers, the data for the excitation proxy at times went to negative values as indicated in the filtered plots for excitation and fluorescence superposed as seen in Figure 5.17.

Across multiple sets of cycles, we demonstrate the trend for one experiment, with respect to the saturation curve. In Figure 5.17, we have plotted six cycles separately by dividing them into three sets (Increasing and decreasing intensity that is two cycles in one set) to look at the dynamics. Blue dots indicate the first set, Red dots indicate the second set and Black dots indicate the third set. We observed a progressive decline in the emission as illustrative of gradual bleaching.

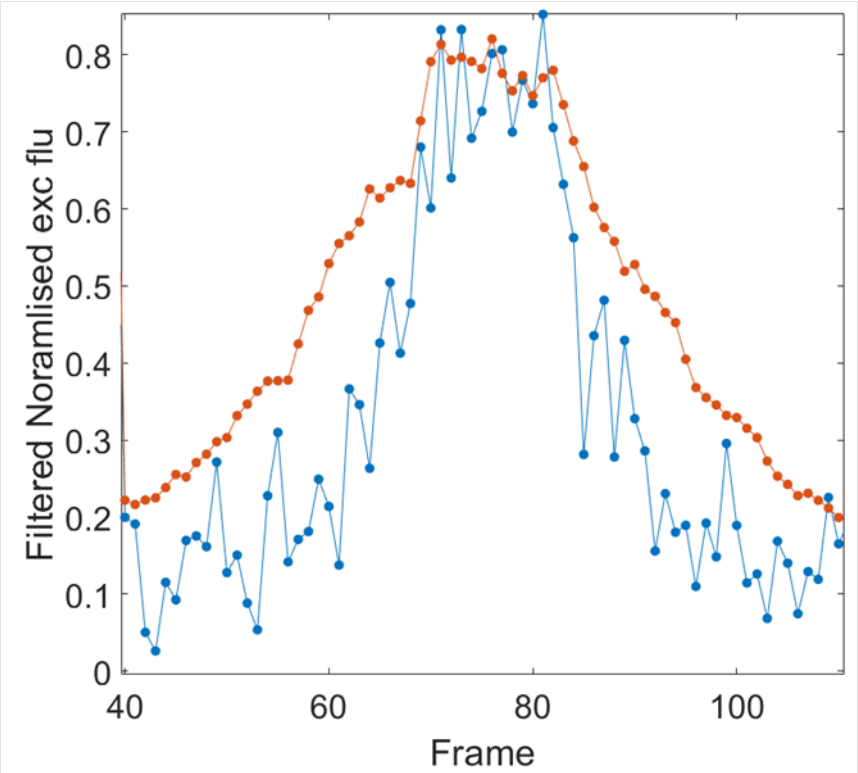

Figure 5.18: Normalised plots for filtered fluorescence and excitation signals. Blue line and dots indicate the excitation proxy from Camera 1 and the orange dots and line indicate the fluorescence signal from Camera 2.

In Figure 5.18 we have the first set of increasing and decreasing excitation intensity of illumination followed by the corresponding fluorescence emission plotted together by normalising each of them individually. For the normalization, we take the two data sets for fluorescence emission and excitation respectively and individually normalize them to the range between 0 to 1 to compare their respective trends as shown in 5.18. We see the trend preserved however we see a lot of noise in the excitation signal especially at lower illumination intensities.

As can be seen from Figure 5.18, the fluorescence and excitation are in tandem as expected, however there is a lot of noise especially with regard to the excitation. This can be further illustrated by plotting the fluorescence vs excitation plot which we ultimately need to fit for the time constants.

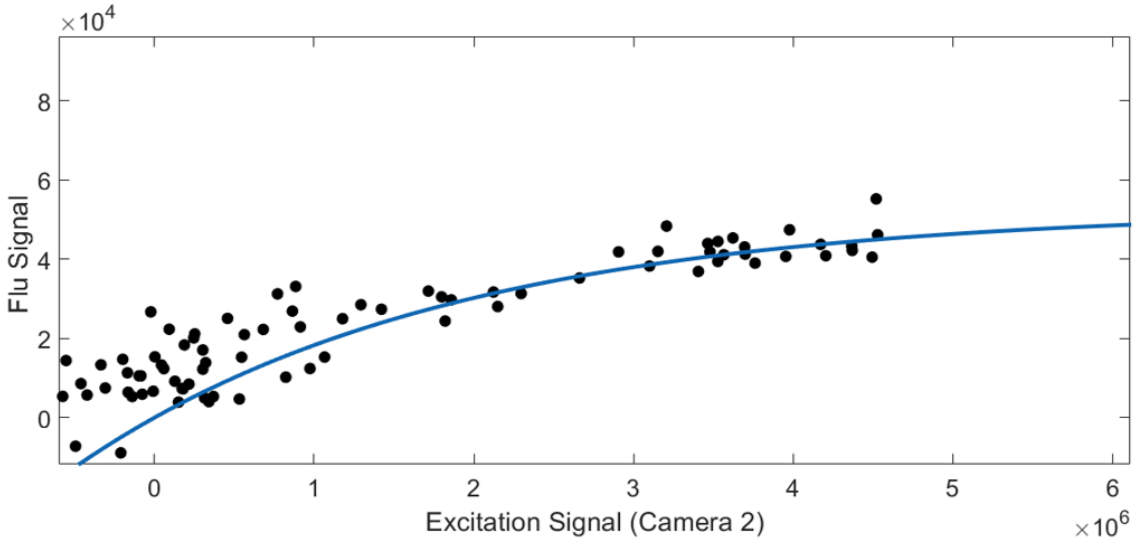

Figure 5.19: Data from set 1 was fit in an approximate functional form. Fluorescence re-scaled to simulated values, elaborated in the next few figures.
The axes represent the number of photons emitted by the fluorescent probe in the Y-axis and the excitation proxy by capturing a part of the laser beam photon number on Camera 2.

General model:
f(x) = a*(1-exp(-b*x))
Coefficients (with 95% confidence bounds):
a = 5.254e+04 (3.86e+04, 6.647e+04)
b = 4.282e-07 (2.068e-07, 6.495e-07)

Goodness of fit:
SSE: 8.769e+09
R-square: 0.5348
Adjusted R-square: 0.529
RMSE: 1.047e+04

Figure 5.20: Fit Parameters

For the fitting, we can consider just the first set which is non-bleached to fit the saturation curve (Figure 5.19) and also look at it in comparison with the simulations (Figure 5.20). In Figure 5.19 we have the set 1 data points. The points appear to be saturating at high powers but we need less variability to distinguish between the linear and saturating regime.

In Figure 5.20 the first set of points are fit with the functional form given by equation 5.21. The fit is as given above.

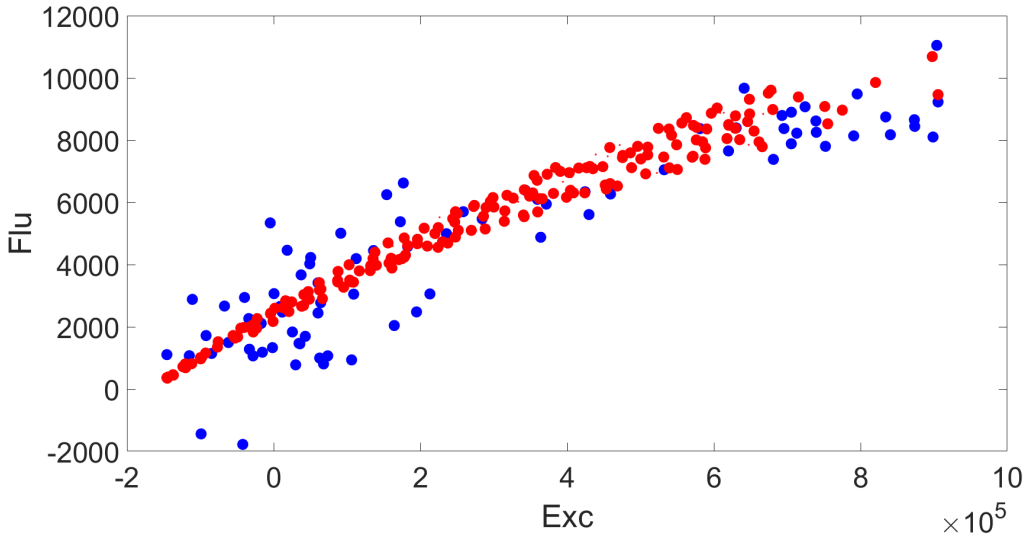

Figure 5.21: Both the experimental data (Blue) and simulated data (Red) plotted together. The simulated data and experimental data re-scaled to match the range.

In Figure 5.21, the excitation and corresponding fluorescence was plotted together for the experiment marked in Blue, and simulation marked in Red. The power and excitation were re-scaled from the simulation to fit the range of the experimental data. The fluorescence signal was re-scaled from the experiment to match the simulation as well. Since we don't have access to the true range and can only operate by a pre-factor that is proportional to the datasets.

As seen in the previous section the noise from the excitation was very large (more than 20%). These fluctuations were due to the non linear dynamic effect of pixel read out from the camera as well as its non specificity at lower powers. The noise is especially large in lower intensity ranges owing to lower SNR. The device needed to do better, much better if we wanted to have lifetime differences between two species of molecules.

5.2 Photodetector as excitation proxy

In this Section we look at the augmentation of the setup using the photodetector mentioned in the Experimental Setup Section. We look at the results with a better excitation proxy, using a photodetector. And then we discuss the results obtained in this setup.

5.3 Excitation Signal

Thus, to have better excitation data, we switch to the photodetector [LCA-S-400K-SI-FS]. The idea for using this was to have a voltage read out from the photodetector for the excitation and see if the noise that we saw in the previous setup gets reduced. The choice of the photodetector was such that it was fast enough to pick up the pulse since the pulse was in the order of microseconds. Thus, a rising function response in the nanoscale with

Rise/fall time [10% − 90%] 900 ns tested at 920 nm and with maximum range for input photon flux, and 5 ns experimentally observed at 532 nm, and with the range for input illumination from 0V- 200V. These characterizations were done to ensure that the pulse could be clearly picked up during the entirety of the experiment. The pulse as well as its response function was characterised as elaborated in the following Section.

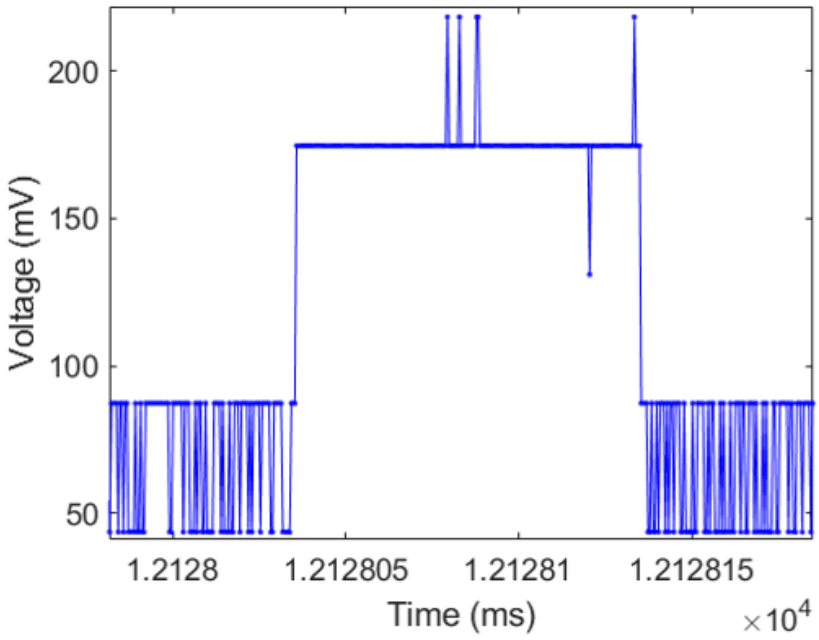

Figure 5.22: Blue line is the pulse as detected by the photodetector for 100 microseconds. The top of the peak as well as ground noise is the digitization error for larger range availability for the signal.

The other important facet of the detector that was characterised was the digitization property and its corresponding range. All detectors adjust their digitization step (which is a measurement rounded to a a certain value in steps; essentially just a step function whose step size is determined as the digitization error) based on the range of measurement. For example a range of 0V to 2V would have a larger digitization step (shown in Figure 5.22), contributing to higher error and uncertainty in the measurements when compared to say operating within the range of 0V to 200 mV. But on the other hand limiting the range to a small value will not give readout values for high power excitations. This was optimized using a set of density filters that gave a good range on the photodetector without adding noise at low excitation power of the laser beam. The density filters contribute to the logarithmic function of the laser beam power as shown in 5.14. Thus, a combination of density filters were used to reduce the range as much as possible. And this had to be further optimised due to the fact that adding high density filters would cut down a lot of light leading to error at low power excitation values as observed while using the camera. The trade off between these two extremes which we needed to span, was made with a combination of precise density filters.

Density filters work by cutting the transmitted light logarithmically as in equation 5.24. We need density filters because, even in the case of low excitation beam proportion (as we had with the previous setup where we had less than 2% of the incident beam redirected to the excitation Camera 1) we still saw that we needed a pretty high OD of 3.2 to not have saturation in the ROI. Even here, we use a photodetector that receives a very small fraction of the incident beam but still we need an OD to not damage or saturate our photodetector. And by playing with the different combinations of the density filters we can pick a suitable combination that falls in the restricted range of the photodetector as well as have significant SNR at low intensities of the excitation beam so that we can avoid noise.

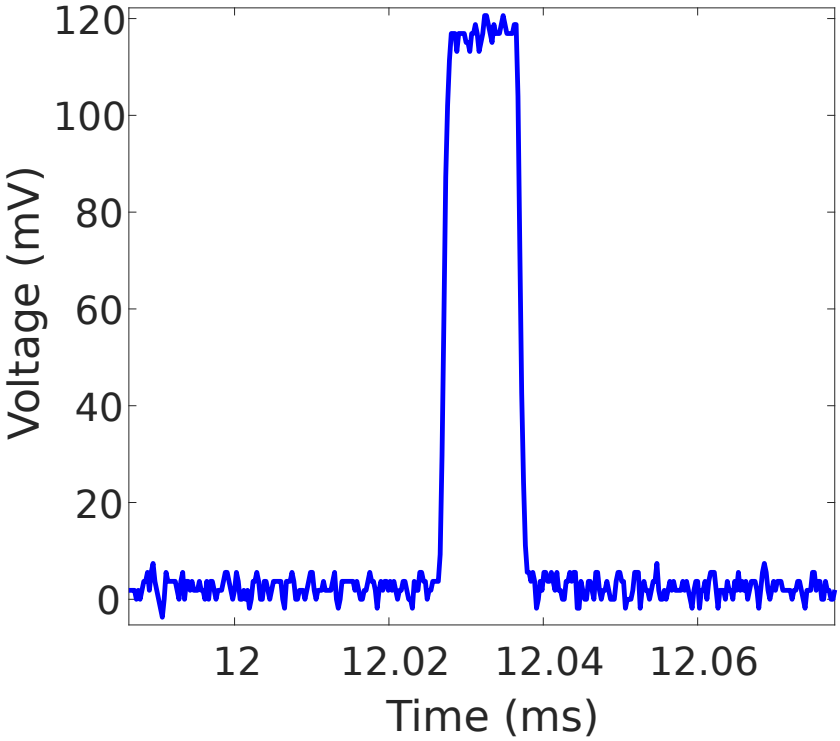

Figure 5.23: Blue line is the pulse as detected by the photodetector for 10 microseconds of laser beam exposure with a density filter of 1.5 and laser power of 5 W attenuated by the rotating density filter to around 1.75 W. The top of the peak is the digitization error which has been optimised to be low.

In Figure 5.23, individual peak is shown. Multiple such pulses for increasing amplitude are used as the proxy for excitation power/intensity. The average across each pulse is computed by taking an average across all points in the pulse. The number of points in the pulse was regulated as well, by programming the detector completely in a bottom-up approach. There are 200 points in the peak of the pulse in Figure 5.23 giving a resolution of 50 ns. The number of points is tuned based on the trade off between the total time for acquisition for the detector vs the precision in the peak.

In Figure 5.24 multiple such pulses have been shown in Blue (Here the OD is 1.5 for the photodetector), along with their corresponding averages for each peak in Orange. The average thus computed was used to plot against the fluorescence signal. The fluorescence signal was also optimised so as to have the minimum possible noise levels by fine tuning the alignment, bead position as well as the Bragg angle from the AOM as indicated in Figure 5.25. This was done methodically by firstly tuning the Bragg angle and the beam to have lowest noise and highest signal, secondly the position of the bead by fine tuning the X and Y coordinates of the location on the camera for maximum signal as the centroid of the beam and finally the positioning as well as the optimised combination of density filters for the detector which we will discuss more in the next section.

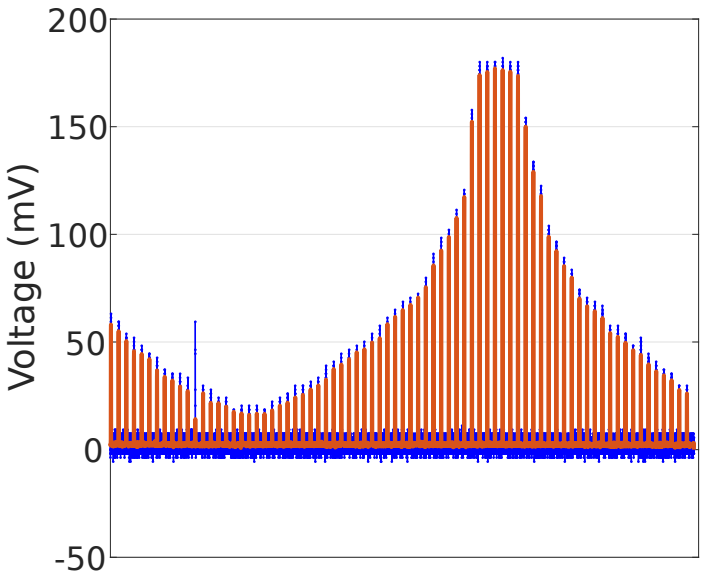

Figure 5.24: Blue line indicates the raw data from the detector pulses and the Orange line indicates the average across every 40 points from the first pulse.

In Figure 5.24 we have the data from the photodetector alone, and we see the continuity of the same trend as the fluorescence emission signal. We can also qualitatively see that these plots look much more in tandem as well as precise when compared to the previous system. The idea of taking an average across the points in the peak versus taking the maximum or the summation of the points of each peak is illustrated in Figure 5.24 which is why this data set was chosen. The maximum is a single point, that could have error either through digitization or laser jitter whereas the average accounts for all the points, enabling a more robust measurement of the excitation proxy value. The Verdi laser at high power setting does jitter (not as much as the low power setting as discussed before) but nevertheless there are some instances of sudden variability in the laser emission at a very small time scale. This is given by one of the points in the peak that appears different from the trend. However you can see that when we take the average, we weight against

such occurrences and thereby the average value is considered. You can also see that other points in this peak our lower than expected. This weighting was optimised across all experiments and fixed for all experiments (automated code in Matlab).

Now that we have characterised the photodetector and illustrated it with an example (which we will also use to fit in the final Section), we move onto explaining the fluorescence signal.

5.4 Fluorescence Signal

The fluorescence signal has been discussed briefly in the previous setup as well as previous section with regard to optimisation. In this Section we build on that to better illustrate using experimental data what we achieve by means of these measurements.

Firstly the fluorescence signal from the bead is taken as the sum across the ROI which is an area around the bead (automatically selected using centroid detection and fixed for all the frames during analysis). This ROI is large and encompasses the bead. The nanobeads are fixed onto a coverslip using the process described in the beginning of the experimental section. And they are highly diluted, allowing us to select a bead such that the bead is not having overlap with other beads. These nanobeads tend to clump together so they are sonicated prior to making the sample to separate them.

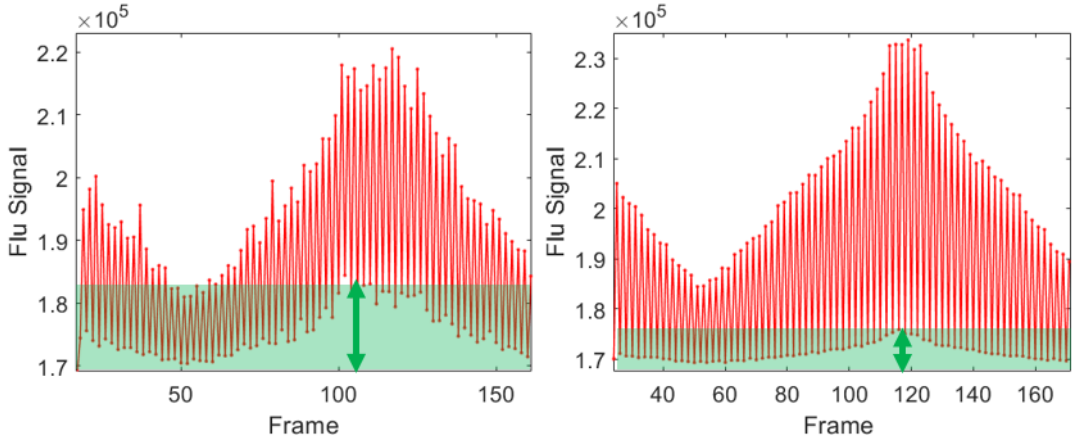

Figure 5.25: Reducing noise in fluorescence signal through alignment. On the left we have a case with higher noise levels, occurring due to presence of the zeroth order excitation beam and on the right we have an improvement through better alignment, using more diaphragms and optimising through adjusting around the Bragg angle of the AOM as well.

The sum of all the photons over all pixels of the corresponding bead is taken to be the fluorescence signal value. Now, using this to plot fluorescence signal vs excitation will yield the saturation plot which we will then use to fit. This has been demonstrated in Figure 5.25. In 5.25, in the left plot we have the noise to be high as illustrated by the shaded Green region. This was reduced by optimising the Bragg angle and fine tuning the diaphragms (all of them), isolating the beam path to remove ambient noise and so on. This was done every time before commencing with the experiment (even in the case of the previous setup as well). Thus, we can see a marked difference between the two. It was a learning curve to learn how to best optimise the excitation beam, both for the photodetector as well as Camera 1.

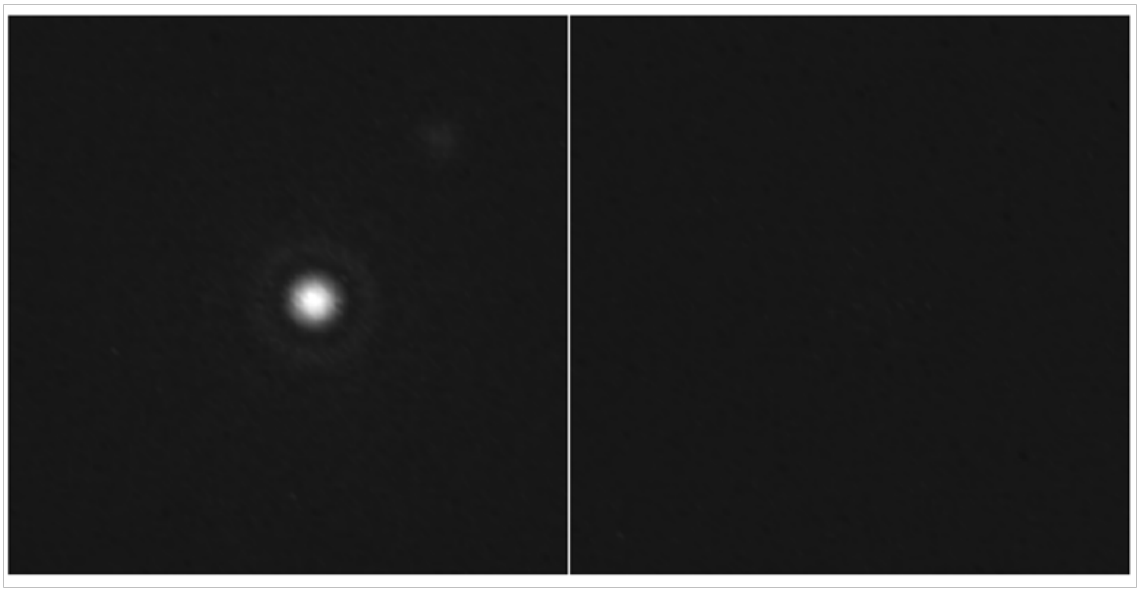

Figure 5.26: Image on the left is with the pulse or the ON frame and image on the right is the frame with no pulse or OFF frame which has the noise (here we don't see it since it is in the absolute scale, and the signal is very high compared to the noise).

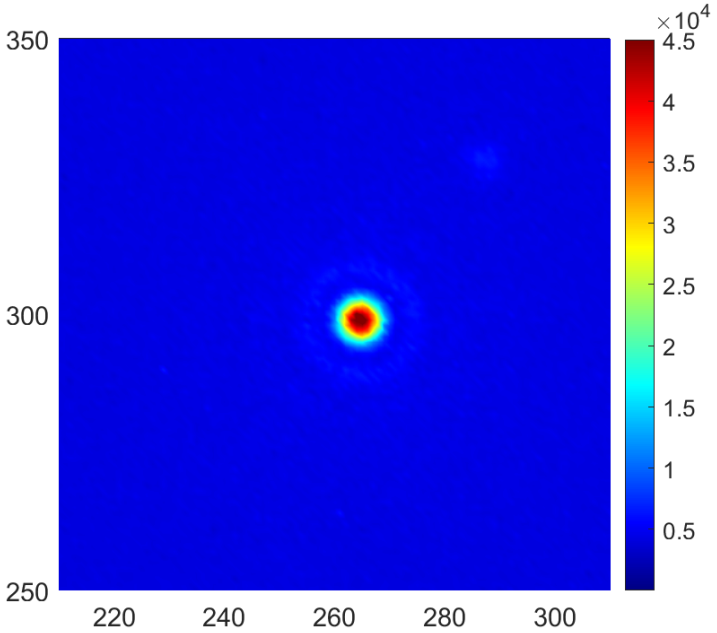

Figure 5.27: Diffraction limited spot of a 100 nm fluorescent nanobead excited at 532 nm. The X-axis and Y-axis as the pixel coordinates and the intensity along the Z-axis indicated as the colorbar.

In Figure 5.26 we have an example of a frame with the pulse on the left and without the pulse on the right, since we have the absolute scale here, we don't see the noise.

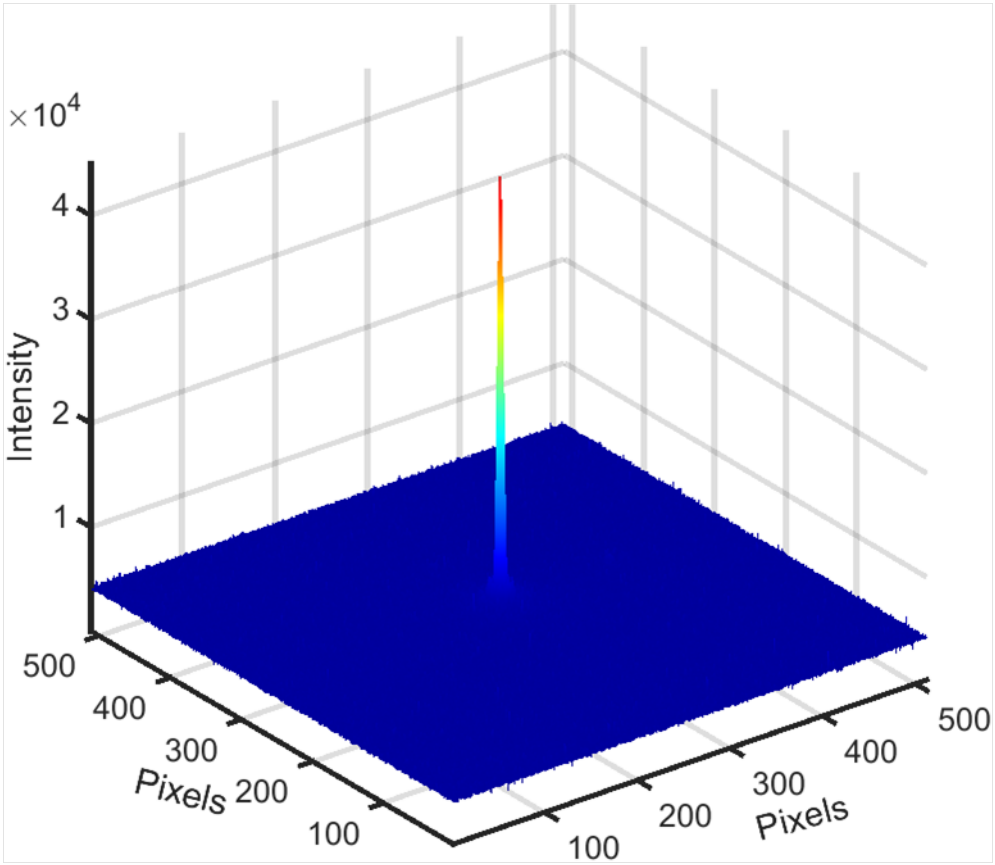

Figure 5.28: Image of the bead illuminated with the imaging area along X-axis and Y-axis as the pixel coordinates and the emission intensity along the Z-axis.

The fluorescent emission intensity of a spherical fluorescent nanobead which is illuminated with the excited beam is plotted with imaging coordinates as well as its emission intensity along the Z-axis in Figure 5.28. The same plot, with a zoomed in view, is projected onto a 2D plane in Figure 5.27, the X and Y axes are the pixels of Camera 1 (512x512). Here we can see that the beam is very bright in the center and the intensity falls radially as is expected in a diffraction limited image. This also illustrates that the illumination is symmetric and centered.

The shape of the bead is also a way to see if our image plane, illumination and so on are good enough. Camera 2 was not removed but in turn used as well, to check this. But since the beam falling on Camera 2 was right after the variable density filter, it was not needed as much since the beam at this point was not going to be perturbed for every experiment.

5.5 Saturation Curve

Now that we looked at both the aspects of the experiment, excitation and fluoresce signal. We proceed to examine them together and look at the saturation curve in this section. We also fit the curve to obtain the fit parameters. We also examine the constraint for saturation by examining the convergence of the fit parameters. Then we proceed to look at some statistics for many acquisitions. We compare two types of beads for their fit parameters and distinguish them based on their fit parameters.

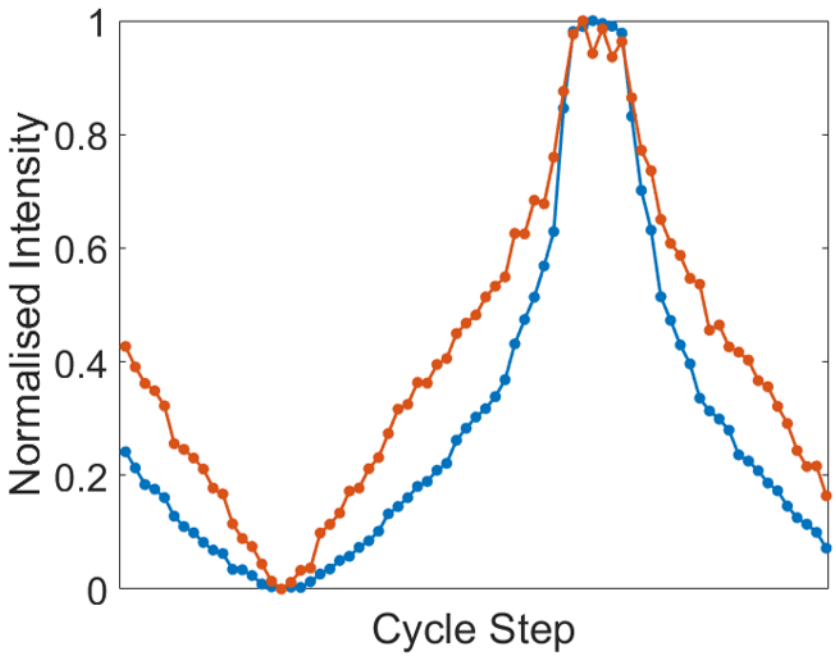

Figure 5.29: Normalised curve for excitation and fluorescence. Blue indicates the excitation and Orange indicates the corresponding fluorescence signal. Each point is for one intensity of excitation and corresponding fluorescence emission.

In Figure 5.29, the average value for each pulse is plotted in Blue and the Orange is the corresponding fluorescence emission signal. To illustrate excitation and its corresponding fluorescence emission from the bead sample. Both excitation and fluorescence are normalised. The fluorescence signal is computed by filtering the noise from the frames without the pulse as mentioned in the previous section. Since we have two images acquired for each power/intensity value of the laser (data point), one image with the laser pulse-corresponding fluorescence signal and the other without (when the AOM is in its "OFF" state). The image without the laser pulse gives us the fluorescence emission due to scattered illumination which was subtracted as the noise for each data point individually. The final fluorescence signal was used to plot the saturation dynamics.

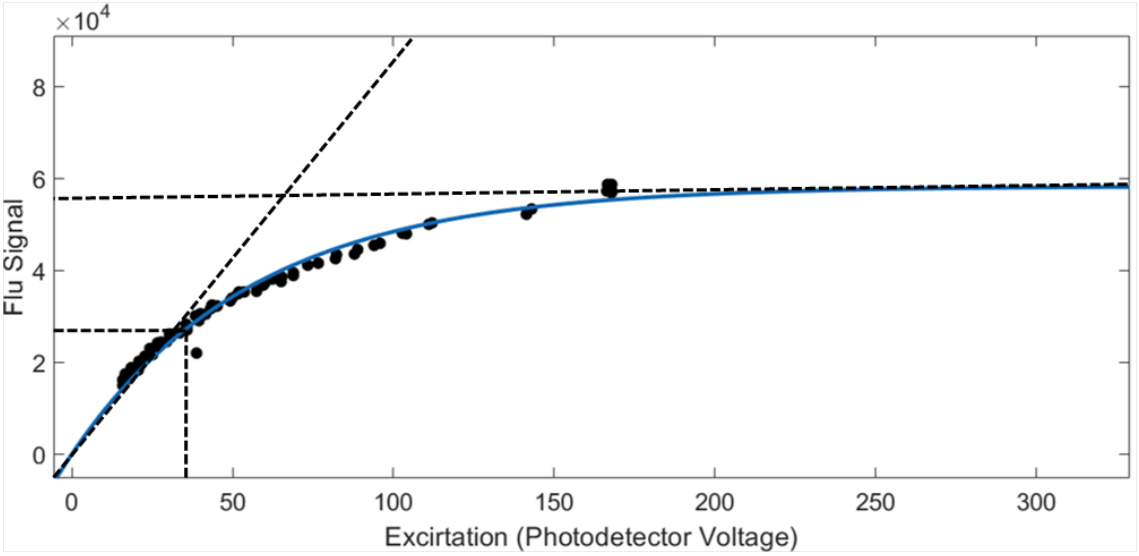

Figure 5.30: The data points are shown in Black and the fit is given by the Blue curve. X-axis is in mV and Y-axis is the fluorescence photons.

In Figure 5.30 we have plotted the saturation curve for the set discussed above and we see that when we fit it with $y = a(1 - e^{bx})$, we get the following curve indicated with a Blue line in Figure 5.30 for the points indicated by Black dots from Figure 5.29. The fit parameter b is of importance to us as it relates to the time constant (from the first Section) and here it is 0.018 ± 0.001 with an R^2 value of 0.98 indicating a very high goodness of fit (CI of more than 2 sigma or 95%). In the next section we take two species of fluorescent nanobeads and examine the robustness of fit as well as distinction between the two using this b fit parameter.

6 Fitting Parameters and Robustness for two Species

We are now ready to look at the robustness of the fitting we carried out in the previous Section. We have seen how important it is for us to be close to saturation both theoretically and experimentally. We have gone beyond the saturation intensity to almost twice its value, to a region of constant fluorescence with excitation. And it was necessary to do so since we needed to have a good and precise fit with high confidence. Only this would enable us to distinguish between two species of molecules with different fluorescent lifetimes. Now we see the degree of convergence of the fit parameters with respect to the number of points taken from the origin. This would help us decide in terms of power whether we need to go to the full maximum.

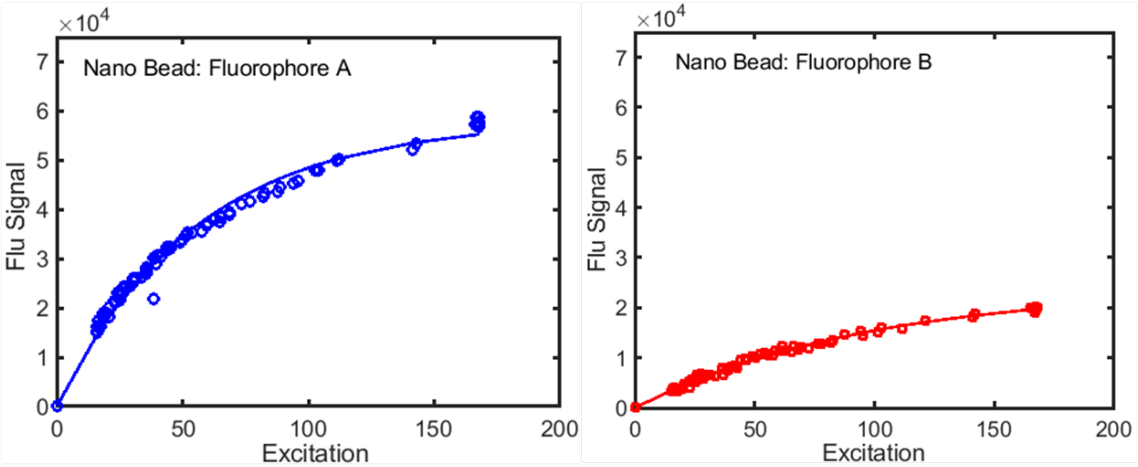

Figure 5.31: Taking two species bead A on the left and bead B on the right were plotted with fluorescence signal vs excitation as done in the case for Figure 5.30.

In Figure 5.31 we have the data and fits for one batch of experiment for each of the species. And both are plotted together in Figure 5.32. Although this is not exactly accurate since both of them are not in the same sample, and were sequentially imaged. So it isn't actually correct to plot them together, however it gives a visual cue to understand how the rate of saturation qualitatively differs for both.

Experimental procedure for characterizing fluorophore has been explained in the previous sections. Here we present a set of experiments to distinguish fluorophores in terms of their response for microscopy application. We have used nanobeads of two fluorophores (A and B) supplied by ThermoFisher [F8800] as bead A and ATTO 565 beads denoted as bead B, in this set of experiments. Their absorption peaks are at 540 nm, and 565 nm, respectively. Similarly, their emission peaks are at 560 nm, and 590 nm, respectively. For each fluorophore characterization, a single bead is isolated in the setup and subjected to increasing intensity of excitation up to 170 (excitation is measured through a proxy which is the photodetector, thus the units are in mV) and then decreased. Corresponding fluorescence intensities are recorded as a function of excitation intensity. Results for two

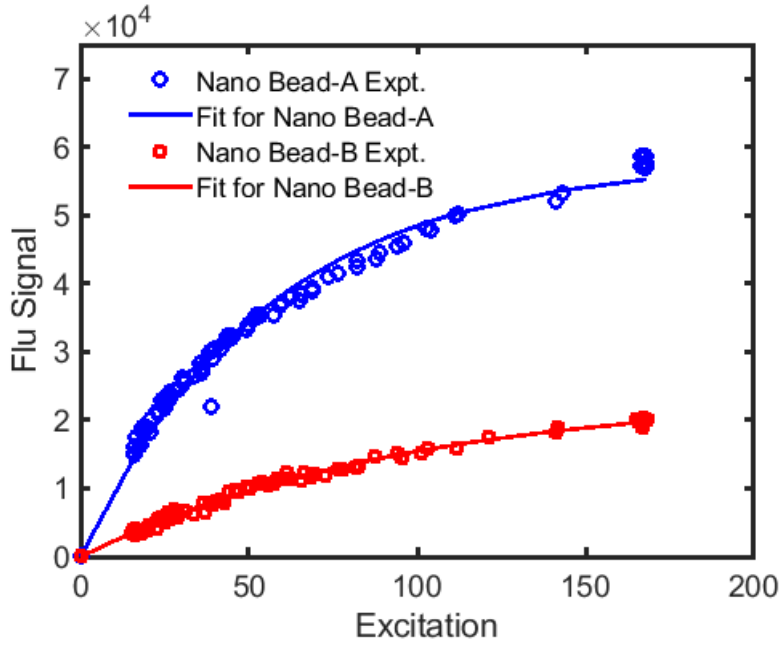

Figure 5.32: Two species plotted together with the excitation proxy along the X-axis in mV and the photon number measured through Camera 1 as the fluorescence signal. The axes being the same as in Figure 5.30. The plot indicates the different trends of saturation for each of the species.

beads are show in Figure 5.32. It is clearly evident that, each bead has different fluorescent intensity for a given excitation intensity (multiple lines in each figure will be explained shortly). Observed saturation intensity for bead A is 5.7x10^4 and for bead B it is 2.4x10^4.

Other, important factor to be kept in mind while designing fluorescence microscopy is problems arising due to photo bleaching. To mitigate photo-bleaching problems, it is desirable to keep the excitation illumination as low as possible. In the Figure 5.32, we plot two types of beads fluorophore emitters data in a single graph. Even when the excitation intensity is below 50 mV, bead A is already having a much higher fluorescence intensity compared to bead B and this depends on the number of fluorophores encapsulated and fluorescing in the bead. Thus, the saturation fluorescence intensity would not be of much consequence when compared to the fit parameter b.

We will discuss more about this below. It is also important to note that we need to trace this fit parameter and its convergence in order to utilise it to probe samples with cut-off excitation. The convergence of this fit parameter will yield to us the minimum excitation range required in order to harness the fit parameter with a strong confidence level. For which we consider here 95% or 2σ estimation.

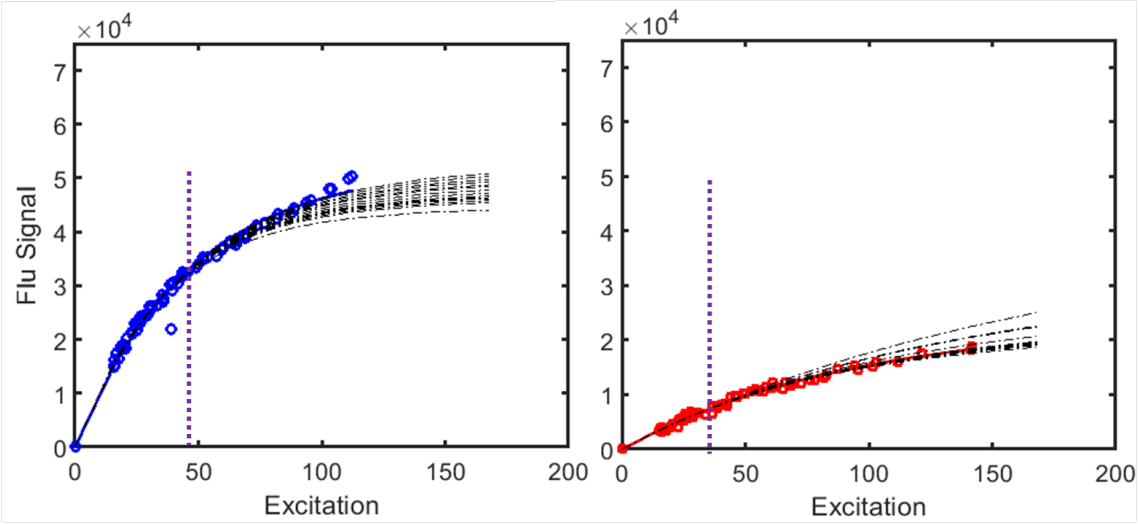

Figure 5.33: The two species bead A on the left and bead B on the right, were plotted with fluorescence signal vs excitation as done in the case for Figure 5.30. Multiple fits were carried out with varying number of points from the origin considered to check for robustness in the calculation of the fit-parameter. The data points are indicated in Red and the fits in Blue and the fits in dotted Black lines. The saturation excitation is also marked in Purple. We see that we need not go to very high laser beam powers to saturate our sample to obtain a robust fit parameter.

To quantify minimum characterizing excitation intensity range, in Figure 5.33 we progressively considered smaller range of the data (from zero excitation to different levels of excitation intensities) and proceed with the curve fitting. Dots are experimental data points, and dotted lines are curve fits with different ranges of excitation intensity data from the experiment. We have 14 such iterations each progressively with increasing number of points. Since the last few points (4 points) are the same intensity. Thus, we have 14 such fits and then we tabulate the fit parameter b for each.

We consider from the above plot various number of data points starting from the origin to evaluate the necessary level of saturation measurement. Since exposing the sample to high laser powers is not ideal, we look at different sets of data up to different points of excitation power to look at the lowest laser power at which the fit parameter converges. This will indicate the laser power at which we can obtain a robust fit parameter b without reaching high laser power excitation values which will reduce the possibility of phototoxicity. In 5.34 the fit parameter is plotted for each such set, as a function of the corresponding maximum excitation power. That is, for example say we take 40 points from the origin that would include points up to a certain maximum excitation say 50 mV which is the value represented along the X-axis. Each point close to the non-linear regime in the saturation dynamics plot (region of constant fluorescence) gives information on the robustness, which is why we take each point in the non-linear regime as one of the sets for the fit (14 such sets).

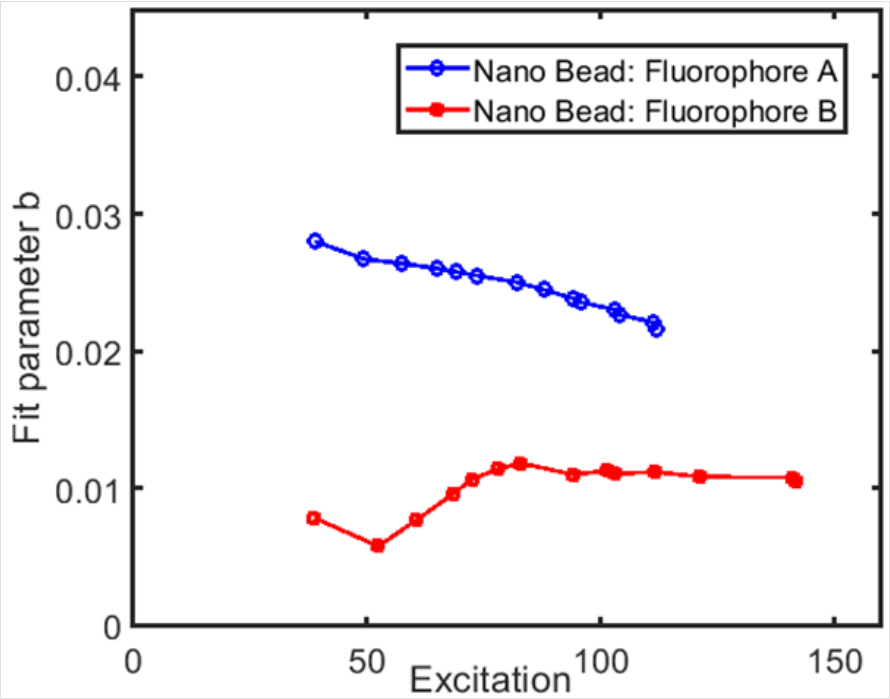

Figure 5.34: The fit parameters for varying the number of points for each species is plotted. The threshold for constant value parameter for each case is evident. The Blue curve is for type A and the Red curve is for type B.

In Figure 5.34, we plot the exponent fit parameter b, as a function of of excitation for both bead A and bead B. For bead B, around an excitation intensity corresponding to 100 mV is sufficient to estimate the characteristic feature of fluorophore, while for bead A we need to go up to 125 mV. These are the values of excitation laser power beam for which we see a convergence of the fit parameter b. Both these excitation values are much lower than the excitation intensity required for saturation. The values here are indicated in mV since we have the proxy for excitation and not the actual excitation photon number measured through the photodetector. Thus, we use excitation proxy in mV through the detector for the excitation power, intensity and photon count interchangeably as terms. For microscopy, in order to distinguish fluorophores, excitation intensity corresponding to around 50 mV is more than sufficient, to identify and label the two beads distinctly. This is very important if we want to move to a biological sample and prevent phototoxicity. We see that for very low values of excitation power, the fit parameter is different for the two species, but has not converged. This is due to the data set being small as well as lying primarily close to the origin and the linear regime where we have the excitation and the corresponding fluorescence signal increasing proportionally. For our fit parameters to be robust we need to have more data points closer to the non-linear regime.

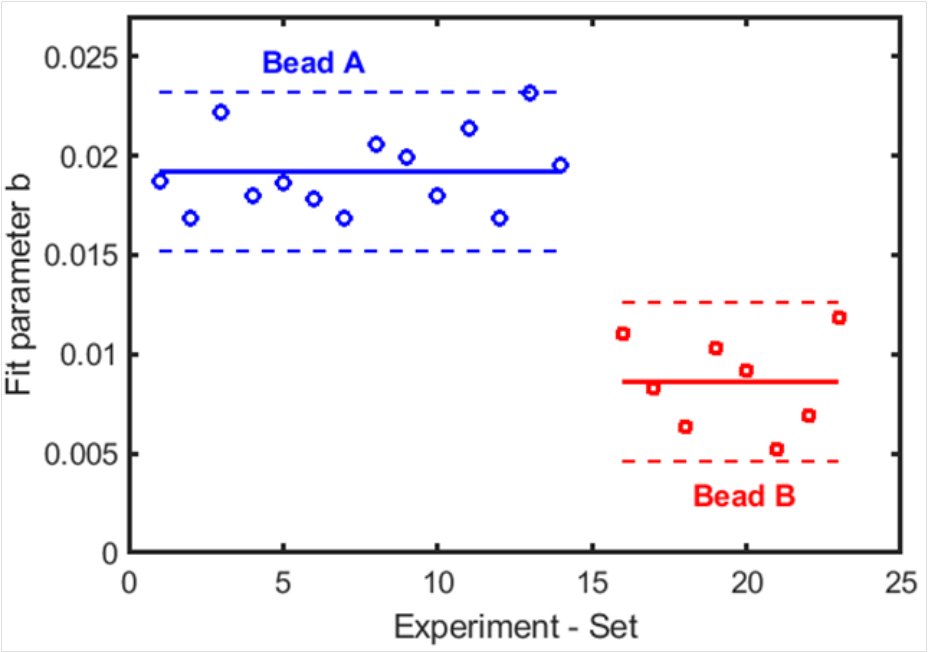

Figure 5.35: The fit parameter along the Y-axis for many acquisitions with different beads of the same species is plotted with Blue being type A and Red being type B. The solid line is the average for each of the species and the dotted line is the 95% confidence interval (2 sigma) for each species.

We have seen how robust the fit gets with additional points and how we can optimise the level of the maximum laser power to avoid phototoxicity. The experiment was repeated multiple times for many fluorescent nanobeads of each species. Now we look at many the fit parameters for all such acquisitions for each of the species. In Figure 5.35 and Figure 5.36 we have many experiments for each of which we look at the b fit parameter. That is, we repeat the process done above for one bead, on multiple beads of two different species and collate the statistics.

We see in Figure 5.35 that the fit parameter is plotted along the Y-axis and the experiment set number along the Y-axis. The initial acquisitions were done for the first kind of species (type A) and the second set (type B) on the right over many days. The acquisitions are marked in Blue for type A and Red for type B. The solid line indicates the average value for the fit parameter b and the dashed lines indicate the 2 sigma level or confidence level of $\sim 95\%$. In Figure 5.35 we repeat what we did previously by taking points from the origin increasingly, to plot the convergence of the fit parameter for each experiment for type B. Initial points close to the origin can either be over-estimated or underestimated with respect to the fit parameter, and it depends on the guess point/initial point from which you begin the fit. The initial values don't fall within 2 σ and therefore we cannot be confident while reporting values close to the origin (low intensity illumination). In Figure 5.36 we represent the data with the mean value and error bars. The experiments were carried out exactly as in the previously discussed case. The fit parameter b is a function

of the lifetime of the fluorescent probe. The lifetime of the fluorophore is defined by the following relation through:

$$\tau \quad \propto \quad \frac{Pulse \quad Duration}{(1/b)} \tag{5.25}$$

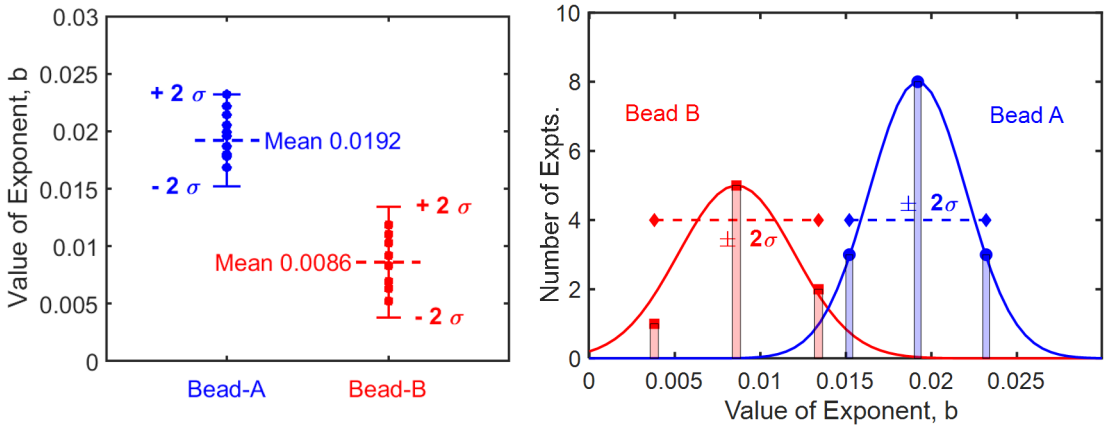

Figure 5.36: Value of the fit parameter b, (a) for Bead-A and Bead-B, obtained in different experimental runs, (b) distribution of b values for two beads. Fit parameter b for Bead-A and Bead-B have overlap beyond 2 σ.

To summarise we have discussed the theory as well as experimental implementation of a new technique to conduct FLIM on a fluorescent nanobeads. We have characterised all the experimental components, along with progressively motivating the reason behind each component. The idea was primarily motivated for using a CW laser. And finally we look at experimental results and statistics associated with it to distinguish two species of fluorophores. In the next Chapter we look at another new approach to do FLIM using integrated fluorescence flux.

7 Conclusion

In this Chapter we presented a novel method which uses continuous laser for studying saturation flux dynamics of a fluorophore. The continuous laser is gated to pulses in the order of tens of microseconds so as to prevent bleaching of the sample. Continuous exposure to the laser excitation would invariably bleach the sample due to phototoxicity. The pulse width used in our experiment was 10 μs. The phenomena of saturation was computationally simulated. The results from Monte Carlo based simulations are presented which indicated how fluorescence lifetime impacts saturation emission-flux of a fluorophore and could be used for classifying flourophores. Through this exercise we demonstrate the possibility of distinguishing fluorophores based on their saturation emission flux, which is a proxy for their lifetime. An experimental setup was designed and built, which has capability to illuminate and excite a fluorescence nano-bead. Excitation from a continuous laser

was gated in the microsecond range using a simple acousto-optic modulator. Both illumination intensity and the fluorescence emission intensity by the nano-bead are recorded. For the excitation signal we use a photodetector voltage value as a proxy to obtain a precise readout. Since we are interested in multiplexing it is not necessary to calibrate the system to obtain the actual lifetime of the probes but to rather differentiate them into two species. This can be extended to do FLIM once the system has been calibrated for a fluorescent probe with a known lifetime. The variation of the detected signal as a function of the excitation power, when increased gradually up to saturation fluorescence emission enabled us to characterize fluorescence lifetime. Hence, using this approach we have shown for two nano-beads having different species of fluorophores (F8800 ThermoFisher and ATTO 565 both having a size of 100 nm diameter), that saturation dynamics as distinct. The exponent that fits the variation of excitation intensity with corresponding emission flux is extracted by curve fitting. We have shown that the exponent, b obtained by this method is distinct and using value of "b", we can distinctly label these two fluorophores with 95 % confidence. The configuration presented in this chapter uses continuous laser, setup is much simpler and inexpensive, which makes this as a promising method for multiplexing based on fluorescence lifetime imaging.

Important extension of this, method is to deploy this in biological environment and do super-resolution microscopy of biological samples.

Chapter 6

New technique of DPFLIM

Summary

In this chapter we introduce a new approach for doing FLIM measurements using two gated pulses from a SCW laser. This approach has not been experimentally implemented before and has a unique advantage in terms of measuring integrated fluorescence emission as a proxy for lifetime of fluorescent probes. This technique utilises integrated fluorescence flux which allows for camera acquisitions in the order of milliseconds as opposed to probing the system at a sub-nanosecond regime for lifetime based multiplexing. We demonstrate mathematically how this can be achieved and derive the necessary experimental conditions for this approach. This novel experimental technique is implemented through an experimental setup which is described in depth.

Contents

1 Introduction and theory for DPFLIM

In the previous chapter we saw an alternative way of doing FLIM which has not been touched upon theoretically or empirically before. In this chapter we discuss a time based FLIM technique which utilises a SCW puled laser to do FLIM with only two pulses. This has been theoretically described [MÜLLER, 1995].

Briefly speaking the parameters of this technique can be described as follows. We need to ensure that the molecules are transitioning from the ground state to near steady state excitation achieved with short temporally tunable pulses generated from the pulsed laser with a tunable delay. The key element in this technique is the delay line introducing a "second pulse". Much like the previous technique saturation here is vital for steady state excitation. This technique is implemented in conjunction with a confocal head (confocal focusing system) and a detector whose dead time must be shorter than the lifetime of the fluorophore emitter in question.

This technique is motivated to study the contrast of lifetimes in terms of change in the environmental conditions or the structure of the fluorophore emitter. As stated in [MÜLLER, 1995] the advantages of using lifetime measurement against the conventional intensity based microscopy is that it offers discernible differences in terms of detection with respect to the background and it can also be implemented as a ratio based imaging technique for quantifying differences in the environment or structure of fluorophore emitters.

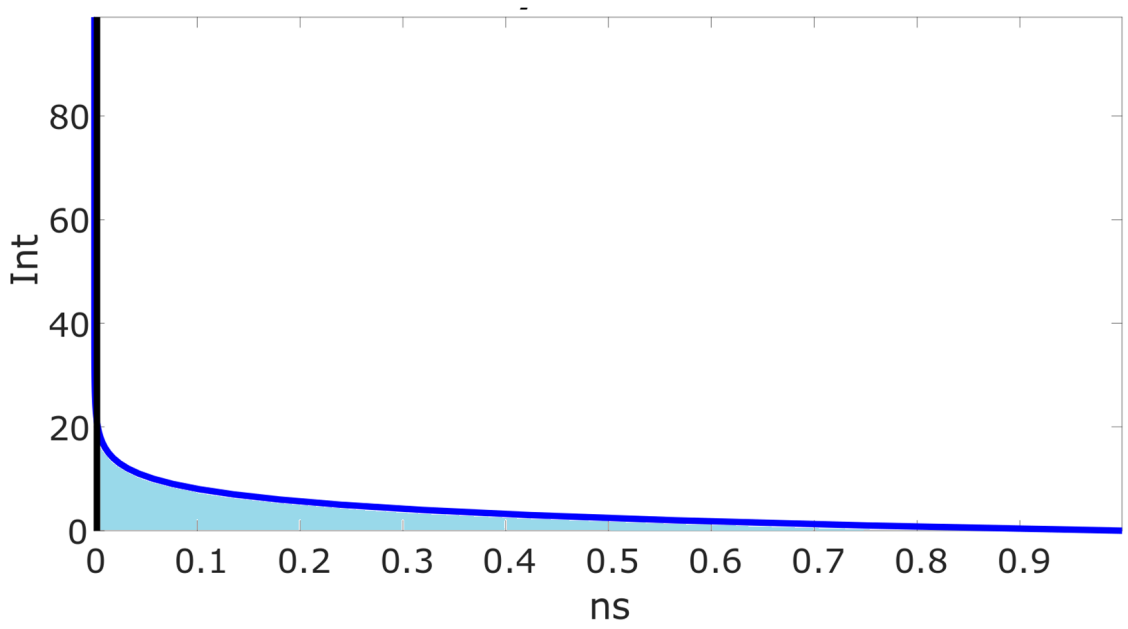

Figure 6.1: Single pulse excitation followed by characteristic relaxation time for ATTO 647N fluorophore emitter indicated in blue. Black line indicates the time at which pulse was supplied, in this case at $t = 0$. The decay dynamics occurs in nanoseconds. The Y-axis is the counts from 0 to 100 of the emitted fluorescence (N) proportional to intensity.

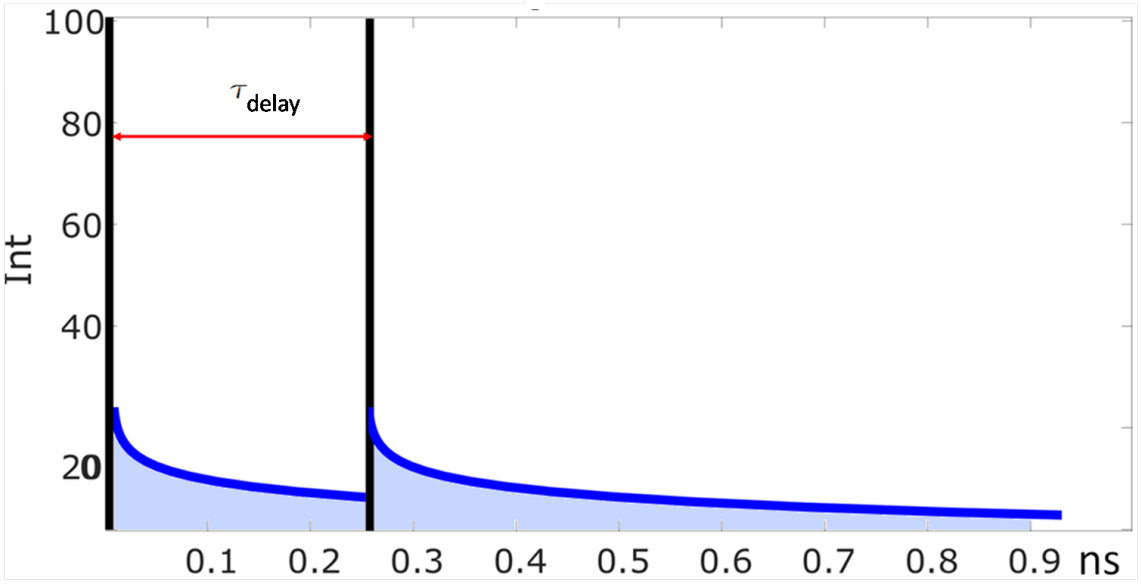

Figure 6.2: Double pulse excitation for ATTO 647N fluorophore emitter, with the two pulses separated by time τ_{delay} which is shorter than the decay time. This delay time is introduced by a second pulse with a larger path length than the first pulse as described below. The blue lines indicate the relaxation dynamics and the shaded blue region is the integrated flux.

In Figure 6.1, the total fluorescence intensity integrated/area under the indicated curve due to a single pulse which excites the fluorescence emitter from the ground state to the excited state is shown. This integrated flux is for a single pulse on the sample. And in Figure 6.2, the sample with the fluorophore emitters are irradiated with two consecutive pulses with a time delay indicated by τ_{delay}. The delay time period can be modulated by increasing the path length of the second pulse compared to the first pulse; more of which will be discussed in the experimental implementation. What happens in this scenario is the fluorophores which have relaxed back to the ground state after the first pulse (in a very short time window), get excited with the second pulse. In the second scenario with the two pulses, the total fluorescence intensity is measured. Which is indicated by the shaded area, since we have to integrate all the fluorophores emitted and the functional form is the exponential as discussed in Chapter 4.

The ratio between the two cases with the two pulses and one pulse gives the fluorescence lifetime of the fluorophore emitter. And for this to be valid it is important for the condition of the steady state excitation to hold, that is, the sample has to be saturated to be mathematically accurate to the derivation for the lifetime through looking at the ratio as a function of the delay time τ_{delay}. This will imply the maximal contrast in the ratios between two species with different lifetimes. That is, the sample must be excited in such a way that all the fluorophore emitters get excited and then they stochastically decay.

Which is decided by the exponential decay curve, most molecules decay very quickly and few molecules take a long time to decay. The molecules that have quickly decayed, are excited again when the second pulse comes along after the delay. And all, not just few, all of the molecules that have decayed are once again excited. This is important to distinguish because it sets up the premise for the importance of saturation in this technique as well. Only then can we take the whole integrated area under these curves to be valid. Otherwise it is a close approximation and the ratio will yield an approximate lifetime which might not be completely useful for differentiating between different emitters or the ambient environment based on the contrast in lifetime alone. Also, in this approach, we assume that only radiative absorption and relaxation occurs and not other pathways. Non-radiative processes, phosphorescence, quenching and bleaching aren't accounted for since they will induce a change in the ratio measured. These modifications can also be incorporated in an 'effective' fluorescence lifetime, that would not affect the method discussed here [MÜLLER, 1995].

1.1 Mathematical Derivation

Here we consider fluorescent probes that are mono-exponential and a simple transition from the ground state to the excited state. This technique will be able to differentiate molecules that could have more complex fluorescence provided the effective transition rates are very different. Let the fluorophores be in ground state indicated by N_0 and excited state N_1 as follows, the total number of fluorophore emitters

$$N \quad = \quad N_0 \quad + \quad N_1 \tag{6.1}$$

The fluorescence signal/intensity can be defined from Chapter 4 equation 4.1 as follows for

$$I(t) \quad = \quad cN_1 e^{\frac{-t}{\tau_{flu}}} \tag{6.2}$$

And here N_1 has maximum number of fluorescence emitters since the sample is saturated with the excitation beam completely. τ_{flu} is the fluorescence lifetime. The integrated intensity in time which is what is measured by the camera/detector is given by the following integral form of equation 6.2.

$$I_1 \quad = \quad N_{1max}\tau_{flu} \tag{6.3}$$

Similarly integrated the function in Figure 6.2 by parts from time 0 to τ_{delay} and then τ_{delay} to infinity and using equation 6.1, we obtain the expression for the integrated intensity

$$I_2 \quad = \quad N_{2max}\tau_{flu}[2 - e^{\frac{-\tau_{delay}}{\tau_{flu}}}] \tag{6.4}$$

And the ratio of equation 6.4 to equation 6.3 gets rid of all the constants and finally we have the expression for the lifetime as follows,

$$Ratio \quad = \quad \frac{I_2}{I_1} \quad = \quad [2 - e^{\frac{-\tau_{delay}}{\tau_{flu}}}] \tag{6.5}$$

The ratio is independent of the fluorescence intensity. The explicit use of I_1 and I_2 is not strictly required as I_2 (at t = 0) could be used as reference instead of I_1. But the usage of both I_1 and I_2 are useful for cases where bleaching occurs and is used to calibrate the system [MÜLLER, 1995].

1.2 Ratio parameters

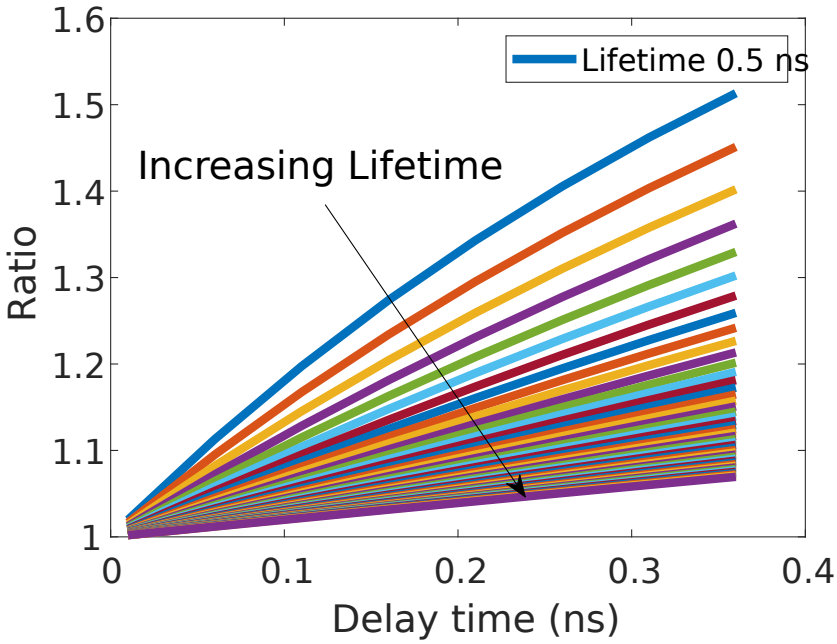

Figure 6.3: Ratio vs Delay time plotted for different lifetimes. We see that upon decreasing the lifetime the change in ratio becomes relatively more.

In this section we vary the lifetime τ_{flu} and the delay time to see the change in the Ratio parameter. In Figure 6.3 we have the delay time along the X-axis and the Ratio along the Y-axis. We see upon increasing the lifetime that the Ratio across different delay times changes less compared to lower lifetimes. Thus, for a given lifetime increasing the delay time gives a higher ratio.

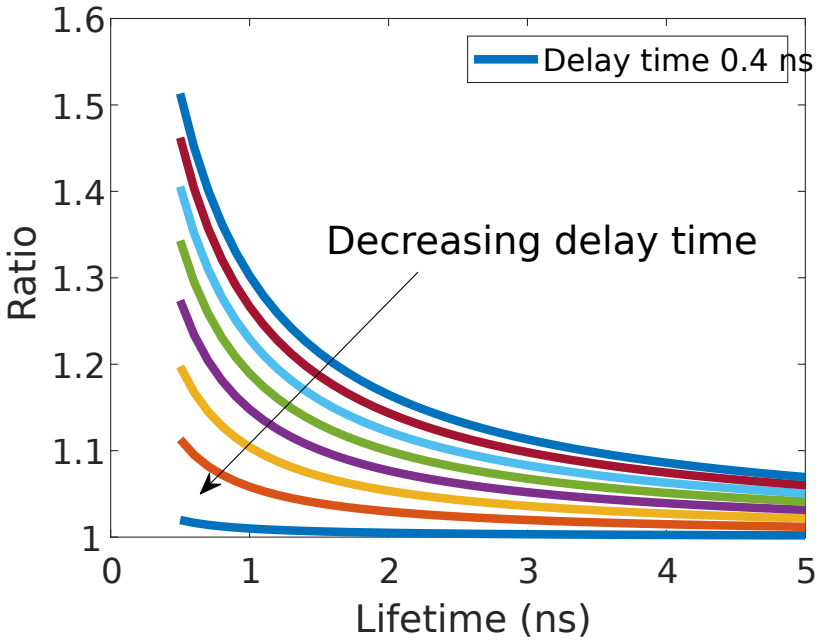

Figure 6.4: Ratio vs Lifetime for different delay times. We see that upon increasing the delay time the change in ratio becomes relatively more.

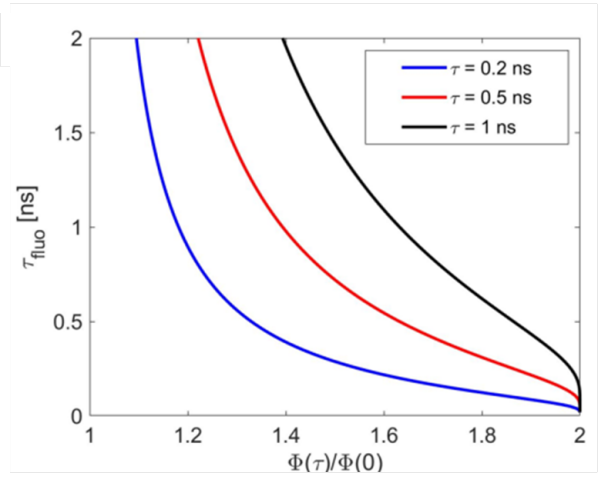

Figure 6.5: For different delay times 0.2 ns (Blue), 0.5 ns (Red) and 1 ns (Black) plotted with the fluorescence lifetime τ along the Y-axis and the ratio along the X-axis

In Figure 6.4 we have the lifetime along the X-axis and the Ratio along the Y-axis. We see upon decreasing the delay time between the two pulses the Ratio across different lifetimes changes less compared to larger delay times between the pulses. Thus, for a given lifetime, increasing the delay time gives a more distinct ratio which can be used to better separate the two species. Since the lifetime is what we wish to probe and the delay time between the two pulses is in our control. In the next Figure 6.5 we have three different delay times between the pulses, with 0.2 ns (Blue), 0.5 ns (Red) and 1 ns (Black) plotted with the fluorescence lifetime τ along the Y-axis and the ratio along the X-axis. This is

another representation of the two plots above where we plot the ratio vs the lifetime to see the dependence between the two.

Thus, we can conclude from this that its optimal to probe species that have a shorter lifetime with a longer delay. The delay (τ_{delay}) is changed by changing the optical path length difference between the two pulse paths. In order to have a larger distinction between the ratios of different species it is important to have a range of optical path lengths and probe the ratio of the integrated photon flux across different delays. This will add to the precision of the measuremnts. We will discuss more on the experimental implementation of this aspect in the next Section.

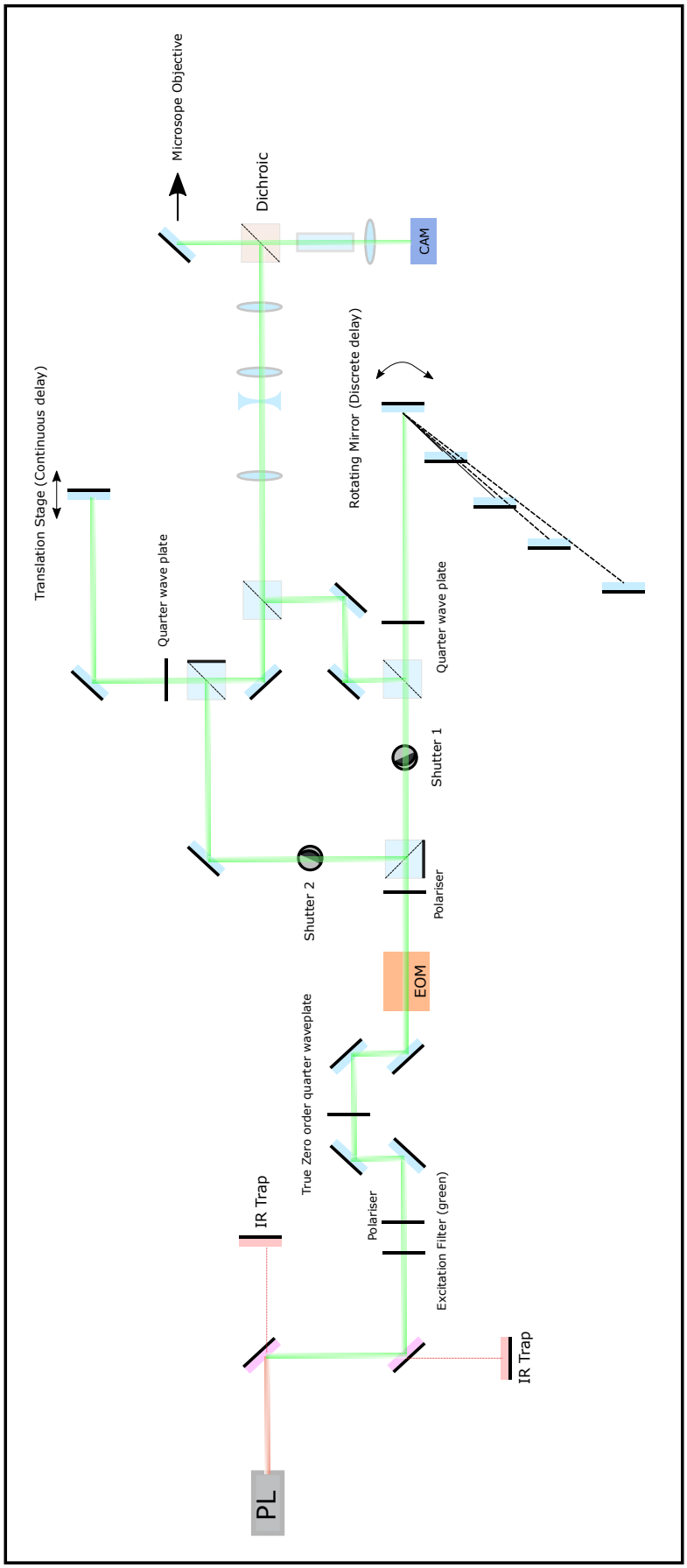

Figure 6.6: Experimental Setup for DPFLIM.

2 Experimental Implementation

In this Section we will look at the experimental implementation of the theory that we have discussed before. In order to illustrate the concept implemented in a system, we first schematically represent what we wish to achieve.

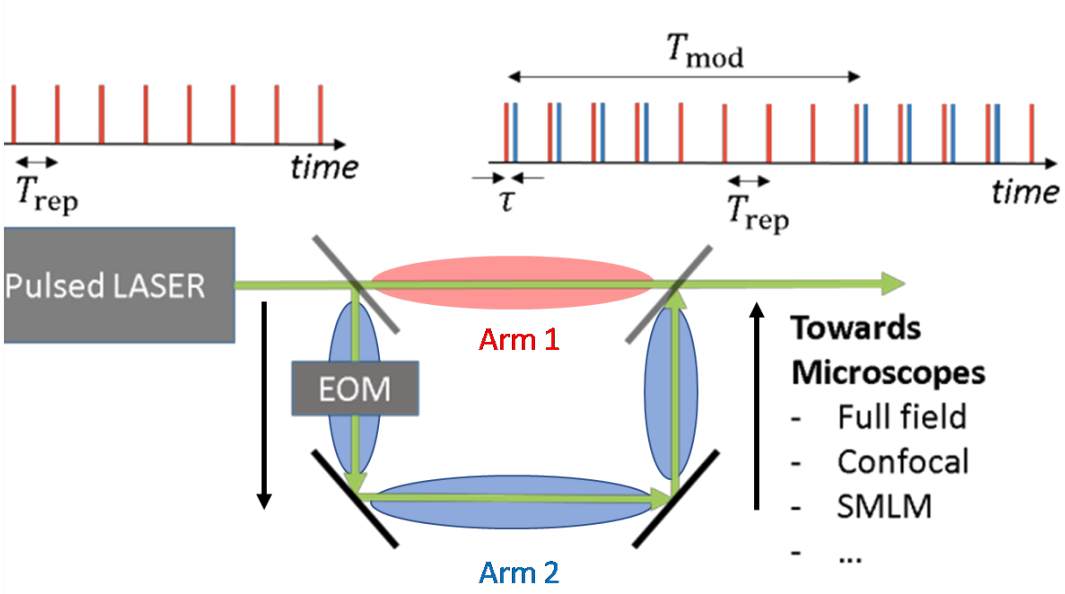

Figure 6.7: Schematic representation of the experimental implementation of DPFLIM, The pulsed laser with the beam split into two arms. Arm 1 depicted in Red and Arm 2 in Blue. Recombined for the illumination (with both arms).

In the Figure 6.7 we have a schematic representation of our setup. On top we have a series of pulses in time, indicated in Red from Arm 1 with a repetition rate indicated as T_{rep}. The pulses from Arm 2 indicated in Blue are pulses introduced after a time delay indicated here as τ_{delay}. The whole set is repeated by a time period of T_{mod}. In the setup, we have a pulsed laser indicated in Green which has two arms. Arm 1 is indicated in Red and Arm 2 is indicated in Blue. This corresponds to the pulses depicted on top in the figure with Red being the pulses and Blue being the pulses with a delay. This time delay is introduced via a difference in the path length of the beam. Initially the beam starts out, is then split into two arms and one of the arms (the Blue Arm 2) has a temporal delay due to a longer optical path length. The ingenious part of this approach is that we have now transposed out the time domain to a spatial domain. So the problem of approaching nanosecond scales is not difficult at all via path length as opposed to doing it in the time domain. And the second aspect is the use of integrated flux which is more readily available as far as detection is concerned.

On the previous page in Figure 6.6 we have the whole experimental implementation schematic diagram of the system we described. And then we move on to describing each

component. We use a SCW pulsed laser as the excitation source due to the fact that we can pick up a range of excitation wavelengths adaptable to different molecules. And we can have the pulses in the picosecond range.

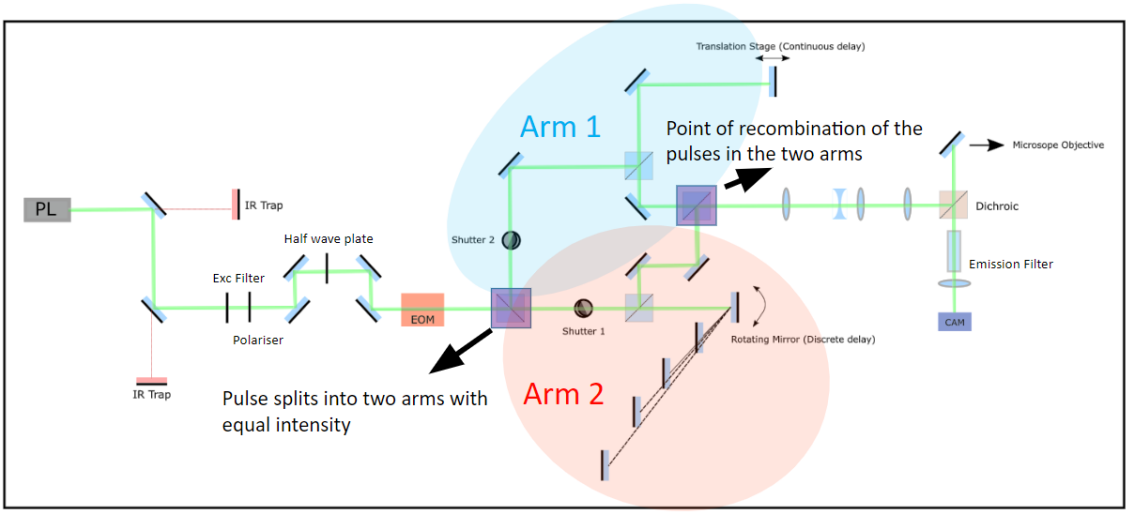

Figure 6.8: Schematic of the setup . The optical path lengths for Arm 1 and Arm 2 indicated in Blue and Red respectively.

In Figure 6.8 we begin by directing the beam from a super continuum pulsed laser using Fianium laser [Fianium SC 400 series] to a filter [Thorlabs FL05780-10] that transmits the IR component and reflects the visible component of the SCW laser beam as indicated in the Figure (Red beam has the IR component). This process is repeated, to filter out all possible IR part of the beam. This is vital for both the safety of the optical components, sample as well as for the experiment. Since most pulsed lasers are IR centric and have very high energy IR component as part of their beams. The IR component of the beam is directed into an IR beam trap [Thorlabs BT610/M]. The beam filtered with the two IR filters passes through an excitation filter from Semrock (522 nm to 582 nm) [562, 40: TXRED-4040C-000] that sends the excitation beam indicated in Green. The beam has a series of mirrors [Thorlabs, BB1-E02] added to use it to align the system (give some working distance) and passes through a half wave plate ($\lambda/2$)[Thorlabs WPH10M-532]. The half wave plates are used to adjust the polarisation of the beam and we will discuss why this is necessary below. To continue, the beam then passes through the Glan-Thompson polariser [Thorlabs GTH5M-A] and then through the *Electro-Optic Modulator* (EOM) [Thorlabs EO-AM-NR-C4] which is used to modulate the beam to the desired frequency for T_{mod} in Figure 6.7. The beam then passes into the polarizing beam splitter cube [Thorlabs VA5-PBS251/M] which has a polariser attached to it and circularly polarises the beam, splitting it into two arms. This step is important to make sure that we have the same amplitude of the beam in both the arms which can be adjusted via adjusting the polarisation of the beam before it impinges on to the beam splitter cube. And its also important to collect and recombine the beam back into a single optical path as well, as

we describe below.

The two arms have shutters so that we have the autonomy to select the beam in the arm of our choice to illuminate the sample. Shutter 1 was from Newport [Electronic Shutter with up to 150 Hz frequency 76992] and Shutter 2 [Thorlabs SH05R/M]. Both arms have a second beam splitter cube that transmits one polarisation and reflects the other polarization which occurs upon reflection. For the optical delay, the path length was tweaked on both arms. On Arm 1 we have a continuous translation stage [Thorlabs DDS300/M] with 30 cm of travel and with a mirror to reflect the beam back into the arm thereby adding two times the path length. And on Arm 2 we have a rotating mount [Thorlabs ELL18K/M] with a mirror and 4 mirrors placed at different fixed distances. The rotation stage itself was placed far from the beam splitter cube. The rotation stage rotates at fixed angles (programmed steps based on where the receiving mirrors are located) to direct the beam to the fixed mirrors indicated via the dotted line for each of them and they reflect back here again adding twice the wavelength. The position of the mirrors were chosen such that we can have 1 ns (up to 5 ns was possible, accommodated to around 30 cm/1 ns to have sub-nanosecond path difference) of path length variability between the pulses which was more than sufficient since we need sub-nanosecond time delay for the experiment. The beams were then aligned and directed back into a beam splitter cube that recombined the two beams into one optical path. This was then compressed using a confocal system and directed into the microscope.

2.1 Results

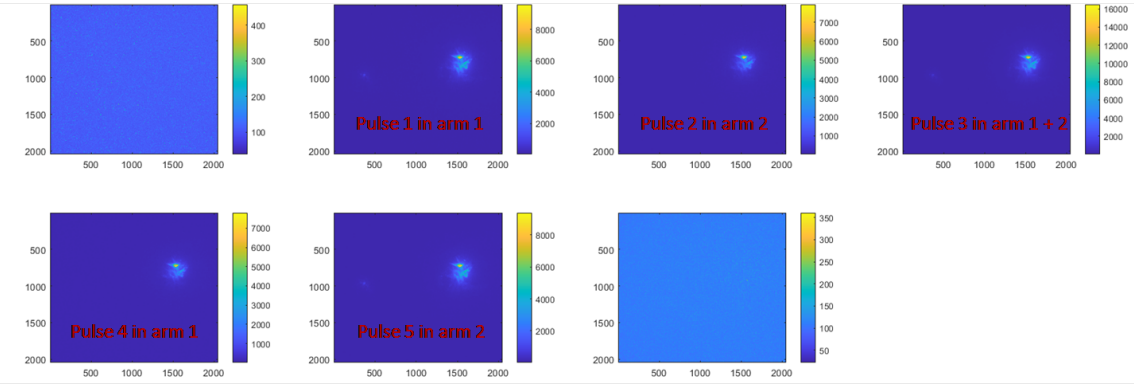

Figure 6.9: COS7 Cell sample illuminated through the excitation beam from Arm 1 and then from Arm 2 followed by both the arms and then Arm 1 and Arm 2 again. The first and last images are references with no illumination on the sample.

The results of the setup are shown in this Section. We see that we need three scenarios. Firstly, we have the pulse from Arm 1, wherein Shutter 1 is ON (in Arm 2), thereby allowing only Arm 1 illumination. The same thing with excitation from Arm 2. Wherein Shutter 2 is ON (in Arm 1) giving only excitation from Arm 2, then we have two pulses

together illumining the sample. So all these scenarios shown in Figure 6.9 are exactly what we play out in Figure 6.10 below.

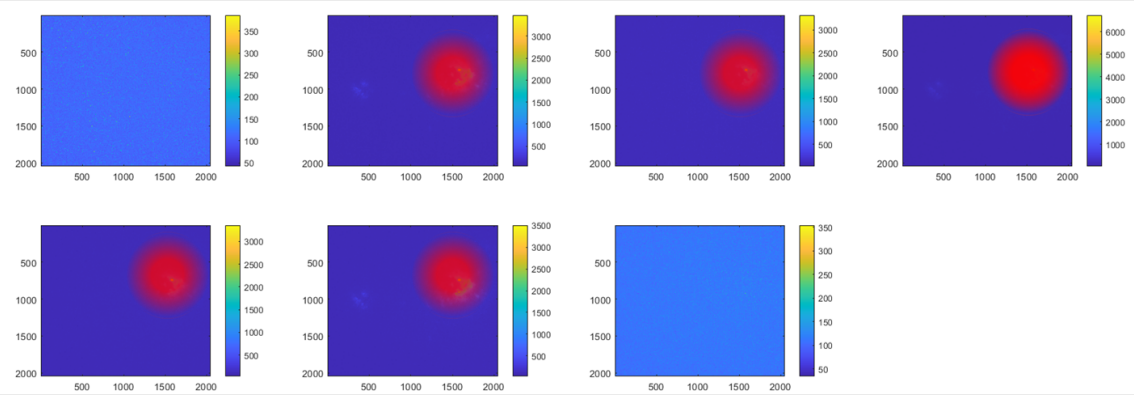

Figure 6.10: Schematic illumination for the above figure with COS7 Cell sample illuminated through the excitation beam from Arm 1 and then from Arm 2 followed by both the arms (more intense illumination) and then Arm 1 and Arm 2 again. The first and last images are references with no illumination on the sample.

We see here that the signal that we have as fluorescence from the camera is basically the integrated fluorescence flux over a timescale of 10 ms (exposure time of the camera). The integrated photon flux is the area under the plot given in Figure 6.2 and Figure 6.1. Which is the total number of photons emitted by the fluorescent probe due to the single pulse from Arm 1 as given in Figure 6.1, and with two pulses from Arm 1 and Arm 2 as shown in Figure 6.2. The camera is triggered to image the fluorescent probe when both the pulses are used to excite it, as well as when the single pulse from Arm1 is present. This gives us the ability to calculate the ratio of the image with both the pulses to when either one of the pulses (either from Arm 1 or Arm 2). The ratio is a function of the lifetime provided we are operating under saturation, where excitation of a molecule has a probability of 1, as discussed in the previous Section. Saturation plays a pivotal role in determining lifetime here since we assume saturation for the derivation (ratio of the image with the two pulses to that with one pulse).

In order to check for saturation we need to compare the individual pulses to that of the combined pulse. So we plot the following 2× mean flux ($Flux_{mean}$) of each arm - flux of both arms (combined pulses) ($Flux_{twopulses}$) vs flux of both arms (combined pulses).

$$2Flux_{mean} \quad - \quad Flux_{twopulses} \quad vs \quad Flux_{twopulses} \tag{6.6}$$

The mean flux for each arm has to be constant (since we ensure that the laser beam intensity through the half wave plate that its divided equally across the two arms). This is done experimentally by adjusting the orientation of the half wave plate to have equal intensity in the two arms by dividing the beam into orthogonal polarizations. The $Flux_{twopulses}$ is the total integrated photons emitted by the fluorescent probe when exposed to both the

pulses from the two arms separated by a temporal delay. Close to saturation we should see a plateauing of the difference between the two with respect to the combined $Flux_{twopulses}$. This would imply that the fluorescence is saturating since the difference between the signal from the single pulse case and the two pulse case becomes independent and constant of the two pulse case.

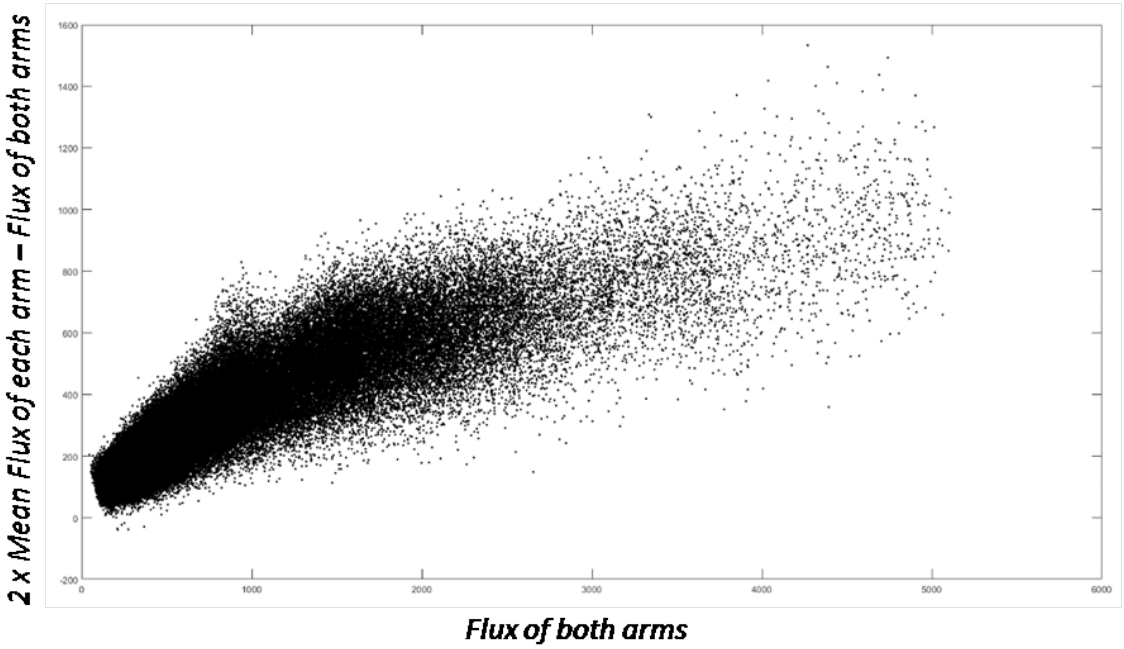

Figure 6.11: For each pixel on the Camera we have the corresponding values plotted to check for saturation. We don't see saturation since we expect there should not be any difference between the pulse from one arm vs the two pulse case, in terms of fluorescence.

We see that from this raw data plotted in Figure 6.11 for each pixel on the camera an increasing trend for the fluorescence signal. But here we see that the points are not close to constant or zero but have an increasing trend. This indicates that we are close to saturation for the sample but not yet in terms of the energy, as we require saturation with a single pulse itself for the theory to be valid we make an improvement in terms of the laser as well as the focusing capacity by using a confocal scanning system that can better compress and focus the beam. Each pulse should have enough intensity to saturate the whole sample and thereby provide the conditions in which the theory can hold. In the next Section we discuss on improvements that can help to saturate the sample and AOI.

2.2 Changing components

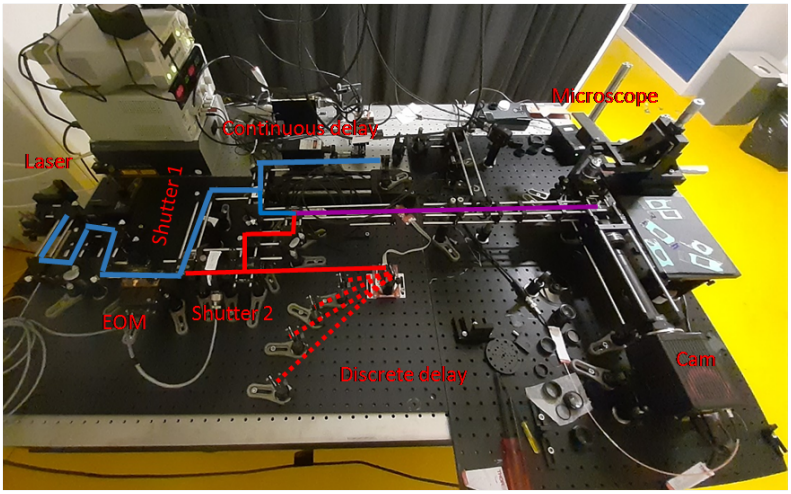

Figure 6.12: The setup as indicated schematically in Figure 6.8. The path length in Arm 1 indicated in Blue and in Arm 2 indicated in Red with the recombined beam in Purple

As discussed in the previous Section, in order to improve the system, we replace the laser (original setup shown in Figure 6.12 with SCW) (SuperK Fianium series used for STED) pulsed laser and the detection instead of using a simple microscope and a camera to a confocal head and a photodetector. As discussed in Chapter 4 we know the advantages of having a confocal system that focuses very well on the sample with a single photon detector that makes lifetime measurements. This can directly yield results in terms of lifetime.

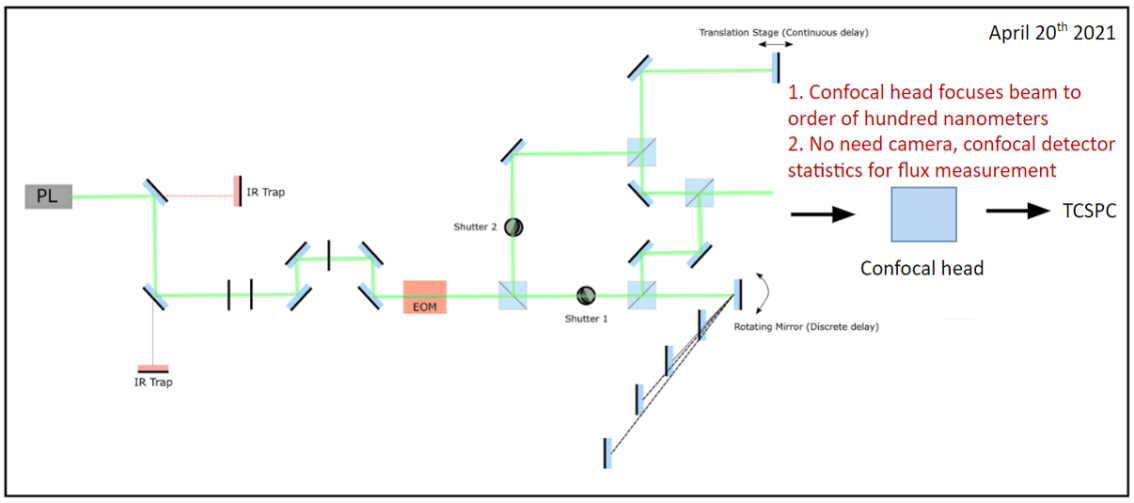

Figure 6.13: Improving the system with a confocal scanner and the TCSPC single photon detector along with the updated laser.

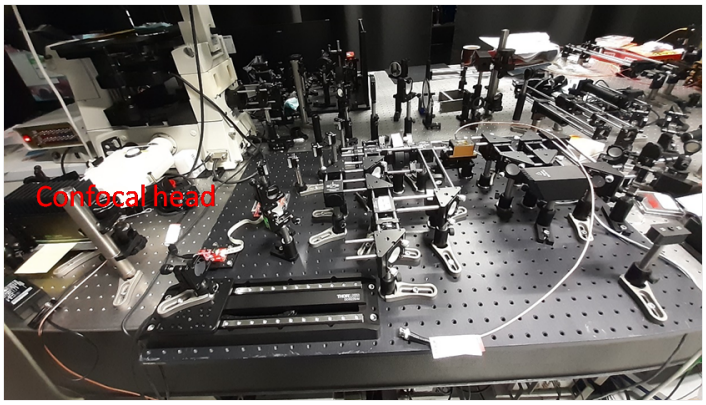

Figure 6.14: Setup after modifications of replacing detector with confocal head along with a new laser.

In Figure 6.13 and 6.14 we summarise the changes in the setup so that this information can be presented at a single glance. In Figure 6.14 is the actual picture of the setup after replacing the detector with the confocal head and the new laser.

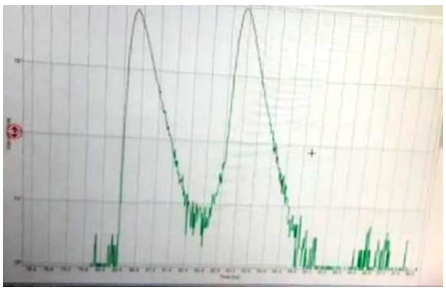

Figure 6.15: Corroborating the intensity given by the photon count from the two arms as shown by the two separated peaks in Green using the TCSPC. The photon count from Arm 1 is indicated on the left and Arm 2 on the right.

As we mentioned in the previous section, we use the half-wave plate to ensure that we have equal intensities across the two arms. We also check for this in the pulses through the Time Correlated Single Photon Counting (TCSPC) as shown in the Figure 6.15. Where we see that the photon count from both the arms (having a distinct time delay that is large) are equal. This further augments our ability to fine-tune the intensities across the two arms prior to the start of the experiment.

3 Conclusion

This chapter presents the theory and experimental setup for another, alternate method to FLIM. In this method we have used "double pulse" from a single pulse laser. We have presented a configuration in which single pulse of the excitation laser was split, and made to travel along two paths, and a delay is introduced between these two paths before these pulses illuminate the sample. The known delay is introduced by adding additional

optical-path along one of the paths. Additional path is 30 cm per one nanosecond delay. We have shown here, how the ratio between the integrated intensities of two consecutive pulses (with a tuneable delay), along with a single pulse is related to the lifetime of a fluorophore. With this simple arrangement we can easily measure lifetime of a fluorophore and can be used for multiplexing.

Further development of this method into a device for microscopy and multiplexing, is being successfully pursued in our group with collaboration at ISMO, Paris Saclay.

Conclusion and Outlook

1 Conclusions

Introduction to various imaging techniques and relevant theoretical background are presented in starting two Chapters of the thesis. Super-resolution microscopy is an important tool for elucidating molecular dynamics and their arrangements in a cell. Super-resolution, at the nano-meter scale, is achieved by localization of individual fluorescence-labelling molecules and the technique is single molecule localisation microscopy (SMLM). One of the requirements for the biological imaging applications is the multiplexing ability to label various types of biomolecules simultaneously. In this context, we here in the thesis, have presented a set of new multiplexing-demixing strategies, one based on the emitted flux of the fluorophore, and two other methods based on lifetimes of the fluorophores.

In Chapter–3 of the thesis, we have presented a new technique based on the emitted-flux from the fluorophore for multiplexing. Emitted flux of a fluorophore depends on the type of the molecule (species), apart from other factors such as its illumination, collection efficiency and its local chemical environment through its quantum yield. However, in a given imaging environment, when all these parameters are more or less constant, emitted fluxes can be used to distinguish different species of fluorophores. In Chapter–3, we demonstrate how this approach can be used for simultaneous imaging with multiplexing. For this purpose, illumination is made uniform using the Adaptive Scanning for Tunable Excitation Regions (ASTER) system. Demonstration of the new strategy is done with DNA-PAINT (Points Accumulation for Imaging in Nanoscale Topography-PAINT) which enables us for accurate flux measurements due to the long ON-time of the emitters. As illustrated in Figure 3.37 and Figure 3.38, two species (ATTO 647N and ATTO 655) have distinctly different photon fluxes. However, also note that these two species have substantially overlapping emission spectra (Figure-3.18). We used ATTO-647N and ATTO-655 to tag tubulin and clathrin respectively in the COS7-cell line. The result of demixing using flux-based technique proposed here is calibrated against spectral-demixing method. We also demonstrate in a given image, a smaller region of interest (ROI) containing two species of fluorophores, proposed technique is efficient in segregating and labeling them as two distinct species (for example see Figure 3.16). The effectiveness of the flux-based technique

was further characterized and quantified by taking a zoomed-in part of the image (refer Figure 3.17). In this case, both in tubulin and clathrin structures of the COS7 cell, we observed for number of molecules which are mislabeled, due to overlapping 'flux-spectra' of two species. This analysis indicated a crosstalk to the extent of 8-25 % (see Figures 3.15 and 3.17) and quantified the effectiveness of the classification. In summary of this chapter, a groundbreaking flux-based multiplexing technique has been presented, showcasing an exceptional accuracy ranging from 80% to 95%. The spectral demixing approach introduces a minimal cross-talk of approximately 5% ([Mau, 2020]). Notably, the rejection rate within spectral demixing spans 30% to 50% ([Mau, 2020]), while the flux-based multiplexing approach yields rejection rates of 25% for DNA-PAINT and a substantial 75% for STORM fluorescent probes due to its short ON times. This underscores the remarkable performance of the fluorescence flux-based demixing technique, particularly for molecules with comparable absorption-emission spectra, a challenge unresolved by state-of-the-art techniques such as spectral demixing. Consequently, a groundbreaking avenue emerges for multiplexing employing a singular excitation laser and a single detection channel. Additionally, this technique facilitates the selection of less phototoxic fluorophores in the red domain (emission in red). Its efficacy has been successfully demonstrated as a standalone method in both DNA-PAINT and STORM, serving as a valuable augmentation to existing multiplexing methodologies by introducing an additional parameter for the disentanglement and classification of diverse species of fluorescent probes. Thus, Chapter–3 of the thesis proposes and demonstrates a new flux-based multiplexing technique for super resolution imaging.

New flux-based multiplexing technique demonstrated here, unlike standard multiplexing methods, has many advantages. Here we briefly indicate few of them. New technique does not require sequential acquisition of the fluorescence signal, targeting one species at a time. Also, in the new technique as the imaging is simultaneous for both species, it prevents drifts and noises. Flux-based method does not require multiple excitation lasers, additional filters, moreover, spectrally overlapping fluorophores could be used for labelling (as long as two species have distinct emission fluxes). Hence proposed new technique is less cumbersome and relatively inexpensive. Flux-based demixing can be used as a standalone technique or combined with a spectral demixing approach to enhance the identification of species by adding one more dimension to the analysis.

The second part of the thesis focuses on novel approaches to perform fluorescence lifetime imaging (FLIM) based on the emitted flux. Fluorescence lifetime is also characteristic feature of a species. Based on which we have proposed demonstrated to use saturation flux dynamics as a device for multiplexing in imaging application. Conventionally, lifetime measuring apparatus uses femtosecond pulsed lasers combined with fast monodetectors to achieve the time resolution needed in the nanosecond and sub-nanosecond range. Implementing conventional lifetime apparatus for imaging as a technique for multiplexing and

demixing is not practical. Keeping this factor in mind, we in the thesis proposed flux-based strategies to avoid the need of using fast and expensive lasers monodetectors. In the saturation regime, the emitted flux from a fluorophore is linked to the fluorescence lifetime.

Introduction and theoretical background for the FLIM is presented in Chapter–4. In the Chapter-5, a novel method is presented that uses continuous laser for studying saturation flux dynamics of a fluorophore. Through which we demonstrate how to distinguish two species of fluorophores. Initially a Monte Carlo simulation-based analysis is carried out to show how fluorescence lifetime impacts saturation emission-flux of a fluorophore (refer Figure 5.7). Simulation is done along with certain noise level arising due to collection and illumination systems used for imaging a nano-bead containing fluorophore species. This exercise clearly indicates the possibility of distinguishing fluorophores based on their saturation emission flux, which is a proxy for their lifetime. An experimental setup was built as shown in the schematic diagram (refer Figure 5.12), which has capability to illuminate a nano-bead having a fluorescein species to excite the molecule. Illumination from the excitation laser is gated in the microsecond range using simple acousto-optic modulator. Both illumination intensity and the fluorescein intensity emitted by the nano-bead is recorded. During a single gated light-pulse, for a given illumination intensity, fluorescence lifetime determines maximum number of fluorescence absorption-emission cycles it can go through. Number of emission cycle thus determines the emission flux. The variation of the detected signal as a function of the excitation power, when increased gradually up to emission saturation enable us to characterize fluorescence lifetime. Hence, using this approach we show (refer Figure 5.35) for two nano-beads having different species of fluorophores (F8800 and ATTO 565), saturation dynamics is distinct. The exponent that fits the variation of excitation intensity with corresponding emission flux is extracted by curve fitting. We show that the exponent, b obtained by this method is distinct (see Figures 5.36 and 5.37) and using value of "b", we can distinctly label these two fluorophores with 95 % confidence (see Figure 5.37). Even the rate of change of emission-flux, with excitation in the lower-rage of excitation intensity, is remarkably different for these two fluorophores. Hence, one may use this to distinguish them, that could circumvent problems associated with photo-bleaching. The configuration presented in this chapter uses continuous laser, setup is relatively simple and inexpensive, still successful in distinguishing fluorophores with 95 % confidence. Which makes this as a promising method for multiplexing for super resolution imaging.

Finally, we have presented another alternative approach to FLIM, by focusing on the traditional setup with a pulsed laser but using the integrated flux of two pulses - DPFLIM (Double Pulse Fluorescence Lifetime Imaging). Here, first we mathematically connect the ratio between the integrated intensities of two consecutive pulses (with a tuneable delay), along with a single pulse to the lifetime of a fluorophore. The theory and experimental

setup of the technique have been explained. Delay between the two pulses in this method is achieved by splitting the light pulse along two paths, and introducing the delay by having an additional path-length (of 30 cm per nanosecond) in the second path. Further development of this method into a device for microscopy and multiplexing, is successfully pursued in our group with collaboration of a PhD student, Mr. Laurent Le at ISMO, Paris Saclay.

Thus, the thesis presents a detailed introduction to super resolution imaging, along with the need for multiplexing for biological imaging. Thesis proposes and demonstrates using fluorescence flux as a method to distinguish fluorophores that can be used independently or along with an existing method (such as spectral demixing) to distinguish fluorophores. In the second approach, thesis proposes and demonstrates fluorescence lifetime as a tool to be used for multiplexing. Under this approach, we have proposed and demonstrated two methods one using continuous laser (with gating) and other using pulsed laser (along with varying delay between two pulses) for distinguishing fluorophores based on their lifetimes.

2 Work in Progress

In Chapter 6 we saw that the DPFLIM setup was being upgraded to have better focus and more energy to make lifetime characterisations. Also in continuation with Chapter 5, there have been improvements in the experimental system with regards to further automation.The results presented in Chpater 5 are from the experimental setup which is automated with the rotating variable density filter for modulation of laser power. The system is further augmented with a second AOM (Figure 7.16) for having a faster control over the power variation and reducing the noise especially under low light excitation condition as shown in the Figure 7.17.

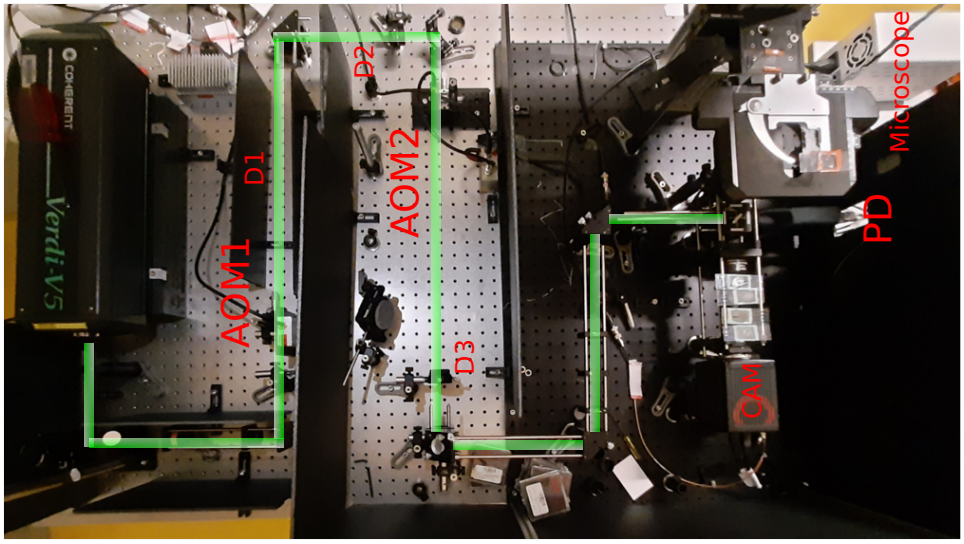

Figure 7.16: Setup with two AOMs. Green indicates the beam path. D1, D2 and D3 are the diaphragms and PD is the photodetector.

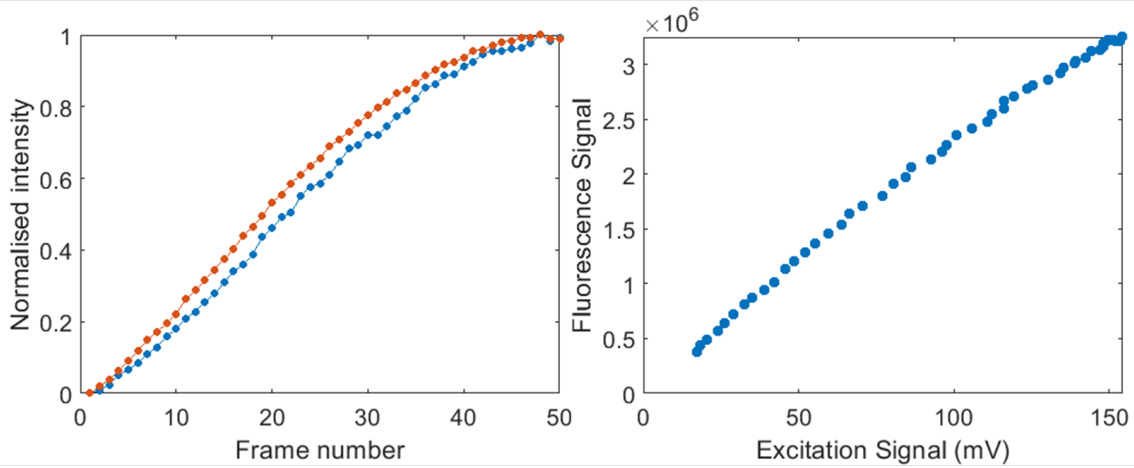

Figure 7.17: Left: Normalised values of excitation and fluorescence signal with 50 data points in one cycle. Right: plot of fluorescence vs excitation for the same dataset, illustrates reduction in noise and increase in rapidity of data collection nearly 100 fold.

3 Outlooks

New flux-based multiplexing has been demonstrated here to distinguish two different proteins, but could be further extended to three proteins. Local analysis developed within this work to discriminate between species, will also play a major role. Since this technique can give information based on the changes in the local environment. Interestingly so far in this area, multiplexing in SMLM has not been presented in combination with a 3D imaging strategy. Since flux dependence axially has been demonstrated, combining this with multiplexing would give z-localisation as well. Flux-based multiplexing can be implemented with conventionally used technique such as PSF engineering but also in combination with supercritical angle (evanescence emission) axial nano-ruler for z-localization. In particular in this last case, SAF information being retrieved by using two cameras to compare under-critical and supercritical emission, introducing a conventional spectral demixing strategy would rather complicate the optical implementation to create four different channels (under critical for multiplexing-two channels and supercritical for z-localization-two channels). Flux-based demixing can directly exploit the acquired information. Outlook of this project would involve extending to multiple excitation sources (tuning the flux independently) with many excitation wavelengths and combining this technique with measurement of other parameters such as z-localization. And importantly, to explore the correlation between species category and spatial configuration. Since molecules that are closer in a certain morphological and spatial structure are more likely to be of the same species, this component can be used to augment the de-mixing process as an added parameter. This would work best for targets that are morphologically distinct such as Clathrin and Tubulin. And finally using these sets of raw images and post classified images using flux-based demixing to develop machine learning based algorithms to automate the process and make predictions on the category of the fluorescent probe in a guven sample.

The new FLIM implementation developed here based on the CW laser, is promising and will be associated with a scanning system to allow imaging on a larger field of view. We also plan to apply it soon on biological samples with known lifetime. This development is driven to offer an original combination between SMLM and lifetime measurements, we will perform these measurements on recently developed fluorescent probes which can blink in living cells while also reporting on their local environment.

List of publications

International Conferences (first author)

Surabhi K Sreenivas, Emmanuel Fort, Sandrine Lêveque Fort. "*New low cost multiplexing for super resolution imaging*". Optogen, Sorbonne Université Campus Pierre et Marie Curie Paris, 2022.

Surabhi K Sreenivas, Emmanuel Fort, Sandrine Lêveque Fort. "*Single Molecule Flux Demixing*". SMLMS, Institut Langevin Paris, 2022.

List of Figures

List of Tables

Bibliography

[Basché, 2008] Thomas Basché, WE Moerner, M Orrit, and UP (eds Wild. *Single-molecule optical detection, imaging and spectroscopy*. John Wiley & Sons, 2008 (cit. on pp. 6, 34).

[Böhmer, 2001] Martin Böhmer, Francesco Pampaloni, Michael Wahl, Hans-Jürgen Rahn, Rainer Erdmann, and Jörg Enderlein. "Time-resolved confocal scanning device for ultrasensitive fluorescence detection". *Review of Scientific Instruments* 72.11 (2001), pp. 4145–4152. eprint: https://doi.org/10.1063/1.1406926 (cit. on pp. 83, 84).

[Bon, 2015] Pierre Bon, Nicolas Bourg, Sandrine Lécart, Serge Monneret, Emmanuel Fort, Jérôme Wenger, et al. "Three-dimensional nanometre localization of nanoparticles to enhance super-resolution microscopy". *Nature Communications* 6 (2015) (cit. on p. 13).

[Bouchet, 2019] D. Bouchet, J. Scholler, G. Blanquer, Y. De Wilde, I. Izeddin, and V. Krachmalnicoff. "Probing near-field light–matter interactions with single-molecule lifetime imaging". *Optica* 6.2 (2019), pp. 135–138 (cit. on p. 87).

[Bourg, 2016] Bourg and Leveque-Fort. "Nanoscopie de fluorescence tri-dimensionnelle pour la biologie". *PhD thesis, University Paris-Saclay* (2016), pp. 11–150 (cit. on pp. 2, 5, 8, 10).

[Bowman, 2019] Adam Bowman, Brannon Klopfer, Thomas Juffmann, and Mark Kasevich. "Electro-optic imaging enables efficient wide-field fluorescence lifetime microscopy". *Nature Communications* 10 (2019) (cit. on pp. 84, 85).

[Cabriel, 2019a] Clément Cabriel, Nicolas Bourg, Pierre Jouchet, Guillaume Dupuis, Christophe Leterrier, Aurélie Baron, et al. "Combining 3D single molecule localization strategies for reproducible bioimaging". *Nature Communications* 10 (2019) (cit. on pp. 28, 29).

[Cabriel, 2019b] Cabriel and Leveque-Fort. "Three-dimensional and multicolour approaches in super-resolution fluorescence microscopy for biology". *PhD thesis, University Paris-Saclay* (2019), pp. 11–200 (cit. on p. 13).

[Celebrano, 2010a] Michele Celebrano, Philipp Kukura, Alois Renn, and Vahid Sandoghdar. "Direct detection of single molecules by optical absorption" (2010) (cit. on pp. 92, 97).

[Celebrano, 2010b] Michele Celebrano, Philipp Kukura, Alois Renn, and Vahid Sandoghdar. "Direct detection of single molecules by optical absorption" (2010) (cit. on p. 107).

[Chang, 1997] Jenghwa Chang, Harry Graber, and Randall Barbour. "Imaging of fluorescence in highly scattering media". *IEEE transactions on bio-medical engineering* 44 (1997), pp. 810–22 (cit. on pp. 96, 101).

[Chaze, 2016] William Chaze, Ophélie Caballina, Guillaume Castanet, and F. Lemoine. "The saturation of the fluorescence and its consequences for laser-induced fluorescence thermometry in liquid flows". *Experiments in Fluids* 57 (2016) (cit. on pp. 93, 95).

[Chekalyuk, 1981] A.M. Chekalyuk, V.V. Fadeev, G.M. Georgiev, and Zh.S. Nickolov. "Application of laser induced saturation of molecular fluorescence for lifetime measurements". *Optics Communications* 38.3 (1981), pp. 177–181 (cit. on p. 98).

[Chien, 2019] Miao-Hsuan Chien, Mario Brameshuber, Benedikt Rossboth, Gerhard J. Schütz, and Silvan Schmid. "Single-molecule Optical Absorption Imaging by Nanomechanical Photothermal Sensing at Room Temperature". *Conference on Lasers and Electro-Optics*. Optica Publishing Group, 2019, SW3L.7 (cit. on p. 107).

[Chien, 2018] Miao-Hsuan Chien, Mario Brameshuber, Benedikt K. Rossboth, Gerhard J. Schütz, and Silvan Schmid. "Single-molecule optical absorption imaging by nanomechanical photothermal sensing". *Proceedings of the National Academy of Sciences* 115.44 (2018), pp. 11150–11155. eprint: https://www.pnas.org/doi/pdf/10.1073/pnas.1804174115 (cit. on p. 97).

[Civitci, 2020] Fehmi Civitci, Julia Shangguan, Ting Zheng, Kai Tao, Matthew Rames, John Kenison, et al. "Fast and multiplexed superresolution imaging with DNA-PAINT-ERS". *Nature Communications* 11 (2020) (cit. on p. 24).

[Datta, 2020a] Rupsa Datta, Tiffany Heaster, Joe Sharick, Amani Gillette, and Melissa Skala. "Fluorescence lifetime imaging microscopy: Fundamentals and advances in instrumentation, analysis, and applications". *Journal of Biomedical Optics* 25 (2020), p. 1 (cit. on p. 93).

[Datta, 2020b] Rupsa Datta, Tiffany M. Heaster, Joe T. Sharick, Amani A. Gillette, and Melissa C. Skala. "Fluorescence lifetime imaging microscopy: fundamentals and advances in instrumentation, analysis, and applications". *Journal of Biomedical Optics* 25.7 (2020), p. 071203 (cit. on pp. 78, 79).

[Devauges, 2011] Viviane Devauges. "Microscopie de fluorescence résolue en temps et en polarisation pour le suivi d'interactions protéiques en neurobiologie". Theses. Université Paris Sud - Paris XI, 2011 (cit. on pp. 80–82).

[Dupuis, 2013] Guillaume Dupuis, Nadia Benabdallah, Aurélien Chopinaud, Céline Mayet, and Sandrine Lévêque-Fort. "Time-resolved wide-field optically sectioned fluorescence microscopy". *Three-Dimensional and Multidimensional Microscopy: Image Acquisition and Processing XX*. Ed. by Carol J. Cogswell, Thomas G. Brown, Jose-Angel Conchello, and Tony Wilson. Vol. 8589. International Society for Optics and Photonics. SPIE, 2013, 85890H (cit. on p. 75).

[Ernest, 2011] Cheryl Ernest. "High-Resolution Studies of the Ã ^{1}A– X ^{1}AElectronic Transition of Formaldehyde: Spectroscopy and Photochemistry" (2011) (cit. on pp. 73, 74).

[Fölling, 2008] Jonas Fölling, Mariano Bossi, Hannes Bock, Rebecca Medda, Christian Wurm, Birka Hein, et al. "Fluorescence nanoscopy by ground-state depletion and single-molecule return". *Nature methods* 5 (2008), pp. 943–5 (cit. on p. 27).

[Georgieva, 2020] Hristina Georgieva, Marco López, Helmuth Hofer, Justus Christinck, Beatrice Rodiek, Peter Schnauber, et al. "Radiometric characterization of a triggered narrow-bandwidth single-photon source and its use for the calibration of silicon single-photon avalanche detectors". *Metrologia* 57 (2020) (cit. on p. 98).

[Georgieva, 2016] Mariya Georgieva, Diego Cattoni, Jean-Bernard Fiche, Thibaut Mutin, Delphine Chamousset, and Marcelo Nollmann. "Nanometer resolved single-molecule colocalization of nuclear factors by two-color super resolution microscopy imaging". *Methods* 105 (2016) (cit. on p. 28).

[Ghauharali, 1997] Rick I. Ghauharali, Michiel Müller, Arjan H. Buist, Thomas S. Sosnowski, Theodore B. Norris, Jeff Squier, et al. "Optical saturation measurements of fluorophores in solution with pulsed femtosecond excitation and two-dimensional CCD camera detection". *Appl. Opt.* 36.18 (1997), pp. 4320–4328 (cit. on p. 94).

[Gimber, 2022] Niclas Gimber, Sebastian Strauss, Ralf Jungmann, and Jan Schmoranzer. *Simultaneous Multicolor DNA-PAINT without Sequential Fluid Exchange Using Spectral Demixing*. 2022 (cit. on p. 23).

[Gómez-García, 2018] Pablo A. Gómez-García, Erik T. Garbacik, Jason J. Otterstrom, Maria F. Garcia-Parajo, and Melike Lakadamyali. "Excitation-multiplexed multicolor superresolution imaging with fm-STORM and fm-DNA-PAINT". *Proceedings of the National Academy of Sciences* 115.51 (2018), pp. 12991–12996. eprint: https://www.pnas.org/doi/pdf/10.1073/pnas.1804725115 (cit. on pp. 24–26).

[Gorpas, 2019] Dimitris Gorpas, Jennifer Phipps, Julien Bec, Dinglong Ma, Sebastian Dochow, Diego Yankelevich, et al. "Autofluorescence lifetime augmented reality as a means for real-time robotic surgery guidance in human patients". *Scientific Reports* 9 (2019), p. 1187 (cit. on p. 73).

[Grauw, 2001] C. J. de Grauw and H. C. Gerritsen. "Multiple Time-Gate Module for Fluorescence Lifetime Imaging". *Applied Spectroscopy* 55.6 (2001), pp. 670–678. eprint: https://doi.org/10.1366/0003702011952587 (cit. on pp. 79, 80).

[Gregor, 2005] Ingo Gregor, Digambara Patra, and Jörg Enderlein. "Optical Saturation in Fluorescence Correlation Spectroscopy under Continuous-Wave and Pulsed Excitation". *ChemPhysChem* 6.1 (2005), pp. 164–170. eprint: https://chemistry-europe.onlinelibrary.wiley.com/doi/pdf/10.1002/cphc.200400319 (cit. on p. 98).

[Gustafsson, 2000] M. G. L. Gustafsson. "Surpassing the lateral resolution limit by a factor of two using structured illumination microscopy". *Journal of Microscopy* 198.2 (2000), pp. 82–87. eprint: https://onlinelibrary.wiley.com/doi/pdf/10.1046/j.1365-2818.2000.00710.x (cit. on p. 9).

[Hell, 1994] Stefan W. Hell and Jan Wichmann. "Breaking the diffraction resolution limit by stimulated emission: stimulated-emission-depletion fluorescence microscopy". *Opt. Lett.* 19.11 (1994), pp. 780–782 (cit. on p. 6).

[Isbaner, 2016] Sebastian Isbaner, Narain Karedla, Daja Ruhlandt, Simon Christoph Stein, Anna Chizhik, Ingo Gregor, et al. "Dead-time correction of fluorescence lifetime measurements and fluorescence lifetime imaging". *Opt. Express* 24.9 (2016), pp. 9429–9445 (cit. on pp. 87, 88).

[Jensen, 1992] Craig C. Jensen and Hartmut Schröder. "Complete optical analysis of an UV laser dye using saturation techniques". *Appl. Opt.* 31.33 (1992), pp. 7012–7021 (cit. on pp. 97, 98).

[Kaur, 2017] A. Kaur, Z. Lim, K. Yang, and E.J. New. "8.14 - Fluorescent Sensors for Biological Metal Ions". *Comprehensive Supramolecular Chemistry II*. Ed. by Jerry L. Atwood. Oxford: Elsevier, 2017, pp. 295–317 (cit. on p. 76).

[Kumar, 2016] Suraj Kumar, Aditya Singh, Vijay R. Singh, Jude B. George, and J. Balaji. "Saturation Dynamics Measures Absolute Cross Section and Generates Contrast within a Neuron". *Biophysical Journal* 111.6 (2016), pp. 1328–1336 (cit. on pp. 97, 103, 107).

[Kwon, 2015] Jiwoong Kwon, Jihee Hwang, Jaewan Park, Gi Rim Han, K. Young, and Seong Kim. "RESOLFT nanoscopy with photoswitchable organic fluorophores". *Scientific Reports* 5 (2015), p. 17804 (cit. on p. 11).

[Lagarto, 2017] Joao Lagarto, Jonathan Hares, Christopher Dunsby, and Paul French. "Development of Low-Cost Instrumentation for Single Point Autofluorescence Lifetime Measurements". *Journal of fluorescence* 27 (2017) (cit. on p. 89).

[Lampe, 2012] André Lampe, Volker Haucke, Stephan J. Sigrist, Mike Heilemann, and Jan Schmoranzer. "Multi-colour direct STORM with red emitting carbocyanines". *Biology of the Cell* 104.4 (2012), pp. 229–237. eprint: https://onlinelibrary.wiley.com/doi/pdf/10.1111/boc.201100011 (cit. on p. 18).

[Lin, 2012] Po-Yen Lin, Shin-Shian Lee, Chia-Seng Chang, and Fu-Jen Kao. "Long working distance fluorescence lifetime imaging with stimulated emission and electronic time delay". *Opt. Express* 20.10 (2012), pp. 11445–11450 (cit. on p. 86).

[Marquer, 2011] Catherine Marquer, Viviane Devauges, Jack-Christophe Cossec, Géraldine Liot, Sandrine Lécart, Frédéric Saudou, et al. "Local cholesterol increase triggers amyloid precursor protein-Bacel clustering in lipid rafts and rapid endocytosis". *The FASEB Journal* 25.4 (2011), pp. 1295–1305. eprint: https://faseb.onlinelibrary.wiley.com/doi/pdf/10.1096/fj.10-168633 (cit. on p. 75).

[Mau, 2020] Mau and Leveque-Fort. "Développements pour l'imagerie quantitative et à haut contenu en microscopie de fluorescence classique et super-résolue". *PhD thesis, University Paris-Saclay* (2020), pp. 11–200 (cit. on pp. 21, 22, 35–37, 71, 154).

[Maus, 2001] Michael Maus, Mircea Cotlet, Johan Hofkens, Thomas Gensch, Frans C. De Schryver, J. Schaffer, et al. "An Experimental Comparison of the Maximum Likelihood Estimation and Nonlinear Least-Squares Fluorescence Lifetime Analysis of Single Molecules". *Analytical Chemistry* 73.9 (2001), pp. 2078–2086. eprint: https://doi.org/10.1021/ac000877g (cit. on p. 88).

[MÜLLER, 1995] M. MÜLLER, R. GHAUHARALI, K. VISSCHER, and G. BRAKENHOFF. "Double-pulse fluorescence lifetime imaging in confocal microscopy". *Journal of Microscopy* 177.2 (1995), pp. 171–179. eprint: https://onlinelibrary.wiley.com/doi/pdf/10.1111/j.1365-2818.1995.tb03547.x (cit. on pp. 138, 140, 141).

[Pelet, 2004] S. Pelet, M.J.R. Previte, L.H. Laiho, and P.T. C. So. "A Fast Global Fitting Algorithm for Fluorescence Lifetime Imaging Microscopy Based on Image Segmentation". *Biophysical Journal* 87.4 (2004), pp. 2807–2817 (cit. on p. 88).

[Phillips, 1985] D. Phillips, R.C. Drake, D.V. O'Connor, and R.L. Christensen. "Time Correlated Single-Photon Counting (Tcspc) Using Laser Excitation". *Instrumentation Science & Technology* 14.3-4 (1985), pp. 267–292. eprint: https://doi.org/10.1080/10739148508543581 (cit. on p. 78).

[Polisseni, 2016] Claudio Polisseni, Kyle D. Major, Sebastien Boissier, Samuele Grandi, Alex S. Clark, and E. A. Hinds. "Stable, single-photon emitter in a thin organic crystal for application to quantum-photonic devices". *Opt. Express* 24.5 (2016), pp. 5615–5627 (cit. on p. 98).

[Ross, 2008] Justin Ross and David Jameson. "Time-resolved methods in biophysics. 8. Frequency domain fluorometry: Applications to intrinsic protein fluorescence". *Photochemical photobiological sciences : Official journal of the European Photochemistry Association and the European Society for Photobiology* 7 (2008), pp. 1301–12 (cit. on p. 82).

[Schreiber, 2018] Benjamin Schreiber. "Selective and enhanced fluorescence by biocompatible nanocoatings to monitor G-protein-coupled receptor dynamics". PhD thesis. 2018 (cit. on p. 3).

[Suhling, 2019] Klaus Suhling, Liisa M. Hirvonen, Wolfgang Becker, Stefan Smietana, Holger Netz, James Milnes, et al. "Wide-field time-correlated single photon counting-based fluorescence lifetime imaging microscopy". *Nuclear Instruments and Methods in Physics Research Section A: Accelerators, Spectrometers, Detectors and Associated Equipment* 942 (2019), p. 162365 (cit. on p. 80).

[Szalai, 2021] Alan Szalai, Bruno Siarry, Jeronimo Lukin, David Williamson, Nicolás Unsain, Alfredo Caceres, et al. "Three-dimensional total-internal reflection fluorescence nanoscopy with nanometric axial resolution by photometric localization of single molecules". *Nature Communications* 12 (2021), p. 517 (cit. on pp. 34, 35).

[Thompson, 2002] Russell E. Thompson, Daniel R. Larson, and Watt W. Webb. "Precise Nanometer Localization Analysis for Individual Fluorescent Probes". *Biophysical Journal* 82.5 (2002), pp. 2775–2783 (cit. on p. 8).

[Wade, 2019] Orsolya K. Wade, Johannes B. Woehrstein, Philipp C. Nickels, Sebastian Strauss, Florian Stehr, Johannes Stein, et al. "124-Color Super-resolution Imaging by Engineering DNA-PAINT Blinking Kinetics". *Nano Letters* 19.4 (2019), pp. 2641–2646. eprint: https://doi.org/10.1021/acs.nanolett.9b00508 (cit. on p. 26).

[Wong, 2020] Ka-Leung Wong, Jean-Claude G. Bünzli, and Peter A. Tanner. "Quantum yield and brightness". *Journal of Luminescence* 224 (2020), p. 117256 (cit. on p. 32).

[Zhang, 2015] Zhengyang Zhang, Samuel J Kenny, Margaret Hauser, Wan Li, and Ke Xu. "Ultrahigh-throughput single-molecule spectroscopy and spectrally resolved super-resolution microscopy". *Nature methods* 12.10 (2015), pp. 935–938 (cit. on p. 24).

RÉSUMÉ

La microscopie de fluorescence super-résolue par localisation de molécules uniques appelée *Single Molecule Localisation Microscopy* (SMLM) offre une sensibilité compatible avec l'émission d'un émetteur individuel et une résolution de l'ordre de dizaines de nanomètres. La SMLM s'impose actuellement comme un outil important pour identifier les assemblages moléculaires au sein d'une cellule. Dans ce contexte, le multiplexage, c'est-à-dire l'imagerie simultanée de plusieurs émetteurs fluorescents permettant de révéler différentes biomolécules, reste un défi à relever. Dans cette thèse, les caractéristiques de fluorescence des émetteurs, telles que le flux, sont utilisées comme une nouvelle source de contraste pour imager différentes protéines, et permet également de venir améliorer des approches de demixage basées sur les propriétés spectrales des fluoropphores. La deuxième propriété, la durée de vie de fluorescence, est utilisée pour concevoir de nouvelles approches pour l'imagerie de fluorescence résolue en temps FLIM. Généralement, l'identification de différentes protéines est basée sur une méthode d'acquisition séquentielle de fluorophores ayant des spectres d'émission suffisamment différents. Ces méthodes présentent différents inconvénieents comme l'utilisation couteuse de plusieurs lasers, en fonction des gammes de longueur d'onde utilisées l'imapct des aberrations chromatiques peut entrainer des biais de mesures importants, de plus la vitesse d'acquisition est nécéssairement impactée par la nécessité des acquisitions successives. Dans la première partie de cette thèse, une nouvelle stratégie de démixage est présentée, basée sur le flux de fluorescence d'un fluorophore. Lorsque des facteurs tels que l'illumination, l'efficacité de la collection et son environnement chimique local sont contrôlés, le flux détecté dépend du type d'émetteur du fluorophore, et peut être utilisé pour distinguer différentes espèces. Comme cette technique est indépendante des spectres d'émission, elle peut être appliquée à des fluorophores dont les spectres sont très proches, et peut être mise en œuvre avec un système de microscopie SMLM monocameéra standard SMLM sans nécéssité de matériel supplémentaire. De plus, cette approche peut également permettre d'améliorer l'efficacité du démixage dans un système de spectral demixing conventionnel. La deuxième partie de la thèse se concentre sur de nouvelles approches pour la microscopie de fluorescence résolue en temps *Fluorescence Lifetime Imaging Microscopy* (FLIM) basé sur le flux émis. Nous proposons deux nouvelles stratégies basées sur le flux dans lesquelles il n'est pas nécessaire d'utiliser un laser pulsé ou un système de détection rapide et coûteux. Dans le régime de saturation d'un fluorophore, le flux émis dépend de la durée de vie de la fluorescence. Cela peut être utilisé pour estimer les durées de vie et pour distinguer deux émetteurs fluoroscents. Dans la première configuration, on utilise un laser continu déclenché pendant des portes dans la gamme des microsecondes afin de saturer le fluorophore. À saturation, le flux détecté dépend du nombre maximal de cycles d'absorption-émission de fluorescence et donc de la durée de vie de la fluorescence. La variation du signal détecté en fonction de l'excitation jusqu'à la saturation nous permet de retrouver la durée de vie de fluorescence. Comme preuve de concept, nous avons pu distinguer deux types de billes fluorescentes incorporant deux fluorophores de durée de vie différentes. La deuxième configuration implique l'utilisation d'un laser pulsé avec une ligne à retard optique pour contrôler le délai entre deux impulsions successives. A saturation, en raison de l'anti-bunching, le signal détecté intégré sur une série donnée de doubles impulsions dépend du retard entre ces impulsions. La durée de vie de la fluorescence peut être extraite à partir d'acquisitions de signaux avec un retard variable. La théorie de cette technique et la configuration du montage sont présentées dans cette thèse.

MOTS CLÉS

Super-résolution, Microscopie, Multiplexage, Flux, SMLM, FLIM, Saturation

ABSTRACT

Single Molecule Localization Microscopy *Single Molecule Localisation Microscopy* (SMLM) is a one of the super-resolution fluorescence microscopy, it exhibits a sensitivity down to an individual emitter and offers a resolution in the order of tens of nanometers. SMLM is central in unravelling molecular assemblies and molecular dynamics within a cell. In this context multiplexing which is the imaging of multiple fluorophore emitters simultaneously via labelling of various types of bio-molecules is still a challenge and is highly desirable. In this thesis fluorescence characteristics of fluorophore emitters such as flux is presented as a novel technique for multiplexing but also improved approach for spectral demixing, and the second property being lifetime is used to design new techniques theoretically and experimentally for Fluorescence Lifetime Imaging FLIM. Multiplexing and demixing is either based on a method of sequential acquisition of targeted fluorophores or with fluorophores having sufficiently different spectra. These methods are expensive setups due to multiple laser, prone to chromatic aberrations and slow in terms of acquisition. In the first part of this thesis, a novel demixing strategy is presented based on fluorescence-flux of a fluorophore. When factors such as illumination, collection efficiency and its local chemical environment are controlled, detected flux depends on the type of fluorophore emitter, and can be used to distinguish different species and perform simultaneous demixing. As the technique is independent of emission spectra, this technique can be applied to spectrally overlapping fluorophores, and can be implemented with standard SMLM monocamera system with no additional hardware. This can also further enhance the efficiency of demixing in a conventional spectral demixing system. The second part of the thesis focuses on novel approaches to perform *Fluorescence Lifetime Imaging Microscopy* (FLIM) based on the emitted flux. We propose two new flux-based strategies in which one does not require a pulsed laser or a fast and expensive detection systems. In the saturation regime of a fluorophore, emitted flux depends on fluorescence lifetime. This can be used to estimate lifetimes and to distinguish two fluorophore emitters. In the first configuration, a continuous wave laser gated in the microsecond range is used that can saturate the fluorophore. At saturation the detected flux depends on the maximum number of fluorescence absorption-emission cycles and hence on the fluorescence lifetime. The variation of the detected signal as a function of the excitation up to saturation enables us to retrieve the fluorescence lifetime. As a proof of concept, we distinguish two types of fluorophore beads with this configuration. The second configuration involves the use of a pulsed laser with an optical delay line to control the time delay between two successive pulses. At saturation, due to anti-bunching, detected signal integrated over a given series of double pulses depends on the delay. The fluorescence lifetime can be retrieved from signal acquisitions with a varying delay. The theory for this technique and the configuration of the setup are presented in this thesis.

KEYWORDS

Super-resolution, Microscopy, Multiplexing, Flux, SMLM, FLIM, Saturation